PROGRESS IN RESEARCH

April 1, 2020 - March 31, 2021

CYCLOTRON INSTITUTE

Texas A&M University

College Station, Texas

PROGRESS IN RESEARCH

APRIL 1, 2020 - MARCH 31, 2021

Prepared By

The Cyclotron Institute Staff

Texas A&M University

College Station, TX 77843-3366

Phone: (979) 845-1411
Fax: (979) 845-1899

Web: http://cyclotron.tamu.edu

August 2021

TABLE OF CONTENTS

SECTION II: HEAVY ION REACTIONS

SECTION III: NUCLEAR THEORY

SECTION IV: RADIOCHEMISTRY

SECTION V: SUPERCONDUCTING CYCLOTRON, INSTRUMENTATION AND RIB UPGRADE

Introduction
April 1, 2020 – March 31, 2021

Progress in research and operations at the Texas A&M Cyclotron Institute is summarized in this report for the period April 1, 2019 through March 31, 2020. The period covered by this report was unprecedented as the COVID-19 pandemic raged world-wide. The CI continued operations throughout this time with new procedures to ensure that we could run as safely as reasonably achievable. In the beginning of this period, operations were limited to the radiation effects program due to its importance to national security. While operations for the discovery science portion of the program was put on hold initially, we were able to resume full operation during the summer with new procedures that limited access to the operations portions of the building and reduced person density throughout the facility. In February Texas experienced an extreme weather event, which caused significant damage to infrastructure throughout the state and here on campus. Due to heroic efforts on the part of our operations staff the cyclotrons survived with minor issues and only about 2 weeks of lost running time. The CI has had a remarkably productive year despite the circumstances and I am indebted to the dedicated operations staff that kept the facility running during this challenging period.

The K500 provided 4129 hours of beam for both science and radiation effects testing despite the pandemic, which caused an enormous problem with handling unscheduled maintenance issues. A particular issue occurred in November with the catastrophic failure of the twenty-five-year-old ECR ion source servicing the K500 cyclotron. Luckily, a new ECR ion source was in the final stage of assembly. In this reporting period, 1544 hours of beam time was lost to unscheduled maintenance. The K150 cyclotron provided 3767 hours of beam on target and continues to be used by external customers for radiation effects testing with its proton and 15 MeV/u heavy-ion beams, two of which are newly developed.

The format of this report follows that of previous years. Sections I through IV contain reports from individual research projects. Operation and technical developments are given in Section V. Section VI lists the publications with Cyclotron Institute authors and outside users and the Appendix gives additional information including talks presented by members of the Institute during the past year. Once again, the full volume of this year's Progress in Research is available only on our web site (http://cyclotron.tamu.edu). Since most of the contributions presented here are truly reports on progress in research, results and conclusions should not be quoted from the report without the consent of the authors.

I am indebted to Dr. Y.-W. Lui for assembling this report.

S.J. Yennello
August 11, 2021

SECTION I

NUCLEAR STRUCTURE, FUNDAMENTAL INTERACTIONS AND ASTROPHYSICS

Neutron-induced triple-alpha enhancement: measuring neutron-induced reactions with TexAT

J. Bishop,[1] C.E. Parker,[1] G.V. Rogachev,[1-3] S. Ahn,[1,2] C.R. Brune,[4] K. Brandenburg,[4] R. Charity,[5] J. Derkin,[4] N. Dronch,[5] G. Hamad,[4] Y. Jones-Alberty,[4] Tz. Kokalova,[6] E. Koshchiy,[1] V. Ohstrom,[5] S. Paneru,[4] S.T. Marley,[7] T.N. Massey,[4] Z. Meisel,[4] R. Smith,[8] L.G. Sobotka,[5] D. Soltesz,[4] A.V. Voinov,[4] and J. Warren[4]

[1]*Cyclotron Institute, Texas A&M University, College Station, Texas 77843*

[2]*Department of Physics & Astronomy, Texas A&M University, College Station, Texas 77843*

[3]*Nuclear Solutions Institute, Texas A&M University, College Station, Texas 77843*

[4]*Department of Physics & Astronomy, Ohio University, Athens, Ohio 45701*

[5]*Department of Chemistry, Washington University, St. Louis, Missouri 63130*

[6]*School of Physics & Astronomy, University of Birmingham, Edgbaston B15 2TT, United Kingdom*

[7]*Department of Physics and Astronomy, Louisiana State University, Baton Rouge, Louisiana 70803*

[8]*College of Business, Technology and Engineering, Sheffield Hallam University, Sheffield S1 1WB, United Kingdom*

The triple-alpha reaction, by which helium is fused to form carbon, is an important reaction mechanism to overcome the A=5, 8 bottleneck which is facilitated by the Hoyle state at 7.65 MeV. The reaction rate is determined by the radiative width, i.e. how often the Hoyle state decays to end up with carbon-12 in the ground state. As well as the sequential gamma-decay and pair-production, it was demonstrated that in certain astrophysical environments, an alternative decay path can dominate (by up to a factor of 100): that of neutron up-scattering [1]. In this situation, a low-energy neutron interacts with the excited nucleus and carries away a large amount of energy such that the nucleus can de-excite to the ground state (or the first-excited state). The cross section for this interaction is unknown due to the experimental difficulties in measuring it. To determine this cross section, the time-reversed reaction has been studied for the first time using TexAT [2] which will allow for a measurement of the enhancement of the triple-alpha rate via the effect of the neutrons.

The time-reversed reaction is that of $^{12}C(n,n_2)3\alpha$ and must be studied in the astrophysically-relevant energy regime of between the threshold at 8.3 MeV, and 10 MeV. This experiment therefore required a high-intensity, monochromatic, collimated neutron source such as that available at Ohio University [3] via the D(d,n) reaction. This well-suited neutron beam is then incident upon TexAT, filled with 50 Torr CO_2 where the charged-particle products can be measured.

This CENTAUR experiment represented a large collaboration; TAMU, LSU and WashU as well as collaborators at Ohio University, Sheffield Hallam University (UK) and the University of Birmingham (UK). The experiment was finished in August 2021 following COVID-related restrictions easing.

The analysis of this data set has been almost fully completed and a manuscript is currently in production.

The properties of the neutron beam were benchmarked by measuring a single energy with a pulsed beam to measure the neutron energy spectrum using the time-of-flight with an NE213 detector placed at 30 m from the source. The comparison between the expected neutron energy spectrum from a

GEANT4 simulation in comparison to the n-TOF spectrum is shown in Fig. 1 which shows excellent agreement.

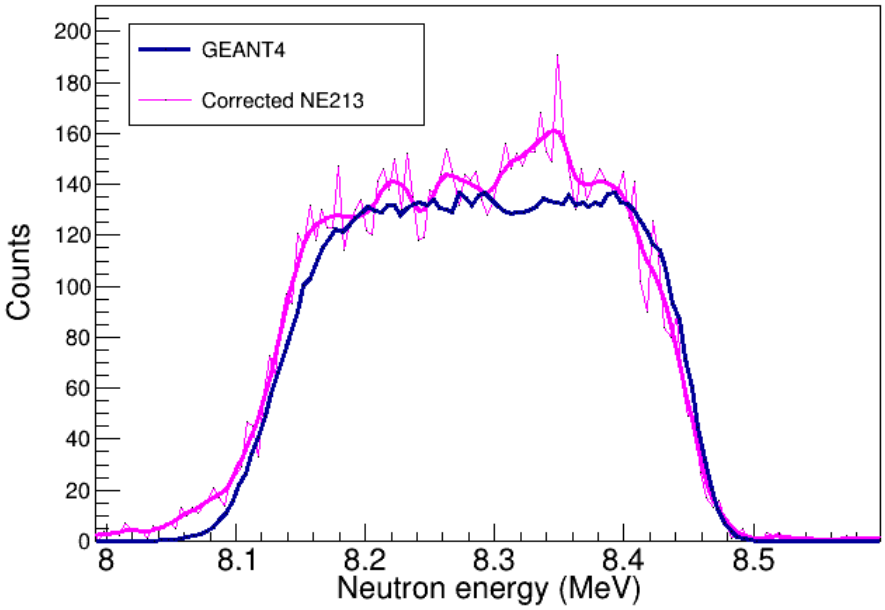

Fig. 1. n-TOF spectrum from the NE213 detector at 30 meters (magenta), in comparison to the GEANT4 simulation (blue) showing excellent agreement.

The $^{12}C(n,n_2)3\alpha$ cross section was seen to have behavior that was at odds with Hauser Feshbach predictions, instead being strongly-fed through a series of states in ^{13}C which also have large $^{12}C(n,a_0)$ widths. The preliminary cross sections are shown in Fig. 2. In addition, the cross sections for the

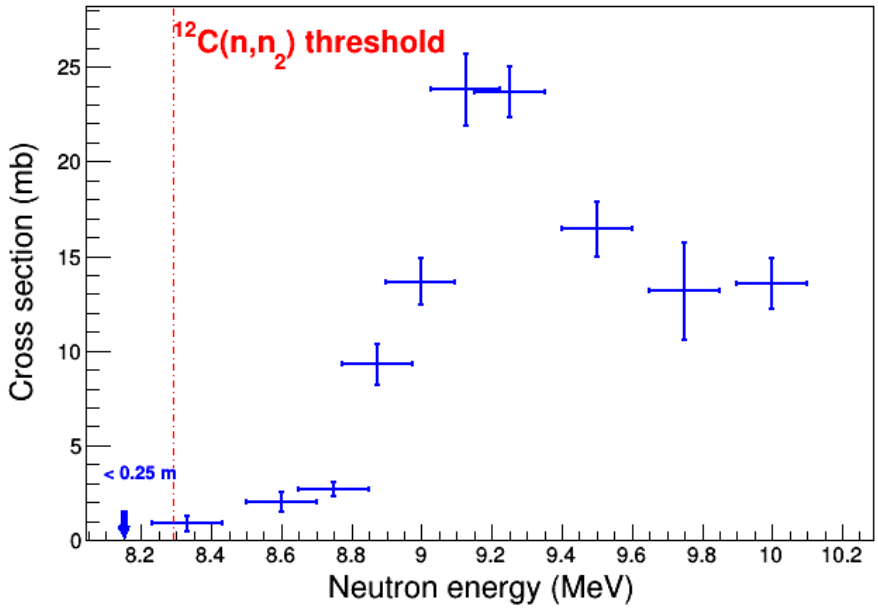

Fig. 2. Preliminary cross section for the population of the Hoyle state via the $^{12}C(n,n_2)3a$ reaction.

$^{12}C(n,a_0)$, $^{12}C(n,a_1)$, $^{16}O(n,a_0)$ and $^{16}O(n,a_1)$ reactions have also been extracted from the data which are not only important for nucleosynthesis calculations but are pivotally important for understanding gas-forming reactions in next-generation nuclear reactors.

[1] M. Beard, S. M. Austin and R. Cyburt, Phys. Rev. Lett. **119**, 112701 (2017).
[2] E. Koshchiy *et al.*, Nucl. Instrum. Methods Phys. Res. **A957**, 163398 (2020).
[3] Z. Meisel *et al.*, Phys. Procedia **90**, 448 (2017).

New approach for neutrons discovers problems with the understanding of the important astrophysical reaction $^{13}C(\alpha,n)$

V.Z. Goldberg, G.V. Rogachev, A.K. Nurmukhanbetova, E.M. Gazeeva , M.S. Golovkov, A.A. Bezbakh, D.K. Nauruzbayev, Zh. Kurmanaliyev, A. Serikov, and B. Zalewski

The present work applies the TTIK method [1] to measurements of the excitation function of the $^{13}C(\alpha, n)$ reaction. We used the time-of-flight (TOF) technique (neutron detector time relative to the RF of the beam) for neutron energy measurements. The choice of the reaction was based on the fact that the excitation functions for the $^{13}C(\alpha, n)$ reaction have been studied at a broad range of α-particle energies and because of the importance of this reaction for the nucleosynthetic s process[2]. Additionally, our results can be compared to a very comprehensive and recent analysis of the data relevant to this reaction made by the University of Notre Dame group [3]; this reference also contains a comprehensive review of previous studies.

The experiment was performed at the DC-60 heavy-ion cyclotron in Nur-Sultan (Kazakhstan) using beam energies of 13.0 and 14.3 MeV. The cyclotron parameters were tuned to provide a beam bunch with optimal time resolution at the expense of beam intensity. The beam width was about 2 ns with ≈0.2% energy resolution at a beam intensity of a few nA. The beam parameters were controlled by monitor detectors, described below. The experimental setup is presented in Fig. 1. The cylindrically shaped scattering chamber (15.5 cm diameter and 53.0 cm length) was made of stainless steel with a wall thickness of 0.25 cm and filled with helium of 99.99% purity. The ^{13}C beam from the cyclotron entered the scattering chamber through a thin entrance window made of 1.9-μm Ti foil. Four monitor silicon detectors were mounted on a ring shaped holder inside the chamber in order to detect the ions elastically scattered from the entrance window.

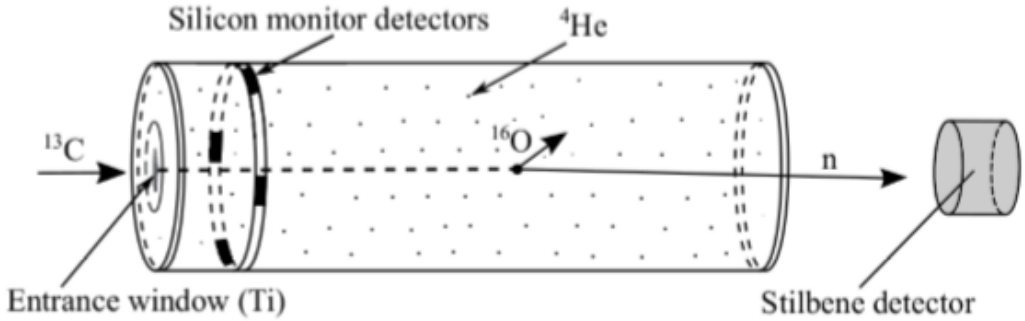

Fig. 1. Experimental layout.

The neutron detector was a stilbene crystal of cylindrical shape (8 cm diameter, 5 cm thickness) optically coupled with Photonis XP 4312/B photomultiplier.

Fig. 2 demonstrates a combined excitation function using both the 13.0 and 14.3 MeV ^{13}C measurements. The overlapping region in these measurements was ~2.73-2.87 MeV c.m. The solid line in Fig. 2 shows R-matrix calculations with the parameters of Ref. [2]. The disagreement between these calculations and our measurements is evident. Finding no obvious mistakes in either our work or that of the comprehensive work of [3], we looked to older experimental data for additional insight. The very old work by Walton et al. [4] did, in fact, provide some insight. These old excitation functions for the ^{13}C(α,n) reaction at symmetric forward and backward angles (31° and 149°) were compared with R-matrix calculations with contemporary parameters [3]. We found that the data[4] in the forward hemisphere (31°) agree with the R matrix calculations[3]. However, in the backward hemisphere, the data [4] disagree with the calculations in a similar way as it shown in Fig.2

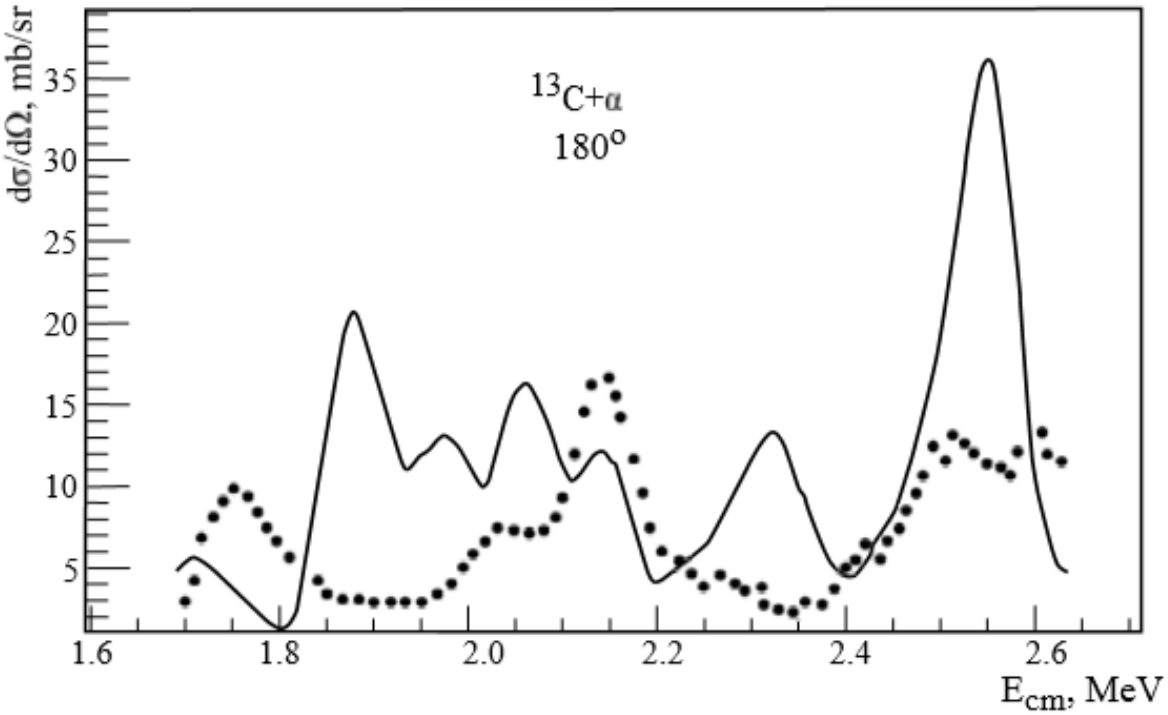

Fig. 2. The excitation function for the ^{13}C(α, n) reaction at 180°. The bold curve is R-matrix calculations with parameters of Ref. [3].

The present measurements, planned as a test, revealed an interesting result. Evidently, the new result is related to the unusual geometry. Obtaining equivalent data with the conventional approach would require neutron measurement at angles close to 180°, a difficult measurement. The physical basis of the observed discrepancy likely resides in an unaccounted interference of one or more broad (low spin) level(s) of opposite parity. A manifestation of such levels, if they are broad, might be attributed to a background in an analysis of forward angle data.

It is not easy to predict the eventual applications of the specific TTIK approach described in the present work for the first time. (This was also the case in the original TTIK work [1].) One might imagine that the TTIK technique described here could be used to study (α,n) reactions on gas targets, many of

which have not been thoroughly investigated. The simplicity of the TTIK approach is attractive, even more so when the reactions are induced by low-intensity secondary beams. In such cases, each beam particle would be tracked, removing a significant source of the ultimate center-of-mass energy uncertainty. More details of this study one can find in Ref.[5]

The authors are indebted to Dr. S. Yennello for attention to the work and permanent support and to Dr. Lee Sobotka for reading the draft, for valuable comments and the discussion.

[1] K. Artemov, O. Belyanin, and A. Vetoshkin, Sov. J. Nucl. Phys. (USSR) **52**, 634 (1990).

[2] R. Gallino, C. Arlandini, M. Busso, M. Lugaro, C. Travaglio, O. Straniero, A. Chieffi, and M. Limongi, Astrophys. J. **497**, 388 (1998). doi:10.1086/305437.

[3] M. Heil, R. Detwiland and M. Wiescher, Phys. Rev. C **78**, 025803 (2008); doi:10.1103/PhysRevC.78.025803.

[4] R.B. Walton, J.D. Clement, and F. Boreli, Phys. Rev. **107**, 1065 (1957); doi:10.1103/PhysRev.107.1065.

[5] V. Z. Goldberg, G.V. Rogachev, A.K. Nurmukhanbetova, E.M. Gazeeva , M. S. Golovkov, A.A. Bezbakh, D.K. Nauruzbayev, Zh. Kurmanaliyev, A. Serikov, and B. Zalewski, Phys. Rev. Research **2**, 032036(R) (2020).

New era of resonance reaction studies

V.Z. Goldberg and G.V. Rogachev

This review articles shows how a new experimental approach to resonant reactions (the TTIK method) resulted in different physics discussed in a study of resonances. The authors consider investigations of the alpha cluster structure of atomic nuclei, the first observations of exotic proton rich nuclei and analogs of the exotic neutron rich nuclei in resonant reactions.

A special interest is related with the very new applications of the method: observation of multiparticle processes in resonant reactions developed at Texas A&M University [1] and to the reactions with neutrons in the final state [2]. The first publication [2] of the application to the key astrophysical $^{13}C(\alpha,n)$ reaction showed that new approach can be an important test of previous analysis.

This report is published in Phys. Atomic Nuclei **83**, 513 (2020).

[1] M. Barbui, K. Hagel, J. Gauthier, S. Wuenschel, R. Wada, V.Z. Goldberg, R.T. deSouza, S. Hudan, D. Fang, X.-G. Cao, and J.B. Natowitz, Phys. Rev.C **98**, 044601 (2018)

[2] V.Z. Goldberg, E.M. Gazeeva, M.S. Golovkov, A.A. Bezbakh, D.K. Nauruzbayev, A.K. Nurmukhanbetova, Zh. Kurmanaliyev, A. Serikov, B. Zalewski, and G.V. Rogachev, Phys. Rev. Res **2**, 032036(R) (2020)

Probing a possible excited state of tritium via the ^{6}He(p,t)α reaction with TexAT

C.E. Parker,[1] G.V. Rogachev,[1] D.P. Scriven,[1] J. Bishop,[1] E. Koshchiy,[1] E. Aboud,[1] S. Ahn,[1,*] M. Barbui,[1] A. Bosh,[1] E. Harris,[1] C. Hunt,[1] Z. Luo,[1] M. Roosa,[1] B.T. Roeder,[1] and A. Saastamoinen[1]
[1]*Cyclotron Institute, Texas A&M University, College Station, Texas 77843*

The ^{3}H nucleus, or triton, is a well-studied few-body system. However, there remains uncertainty as to whether an exited state, t*, exists or rather, if there are specific reaction dynamics that lead to a resonance-like behavior in the n-d channel. Two previous experiments studying ^{6}He(p,t)α by D.V. Aleksandrov [1] and G.V. Rogachev [2] observed an enhancement in the final α-particle spectrum corresponding to an excitation energy of about 7 MeV in the triton. This enhancement was not able to be differentiated as an excited state or some sort of a final-state interaction due to the measurements being done at single beam energies.

To overcome the limitations of the single-beam energy measurements, the Texas Active Target Time Projection Chamber [3] (TexAT TPC) has been utilized for the current experiment. Using a thick target allows one to measure the incoming ^{6}He beam at multiple energies simultaneously as the beam loses energy in the gas. The pixelated Micromegas (MM) region allows for reconstruction of reaction tracks while the Si+CsI detector wall at forward angles collects the reaction products that are too energetic to stop fully in the gas. The goal of such an experiment is to reconstruct the ^{6}He(p,t) Q-value for multiple energy slices along the beam axis using a reconstructed vertex location and energy deposited by the α-particle in one of the Si detectors. Observing the shape of the outgoing α-particle spectrum can indicate whether a peak as a function of energy is present, therefore whether t* exists.

Fig. 1 shows a cartoon of the schematic for the October 2020 measurement, which was performed at the Texas A&M Cyclotron Institute using the K150 cyclotron and the Momentum Achromat Recoil Separator [4] (MARS) beamline. The active target was 260 Torr isobutane (C_4H_{10}) gas inside the main TexAT volume and the ^{6}He beam was part of a ^{9}Li/^{6}He/^{3}H cocktail beam produced by MARS using a primary ^{7}Li beam on an ^{18}O gas cell. The initial ^{6}He beam was 40 MeV at the MARS silicon detector during the setup and tuning. After passing through a monitoring scintillator, thin aluminum degraders, and the Havar entrance window to the TexAT chamber, the beam energy was about 32.5 MeV. Uncertainty in the beam energy comes from the ^{6}He energy loss in the isobutane, including the beam spot size enlarging in the gas, and from the final slit settings of MARS. However, this beam was still suitable for measuring multiple energy slices along the active MM region of TexAT with about 1 MeV Q-value energy resolution.

Selection of events is done by checking for energy deposited in the side regions of the MM with a corresponding hit in one of the Si detectors on the same side. In addition to the desired ^{6}He(p,t) events, there will of course be background, especially at lower α-particle energies. To demonstrate that the analysis code was functioning, the ^{6}He(p,t) ground state events were the initial focus due to the high, positive reaction Q-value of 7.5 MeV. Events with Si detector hits greater than 16 MeV were selected to eliminate the scattered ^{3}H and ^{6}He beam particles from the initial analysis. Background in this region was

[*] presently at Center for Exotic Nuclear Studies, Institute for Basic Science, Daejeon, 34126, Korea

mostly due to ^{6}He elastically scattering from the protons or ^{12}C in the isobutane. Using the Q-value of 0 MeV for the elastic processes, coupled with eliminating short arm lengths indicative of ^{12}C scattering helps to clean up the ^{6}He(p,t) ground state spectrum.

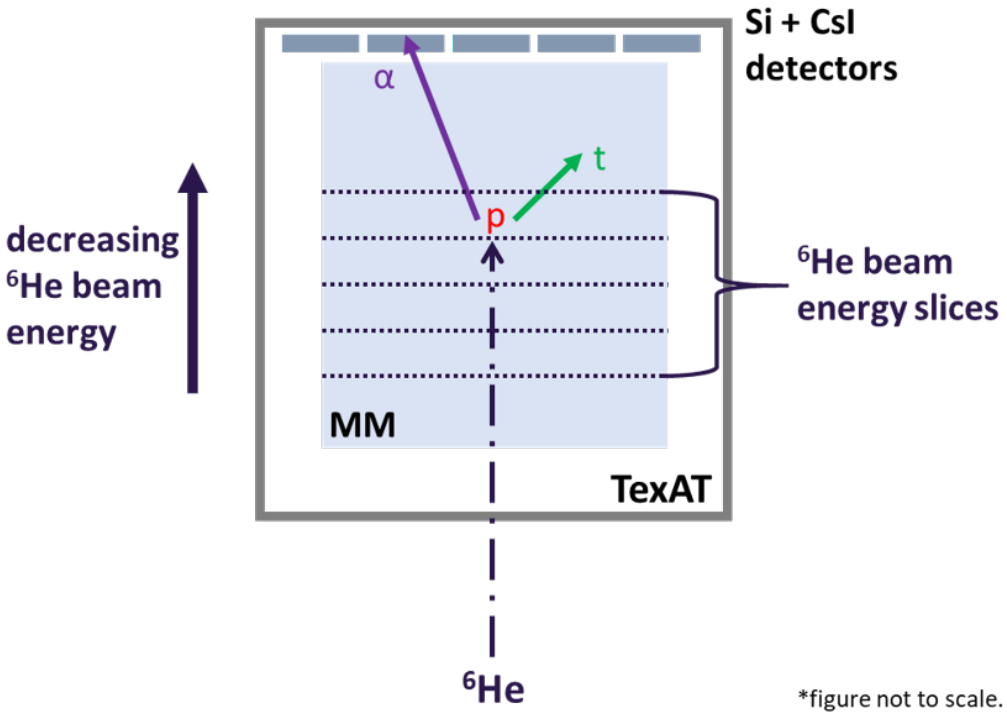

Fig. 1. Concept for ^{6}He(p,t) measurement and subsequent analysis technique using TexAT.

As part of the calculations for the ^{6}He(p,t) track fits, the energy of the beam and the outgoing α-particle at the reaction vertex and the angles of the two outgoing arm tracks are calculated. Utilizing the kinematics for the α-particle track angle versus other particle track angle provides a distinct cut for desired ground state events, and the resulting Q-value plot is shown in Fig. 2. This is an exciting feat because not only does it indicate that the analysis code is working, but more importantly because it represents the first successful two-nucleon transfer reaction using TexAT!

The next steps will focus on the potential t* events, which are more realistically going to be d+n events; the three-body decay to p+n+n is not possible at this energy. The kinematics for the reconstructed vertex α-particle energy versus α-particle angle will be important to distinguish the ground state events from the potential t* events, especially as one reduces the Si detector energy cut. An anti-gate for the ground state events can be implemented because they are separated, reducing uncertainty in the remaining events to analyze. Additionally, working with the well-benchmarked GEANT4 simulation for TexAT will help shed light on how the tracks for the t* decay to the d+n channel should look.

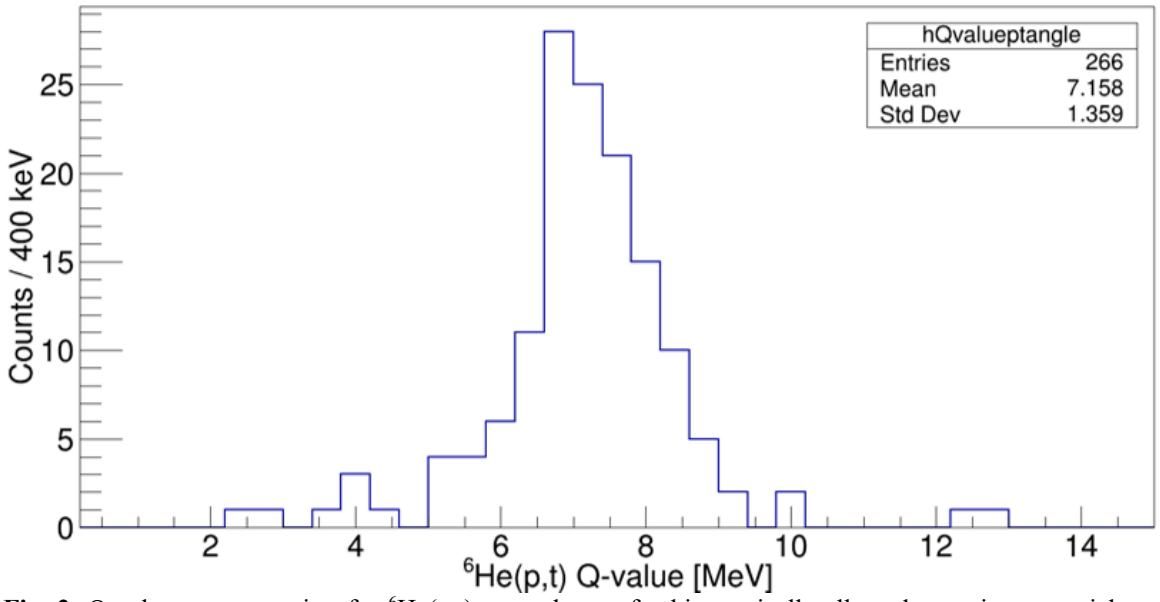

Fig. 2. Q-value reconstruction for ^{6}He(p,t) ground state for kinematically-allowed outgoing α-particle angles. The deviation from the expected 7.5 MeV is likely in part due to uncertainty in the assumed ^{6}He beam energy used in the calculations.

[1] D.V. Aleksandrov *et al.*, JETP Lett **59**, 320 (1994).

[2] G.V. Rogachev *et al.*, Phys. Rev. C **68**, 024602 (2003).

[3] E. Koshchiy *et al.*, Nucl. Instrum. Methods Phys. Res. **A957**, 163398 (2020).

[4] R.E. Tribble *et al.*, Nucl. Instrum. Methods Phys. Res. **A285**, 441 (1989).

United States Nuclear Structure Data Program (USNDP) and Evaluated Nuclear Structure Data File (ENSDF) at Texas A&M Evaluation Center of Cyclotron Institute

N. Nica and J.C. Hardy

For more than a century, nuclear data evaluation has made important contributions to nuclear science. A search in the *Nuclear Science Reference* (NSR) database maintained at the National Nuclear Data Center (https://www.nndc.bnl.gov/nsr/) on the author "M. Curie" produces a paper titled "*The Radioactive Constants as of 1930*" [1]. The introduction to this paper states that "*the need has arisen for the publication of special Tables of the Radioactive Constants*" and continues, "*This responsibility has been assumed by the International Radium Standards Commission chosen in Brussels in 1910 (...)*". Here we have the origin of what today is known as nuclear data evaluation.

Starting with the first generation of nuclear chemists and physicists, when measurements were already producing a multitude of diverse and sometimes conflicting data, it became evident that assembling and reconciling the data from all across the published literature was a tedious and difficult task. Nevertheless, only after such a systematic analysis could the community arrive at recommended "practical standards," which could then be updated periodically to reflect the continuous improvements in knowledge and technology. Soon nuclear data evaluation became a specialized branch of research in its own right.

After the Second World War most of this activity was taken across the Atlantic and hosted by the United States Nuclear Structure Data Program (USNDP), which maintains the Evaluated Nuclear Structure Data File (ENSDF) database. While mostly undertaken by U.S. national laboratories, it has expanded to a relatively small number of university research labs, which has included the Texas A&M Cyclotron Institute since 2005. For more than a decade, the Texas A&M effort was financed by a contract with Brookhaven National Laboratory, but in 2017 it started to receive direct financing through the DOE Grant DE-FG03-93ER40773, "Cyclotron-based Nuclear Science". Moreover since May 2017 Texas A&M Cyclotron Institute has been recognized and invested as an independent ENSDF Data Evaluation Center included within the Nuclear Structure and Decay Data international network.

Between 2005 and 2015, we completed and published the following full mass-chain evaluations: the superheavy A=252 mass chain [2]; the very data-rich mid-mass chains, A=140 [3], A=141 [4], A=147 [5] and A=148 [6]; and the relatively lighter chains, A=97 [7] and A=84 [8], the latter in a large international collaboration. In collaboration with B. Singh and a group of authors from McMaster University, Canada, we also published the A=77 [9], A=37 [10], A=36 [11], and A=34 [12] mass chains. At the beginning of 2016, we published another large mass chain, A=157, in Nuclear Data Sheets [13], followed by A=158 in 2017 [14], the renewed full evaluation of A=140 in 2018 [15], and A=155 in 2019 [16]. Finally, after its initial submission in Sep. 2018, our A=153 evaluation was published at the end of 2020 [17], having been delayed by a newly elaborated peer review process. In Aug 2020 we finalized and submitted a renewed evaluation of the A=141 chain to NNDC, which was our commitment for the USNDP data effort for FY 2020.

After the last decade's critical shortage of new ENSDF evaluators, the generational crisis extended to the ENSDF reviewers as well, following the retirement of most of the senior evaluators. As a

result, we were required to undertake two full mass chain reviews in 2020 and early 2021. In the last few years a more demanding quality standard for the ENSDF data has been implemented. This consists, first, of a pre-review process immediately after the first submission of a newly evaluated mass chain, which establishes whether the mass chain is accepted into the review pipeline. If accepted, the manuscript then enters the review process itself. Finally, there is an editorial review before publication. When combined with the large size of the mass chains we are responsible for, this generates typical intervals of 2-3 years or more spent by a mass chain in the publication pipeline. This explains the long publication cycles of the mass chains A=160, A=153, and A=147 submitted respectively in 2017, 2018, and 2019. Of these, A=153 has finally been published; most of the after-review work for A=160 has been completed with the mass chain ready for the final editorial review; and the after-review work for A=147 is planned to start soon.

In Sept 2020 we started the new full evaluation of the mass chain A=162, covering all publications since Nov 2007. The mass chain consists of the following isobars, in total, 17 nuclei: Nd, Pm, Sm, Eu, Gd, Tb, Dy, Ho, Er, Tm, Yb, Lu, Hf, Ta, W, Re and Os. Our bibliographical searches (dated May 26, 2021) found that in the interval since Nov 20, 2007, 422 papers have been published relating to this mass chain, of which 386 are primary references (more important), and 88 are experimental (the most important). This work is in progress.

[1] M. Curie, A. Debierne, A.S. Eve, H. Geiger, O. Hahn, S.C. Lind, S. Meyer, E. Rutherford, E. Schweidler, Rev. Mod. Phys. **3**, 427 (1931).
[2] N. Nica, Nucl. Data Sheets **106**, 813 (2005).
[3] N. Nica, Nucl. Data Sheets **108**, 1287 (2007).
[4] N. Nica, Nucl.Data Sheets **122**, 1 (2014).
[5] N. Nica, Nucl. Data Sheets **110**, 749 (2009).
[6] N. Nica, Nucl. Data Sheets **117**, 1 (2014).
[7] N. Nica, Nucl. Data Sheets **111**, 525 (2010).
[8] D. Abriola *et al.*, Nucl. Data Sheets **110**, 2815 (2009).
[9] B. Singh and N. Nica, Nucl. Data Sheets **113**, 1115 (2012).
[10] J. Cameron, J. Chen, B. Singh, and N. Nica, Nucl. Data Sheets **113**, 365 (2012).
[11] N. Nica, J. Cameron, and B. Singh, Nucl. Data Sheets **113**, 1 (2012).
[12] N. Nica and B. Singh, Nucl. Data Sheets **113**, 1563 (2012).
[13] N. Nica, Nucl.Data Sheets **132**, 1 (2016).
[14] N. Nica, Nucl.Data Sheets **142**, 1 (2017).
[15] N. Nica, Nucl.Data Sheets **154**, 1 (2018).
[16] N. Nica, Nucl.Data Sheets **160**, 1 (2019).
[17] N. Nica, Nucl.Data Sheets **170**, 1 (2020).

Shell structure and evolution through spectroscopy of beryllium isotopes

M. Roosa, G. Christian, G. Rogachev, S. Ahn, E. Bennett, J. Bishop, S. Dede, C. Hunt, H. Jayatissa, E. Koshchiy, R. Malecek, S. Ota, C. Parker, D. Scriven, and S. Upadhyayula

This project aims to develop the capacity to use the TEXas Active Target (TexAT) Time Projection Chamber (TPC) for transfer reaction studies [1]. We plan to accomplish this with a two-step experimental program, extracting spectroscopic factors to low-lying states in ^{11}Be and ^{12}Be with the ^{12}B(d,^{3}He)^{11}Be and ^{13}B(d,^{3}He)^{12}Be reactions, respectively. The first experiment aims to complement existing neutron-removal and neutron-addition spectroscopic data for ^{11}Be, studying the overlap between the ^{12}B ground state and low-lying excited states in ^{11}Be [2]. Because the ^{11}Be system is well studied, this experiment will also help to establish the validity of using an Active Target Time Projection Chamber (AT-TPC) for transfer reaction studies – with the eventual goal of coupling TexAT to the forthcoming TexNEUT p-Terphenyl neutron detector to study neutron-unbound states. Once the transfer-reaction experiment is verified to work in the ^{11}Be case, we will move to the less-studied ^{12}Be nucleus, where we will again investigate the overlap between ^{13}B$^{(gs)}$ and low-lying states in ^{12}Be.

Data for the ^{11}Be study was taken during May 2019 at the TAMU Cyclotron Institute using the K500 cyclotron and MARS [3]. Starting with a ^{14}C^{4+} beam at 30MeV/u, we used a 1 mm ^{9}Be target to produce 10^5 pps of ^{12}B at 259.5 MeV/u ± 4%. This beam was delivered to the TexAT experimental set-up where it was impinged on a 200 torr deuterated methane target composing the TexAT active volume. TexAT includes a MicroMeGAS pad plane which provides full momentum reconstruction in the gas target, which, as shown illustrated in Fig. 1, is accompanied by a wall of Si-CsI telescopes positioned perpendicular to the beam axis with a plastic scintillator at the 0^{o} position relative to the beam axis. The solid-state detectors are used to identify particles that do not stop in the gas volume.

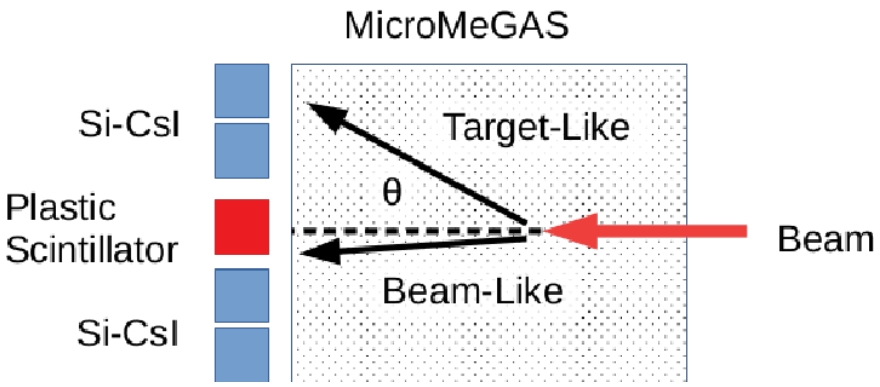

Fig. 1. Cartoon showing the arrangement of detectors inside the TexAT chamber with the target-like ejectile and beam-like ejectile of a beam induced event labeled.

Substantial progress towards establishing light-ion particle identification (PID) has been made during the past year. This is demonstrated in Fig. 2, which shows a spectrum of energy deposited in the Si detector vs. the mean energy loss in the gas (the ^{3}He ions of interest are not energetic enough to reach the CsI detectors, so gas vs. Si energies are required for PID). To construct this plot, we measure the energy

loss in the MicroMeGAS by taking the average amplitude measured in the strips of one side of TexAT and plot that vs. the calibrated Silicon energy. Two distinct loci are evident in the plot, which are consistent with expected locations of Z=1 and Z=2 particles. It is important to note that the expected sharp upward slope for events below ~5 MeV Si energy deposition is not present. However, this may be accounted for by the dE averaging process, which, for low energy particles, will under report when used as a proxy for total energy loss. This under-reporting is due to the rapid changes in the stopping power that occur as the lower-energy particles traverse the gas. As such, we tentatively assign Z=2 to the band starting around 2500 channels on the y-axis.

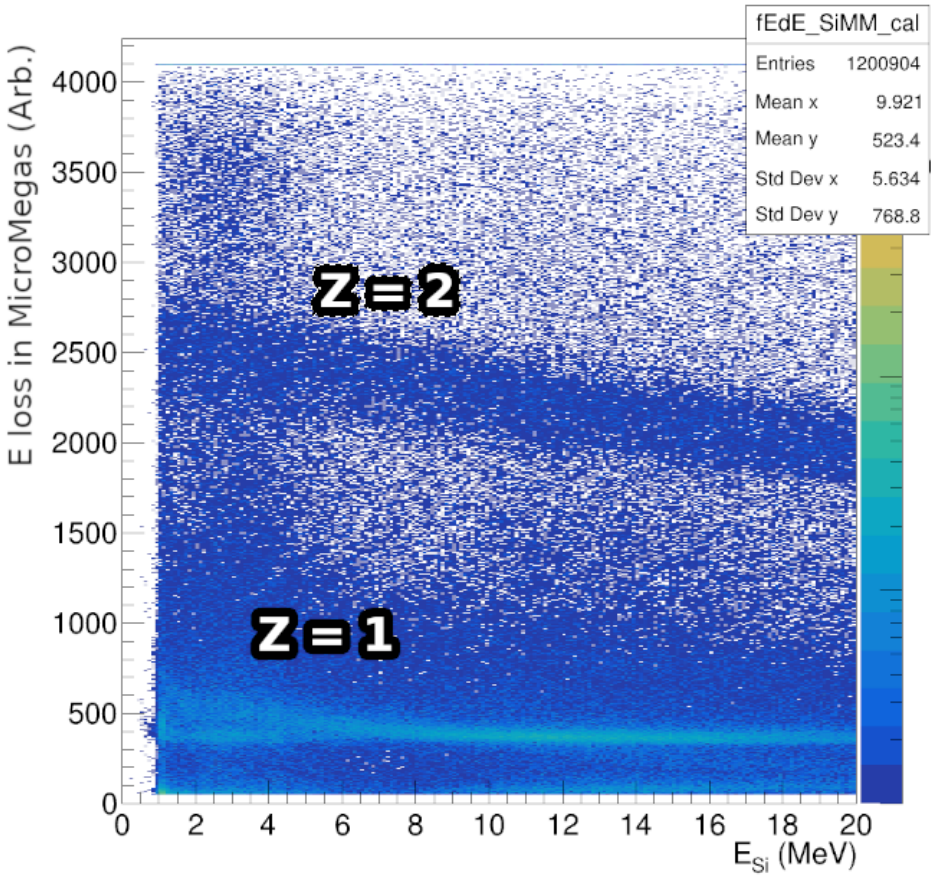

Fig. 2. The measured energy loss in the MicroMeGAS in arbitrary units versus measured Silicon energy

The PID component of this analysis is pending validation. We plan on using kinematics from the reconstructed tracks from the MicroMeGAS in conjunction with the PID shown above to establish more precise light-ion identification.

The beam has already been developed for the ^{12}Be run and we can expect 1.5 x 10^4 pps of incident ^{13}B. We are, however, waiting until the analysis of the first experiment is completed before moving on.

[1] E. Koshchiy *et al.*, Nucl. Instrum. Methods Phys. Res. **A957**, 163398 (2020).
[2] K.T. Schmitt *et al.*, Phys. Rev. Lett. **108**, 192701 (2012).

[3] R.E. Tribble *et al.,* Nucl. Instrum. Methods Phys. Res. **A285**, 441 (1989).

Study of alpha decay branches in ^{19}Ne via the ^{21}Ne(p,t)^{19}Ne reaction

G. Christian,[1-3] E. Bennett,[1,2] W.N. Catford,[4] S. Dede,[1,2] D.T. Doherty,[4] G. Lotay,[4] S. Ota,[1] B. Reed,[4] A. Saastoimonen,[1] and D.P. Scriven,[1,2]

[1]*Cyclotron Institute, Texas A&M University, College Station, Texas 77843*

[2]*Department of Physics and Astronomy, Texas A&M University, College Station, Texas 77843*

[3]*Department of Astronomy and Physics, Saint Mary's University, Halifax Nova Scotia, B3H 3C3, Canada*

[4]*Department of Physics, University of Surrey, Guilford, United Kingdom*

The ^{15}O(α,γ)^{19}Ne reaction is the main reaction controlling breakout of the hot CNO cycle into the rapid proton capture process (rp-process). As such, it is one of the most important reactions determining nucleosynthesis in the rp-process (and related proton capture processes), as well as astronomical observables such as X-ray burst light curves [CYB16]. As a result, experimentally determining the rate of this reaction at the relevant stellar temperatures (~0.2 – 3 GK) is a major goal of nuclear astrophysics.

It is now well established that the ^{15}O(α,γ)^{19}Ne reaction rate at relevant temperatures is completely dominated by the resonance at E_x = 4.033 MeV (E_{res} = 0.505 MeV, $J^\pi = 3/2^+$) [DAV02]. To date, attempts to measure the strength of this resonance directly, e.g. using a recoil separator and ^{15}O rare-isotope beam, have been hindered by low beam intensities. A successful direct measurement would require 10^{10} pps or greater ^{15}O beam intensity at an energy of ~0.160 MeV/nucleon. Current world-best intensities at the appropriate energy are limited to around 10^6 pps, and even next-generation facilities such as FRIB + ReA-3 may well not achieve this intensity. As a result, indirect measurements remain the main prospect for experimentally determining the stellar rate of this key reaction.

The strength ($\omega\gamma$) of the 4.033 MeV resonance in ^{19}Ne is completely determined by its alpha partial decay width, i.e., $\omega\gamma \simeq 2\Gamma_\alpha$. The alpha decay branch of this state is extremely small, which makes its observation challenging. To date, the most widely accepted upper limit on the alpha width is $\Gamma_\alpha <$ 0.011 meV, resulting in a branching fraction of $< 9 \times 10^{-4}$ [DAV02]. That limit was established in an experiment populating the 4.033 MeV state using the ^{21}Ne(p,t)^{19}Ne reaction at E = 43 MeV/nucleon. The (p,t) reaction selectively populates the 4.033 MeV state, which is predominately a two-neutron hole state. Outgoing ^{15}O recoils from alpha decay were selected in a magnetic spectrometer and used to establish alpha decay in coincidence with tritons, which were also detected and momentum analyzed in the spectrometer. That experiment was statistics limited, in part due to measuring tritons emitted at backward center-of-mass angles, where the (p,t) cross section is not maximized. The present project aims to improve upon the previous measurement by using the same measurement technique as [DAV02] but instead measuring forward-angle tritons using a stack of 1.5 mm thick Si detectors placed at forward laboratory angles.

Previous work on this project was focused on simulations, which determined that the resolution of the Si stack detectors was sufficient to separate the 4.033 MeV state (gated on t-alpha coincidences) from neighboring background states, as well as procuring a new scattering chamber and detectors for the measurement. Subsequently, in June 2020, we performed a test run using a 40 MeV/nucleon ^{21}Ne beam from the K500 cyclotron, to commission the Si stack detectors (coupled to the MDM spectrometer) and

characterize background scattering rates in both the Si detectors and the spectrometer focal plane. A key discovery during this test was that an initial halo of the ^{21}Ne beam causes rates in the forward-angle Si detectors to be too large to run at the required beam intensity of 10^8 pps. The halo was successfully eliminated using a ~5mm diameter collimator placed upstream of the CH_2 reaction target. With the collimator in place, rates in the Si detector were manageable, demonstrating that this portion of the system is suitable for the real experiment.

A second focus of the test was establishing heavy-ion particle identification at the MDM focal plane, using the upgraded Oxford detector [SPI19], and determining rates of scattered ^{21}Ne beam incident on the focal plane detectors. Fig. 1(a) demonstrates that clear element separation was achieved in the experiment using signals from the detector's DE anode plate vs. residual energy loss in a thick scintillator. The locus of oxygen recoils, which will be gated on in the real experiment, is clearly separated from the neon beam and other elements.

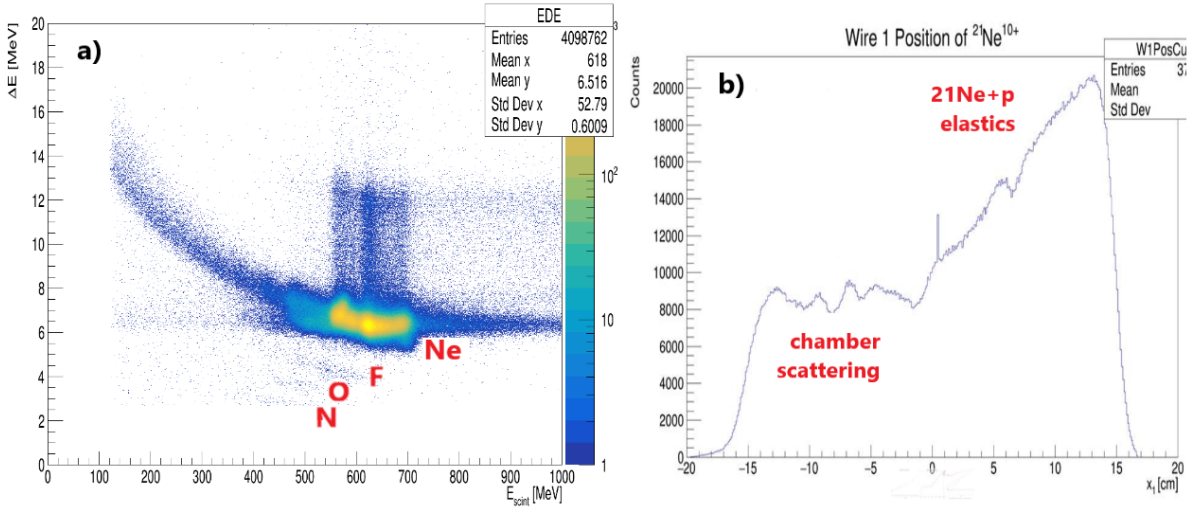

Fig. 1. a) Particle identification spectrum using signals from the DE anode vs. energy loss in a thick plastic scintillator. b) Dispersive (x) position of ^{21}Ne ions at the focal plane, showing two components of the ^{21}Ne background.

A major problem identified during the test experiment was the substantial presence of scattered ^{21}Ne beam in the focal plane. During the test run, the scattered beam rates were too large to run at the optimal beam intensity, since the position-sensitive avalanche wires of the Oxford detector are limited to incident rates below 5,000 pps. We made substantial progress at identifying the source of this background during analysis of the offline test-run data. As shown in Fig. 1(b), the background has two components. The first is backward-angle ^{21}Ne+p elastic scattering from the reaction target. The resulting ^{21}Ne ions have a magnetic rigidity that overlaps with the positive-x (high rigidity) side of the focal plane, with intensity increasing as +x position increases. This is responsible for the increasing intensity seen on the right side of the plot. While this background source is unavoidable, it can be eliminated or reduced by blocking some or all of the right-hand side of the detectors.

The second background source evidently arises from scattering in the vacuum chamber and produces a roughly uniform distribution across the focal plane. RAYTRACE ion-optics calculations, in

combination with the observed test-run data, have been used to determine that this background most likely arises from scattering in the "blocker box" approximately 35 cm upstream of the Oxford detector entrance window. The blocker box contains two thick metal plates on linear drives, allowing some or all of the focal plane detectors to be blocked from beam. According to RAYTRACE, the unreacted ^{21}Ne beam reaches the physical edge of the detector volume approximately in this detector box, which contains numerous scattering surfaces. A straightforward solution to removing this component is to simply remove the blocker box (a second, more simple metal plate can still be used to block the high-rigidity side of the spectrometer as necessary). With the blocker box removed, the unreacted ^{21}Ne ions will instead impinge normal to a flat surface, just outside the detector window. This should effectively block both the unreacted beam and any scattering products resulting in the chamber.

Next steps for this project are to perform a second test run, tentatively slated for August 2021. This run will examine the change in focal plane rates with the blocker box removed. It will also commission a new detector system, combining a newly built position-sensitive PPAC detector with a fast plastic-slow plastic phoswitch detector. The new detector is expected to provide the required DE-E particle identification signals, along with position signals from the PPACs. Crucially, both the PPACs and the phoswitch detectors are very fast, with counting rates $>10^4$ pps possible. This will allow the necessary high beam currents to be run even with substantial ^{21}Ne scattering rates in the focal plane.

[1] R. Cyburt *et al.*, Astrophys J. **830**, 55 (2016), https://doi.org/10.3847/0004-637X/830/2/55
[2] B. Davids *et al.*, Phys. Rev. C **67**, 12801 (2002), https://doi.org/10.1103/PhysRevC.67. 012801
[3] A. Spiridon *et al.* , Nucl Instrum. Methods Phys. Res. **A943**, 162461 (2019), https://doi.org/10.1016/j.nima.2019.162461

Measurement of the half-life of the *T=1/2* mirror decay of ^{29}P

P.D. Shidling, V.S. Kolhinen, N. Morgan, A. Ozmetin, B. Schroeder, V.E. Iacob, and D. Melconian

Mixed Fermi and Gamow-Teller transitions between $T = 1/2$ mirror nuclei are mediated by both the vector and axial-vector component of the weak interaction. Thus, the extraction of V_{ud} from this transition requires the measurement of ft value and any one of the angular-correlation coefficients. ^{29}P is a mixed Fermi and Gamow-Teller transitions and the relatively large uncertainty contribution in the V_{ud} value is dominated by the precision of ρ, the ratio of Gamow-Teller to Fermi matrix elements, which was obtained from a ±12% measurement of the beta asymmetry parameter, A_β [1]. The ft value [2] is known much better, to ±0.4%, with the largest contribution to its uncertainty being the lifetime of the decay. The aim of the present work is to improve the lifetime of ^{29}P so that it no longer dominates the uncertainty in the deduced ft value.

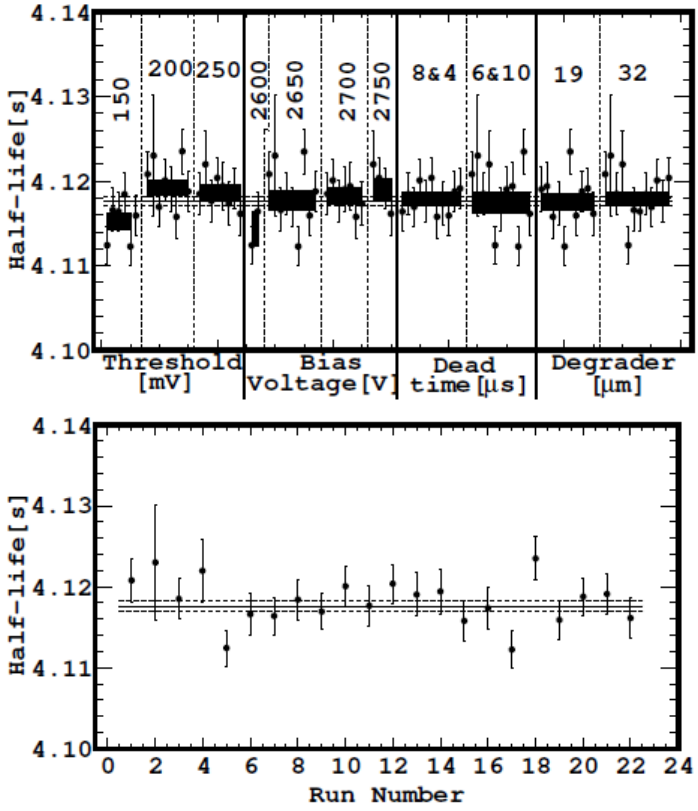

Fig. 1. The half-life obtained for ^{29}P with different experimental conditions. The bottom panel shows the result from all 22 runs. In the top panel the results from all 22 runs appear four times, grouped by threshold settings, bias voltages, deadtime and degrader thicknes. The gray bands represent the limits of the average half-life for a given condition. The average vaue for all the runs appears as solid horizontal line, with the corresponding dashed lines as the statistical uncertainty limits.

After sorting the data last year, the data for all the runs were analyzed and different type of systematic studies were carried out to estimate the dependence of the deduced half-life on experimental conditions, e.g. count rates, detector thresholds, gas-counter bias voltages, etc. Fig. 1 shows the half-life obtained for ^{29}P with different experimental conditions.

The analysis indicates that the half-life of ^{29}P is 4.1217(26) s, where the 2.6 ms uncertainty is purely statistical. We do see a systematic dependence on the "channel-chopping" analysis (removing early times from the fit, which shouldn't change the deduced lifetime). The data is being independently analyzed by other member of the group to cross check the analysis and attempt to limit/remedy this systematic uncertainty; if unsuccessful, we will take new data after doing some maintenance on our fast-tape transport system and thoroughly re-characterizing the gas-proportional counter.

[1] G.S. Masson and P.A. Quin, Phys. Rev. C **42**, 1110 (1990).
[2] N. Severijns, M. Tandecki, T. Phalet, and I.S. Towner, Phys. Rev. C **78**, 055501 (2008).

Precision γ-ray branching ratio measurements for long-lived fission products of importance to nuclear-security applications

M. Bencomo,[1] K. Kolos,[1] J.A. Clark,[2] J.C. Hardy,[3] V.E. Iacob,[3] D. Melconian,[3] E. Norman,[4]
H.I. Park,[3] G. Savard,[2] N.D. Scielzo,[1] and M.A. Stoyer[1]
[1]*Lawrence Livermore National Laboratory*
[2]*Argonne National Laboratory*
[3]*Texas A&M university, College Station, Texas*
[4]*University of California Berkeley, Berkeley, California*

The ^{95}Zr manuscript describing our experimental approach to measure branching ratios of long-lived fission products has been completed and published in NIM A [1]. This article is an important milestone in this effort and will serve as a great reference for future reports describing results obtained with this approach.

In Ref. [2], we reported on the precision measurements of the branching ratios of long-lived ^{156}Eu, the statistics and timing of the experiments, as well as some filtering of the data, including random coincidences. After removing random coincidences, we look at all gamma rays that are visible in the spectrum. Determining the area of all gamma-ray peaks in the random-coincidence-free spectrum is not only necessary to calculate the gamma-ray branching ratios but combined with the peak areas of the gamma-ray singles spectrum, we are able to determine experimentally the efficiency of the beta detector:

$$\epsilon_{\beta,} = \frac{R_{\beta\gamma}}{R_{\beta}} \quad (1)$$

where $R_{\beta\gamma}$ is the rate of the beta-gamma coincidences and R_{β} the rate of gamma singles.

To determine the intensities from the gamma-singles spectrum, the room background must be removed properly. In Fig. 1, we show two of the most intense gamma ray peaks, at 723 keV and 811 keV. Both are transitions coming out of the same energy level, the 1966 keV state. The absolute efficiencies for detecting these transitions with beta detector were calculated to be 0.9765(49) and 0.9799(26), respectively.

After obtaining the experimental efficiencies for all high statistics transitions, we can now compare experimental and simulated efficiencies. The SRIM (Stopping and Range of Ions in Matter) calculations have been made to establish the implantation depth of beam in the carbon foil. This is critical for the β efficiency simulations since the ions are not implanted exactly in the middle of the foil. The depth of implantation was determined by considering the highest yield isotopes in the mass chain, which in this case is ^{156}Nd, ^{156}Pm, and ^{156}Sm. These ions are implanted about ~35 nm deep into the 200-

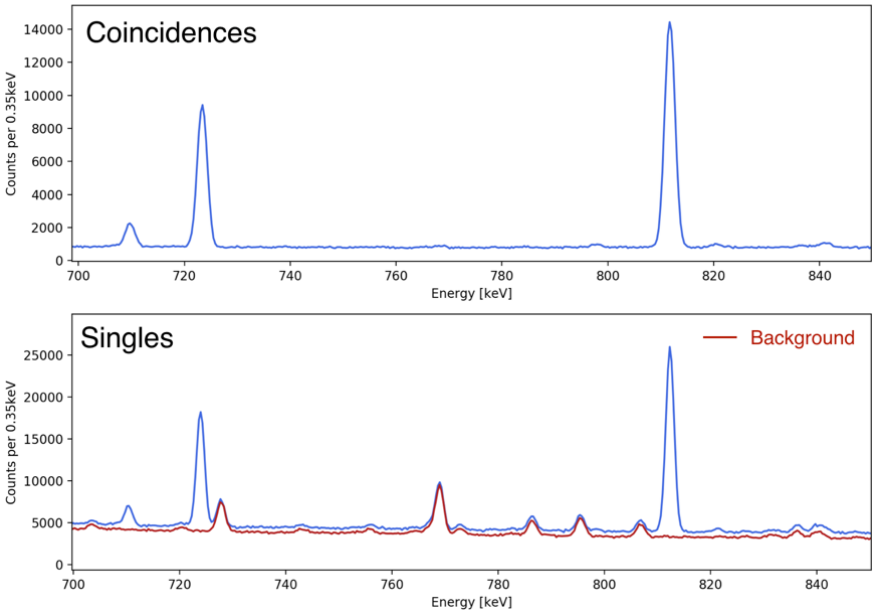

Fig. 1. Gamma ray spectra for the region of 700 to 850 keV region, showing two of the most intense gamma-ray transitions, 723 and 811 keV. (Top) Random coincidence free spectrum. (Bottom) Gamma-ray singles spectrum showing the background spectrum used for subtraction.

nm-thick carbon foil (details shown in Fig. 2). We take into consideration the different rates obtained from CARIBU, as well as the slight difference in implantation depth due to the different Z, for each isotope in the mass chain.

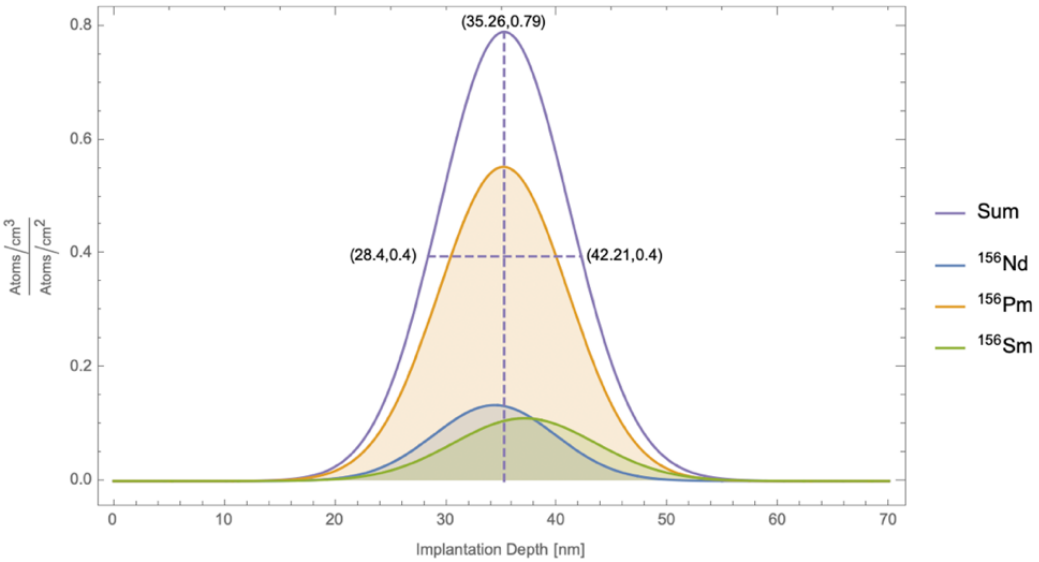

Fig. 2. Implantation depth and distribution of the highest yielding isotopes in the mass chain.

Once the implantation depth has been established, it is folded into our simulations. First, a beta decay simulation is performed, giving as a result a variety of particles associated with the decay (beta, gamma, and conversion electrons) including their decay position, energy, and momentum. From this output, we obtain the beta distributions for each transition (see Fig. 3) and use them as input in our GEANT4 model [1] to simulate the response of the gas counter to the different particles associated with the decay. From these simulations we can compare experimental and simulated efficiencies and determine the efficiency of the beta detector.

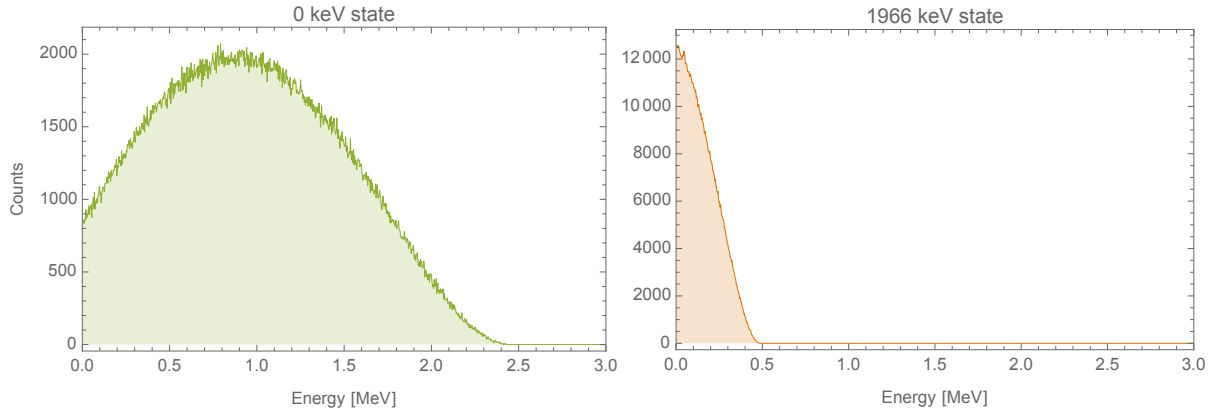

Fig. 3. Simulated beta energy distributions for the ground and 1966-keV state in the decay of ^{156}Eu.

The analysis of the ^{156}Eu data is not yet finalized but preliminary results show promise for the most intense gamma rays, with uncertainties ranging from 0.3-1.0% so far, we do expect an increase to those uncertainties of about 0.2-0.5%. These results do not include the ratio of the overall beta efficiency, ε_β, to the beta efficiency for a particular transition, $\varepsilon_{\beta i}$ (see Eq. 2), as we have not concluded that part of the analysis but we know that that ratio is very close to unity so the numbers will not change significantly. The other terms for the branching ratio equation have been considered and those are the number of beta-gamma coincidences, $N_{\beta\gamma}$, the number of beta singles, N_β, and the efficiency of the germanium detector for a particular energy, ε_γ. Fig. 4 shows a comparison of this work to the current values found in NNDC, the values for our work are listed in Table I with their corresponding uncertainties.

$$BR = \frac{N_{\beta\gamma}}{N_\beta}\frac{1}{\epsilon_\gamma}\frac{\epsilon_\beta}{\epsilon_{\beta i}} \tag{2}$$

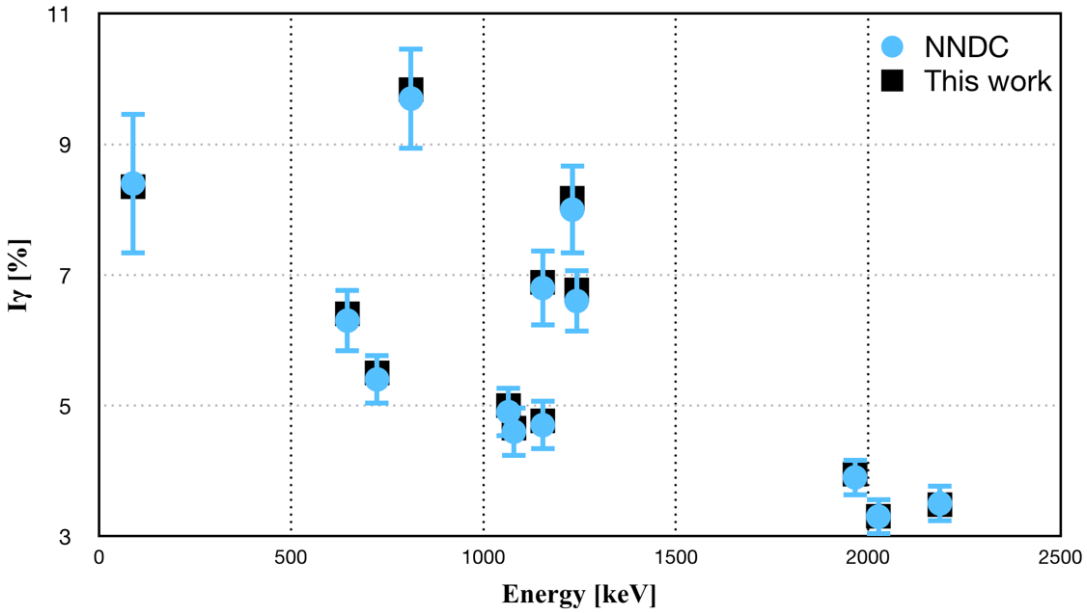

Fig. 4. Gamma-ray branching ratio comparison between current values from NNDC (blue dots) and preliminary results from this work (black squares). Error bars for this work are contained within the markers.

Table I. Preliminary branching ratios for the 14 most intense gamma rays in the decay of Eu-156.

γ-ray energy [keV]	Iγ (this work)	γ-ray energy [keV]	Iγ (this work)
88.97	8.352(30)	1153.67	6.887(46)
599.47	2.135(19)	1154.08	4.755(44)
646.29	6.405(33)	1230.71	8.174(43)
723.47	5.500(31)	1242.42	6.770(38)
811.77	9.837(46)	1965.95	3.949(36)
1065.14	5.000(32)	2026.65	3.305(32)
1079.16	4.655(31)	2186.71	3.483(33)

This work was performed under the auspices of the US Department of Energy (DOE) by the Lawrence Livermore National Laboratory (LLNL) under Contract No. DE-AC52-07NA27344, DE-AC02-06CH11357 (ANL), and DE-FG03-93ER40773 (TAMU), and the University of California under Contract No. DE-AC0376SF0098. This work was supported by the US DOE National Nuclear Security Administration through the Office of Nonproliferation Research and Development (NA-22) under the Funding Opportunity Announcement LAB 17-1763.

[1] K. Kolos, A.M. Hennessy, N.D. Scielzo, V.E. Iacob, J.C. Hardy, M.A. Stoyer, A.P. Tonchev, W.-J. Ong, M.T. Burkey, B. Champine, J.A. Clark, P. Copp, A. Gallant, E.B. Norman, R. Orford, H.I. Park,

J. Rohrer, D. Santiago-Gonzalez, G. Savard, A.J. Shaka, B.S. Wang, and S. Zhu, Nucl. Instrum. Methods Phys. Res. **A1000**, 165240 (2021).

[2] M. Bencomo *et. al.*, *Progress in Research*, Cyclotron Institute, Texas A&M University (2019-2020), p. IV-105.

Weak interaction studies with ^{32}Ar decay (WISArD)

M. Nasser, G. Chubarian, V.E. Iacob, D. McClain, D. Melconian, P.D. Shidling,
and the WISArD Collaboration

The WISArD experiment has been set up at CERN-ISOLDE to investigate fundamental symmetries of the weak interaction, focussing on the β-ν angular correlation coefficient of ^{32}Ar by looking at β-delayed protons emitted from the daughter nucleus ^{32}Cl. As the protons are emitted from the recoiling ^{32}Cl, their MeV-level energy distribution is Doppler-broadened by up to ±15 keV. With a suitable arrangement of detectors, this effect can lead to a kinematic shift which is sensitive to weak currents that are beyond the standard model. In particular, protons from the isobaric analogue state fed by a Fermi-type β decay allow searching for a small contribution of a potential scalar current to the dominant vector current, whereas protons from Gamow-Teller-type β decays allow searching for tensor contributions to the dominant axial-vector current. The WISArD experiment aims for a sensitivity limit of 0.1% for these exotic currents. This approach has been demonstrated recently in a proof-of-principle measurement published in Ref. [1]. This research program is extremely similar to the TAMUTRAP program [2], but as described below (Fig. 1), it is a simpler system (it doesn't involve ion trapping) and

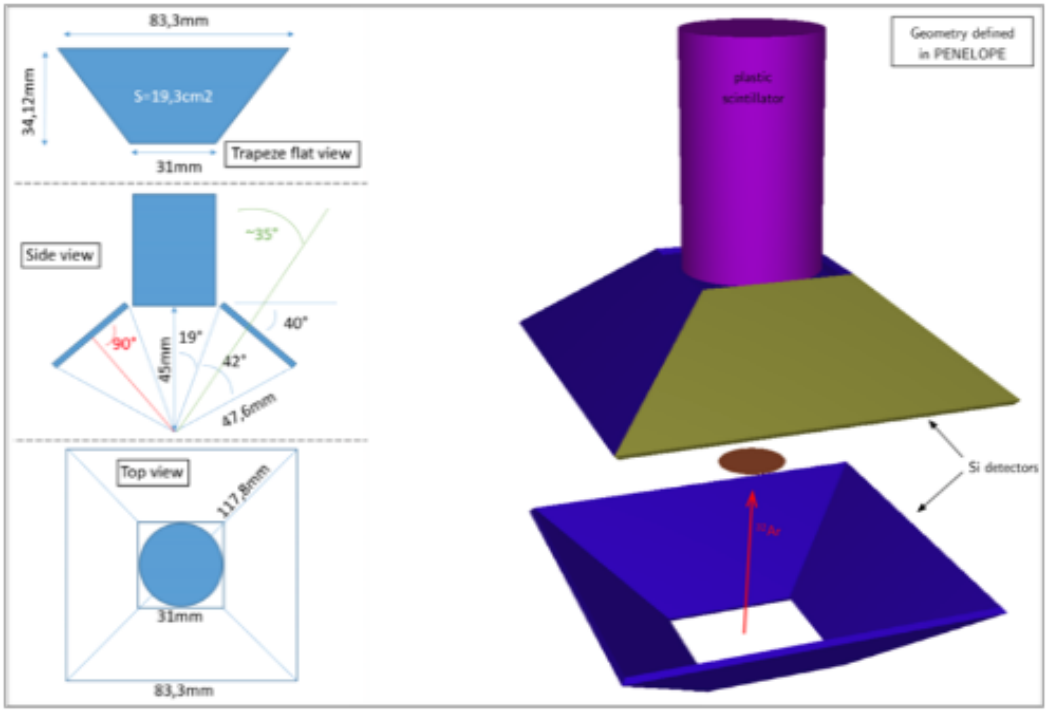

Fig. 1. Experimental setup of the WISArD experiment at CERN-ISOLDE. The right panel shows our implementation of the geometry in PENELOPE. The ^{32}Ar beam will be implanted in the catcher foil. The plastic scintillator will tag βs in coincidence with delayed protons in the upper vs. lower panel of Si detectors to measure the kinematic shift.

the beam is readily available at ISOLDE unlike at the Cyclotron Institute. Thus we have joined the WISArD collaboration out of shared interests and expertise, and expect many from this collaboration will join us in our effort at TAMUTRAP once LSTAR is commissioned and we have radioactive ion beams.

Our specific contribution to the WISArD collaboration is an independent analysis of the upcoming experiment using the PENetration and Energy Loss of Positrons and Electrons (PENELOPE) Monte Carlo program [3] to complement that of our collaborators using GEANT4. Most popular and well-known MC codes currently available (e.g. GEANT4 and EGS5) use multiple-scattering theories to allow the simulation of the global effect of a large number of interactions in a track segment of a given length or step size. These "condensed" simulation algorithms are only approximate and may lead to systematic errors, particularly if the user is not careful about setting an appropriately small step length; even if care is taken, these condensed MCs have difficulties in generating particle tracks in the vicinity of an interface. PENELOPE by contrast[1] is based on a mixed procedure to overcome the potential pitfalls of condensed MCs: soft interactions are simulated using multiple-scattering theories while hard interactions are seamlessly integrated and simulated in detail. Electrons and postirons are strongly susceptible to (back)scattering which is invariably a large concern when estimating systematic uncertainties in precision (<0.1%) β-decay measurements. Thus having a completely independent analysis of the WISArD experiment is extremely important.

Prior to taking ^{32}Ar data for the physics measurement, the collaboration is planning to characterize the low-energy response of the plastic scintillator with a monoenergetic 30-keV electron source. This is important to understand our low-energy threshold of the detector. We have simulated this simple system in PENELOPE, and the comparison to the complementary simulation by our collaborators using GEANT4 (see Fig. 2). Even though the "PENELOPE" package was used in GEANT4, significant differences in the response function are clearly evident. We will compare both simulations to data once the characterization is completed and benchmark both MCs. Presently, we are completing the detailed geometry definitions in PENELOPE for the upcoming experiment which is tentatively scheduled at ISOLDE this fall; our participation is strongly dependent on travel restrictions due to COVID-19. We are also implementing the detailed *R*-matrix calculations of the β-delayed proton decay for a complete theoretical description including interferences; this *R*-matrix calculation will be the basis for the initial β and proton momenta input to both MCs.

[1] Note that though there is a "PENELOPE" package in GEANT4, the basic tracking algorithms are unchanged and so it is not at all the same as the true PENELOPE MC program.

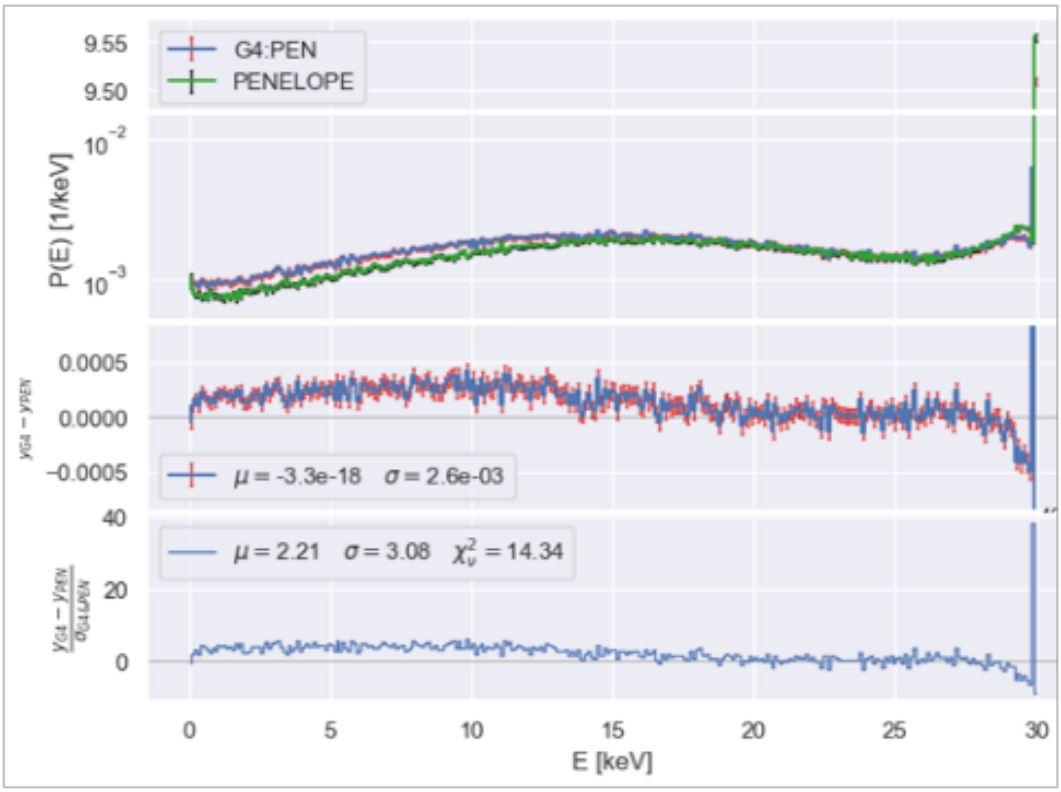

Fig. 2. Comparison of PENELOPE and GEANT4's "PENELOPE" package in a simple geometry: Monoenergetic 30-keV electrons are collimated by a stainless steel aperature and deposited in a plastic scintillator. Note that even in this very basic case, significant differences in the simulated response function are seen.

[1] V. Araujo-Escalona *et al.*, Phys. Rev. C **101**, 055501 (2020).

[2] P.D. Shidling *et al.*, Int. J. Mass Spectrom **468**, 116636 (2021).

[3] F. Salvat, NEA (2019) Workshop Proceedings, Barcelona, Spain (January 2019), OECD Publishing, Paris, https://doi.org/10.1787/32da5043-en (ISBN 9789264489950).

Cold QCD physics with STAR at RHIC

B.E. Aboona, C.A. Gagliardi, T. Lin, and R.E. Tribble
and the STAR Collaboration

Our group continues to play a major role in the STAR spin physics program. Over the past year, our focus has been on measurements of the Collins effect in *pp* and *p*+Au collisions. We have also continued development of trigger algorithms for the STAR Forward Upgrade.

The Collins effect involves the combination of the quark transversity in the proton and the Collins fragmentation function. It manifests itself as azimuthal modulations of identified hadrons about the axes of their parent jets. Last year in *Progress in Research*, we reported on preliminary results that we have obtained for the Collins asymmetry in 200 GeV *pp* data that STAR recorded during 2015. The 2015 measurement included approximately twice the integrated luminosity as STAR recorded for a similar measurement during 2012. Since then, our post-doc Dr. Lin has developed a method to combine the STAR Collins effect measurements from 2012 and 2015, which initially were analyzed in rather different ways. Fig. 1 shows one view of the combined 2012+15 results compared to some recent model

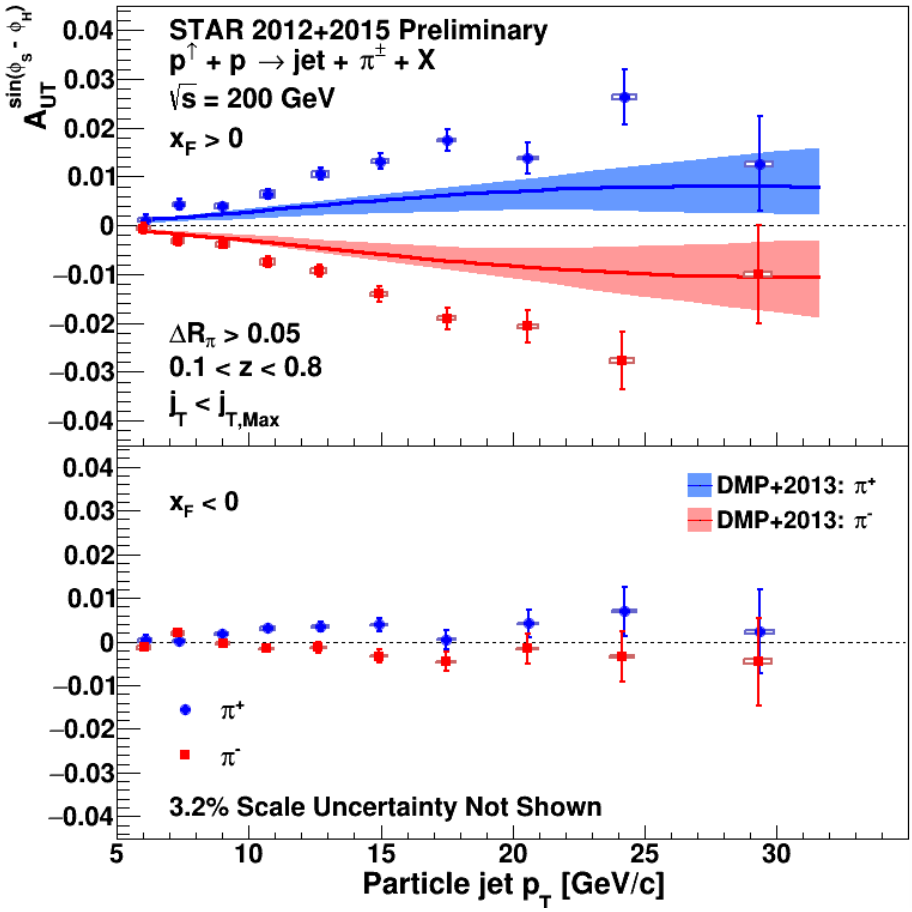

Fig. 1. STAR preliminary Collins effect measurements at mid-rapidity in 200 GeV *pp* collisions as a function of jet p_T, compared to model calculations from [1].

calculations. The final publication describing these STAR results will enter the STAR god-parent committee during the summer. Drs. Gagliardi and Lin will be principal authors, together with J.K. Adkins and R. Fatemi from University of Kentucky and J. Drachenberg of Abilene Christian

Our graduate student B. Aboona is analyzing data that STAR recorded during 2015 to determine the size of the Collins effect in $\sqrt{s_{NN}} = 200$ GeV p+Au collisions. This will provide unique insight into the possible factorization breaking that has been predicted for transverse-momentum-dependent phenomena in hadronic collisions, in addition to a spin-dependent probe of the hadronization mechanism in cold nuclear matter.

Collins effect measurements depend critically on particle identification (PID). STAR primarily relies on *dE/dx* information from the Time Projection Chamber (TPC) for PID. However, in certain momentum ranges, the *dE/dx* bands of different particle types overlap. STAR utilizes time-of-flight (TOF) measurements to provide PID in those cases where *dE/dx* measurements do not suffice.

TOF consists of a start time detector – the vertex position detector (VPD), which covers about half of the solid angle in the pseudorapidity range $4.2 < |\eta| < 5$ – and a stop time detector, the barrel time-of-flight (BTOF) system that surrounds the TPC; see Fig. 2. When TOF is used for full-energy Au+Au collisions, there is high hit multiplicity on both sides of the VPD to provide good start time resolution. However, in *pp* and *p*+Au collisions, one or both sides of the VPD have a low mean hit multiplicity that results in most events having inaccurate or no start time. This led us to consider utilizing "start-less" TOF, which infers the collision time from the measured times of the observed TPC tracks, without reference to a separate start detector. Prior to our work, STAR had only used the start-less TOF mode when analyzing low-energy Au+Au collisions from the RHIC Beam Energy Scan (BES).

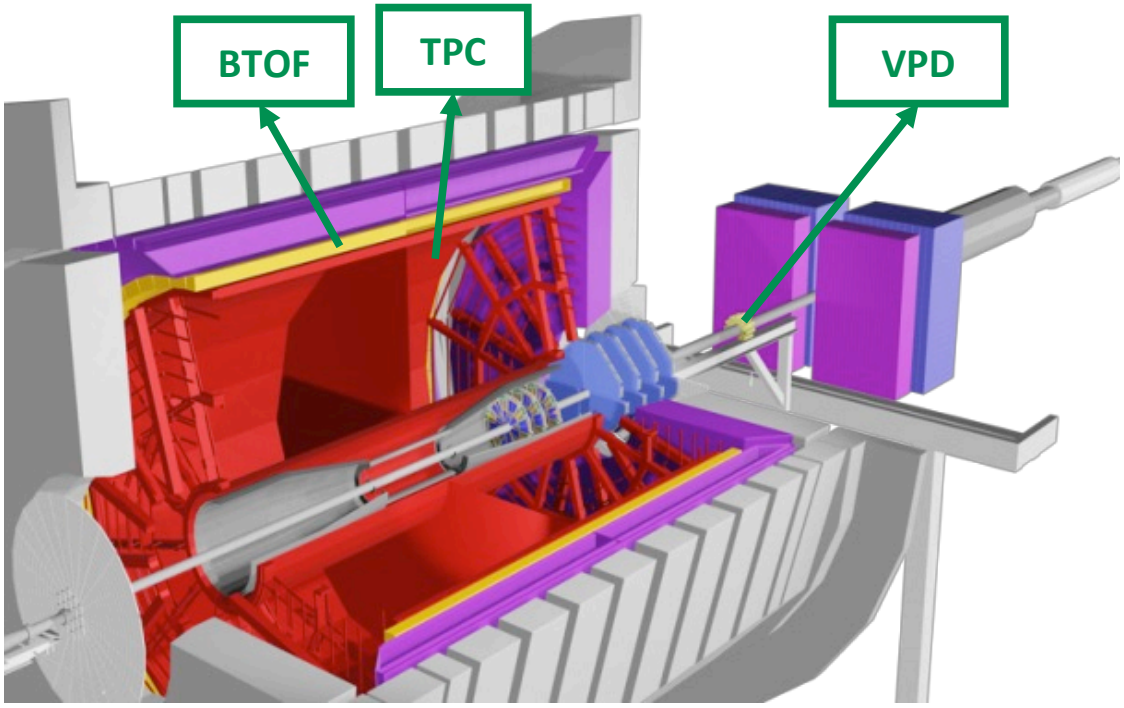

Fig. 2. View of the STAR detector, noting the subsystems that contribute to TOF measurements.

Start-less TOF uses stop times calculated by BTOF and well-identified tracks with BTOF hits to calculate the start time. Low-p_T pions end up providing the highest multiplicity of such tracks. Knowing the start and stop times, we can calculate the time-of-flight for each particle. That flight time is then combined with the path length obtained from the TPC to determine the velocity of the particle. We can obtain the momentum of the particle from the TPC and use it along with the velocity of the particle to calculate the mass of the particle and, thus, identify it.

Upon examining the default start-less TOF codes, we concluded that worthwhile optimizations could be made to multiple areas within the codes. The default start-less TOF codes consist of three main parts, "high purity" pion selection cuts, an outlier rejection algorithm to remove early or late outlier pions, and the last step is to average the start times of the pions that survive the outlier rejection algorithm to get the start time of the collision. Since then, our student B. Aboona has worked to optimize the routines.

We concluded that the default pion selection cut is too generous, so we developed a more restrictive set of cuts for pion selection that yields a higher purity pion sample. Our cuts include an extended upper limit of the momentum range, which was made possible by adding more restrictive *dE/dx* cuts. We also require the candidate pions to have higher-quality track reconstruction and *dE/dx* measurements, and include a vertex pointing accuracy cut to reduce contamination from secondary particles and decays in-flight.

When looking at the default outlier rejection algorithm, we found two main problems. The first problem was that the algorithm is a single-pass rejection loop, where the hits that are rejected depends on the order that the hits appear in the list. The second problem was that the algorithm accepts a very wide range of nominal collision times, which allows for mis-identified particles and other background tracks to make it through the rejection algorithm. In our improved outlier rejection algorithm, we address both issues. We introduce a tighter time range. We also pass iteratively over the candidate list, dropping only the grea allowed time dif n point. Howeve e STAR detecto f initial momen *dx* time correcti for the stop-tin tools to identify g. 3, we see that hit time resoluti erved in *pp*. So ease in efficien ing the measur bias in calculat

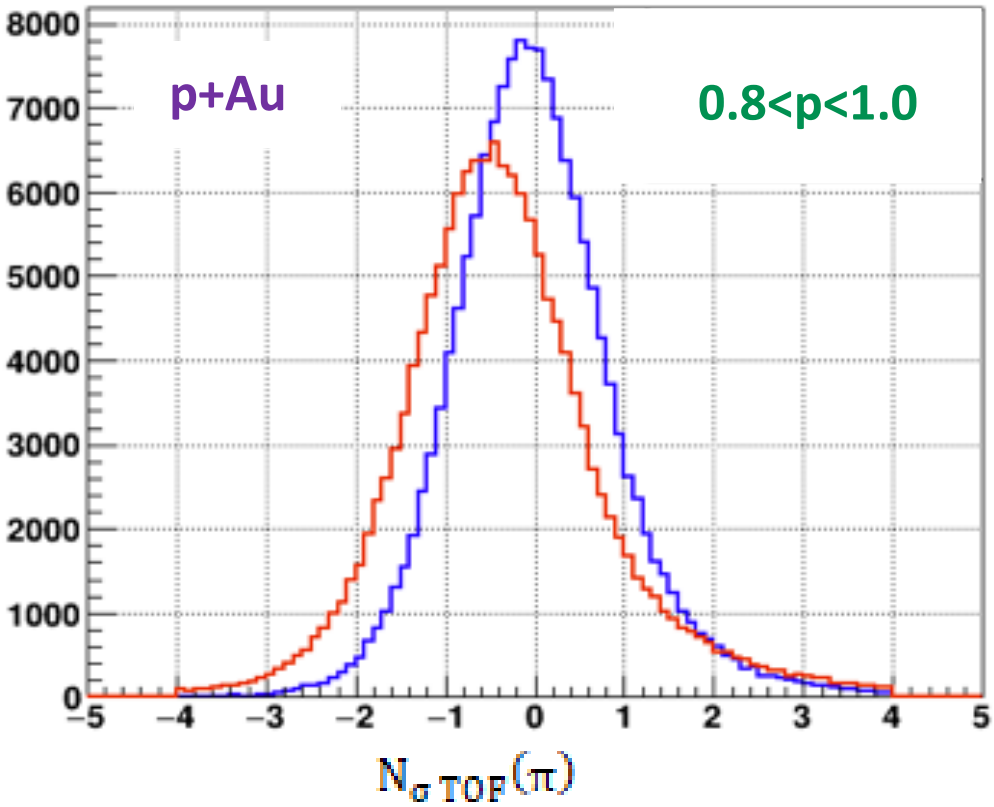

Fig. 3. Measured flight times of pions selected via dE/dx with 0.8 < p < 1.0 GeV/c, measured in units of the intrinsic time resolution. The red curve shows the results using the default start-less TOF algorithm, while the blue curve shows the results obtained when analyzing exactly the same p+Au events with our optimized algorithm.

Our original intention was to develop the optimized TOF routines only for use with *pp* and *p*+Au data from the 2015 and 2017 RHIC runs that have already been converted from raw events to MuDsts. However, during a STAR Analysis Meeting in January, heavy-ion collaborators expressed an interest in using the new routines when analyzing BES-II data. Since then, we have extended the routines so that they now perform similarly both during raw data production and when processing MuDsts. We are now optimizing the parameters for BES-II running conditions, beginning with the 19.6 GeV Au+Au data that STAR recorded during 2019.

During the past year, we have also developed a trigger algorithm for Drell-Yan dielectron events in the STAR Forward Upgrade. The challenge was to identify trigger logic that both selects Drell-Yan events with high efficiency and triggers on the orders-of-magnitude larger cross section of hadronic events at an acceptable rate for the STAR data acquisition system. The algorithm we developed provides ~85% efficiency in 510 GeV *pp* collisions for Drell-Yan events that fall within the Forward Upgrade acceptance, together with a total expected trigger rate of <1 kHz at the expected Run 22 collision rate of 5 MHz. The algorithm has now been verified to fit within the logic constraints of the FPGAs in the Forward Upgrade trigger DEP-IO boards.

Finally, we continue to carry various administrative responsibilities for STAR. Dr. Gagliardi served as one of the two conveners of the STAR Cold QCD and Spin Physics Working Group until the end of 2020. He served on the writing committee for the 2020 STAR Beam Use Request, where he was one of the three lead authors and the lead editor of the write-ups describing the proposed STAR Cold QCD physics programs for RHIC Runs 22 and 24. He also served on the god-parent committees for three different STAR papers during the past year, two from Cold QCD and one from Heavy Flavor. Dr. Lin served on the god-parent committee for a STAR Heavy Flavor paper and serves as the software coordinator for the EEMC. He also served as STAR Period Coordinator for three weeks during the current RHIC run. After completing his term as Period Coordinator, Dr. Lin left the group in Spring 2021 to take a new position as an Assistant Professor at Shandong University.

[1] U. D'Alesio, F. Murgia, and C. Pisano, Phys. Lett. B **773**, 300 (2017).

SECTION II

HEAVY ION REACTIONS

Studying short-lived α-decaying multinucleon transfer reaction products with the active catcher array

A. Hood, A. Abbott, J. Gauthier, K. Hagel, B. Harvey, A. Hannaman, A. Jedele, Y.-W. Lui, L. McCann, A.B. McIntosh, L.A. McIntosh, M. Sorensen, Z. Tobin, R. Wada, A. Wakhle, and S.J. Yennello

There has long been interest in studying the multinucleon transfer (MNT) reaction mechanism at the Cyclotron Institute at Texas A&M University. The active catcher array was developed for the purpose of identifying short-lived α-decaying MNT products. In 2018, the results of an experiment which surveyed the production of α-decaying heavy elements created in the ^{238}U + ^{232}Th reactions at 7.5-6.1 A MeV were published (Ref. 1). The results suggested that heavy and super heavy elements were produced with higher cross sections than had been predicted, though individual product nuclides could not be identified because of limited position and energy resolution. With these encouraging results, subsequent experiments have been performed with lower background and improvements to the detectors that provide higher position granularity and better energy resolution.

One major source of background mentioned in [1] came from α particles emitted by the ternary fissions of products with long-lived isomeric states. The half-lives of these states are similar to the half-lives of the products of interest, as are their α-emission energies. Thus, the approach shifted to looking for α-decaying products with Z and N ranging $84 \leq Z \leq 92$ and $126 \leq N \leq 136$, where fissioning isomeric states are not expected. These products include various isotopes of elements ranging from Po to U. In this mass region, many products decay to stable or longer-lived nuclei by chains of sequential α emission.

In fact, this mass region was highlighted in the work of Zagrebaev & Greiner (2013) as a good candidate for experimental investigation of MNT reactions because of the decay properties of the nuclei (Ref. 2). Zagrebaev & Greiner chose to highlight the reaction ^{192}Os+^{197}Au and predicted production cross sections for elements from At to U. Multiple isotopes of each element with Z up to Ac have predicted cross sections larger than 1 μb (see Fig. 1). This system, and systems like it, have been of interest to our group for the past few years.

During the years 2017-2019, Wakhle *et al.* conducted three experiments investigating short-lived α-decaying products of reactions in the systems ^{22}Ne+^{232}Th, ^{197}Au+^{208}Pb, and ^{208}Pb+^{208}Pb (Refs. 3 & 4). Analysis of these data increased understanding of the Struck Instrument Systems 3316 ADCs. As a result of this, this experiment was designed to have zero dead time, so that no events would be missed. This is critical because capturing all of those events enables identification of the products of interest with higher confidence.

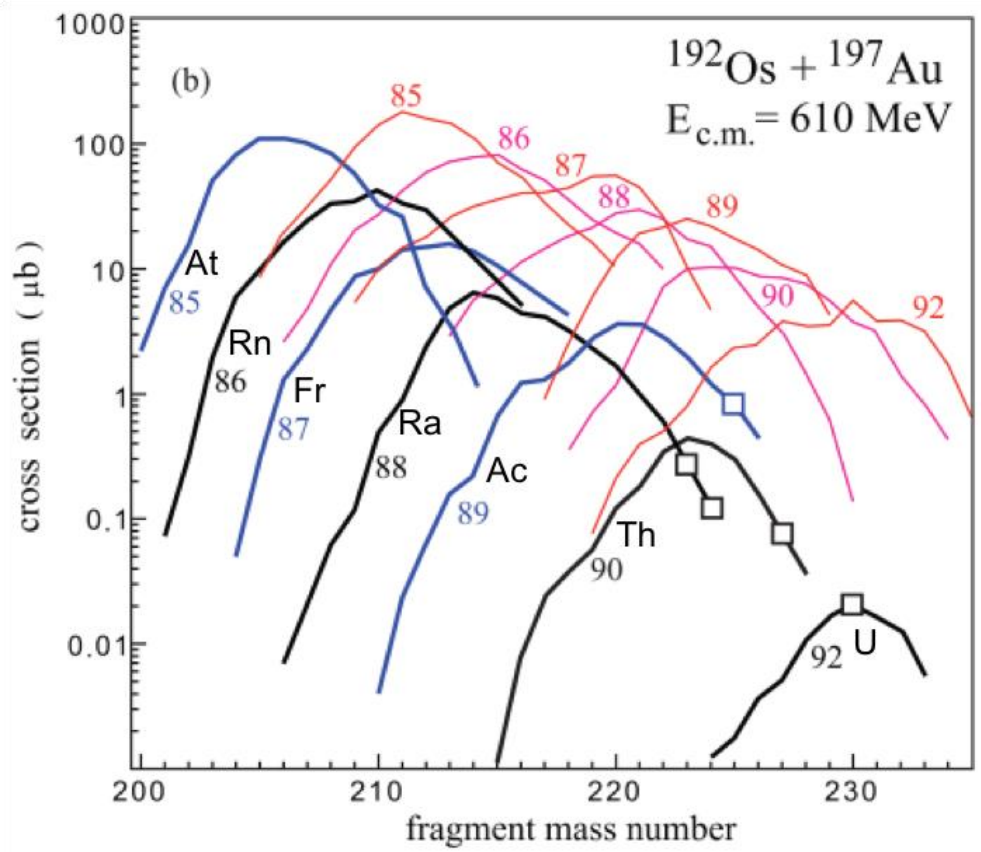

Fig. 1. Predicted cross sections for α-decaying products of multinucleon transfer reactions from ^{192}Os+^{197}Au. The red and pink thin lines show the initial cross sections for the excited products. The blue and black thick lines show the final predicted cross sections for the surviving deexcited nuclei. The boxes are highlighting nuclides that are good candidates for studying via radiochemical separation because they are long-lived. This plot is reproduced from Zagrebaev & Greiner [2].

In the reconstruction of chains of α decays, one must consider the probability that these arise from randomly correlated unrelated events. The number of possible random correlations is smaller when looking in a shorter time span, a smaller energy window, and a smaller spatial area. Analysis of the data from 2017-2018 therefore focused on identifying the shortest-lived reaction products expected based on the predictions for similar systems by Zagrebaev & Greiner. The data show that these nuclei were present, though the SIS 3316 digitizers were not optimized for their detection. This led to a new experiment aimed at producing and detecting these nuclei.

Inspired by the work of Zagrebaev & Greiner, production of an Os beam at the Cyclotron Institute was tested. We measured the beam intensity upstream of the MDM spectrometer with an electron-suppressed Faraday cup and determined that we were receiving 10^9 pps. However, during the test, the Os seemed to cause problems with the ion source. In order to measure a system very close in

mass to ^{192}Os + ^{197}Au, ^{197}Au +^{197}Au was used instead. This system is expected to have the same products of interest, produced in slightly higher quantities.

This experiment was optimized for the production and detection of the three isotones: ^{220}Rn, ^{221}Ac, and ^{222}Th. These three nuclei were targeted because of the interesting properties of their decay chains. Each isotone decays via three quick and high-energy alpha emissions, ending in a very long-lived or stable nuclide. Fig. 2 shows the decay chain of ^{220}Rn, highlighting the half-lives and the α Q-values for

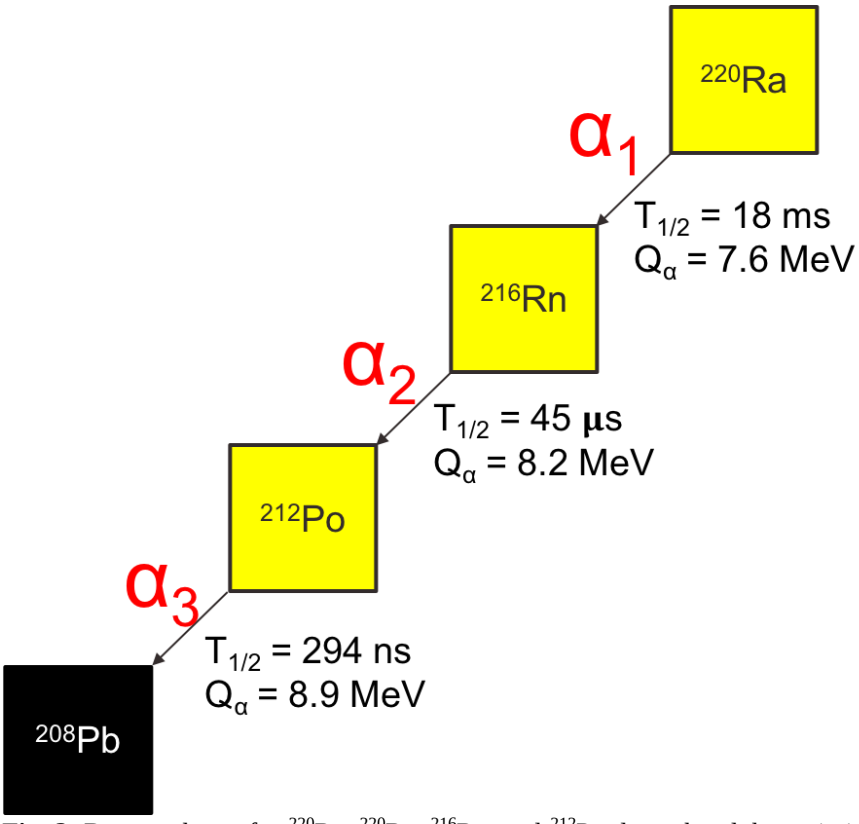

Fig. 2. Decay scheme for ^{220}Ra. ^{220}Ra, ^{216}Rn, and ^{212}Po decay by alpha emission with the shown half-lives and alpha emission energies. The decay chain ends at the stable ^{208}Pb nucleus.

each of the three decays. The first alpha decay in these chains is likely to be captured alone in a waveform. Then, when the second alpha decay triggers the acquisition, the third alpha decay is also seen in the same waveform. This is expected because the half-life of the granddaughter is very short (~ 300ns) and the SIS 3316 ADCs are set to capture a 2,000ns waveform. An example waveform with two high energy α particles is shown in Fig. 3. This waveform was collected in April 2021 and is a candidate for the decays of ^{216}Rn and ^{212}Po, resulting from the decay of ^{220}Ra. When looking only at high-energy alpha decay events occurring so closely in time, the chance that they are randomly correlated events is extremely small, given the amount of high-energy α particles seen in the Wakhle *et al.* data. The third decays in the chains of ^{221}Ac and ^{222}Th are similarly short-lived and we expect to see similar double α particles in a single waveform for them. By targeting these nuclei, their unique decay properties may

allow us to make a positive identification of these product isotones, though the energy resolution will not be sufficient for elemental distinction.

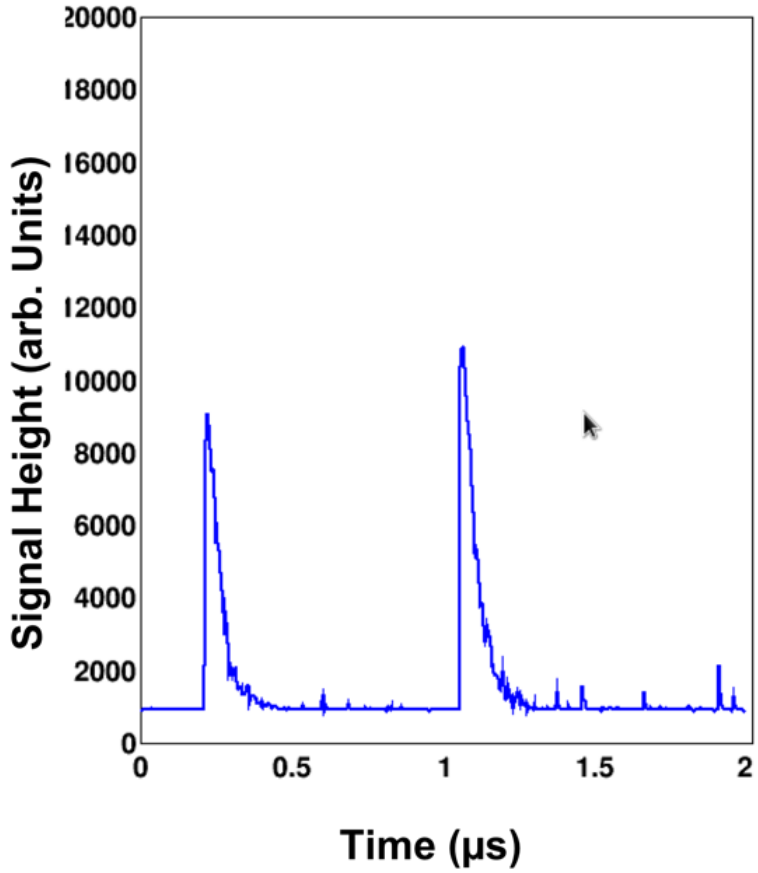

Fig. 3. A digitized waveform from the ^{197}Au+^{197}Au multinucleon transfer experiment conducted in April 2021. It has a 2 μs inspection window showing double alpha decays. The relative signal heights show that this is a candidate for the decays of ^{216}Rn and ^{212}Po occurring closely in time.

To further cut down on random correlations, part of the detector setup was improved to have better position resolution. A Hamamatsu H8500C position-sensitive photomultiplier tube (PSPMT) was borrowed from Robert Grzywacz from the University of Tennessee at Knoxville. The detector was cemented to an ISO100 flange, coupled with a quartz light guide segmented into 2mm x 2mm sections and a 500micron thick YAP scintillator. In past experiments, the active catcher array has used single-anode PMTs with cylindrical YAP scintillators that have a diameter of about 2cm. The identification of position was thus limited to that area, as one cannot distinguish multiple sources from a single source in a 2cm area. The PSPMT gives a position resolution of about 2mm, which is dictated by the light guide segment size.

Fig. 4a) shows the active catcher array inside the BBQ pit, as it was for the $^{197}Au+^{197}Au$ experiment in April 2021. Fourteen of the single-anode YAP-PMT detectors were removed to make space for the PSPMT and its flange to be attached to the array mount. Fig. 4b) shows a close up of the PSPMT detector without the mylar foil attached to it. The segments of the light guide can be seen through the clear YAP scintillator cemented to the front of it.

a)  b) 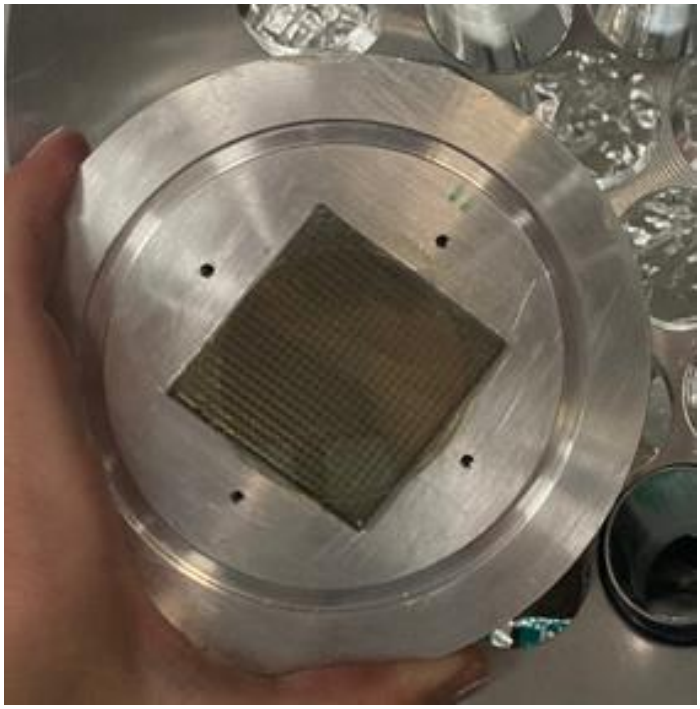

Fig. 4. a) The active catcher array as it was set up for the $^{197}Au+^{197}Au$ experiment in April 2021. b) The ISO100 flange that has a Hamamatsu H8500C position-sensitive photomultiplier tube cemented to it. A segmented quartz light guide and YAP scintillator are cemented to the front of the detector. The 2mm x 2mm segments of the light guide are visible in the image.

This year we also looked into upgrading the active catcher array with an array of diamond detectors. Unfortunately, our tests showed that they do not perform well after being bombarded with the products from our reactions of interest.

During the experiment, while monitoring the data as they were being collected, multiple candidate signals for the double-α single-waveform events, like the one shown in Fig. 3, were observed. To identify those interesting decay chains, the steps that need to be accomplished include:

1. Condition the data for analysis, including energy and position calibration. For overlapping signals in a digitized waveform, the signals need to be fitted and broken into their component contributions.
2. Correlate the daughter and granddaughter decays that are in a single waveform with the decay of the parent nucleus.

3. Identify a single chain of decays in the PSPMT, which will require the development of a clustering algorithm. This will look in a small area for multiple decays because there may be signal sharing of multiple pixels due to isotropic decays.

[1] S. Wuenschel *et al.*, Phys. Rev. C **97**, 064602 (2018).
[2] V.I. Zagrebaev and W. Greiner, Phys. Rev. C **87**, 034608 (2013).
[3] A. Wakhle *et al.*, *progress in Research*, Cyclotron Institute, Texas A&M University (2017-2018), p. IV-30.
[4] A. Wakhle *et al.*, *progress in Research*, Cyclotron Institute, Texas A&M University (2018-2019), p. II-15.

Temperatures in ^{86}Kr+^{12}C reactions are higher than in ^{78}Kr+^{12}C reactions

A.B. McIntosh, L.A. McIntosh, K. Hagel, and S.J. Yennello

Reactions of ^{78,86}Kr + ^{12}C @ 15, 25, 35 MeV/u [1] have been measured with the FAUST (Forward Array Using Silicon Technology) coupled to the QTS (Quadrupole Triplet Spectrometer). The primary motivation for this measurement was the investigation of the asymmetry dependence of the nuclear caloric curve [2-11] via fusion reactions.

Each of the 68 FAUST telescopes consist of a DADL (Dual-Axis Duo Lateral) silicon detector backed by a CsI(Tl)/PD. The DADLs [12,13] used in FAUST [14] resistively split the charge collected on the faces of the detector to determine the position. For protons which deposit very little energy in the silicon detector, this can result in one or more of the four signals from the detector to be below threshold. If the requirement is made that all four signals were above threshold, much of the proton distribution is missed. But events with missing signals can be added back in. For all of some of these, full energy and position information is possible to reconstruct; for others, only energy and position in one of the two dimensions is possible. If three signals are required, the fourth can be calculated since the sum of the two front signals must equal the sum of the two back signals. If two back signals (or two front signals) are missed, the energy and position from the front (or back) is good, but the position information from the back (or front) is lost. If one back and one front are missed, the measured signals contain enough energy that the ΔE-E technique still provides particle ID, the CsI signal can be used with energy loss calculations to determine the total energy of the particle, and the position information in both dimensions can be obtained. If three of the four signals are missing, the same technique as two missing signals can be used, though the position information in one of the two dimensions is lost. This augmentation to the calibration was implemented. The energy distributions of protons are thus measured with greater efficiency up to 100 MeV (the punch-through energy for the CsI). Since the majority of the incomplete proton events are missing two back signals, this recovery procedure still significantly lacks full position information, and for events with full position information, the positions measured are strongly biased toward the center of the detector. The above applies to deuterons and tritons as well but to a lesser extent.

The excitation energy is calculated for each of the six systems (two beam isotopes at three energies each) from the measured fusion residue velocity [15-17]. The recoil effects from evaporation are large enough to preclude accurate event-by-event calculation of the excitation energy, so the mean of the distribution is used to calculate the mean excitation energy.

Temperatures have been extracted using three methods [18] from light charged particles emitted in the fusion reactions. The kinetic slope temperature is the first method used. The velocity distributions of the light charged particles form a ring centered on the residue velocity which can be described by a Maxwell-Boltzmann distribution in the frame of the residue. Fitting [19] these energy spectra in the residue frame provides the slope temperature. This is done separately for each type of evaporated particle. Fig. 1 shows the caloric curve extracted for alpha particles. The temperature rises monotonically with excitation as expected at low excitation. The blue points, corresponding to the neutron-rich ^{86}Kr beam, exhibit higher temperatures than the red points, corresponding to the less-neutron-rich ^{78}Kr beam. Slope temperatures for other light charged particles either show the same behavior (^{6}He, Li) or no difference

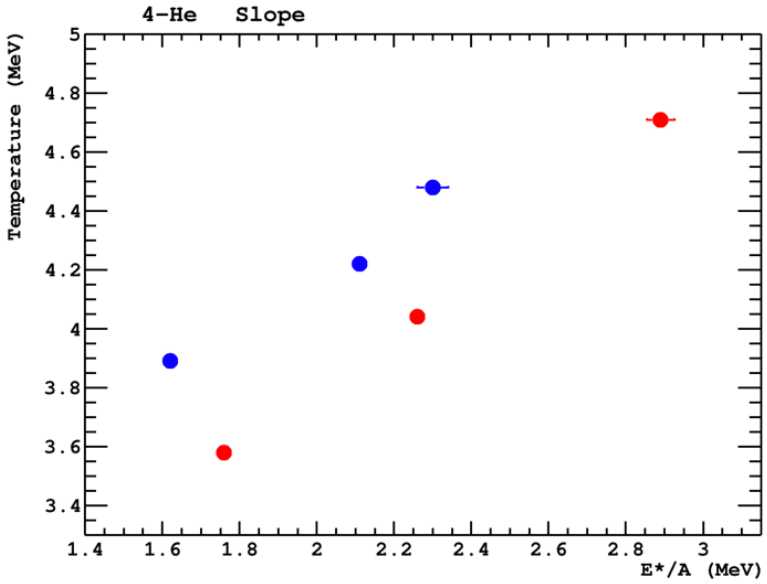

Fig. 1. Alpha particle slope temperatures for $^{86}Kr+^{12}C$ (blue) and $^{78}Kr+^{12}C$ (red).

with uncertainties ($^{1,2,3}H$, ^{3}He). Since the efficiency for detecting residues is not great, kinetic spectra in the frame of the average residue velocity are also calculated to take advantage of improved sample size; slightly higher temperatures are extracted (kinematic smearing), but the neutron-rich systems still show higher temperature. The failure of the lightest isotopes to reproduce this trend, and even to provide increasing T with E*/A, arises from the reduction in effective active area of the detector as a function of increasing particle kinetic energy. Inclusion of the particles that produce fewer than four silicon signals improves the situation somewhat, but the energy-dependent efficiency remains significant. An accurate quantification of the efficiency could allow a correction to be made in the future.

The second method for calculating the temperature is the momentum quadrupole fluctuation thermometer (MQF) [20]. This in principle provides the same information as the other kinetic thermometer, but in practice has different biases. The MQF does not rely on fits, only on the width of a distribution (px^2-py^2), and avoids use of momenta in the direction of the beam to avoid collective effects (though these should be small for the fusion reactions studied here). Fig. 2 shows the MQF temperatures for alpha particles as a function excitation energy. Again, higher temperatures are observed for the more neutron-rich systems. The higher temperatures seen for the MQF are consistent with previous observations [2-4]. A quantum correction [20,21] and a Coulomb correction [22] could change the absolute values but should not change the result that higher temperatures are observed for more neutron-rich systems.

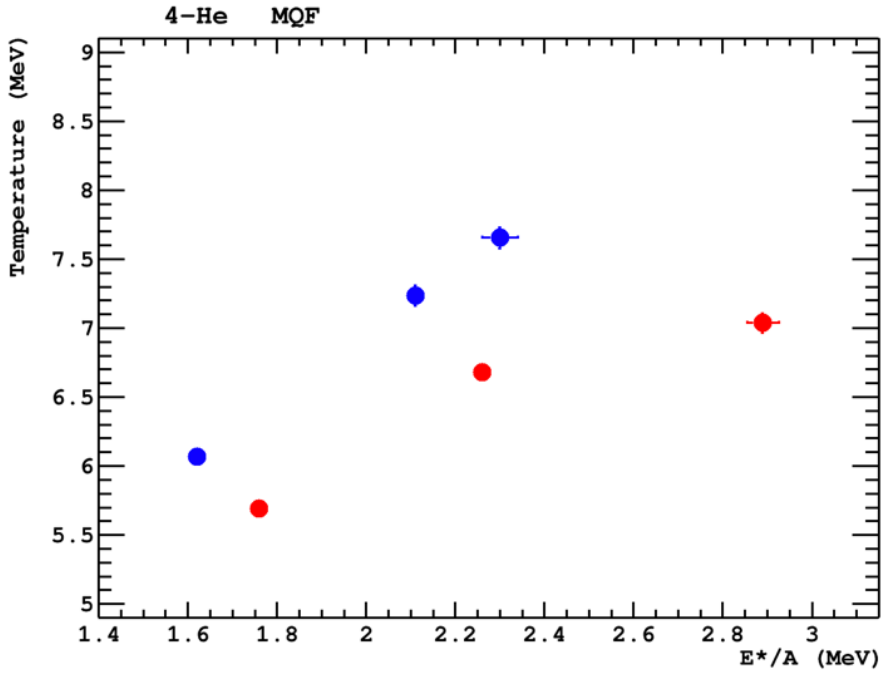

Fig. 2. Alpha particle fluctuation temperatures for $^{86}Kr+^{12}C$ (blue) and $^{87}Kr+^{12}C$

The third method for calculating temperature is the double yield ratio method [Alb1985]. Here, (p/d)/(h/a) and (d/t)/(h/a) are used. The energy dependent efficiencies for Z=1 particles cancels out to first order (as do many other effects). The yields are only calculated where coverage is large. The resulting temperatures are shown in Fig. 3, where it can again be seen that the more neutron-rich system exhibits a

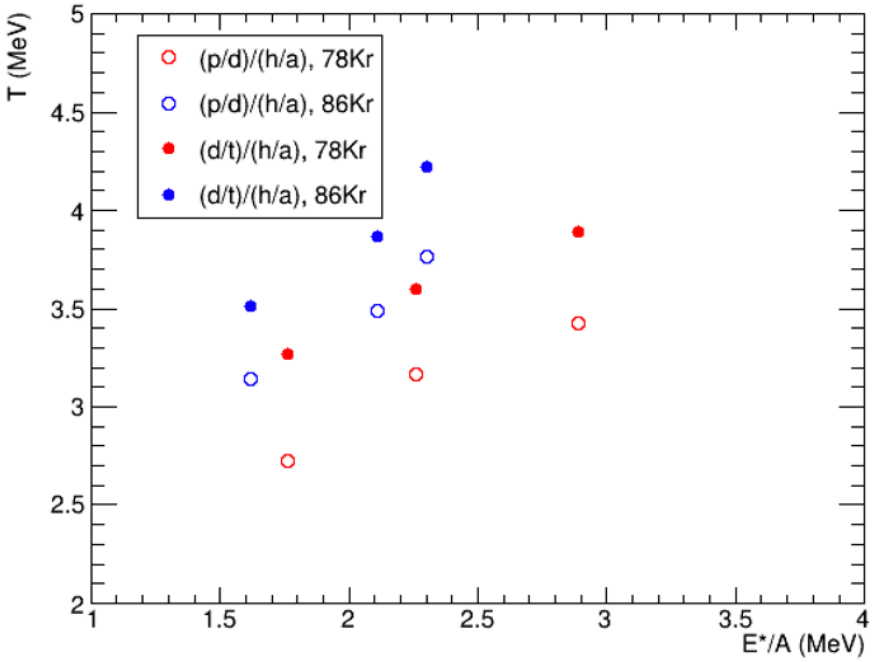

Fig. 3. Albergo temperatures for 86Kr+12C (blue) and 87Kr+12 (red) using two different double isotope ratios.

larger temperature. Temperatures are examined over a range of angles in the residue frame, and though there is a modest variation of the temperature with this angle, the temperatures are always higher for the more neutron-rich system.

The higher temperatures for neutron-rich systems in this Kr+C measurement are at odds with the lower temperatures seen for neutron-rich systems in reactions of Zn+Zn [Mc2013a, Mc2013b, Mc2014], and further investigation is required to resolve this. The use of free neutrons in the Zn+Zn measurement in both the reconstruction of the composition and in the excitation energy is a natural point to begin. However, previous analysis concluded that this autocorrelation was too small to explain the effect; additionally, lower temperatures were seen for more neutron-rich sources even when selecting on entrance channel composition rather than reconstructed composition.

[1] Alan B. McIntosh and Sherry J. Yennello, Eur. Phys. J. Web of Conferences **117**, 07019 (2016).

[2] A.B. McIntosh, A. Bonasera, P. Cammarata, K. Hagel, Heilborn, Z. Kohley, J. Mabiala, L.W. May, P. Marini, A. Raphelt, G.A. Souliotis, S. Wuenschel, A. Zarrella, and S.J. Yennello, Phys. Lett. B **719**, 337 (2013).

[3] A.B. McIntosh, A. Bonasera, Z. Kohley, P.J. Cammarata, K. Hagel, L. Heilborn, J. Mabiala, L.W. May, P. Marini, A. Raphelt, G.A. Souliotis, S. Wuenschel, A. Zarrella, and S.J. Yennello, Phys. Rev. C **87**, 034617 (2013).

[4] A.B. McIntosh, J. Mabiala, A. Bonasera, P. Cammarata, K. Hagel, Z. Kohley, L. Heilborn, L.W. May, P. Marini, A. Raphelt, G.A. Souliotis, S. Wuenschel, A. Zarrella, H. Zheng, and S. J. Yennello, Eur. Phys. J. A **50**, 35 (2014).

[5] C. Sfienti *et al.* (ALADIN2000 Collaboration), Phys. Rev. Lett. **102**, 152701 (2009).

[6] S. Wuenschel, A. Bonasera, L.W. May, G.A. Souliotis, R. Tripathi, S. Galanopoulos, Z. Kohley, K. Hagel, D.V. Shetty, K. Huseman, S.N. Soisson, B.C. Stein, and S.J. Yennello, Nucl. Phys. **A843**, 1 (2010).

[7] V.M. Kolomietz, A.I. Sanzhur, S. Shlomo, and S.A. Firin, Phys. Rev. C **64**, 024315 (2001).

[8] C. Hoel, L.G. Sobotka, and R.J. Charity, Phys. Rev. C **75**, 017601 (2007).

[9] R. Ogul and A.S. Botvina, Phys. Rev. C **66**, 051601(R) (2002).

[10] J.Besprosvany and S.Levit, Phys. Lett. B **217**, 1 (989).

[11] Jun Su and Feng-Shou Zhang, Phys. Rev. C **84**, 037601 (2011).

[12] S.N. Soisson, B.C. Stein, L.W. May, R.Q. Dienhoffer, M. Jandel, G.A. Souliotis, D.V. Shetty, S. Galanopoulos, A.L. Keksis, S. Wuenschel, Z. Kohley, S.J. Yennello, M.A. Bullough, N.M. Greenwood, S.M. Walsh, and C.D. Wilburn, Nucl. Instrum. Methods Phys. Res. **A613**, 240 (2010).

[13] L.A. McIntosh, A.B. McIntosh, K. Hagel, M.D. Youngs, L.A. Bakhtiari, C.B Lawrence, P. Cammarata, A. Jedele, L.W. May, A. Zarrella, and S.J. Yennello, Nucl. Instrum. Methods Phys. Res. **A985**, 164642 (2021).

[14] F. Gimeno-Nogues, D.J. Rowland, E. Ramakrishnan, S. Ferro, S. Vasal, R.A. Gutierrez, R. Olsen, Y.-W. Lui, R. Laforest, H. Johnston, and S.J. Yennello, Nucl. Instrum. Methods Phys. Res. **A399**, 94 (1997).

[15] W. Bohne, H. Morgenstern, K. Grabisch, T. Nakagawa, and S. Proschitzki, Phys. Rev. C **41**, R5 (1990).

[16] D. Fabris, K. Hagel, J.B. Natowitz, G. Nebbia, R. Wada, R. Billerey, B. Cheynis, A. Demeyer, D. Drain, D. Guinet, C. Pastor, L. Vagneron, K. Zaid, J. Alarja, A. Giorni, D. Heue, C. Morand, B. Viano, C. Mazur, C. Ngo, S. Leray, R. Lucas, M. Ribrag, and E. Tomasi, Phys. Lett. B **196**, 429 (1987).
[17] K. Hagel Ph.D. Thesis, Texas A&M University, 1986
[18] A. Kelić, J.B. Natowitz and K.-H. Schmidt, Eur. Phys. J. A **30**, 203 (2006).
[19] R. Yanez, S. Hudan, R. Alfaro, B. Davin, Y. Larochelle, H. Xu, L. Beaulieu, T. Lefort, V.E. Viola, R.T. de Souza, T.X. Liu, X.D. Liu, W.G. Lynch, R. Shomin, W.P. Tan, M.B. Tsang, A. Vander Molen, A. Wagner, H.F. Xi, R.J. Charity, and L.G. Sobotka, Phys. Rev. C **68**, 011602(R) (2003).
[20] Hua Zheng and Aldo Bonasera, Phys. Lett. B **696**, 178 (2011).
[21] Hua Zheng, Gianluca Giuliani, and Aldo Bonasera, Nucl. Phys. **A892**, 43 (2012).
[22] Hua Zheng, Gianluca Giuliani, and Aldo Bonasera, J. Phys. G **41**, 055109 (2014).

Characterization of the AGGIE gas-filled separator

C.M. Folden III[1,2]
[1]*Cyclotron Institute, Texas A&M University, College Station, Texas 77843*
[2]*Department of Chemistry, Texas A&M University, College Station, Texas 77843*

A gas-filled separator has been installed and is in the process of being characterized at the Cyclotron Institute at Texas A&M University. This separator was originally designed at Lawrence Berkeley National Laboratory under the name SASSY II [1] and was an evolution of the previous SASSY gas-filled separator [2]. After being transferred to Yale University and rechristened as SASSYER [3], it was eventually moved to Texas A&M. The device has been renamed again as AGGIE, for Al Ghiorso's Gas-filled Ion Equipment. First characterizations using beam were conducted in 2019 and have continued through this writing.

The device takes advantage of the gas-filled separation technique [2], where a dilute gas (He) is used to provide charge equlibration of fusion-evaporation reaction products. This has the effect of narrowing the product's magnetic rigidity distribution, which can lead to higher transmission efficiencies. This is especially desirable for reactions with small production cross sections. AGGIE consists of two dipole magnets and one quadrupole magnet in a $D_vQ_hD_v$ configuration with a length of approximately 2.5 m. Additional eqiuipment received from Yale included the Multi-wire Avalanche Counter at Yale (MACY), which can be used as an impantation detector; a focal plane array consisting of two adjacent double-sided silicon strip detectors with a total of 120 strips for measuring horizontal position and 40 strips for measuring vertical position; and a set of Mesytec MUX-16 multiplexing electronics which allow all strips to be recorded without requiring dedicated electronics for each. The latter electonics have been successfully integrated into the data acquisition system currently in use by the Heavy Elements Group.

AGGIE was initially characterized using a ^{241}Am source mounted in the target position, and later experiments have utilized nuclear reaction products to determine the influence of magnetic field on transmission. Reactions used for this purpose have included ^{118}Sn(^{40}Ar, xn)$^{158-x}$Er (x =5-6), ^{165}Ho(^{40}Ar, yn)$^{205-y}$At (y = 5-6), and ^{165}Ho(^{35}Cl, 4n)^{196}Po. Average product charge states were estimated according to Eq. 1 in [4]. Beam intensity was monitored via two collimated scattering detectors mounted in the target box at ±30° to the beam axis. The current deposited in the beam dump is also recorded moment-to-moment to provide a relative measure of beam intensity as a function of time.

Combined with increases in beam intensity that have been realized by extracting beam from the K150 cyclotron in first harmonic mode, these studies have shown that the yield of fusion-evaporation products is substantially higher than in similar experiments using the MARS spectrometer [5-9]. These increases in sensivitivty allow for additional nuclear reaction studies and chemical experiments on the homologs of superheavy elements where AGGIE will act as a physical pre-separator. The latter is especially important, given that there are very few facilities worldwide that are capable of conducting experiments with pre-separated homologs. These characterization experiments are ongoing.

[1] A. Ghiorso, J. Radioanal. Nucl. Chem. **124**, 407 (1988). doi:10.1007/bf02041331

[2] A. Ghiorso, S. Yashita, M. E. Leino, L. Frank, J. Kalnins, P. Armbruster, J.P. Dufour, and P.K. Lemmertz, Nucl. Instrum. Meth. A **269**, 192 (1988). doi:10.1016/0168-9002(88)90877-7

[3] J.J. Ressler *et al.*, Nucl. Instrum. Methods Phys. Res. **B204**, 141 (2003). doi:10.1016/S0168-583X(02)01906-7

[4] K.E. Gregorich *et al.*, Phys. Rev. C **72**, 014605 (2005). doi:10.1103/PhysRevC.72.014605

[5] C.M. Folden III, M.C. Alfonso, D.A. Mayorov, K.R. Lawrence, A.A. Alharbi, E. Berdugo, P.J. Cammarata, A.C. Raphelt, B.T. Roeder, and T.A. Werke, Nucl. Instrum. Methods Phys. Res. **A678**, 1 (2012). doi:10.1016/j.nima.2012.02.035

[6] T.A. Werke, D.A. Mayorov, M.C. Alfonso, E.E. Tereshatov, and C.M. Folden III, Phys. Rev. C **92**, 054617 (2015). doi:10.1103/PhysRevC.92.054617

[7] T.A. Werke, D.A. Mayorov, M.C. Alfonso, M.E. Bennett, M.J. DeVanzo, M.M. Frey, E.E. Tereshatov, and C.M. Folden III, Phys. Rev. C **92**, 034613 (2015). doi:10.1103/PhysRevC.92.034613

[8] D.A. Mayorov, T.A. Werke, M.C. Alfonso, M.E. Bennett, and C.M. Folden III, Phys. Rev. C **90**, 024602 (2014). doi:10.1103/PhysRevC.90.024602

[9] D.A. Mayorov, T.A. Werke, M.C. Alfonso, E.E. Tereshatov, M.E. Bennett, M.M. Frey, and C.M. Folden III, Phys. Rev. C **92**, 054601 (2015). doi:10.1103/PhysRevC.92.054601

A new linearization method for NIMROD super telescopes

R. Wada, M. Huang, and K. Hagel

In order to study neutron-proton equilibration study, it is preferable to identify the isotope mass A and Z up to Z~ 20. Most Si-Si pairs in the NIMROD super telescopes can show a clear line for each isotope up to Z<=10. Only a few can resolve isotope above Z>10. Typical two examples are shown in Fig.1. In the upper panel, isotopes up to Z=8 appear as separate lines clearly. In the lower panel, isotopes with Z <=16 can be seen.

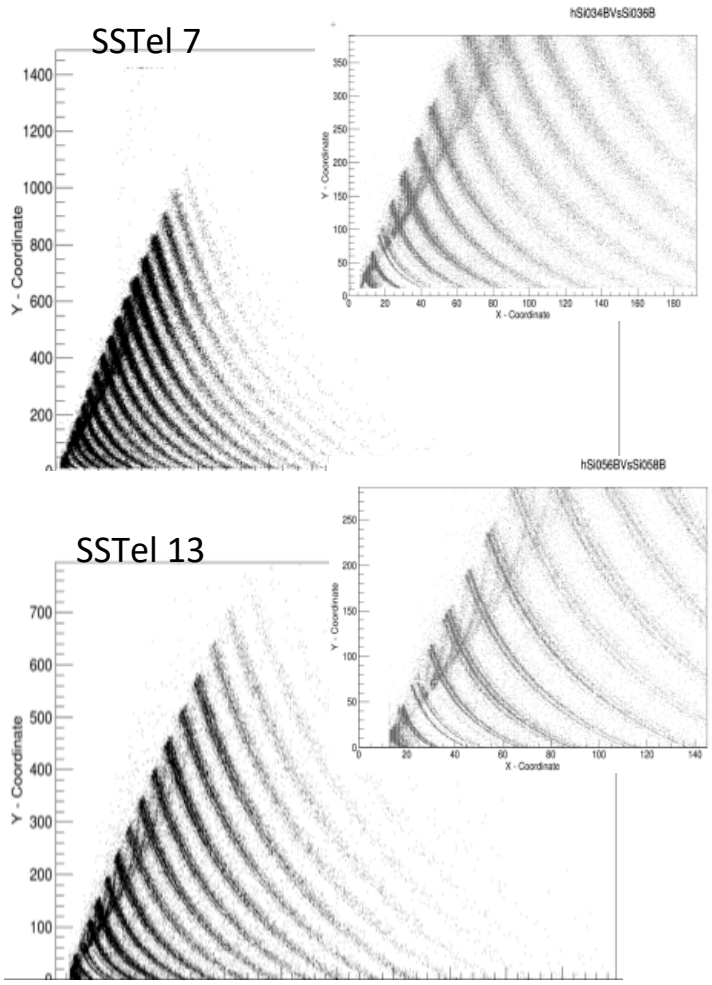

Fig. 1. Si1(dE) vs Si2(E) plot for particles stopped in Si2 detector in super telescopes #7 and #13. Inserts are plots in an expanded scale.

In order to identify the isotopes Z and A, a linearization package is used, in which Z as a real number is assigned for a give data point, using the distance from the nearby A=2Z lines. About 10-20 points are picked for each A=2Z isotopes, if they are identified by a separate line. Therefore in the lower case, A=2Z line can go up to Z=16, but the upper case, it only goes up to Z=10. In order to assign the A and Z values for all in the upper case, the range-energy table are used with the following steps.

1 Si1(dE) on the X axis and Si2 (E) on the Y axis are calibrated for Z=4-10 isotopes lines to match the lines calculated from the range energy tables.

2 Then for Z>10 isotopes, the lines calculated from the range energy tables are used for A=2Z lines for the linearization. (For Z<=10 picked points are used).

In this way, not only the isotopes, but also the Si energy on each axis can be calibrated at a time.

In Fig.2, linearized Z vs Esum (dE+E) are plotted for both cases. Even for isotopes with no distinctive lines, one can reasonably well identify the isotopes up to Z=20. In Fig.3, the extracted Z

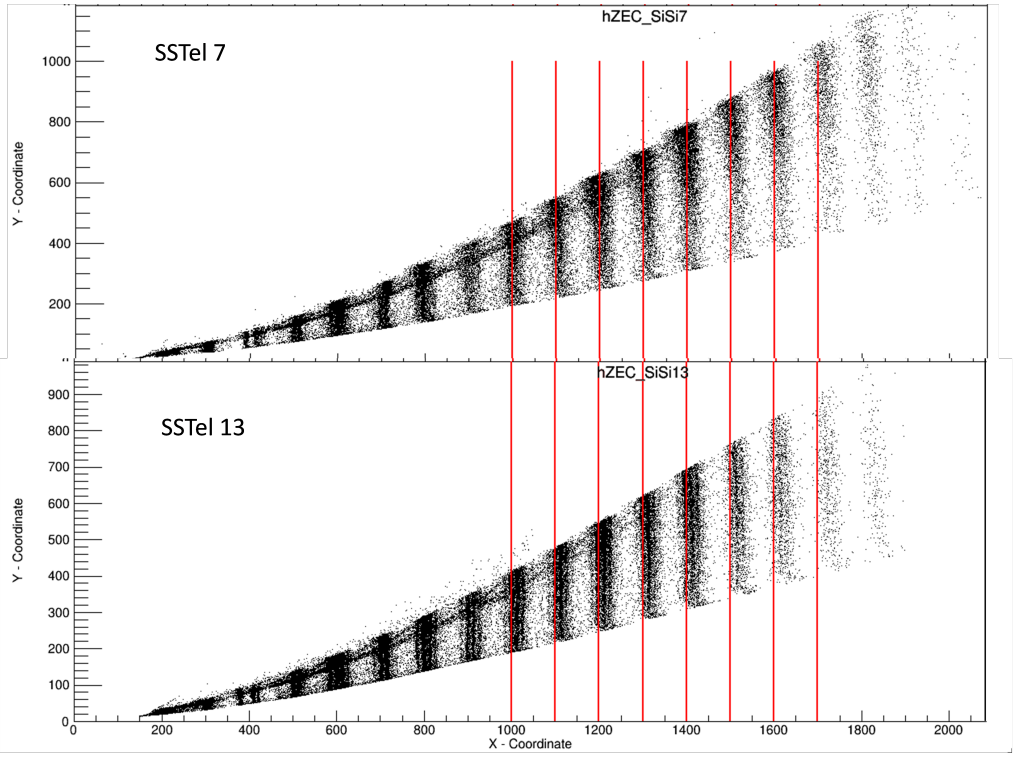

Fig. 2. Linearized Z vs Esum. On the X axis the number correspond Z*100. In the Y axis the energy is given in MeV.

numbers are compared between these two telescopes for Z=0-10 in the upper and Z=10-20 in the lower. Even for those in which no clear lines are observed for individual isotopes like telescope #7, the Z numbers are not only reasonable, though their absolute number is slightly shifted. They can be easily corrected later. For the n/p equilibration study, the widths of the isotope distribution are crucial and they are more or less same as those of telescope #13. When each isotope is fit by a Gaussian in a given Z for telescope #13, the mean and sigma can be extracted. Using these means and widths, one can reasonably well evaluate the isotope yield when no isotope lines are observed like telescope#7. Further study is now underway.

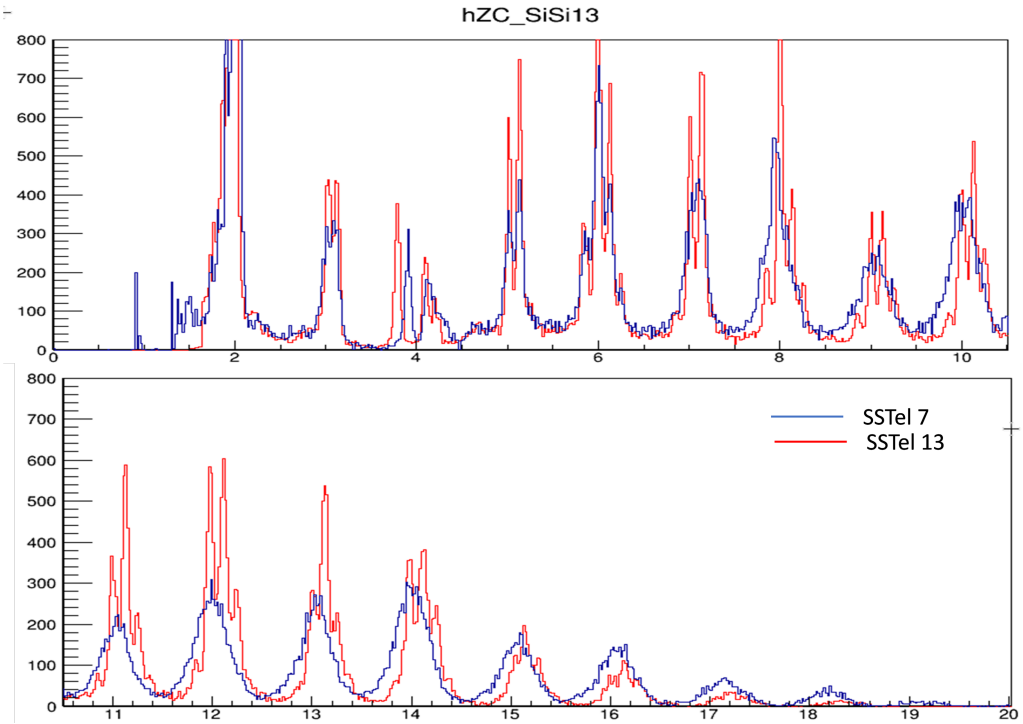

Fig. 3. The projected Linearized Z value on the X axis from Fig.2. Red histogram is from the telescope #13 and the blue represent the Z from the telescope # 7. Z=int(Z) corresponds to isotopes with A=2Z. The fraction indicates the mass difference from the A=2Z isotope.

AMD and inverse spallation reaction with $^{12}C+^{1}H$ at 95 A MeV

R. Wada, G. Tian, R. Han, and A. Ono

The inverse spallation reaction of $^{12}C+^{1}H$ at 95 A MeV from Ref.1 has been used to examine different elements of the stochastic processes in the anti-symmetrized molecular dynamics (AMD)[2-6], focusing on the diffusion process and cluster correlation. The standard AMD code has a quantum blanching process, which is called "diffusion process' to reproduce the multi-fragmentation events from intermediate heavy ion collisions. However in this energy region, excited intermediate mass fragments are copiously generated in general and they cool down by sequential decay process before they are observed in the experiments. Therefore the primary products from AMD are significantly overlayed with those products from the secondary decays. In another words, the experimental products are closely related to both processes, primary dynamics of AMD and secondary decay process of an afterburner and often it is difficult to separate these two processes.

Spallation reactions use light ions, mostly protons, as the incident ions, bombarded on a heavier mass target in the energy range from 100 A MeV to above A GeV. Since the projectile is small, most products are produced from the target. However in the normal kinematics, many products are generated in wider angular and energy ranges. In order to observe all products in flight, reverse kinematic is often used, since all products are produced at the beam direction with similar velocity as the projectile. However this is not true for protons. Protons are generated at all angles with wider energy distribution in the center of mass frame. Therefore in the inverse kinematic reactions, the protons emitted at the

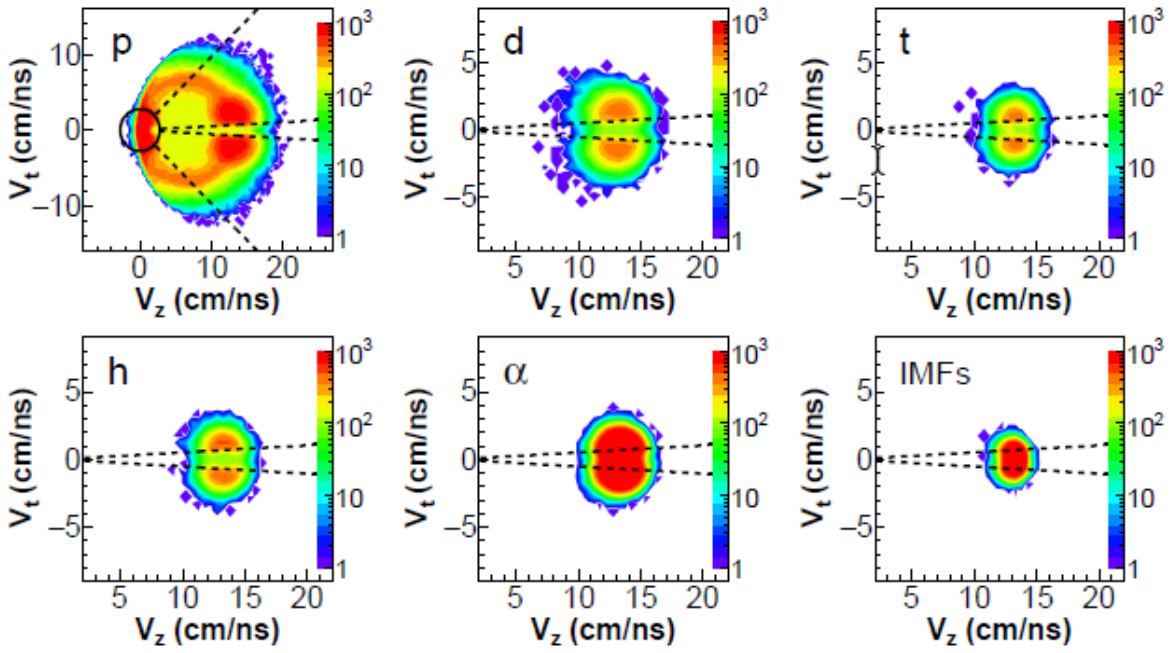

Fig. 1. 2D velocity plots for $^{12}C+^{1}H$ at 95 A MeV from AMD+Gemini simulations for particles indicated in each figure. Same Z scale is used for all.

backward hemisphere may provide a test bench in which only the primary dynamics is dominated with no sequential decay disturbance. These protons may provide a sensitive probe to verify different elements of the stochastic processes incorporated in AMD.

Along the above scenario, $^{12}C+^{1}H$ at 95 A MeV data set from [1] is examined. In Fig.1, two dimensional velocity plots, $d^2\sigma/dVtdVz$, of p, d, t, h, α and IMFs are shown from AMD+Gemini.

The ring and dashed lines indicate the experimental detection limits. Protons show a rather wide distribution with clear three distinct sources, a projectile-like (PLF) source centered near the beam velocity, an intermediate velocity (IV) source with about a half beam velocity and a target-like (TLF) source near the origin and inside the circle, indicating most of them are not observed experimentally. All other clusters show essentially a PLF source alone. The PLF protons, therefore, are produced from two processes, the dynamical process of AMD at early stage and the sequential decay additions of Gemini from heavier clusters at later stages. On the other hand, the IV protons are mainly produced by the AMD dynamics alone, since no excited IV cluster source exists. The IV protons form a ring, which indicate that these protons are produced by quasi-elastic scattering between one nucleon in the target and the projectile proton. These overviews of the velocity distributions confirm the isolated production mechanism of the IV protons, that is, they are produced mainly from the early stage of the dynamics of AMD and therefore detailed study of these protons may provide a sensitive probe for the AMD modeling. Now further detailed study is underway, comparing the AMD predictions with the experimental data.

[1] J. Dudouet *et al.*, Phys. Rev. C **88**, 024606 (2013); http://hadrontherapydata.in2p3.fr.
[2] A. Ono, H. Horiuchi, T. Maruyama, and A. Ohnishi, Prog. Theor. Phys **87**, 1185 (1992).
[3] A. Ono and H. Horiuchi, Phys. Rev. C **53**, 2958 (1996).
[4] G. Tian *et al.*, Phys. Rev. C **95**, 044613 (2017).
[5] G. Tian *et al.*, Phys. Rev. C **97**, 034610 (2018).
[6] R. Han *et al.*, Phys. Rev. C **102**, 064617 (2020).

Experimental study of liquid-gas phase transition in Xe+Sn at 50A MeV

R. Wada, Guoyu Tian, Xueying Liu, Weiping Lin, Xingquan Liu, K. Hagel, and A. Chbihi

The experimental liquid-gas phase transition is studied for Quasi-Projectile(QP) system with A~ 120, using the GANIL data of ^{129}Xe+^{nat}Sn at 50 MeV/nucleon, taken with a 4π detector array INDRA. The experimental details and data analysis are given in Refs.[1-4]. The methods used for characterizing the QP and constructing the caloric curve for the liquid-gas phase transition study are essentially same as those of the previous study, in which the QP is reconstructed from the reactions of ^{40}Ar+^{27}Al, ^{48}Ti, ^{58}Ni at 47 MeV/nucleon, taken with NIMROD [5].

In order to construct QPs, a moving source analysis is employed, as described in the 2019 annual report. Among those, complete events are selected, requiring the 80 <= A_{QP} <= 129. These QP events are further classified into three, multi-fragmentation like (M_{LF}=0), evaporation residue like (M_{LF}=1) and fission-like (M_{LF}=2) events, in which M_{LF} is the multiplicity of "large fragment" with Z>=15 in each event.

In Fig.1 caloric curves are made, using the fluctuation thermometer with p, d, t, h and α. From the probed particle to particle, the caloric curves behave quite differently, which was not expected. The differences among different M_{LF} classes are noticeable and some are quite different. The caloric curve for deuteron worked well for lighter QP system in the previous analysis [5], but it is not the case here.

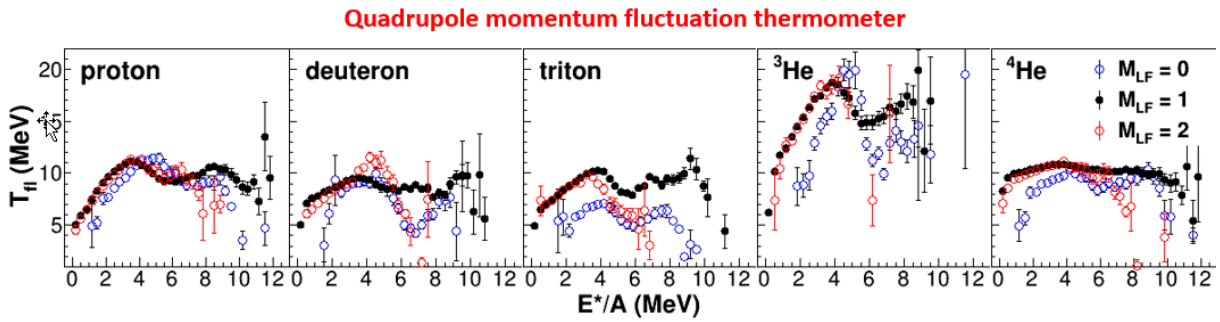

Fig. 1. Caloric curves, using the momentum fluctuation thermometer with p, d, t, h, α from the left to right for M_{LF}=1 (black) and 2 (red) events.

In Fig.2 caloric curves with Albergo thermometer, utilized the ratios of {Y(d)/Y(t)}/{Y(h)/Y(α)} for the different M_{LF} triggers. The caloric curve for MLF=0 shows a smooth increase as E*/A increases. That with M_{LF}=1 on the middle shows a peak at E*/A ~ 4 MeV with T ~ 5.5 MeV and become flat at T ~ 5 MeV for the higher excitation energies. For events with M_{FL}=2, the peak occurs at E*/A ~ 3 MeV, but the temperature is similar (~ 5.5 MeV) and also shows a peak structure. At E*/A > 5 MeV, statistics is getting poor.

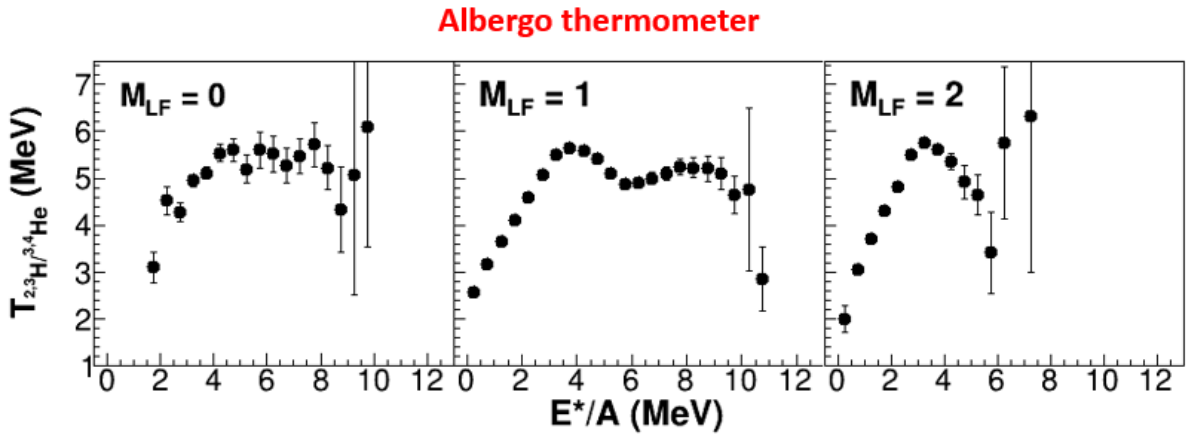

Fig. 2. Caloric cur ves are plotted, using Albergo thermometer for the events with MLF= on the left and 2 on the right.

In Fig.3, the multiplicity of all QP charged particles, M_{CP}, is plotted as a function of E*/A. In Ref.[6] it has been demonstrated that M_{CP} is also a sensitive measure for the liquid-gas phase transition. The shape is very similar to those of protons in Fig.1. These inconsistencies among different measures for different M_{LF} classes are under investigation, using AMD simulations.

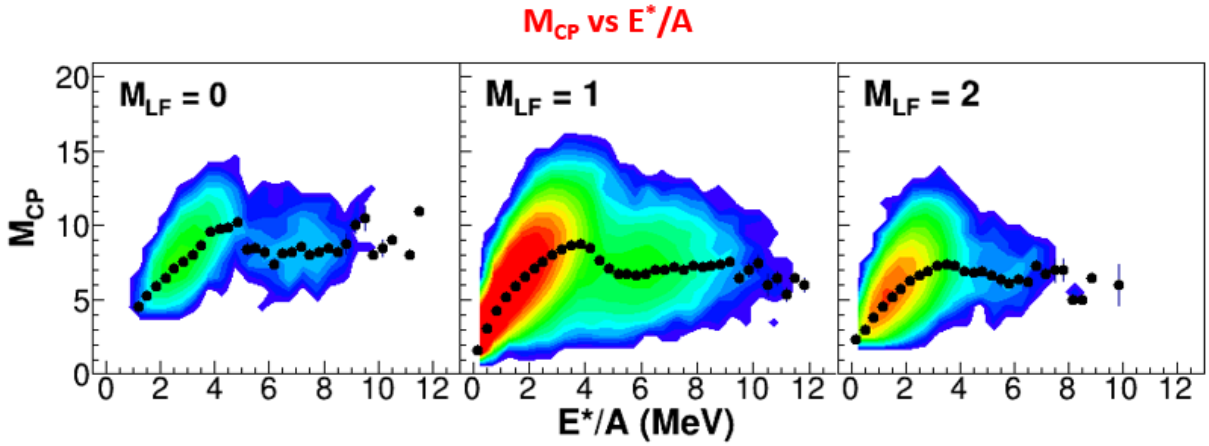

Fig. 3. Charge particle multiplicity in QP events, M, vs the excitation energy for the events with MFF=1 on the left and 2 on the right.

[1] J. Pauithas *et al.*, Nucl. Instrum. Methods Phys. Res. **A357**, 418 (1995).

[2] J. Łukasik *et al.*, Phys. Rev. C **55**, 1906 (1995).

[3] N. Marie *et al*., Phys. Lett. B **391**, 15 (1997).

[4] E. Plagnol *et al.*, Phys. Rev. C **61**, 014606, (1997).

[5] R. Wada, W. Lin, P. Ren, H. Zheng, X.Liu, M. Huang, K. Yang, and K. Hagel, Phys. Rev. C **99**, 024616 (2019).

Toward understanding relativistic heavy-ion collisions with the STAR detector at RHIC

D.M. Anderson, Y. Liu, S. Mioduszewski, and the STAR Collaboration

This project is a study of high-energy heavy-ion collisions at the Relativistic Heavy Ion Collider (RHIC). The focus of the study is on two probes of the dense, partonic matter created in these collisions: 1) direct-photon-triggered jets (and their correlations) and 2) heavy-quarkonium production and suppression.

Investigating Energy Loss through Photon-Triggered Jet Measurements

The hard production of a direct photon back-to-back with a jet (γ-jet) is a probe of the parton energy loss in heavy-ion collisions [1]. In the "γ-jet" coincidence measurement, the measured energy of the trigger particle (the photon) serves as a calibrated baseline for the total energy of the jet particles on the recoil side (i.e. opposite in azimuth) of the trigger. The mean-free path of the γ in the medium is large enough so that its momentum is preserved, regardless of the position of the initial scattering vertex. Thus it does not suffer from the geometric biases, i.e. the non-uniform spatial sampling of hadron triggers due to energy loss in the medium, of e.g. π^0 triggers. Because of the difference in path length traversed, on average, between a direct-g and a π^0 trigger, comparisons of γ-jet to hadron (π^0)-jet measurements can provide insight into the path-length dependence of the energy loss.

As the dominant background to direct photons are π^0 (decaying to two photons), the Barrel Shower Maximum Detector (BSMD) has provided the capability of distinguishing direct photons from neutral pions via the transverse shower shape. Our group has used this method in the measurement of direct photon+hadron correlations [2]. The γ-hadron correlation studies can be extended to studies of γ-triggered jet reconstruction measurements (as has been done at the LHC [3, 4]). The away-side jet will then be reconstructed in coincidence with triggers selected as direct photon candidates or (for $p_T<20$ GeV using the shower shape with the BSMD) identified π^0 triggers. The advantage of this should be the ability to reach lower energy fragments in the jet to study jet-shape modification and possible redistribution of energy.

The Run-14 photon-triggered data set in Au+Au collisions has been fully analyzed for charged jets recoiling from a high-energy neutral (π^0 or γ) trigger. We have chosen to concentrate initially on charged-particle jets, for simplicity, recoiling from the trigger particle. Charged-jet reconstruction is performed using the anti-k_T algorithm from the Fastjet package [5]. A fiducial cut in jet pseudorapidity, $|h_{jet}| < 1-R_{jet}$, where R_{jet} is the jet resolution parameter associated with the radial size of the jet. For the baseline measurement, data from Run-9 p+p collisions have been analyzed. In the past year, we have advanced the baseline measurement toward finalization. The following work has been completed.

1) The energy scale of the trigger has been determined, which is crucial for comparing to theoretical calculations, including PYTHIA [6].

2) Corrections for detector effects calculated from embedding of di-jet Pythia events in Run-9 p+p zero-bias data have been applied. The corrections of jet momentum is done via unfolding of the raw

jet spectrum using a response matrix of detector-level jet momentum vs. particle-level jet momentum. The efficiency for finding jets is applied to the unfolded jet-momentum spectrum.

3) The response matrix has been "smoothed", in order to remove large fluctuations in the response due to limited statistics in the embedding sample.

4) The R=0.2 and R=0.5 jet spectra have been unfolded and are currently being compared to PYTHIA calculations, taking into account the trigger energy scale by weighting to match the true sampled trigger energies.

Unraveling Cold Nuclear Matter Effects in J/Y Suppression

The J/ψ has long been considered one of the most promising direct probes of deconfinement. According to theoretical predictions in 1986 [7], the produced $c\bar{c}$ pair will not be able to form a J/ψ bound state in the QGP, if a sufficiently high temperature is reached where the screening radius is smaller than the binding radius of the J/ψ resonant state. The "Debye" screening radius is the distance at which the color charges of two quarks are screened from one another, so that the confinement force is not able to hold the quarks together. A suppression in the yield of J/ψ was first observed in Pb+Pb collisions by the NA50 experiment at the CERN SPS (see, for example, [8]).

At RHIC, the predicted suppression of J/ψ due to screening in the QGP is much larger than the suppression observed at SPS due to the higher initial density of the produced medium [9]. The RHIC measurements, however, show a level of suppression similar to NA50 at mid-rapidity [10], which is significantly smaller than expectations due to color screening effects alone. This can be understood in a scenario where charmonium is regenerated due to the large initial production of charm + anti-charm quarks at $\sqrt{s_{NN}}$ = 200, in conjunction with their possible thermalization in the created medium [11]. If charm quarks (partially) thermalize in RHIC collisions, then the coalescence of $c\bar{c}$ could lead to a smaller than expected suppression [12].

With counteracting effects, it is a challenge to disentangle the suppression from the regeneration. In addition, there are cold nuclear matter effects [13], including modification of the parton distribution functions ("shadowing") and partonic multiple scattering, that also lead to suppression of heavy quarkonium and need to be disentangled from QGP suppression. In order to quantify effects of deconfinement, cold nuclear matter effects (via p+A collisions) must be measured and disentangled.

Our goal is to measure charmonium production in p+Au collisions as a function of "centrality". Ideally, centrality would be determined using the event activity in the forward region, away from the mid-rapidity region where the J/ψ is reconstructed. However, due to the performance of the STAR Beam-Beam Counters (BBC) in the p+Au running period, we have concluded that we cannot use the BBC for this purpose. Alternatively, we have settled on using the number of primary tracks matched to a TOF hit in underlying event region (NMPTUE) as a measure of the event activity. The NMPTUE was chosen based on the following criteria. The number of tracks matched to TOF was found to be more robust for rejecting pile-up than other track-quality cuts. In order to remove the auto-correlation of centrality with the physics being measured as a function of the centrality, tracks are counted only in the underlying-event region, a region transverse to the direction of the reconstructed particle.

[1] X.N. Wang, Z. Huang and I. Sarcevic, Phys. Rev. Lett. **77**, 231 (1996).
[2] L. Adamczyk *et al.* (STAR Collaboration), Phys. Lett. B **760**, 689 (2016).
[3] S. Chatrchyan *et al.* (CMS Collaboration), Phys. Lett. B **718**, 773 (2013).
[4] (ATLAS Collaboration), ATLAS-CONF-2012-121.
[5] M. Cacciari and G. Salam, Phys. Lett. B **641**, 57 (2006); M. Cacciari, G. Salam and G. Soyez, JHEP **0804** 005 (2008), http://fastjet.fr.
[6] T. Sjöstrand, S. Mrenna, and P. Skands, Comput. Phys. Commun. **178**, 852 (2008).
[7] T. Matsui and H. Satz, Phys. Lett. B **178**, 416 (1986).
[8] M.C. Abreu *et al.* (NA50 Collaboration), Eur. Phys. J. C **39**, 335 (2005).
[9] L. Grandchamp, R. Rapp, and G.E. Brown, Phys. Rev. Lett. **92**, 212301 (2004); A. Capella and E.G. Ferreiro, Eur. Phys. J. C **42**, 419 (2005).
[10] A. Adare *et al.* (PHENIX Collaboration), Phys. Rev. Lett. **98**, 232301 (2007).
[11] P. Braun-Munzinger and J. Stachel, Phys. Lett. B **490**, 196 (2000).
[12] L. Grandchamp and R. Rapp, Phys. Lett. B **523**, 60 (2001).
[13] R. Vogt, Phys. Rev. C **71**, 054902 (2005).

SECTION III

NUCLEAR THEORY

BOOK: Mean-field theory (World Scientific, Singapore, May 2020)

V.M. Kolomietz[1*] and S. Shlomo
[1]*Institute for Nuclear Research of the NAS of Ukraine, Kyiv, Ukraine*

This is an advanced book in many-body theory, which can be adopted as a textbook. It describes recent theoretical and experimental developments in the study of a wide range of static and dynamic properties of atomic nuclei and nuclear matter, described as many-body systems of strongly interacting neutrons and protons. The theoretical approach is based on the concept of the mean-field, describing the motion of a nucleon in terms of a self-consistent single-particle potential well which approximates the interactions of a nucleon with all the other nucleons. The theoretical approaches also go beyond the mean-field approximation by including the effects of two-body collisions. Variational approach is used to derive the self-consistent mean-field, using the Skyrme type effective nucleon-nucleon interaction, in Chapter 1. The many-body problems is described in Chapters 2 and 3 in terms of the Wigner phase-space distribution of the truncated coupled equations of the reduced density matrices, which provides a basis for semi-classical approximations and leads to kinetic equations. Chapters 4 and 5 present results of static properties of nuclei and Chapters 6 and 7 deal with properties associated with small amplitude dynamics. Relaxation processes, due to nucleon-nucleon collisions, are the subjects of Chapter 8. Instabilities and large amplitude motion of excited nuclei and are the subjects of Chapter 9. Chapter 10 deals with the dynamics of hot nuclei. The concepts and methods developed in this book can be used for describing properties of other many-body systems. References to published work by the authors and collaborators, and of other researchers, provide the basis for the advanced topics presented in the book and can be useful for further investigations by interested researchers and students.

The content is listed in the following :

The web site for this book is: https://www.worldscientific.com/worldscibooks/10.1142/11593

[*] Deceased

One-nucleon decay of isoscalar giant multipole resonances in ^{208}Pb

M.L. Gorelik,[1] S. Shlomo, B.A. Tulupov,[2] and M.H. Urin[3]
[1]*Moscow Economic School, Moscow 123022, Russia*
[2]*Institute for Nuclear Research, RAS, Moscow 117312, Russia*
[3]*National Research Nuclear University "MEPhI", Moscow 115409, Russia*

A detailed description of any giant resonance (GR) includes the following characteristics: (i) Strength distribution for a large excitation-energy interval; (ii) Energy-dependent double transition density (which depends only on nuclear structure) and projected one-body transition density (associated with a given one-body probing operator), and; (iii) Partial and total probabilities of direct one-nucleon decay**.** The recently developed particle-hole dispersive optical model (PHDOM) is a microscopically-based extension of the standard continuum-random-phase approximation (cRPA) by taking the spreading effect into account. Within the PHDOM, which is a semi microscopic model, Landau damping and coupling to the continuum are considered microscopically (in terms of a mean field and p-h interaction), while the spreading effect is treated phenomenologically (in terms of a properly parameterized energy-averaged p-h self-energy term). The imaginary part of this term determines the real part via a dispersive relationship, which are added to the real mean field. We have recently implemented [1] the PHDOM to describe the main properties of the isoscalar giant multipole resonances (ISGMPRs) (up to $L = 3$) together with the overtones of isoscalar giant monopole and quadrupole resonances. The model parameters related to a mean field and p-h interaction were taken from independent data accounting for the isospin symmetry and translation invariance of the model Hamiltonian. Parameters of the imaginary part of the strength of self-energy term were adjusted to reproduce in PHDOM-based calculations of ISGMPR total widths for the considered closed-shell nucleus. The calculation results obtained for the ^{208}Pb nucleus, taken as an example, were compared with available experimental data.

To demonstrate the unique ability of the model in describing the branching ratios for direct one-nucleon decay of ISGMPRs, we show the partial and total branching ratios, $b^{\uparrow}_{L,\mu}$ and $b^{\uparrow}_{L}$, evaluated within the PHDOM for ^{208}Pb. The calculated values of the branching ratios were obtained under the assumption of a purely single-hole nature of the product-nucleus states that are populated in the decay process and can be considered as an upper limit of possible values. In Table I we present the branching ratios for direct one-neutron decay of four ISGMPRs in the ^{208}Pb nucleus, which are given together with available experimental data. An approximately two-

Table I. The partial and total branching ratios for direct one-neutron decay of the isoscalar giant multipole resonances (ISGMPRs) into the channel μ. The branching ratios (in %) for ^{208}Pb, evaluated within PHDOM, are given with indication of the respective excitation-energy intervals ($\boldsymbol{\omega_{12}}$ in MeV) and compared with experimental data

	$b^{\uparrow}_{L=0,\mu}$	$b^{\uparrow}_{L=1,\mu}$	$b^{\uparrow}_{L=2,\mu}$	$b^{\uparrow}_{L=3,\mu}$
$\mu^{-1} \setminus \omega_{12}$	12.5 – 15.5 [3]	20 – 25 [2]	9 – 12	16 – 23
$3p_{1/2}$	3.6	1.1	2.8	1.6
$2f_{5/2}$	18.0	5.4	1.5	5.9
$3p_{3/2}$	7.5	2.6	5.8	3.8
$1i_{13/2}$	0.8	11.4	0.2	5.9
$2f_{7/2}$	26.6	9.3	0.2	13.3
$\sum_{\mu} b^{\uparrow}_{L,\mu}$	56.5	29.8	10.5	30.5
$\left(\sum_{\mu} b^{\uparrow}_{L,\mu}\right)_{expt}$	22 ± 6 [3] 14.3 ± 3 [4]	23 ± 5 [2] 10.5 [5]	-	-
$b^{\uparrow,n}_{L}$	56.7	66.8	10.6	37.5

fold excess of the calculated values above the respective experimental values for ISGMR and ISGDR is worth noting. This note is also valid for the calculated values of the branching ratios for direct one-proton decay of ISGDR shown in Table II. However, the description of experimental data is markedly improved upon multiplying the calculated branching ratios $b^{\uparrow}_{L=1,\mu}$ by the experimental values of spectroscopic factors S_{μ} for proton-hole states of the product nucleus ^{207}Tl. The experimental spectroscopic factors S_{μ} are close to unity for the majority of neutron-hole states of the ^{207}Pb nucleus, which are indicated in Table I.

Table II. The branching ratios (in %) for direct one-proton decay of the isoscalar giant dipole resonance (ISGDR) in ^{208}Pb evaluated within PHDOM for the excitation-energy intervals $\boldsymbol{\omega_{12} = 20 - 25}$ MeV, are compared with experimental data.

μ^{-1}	$b^{\uparrow}_{L=1,\mu}$	S_μ [6]	$S_\mu \cdot b^{\uparrow}_{L=1,\mu}$	$\left(b^{\uparrow}_{L=1,\mu}\right)_{expt}$ [2]
$3s_{1/2}$	3.4	0.55	1.9	2.3 ± 1.1
$2d_{3/2}$	3.0	0.57	1.7	
$1h_{11/2}$	0.2	0.58	0.1	1.2 ± 0.7
$2d_{5/2}$	4.1	0.54	2.2	
$\sum_\mu b^{\uparrow}_{L,\mu}$	10.7	-	5.9	3.5 ± 1.8

[1] M.L. Gorelik, S. Shlomo, B.A. Tulupov, and M.H. Urin, Phys. Rev. C **103**, 034302 (2021).

[2] M. Hunaydi *et al.,* Nucl. Phys. **A731**, 49 (2004).

[3] S. Brandenburg *et al.*, Phys. Rev. C **39**, 24448 (1989).

[4] A. Bracco *et al*. Phys. Rev. Lett. **60**, 2603 (1988).

[5] M. Hunaydi *et al.*, Phys. Rev. C **75**, 014606 (2007).

[6] I. Bobeldijk *et al.*, Phys. Rev. Lett. **73**, 2684 (1994).

Semi-classical approximation description of static properties of nuclei

S. Shlomo and A.I. Sanzhur[1]
[1]*Institute for Nuclear Research, 03680 Kyiv, Ukraine*

Investigating many-body nuclear system of strongly interacting neutrons and protons is very challenging. The mean-field approximation, a zero order approximation in perturbation theory, ignoring the interparticle correlations, is widely employed in variable approaches, such as the Hartree-Fock (HF) and Thomas-Fermi (TF) approximations. The mean field approach has been shown to provide good description of a wide range of phenomena of many body-systems. We point out that an important feature of strongly interacting system is that the free two-body nucleon-nucleon interaction is strongly renormalized inside the system, leading to a parametrized effective nucleon-nucleon interaction. The adopted effective interaction provides the saturation properties of the nuclear system which exhibits the properties of gas (shell model) and a Fermi liquid simultaneously. The Wigner transform (WT) provides a reformulation of quantum mechanics in terms of classical concepts. For many-body Schrodinger equation, coupled hierarchy equations for Wigner distribution functions (WDF) of the reduced density matrices can be derived. Simple semi-classical equations for static and dynamic properties of a many body system are then obtained by truncating the set of the coupled equations.

As an example, we present below results of calculations of the deformation energy $E_{\rm def}$ of ^{240}Pu carried out within the semi-classical extended Thomas Fermi approximation (ETFA) and compare with the results obtained within the liquid drop model (LDM). In the ETFA calculation we: (i) Employed the direct variational method with trial proton and neutron densities $\rho_p(\mathbf{r})$ and $\rho_n(\mathbf{r})$ that are generated by diffuse-layer profile functions, and determine the stationary energy with respect to variations of these profiles, and; (ii) Adopted the modified well-known two-parameters “Funny-Hills" form {c,h}, where c and h are the elongation and neck parameters, respectively, to describe the shape of the deformed nucleus. The LDM deformation energy $E_{\rm def}^{(\rm LDM)}$ is determined by the Coulomb energy and the shape factor. In Fig. 1 we present the results [1] of numerical calculations of the ETFA deformation energy for ^{240}Pu, using the Skyrme interactions SkM*, SLy230b, T6, and KDE0. The different lines in Fig. 1 show the dependence of the optimal deformation energy $E_{\rm def}^{(\rm ETFA)}$ (fission trajectory) on the elongation parameter *c*. The cross at the end of a line in Fig. 1 is the location of the scission point. Note that the deformation energy is quite sensitive to the Skyrme interaction parametrization, but the scission point depends only slightly on the specific Skyrme interaction. We also present in Fig. 1 the results of the LDM calculations. It is seen in Fig. 1 that the LDM results significantly underestimate the fission barrier energy B_f (below 1.0 MeV), compared to the ETFA results (above 4.0 MeV). Also, the sensitivity of the neck parameters on the Skyrme-interaction parametrization is stronger for the LDM case than for the ETFA. These significant differences between the LDM and ETFA results are due to the finite diffuse-layer effects in the ETFA approach, which are sensitive to the gradient terms (surface terms) in the Skyrme interaction and depend on the deformation parameters. The finite diffuse layer in the ETFA approach, which is missing in the LDM approach, produces the curvature correction to the surface energy of liquid drop that leads to a significant effect of diffuse layer on the fission barrier.

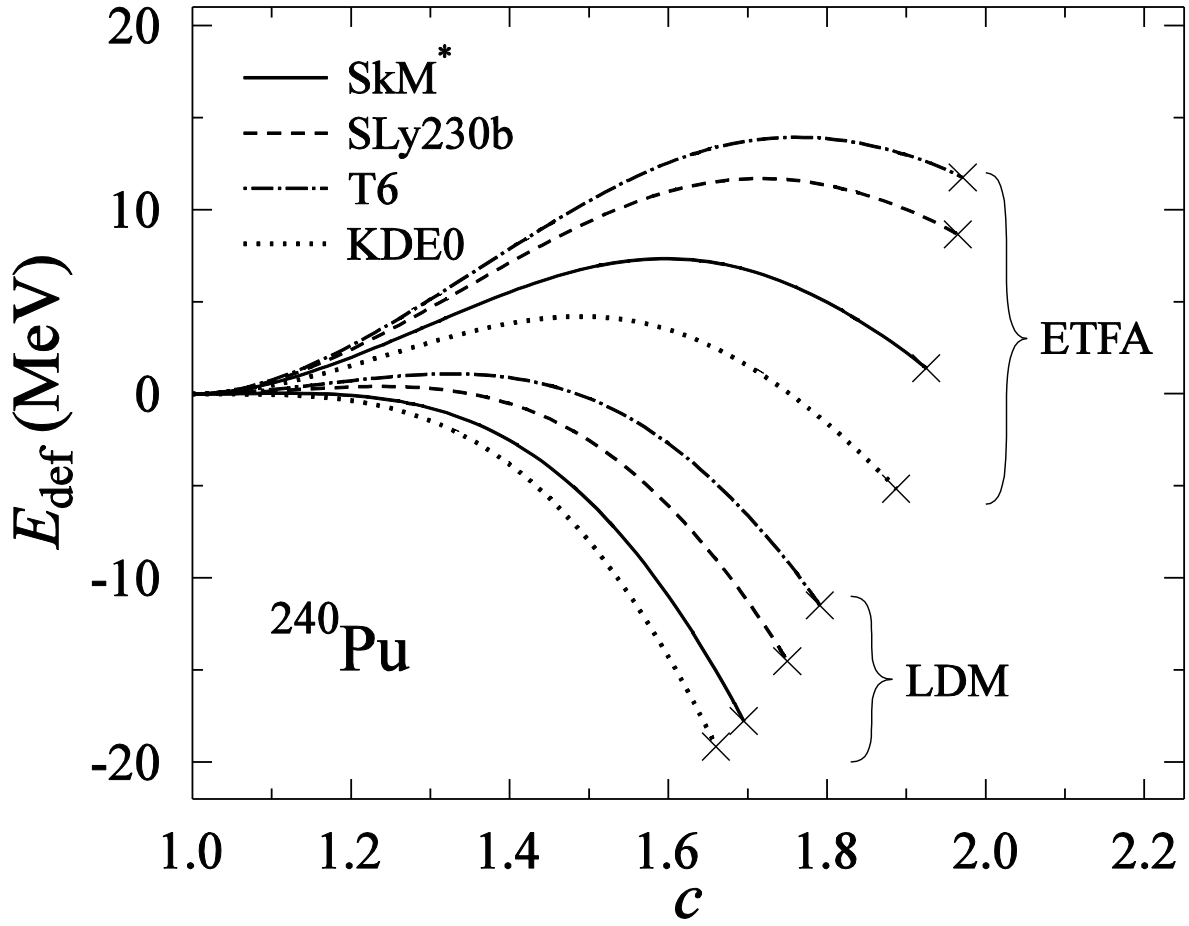

Fig. 1. The dependence of the deformation energies E_{def} of ^{240}Pu for different Skyrme interactions (see text) on the fission trajectory. The four upper lines are for the ETFA and lowest lines are for the LDM approach. The crosses on the lines indicate the scission points

[1] S. Shlomo and A.I. Sanzhur, Mod. Phys. Lett. A **36**, 2130008 (2021).

Sensitivity of centroid energies of giant resonances to bulk nuclear matter properties

S. Shlomo, A.I. Sanzhur,[1] and G. Bonasera
[1]*Institute for Nuclear Research, National Academy of Sciences of Ukraine, Kyiv, Ukraine*

The development of a modern and more realistic nuclear energy density functional (EDF) is the subject of enhanced activity, since it is very important for accurate prediction of properties of nuclei, such as giant resonances (GR), at and far from stability, of nuclear matter (NM) and Astrophysical phenomena. To determine constraints on bulk properties of NM, such as the incompressibility coefficient, $K_{\rm NM}$, effective mass, m^*/m, symmetry energy coefficient, J, and its first, L, and second, K_{sym}, derivatives, and the enhancement coefficient, κ, of the energy weighted sum rule (EWSR) of the isovector giant dipole resonance (IVGDR), we have investigated their sensitivities to centroid energies, E_{CEN} , of isoscalar and isovector GRs with multipolarities L = 0 – 3. For this purpose we have carried out [1-4] fully self-consistent Hartree-Fock (HF) based random-phase-approximation (RPA) calculations of the strength functions $S(E)$ and centroid energies E_{CEN} of GRs for a very wide range of nuclei, using 33 commonly employed effective nucleon-nucleon interaction of the Skyrme type, and determined the Pearson linear correlation coefficient C between each E_{CEN} and each bulk property of NM. We also determined constraints on NM properties by comparing with available experimental data on E_{CEN} of GRs.

The calculated Pearson linear correlation coefficients between different sets of NM properties are shown in Table I. We point out that the value of each NM property varies over a wide range. It is also

Table I. Calculated Pearson linear correlation coefficients, C, for NM properties. The parameters of all 33 Skyrme effective nucleon-nucleon interactions were used to calculate C.

	$K_{\rm NM}$	J	L	$K_{\rm sym}$	m^*/m	κ	$W_0\ (x_w = 1)$
$K_{\rm NM}$	1.00	0.03	0.30	0.43	-0.37	-0.02	0.03
J	0.03	1.00	0.72	0.49	0.07	-0.24	-0.25
L	0.30	0.72	1.00	0.91	-0.15	-0.13	-0.08
$K_{\rm sym}$	0.43	0.49	0.91	1.00	-0.41	-0.08	0.05
m^*/m	-0.37	0.07	-0.15	-0.41	1.00	-0.63	-0.19
κ	-0.02	-0.24	-0.13	-0.08	-0.63	1.00	-0.03
$W_0\ (x_w = 1)$	0.03	-0.25	-0.08	0.05	-0.19	-0.03	1.00

seen from Table I that there are only weak correlation between the values of $K_{\rm NM}$, and m^*/m, medium correlation between m^*/m and κ, and medium correlations between the symmetry energy coefficients J, L, and K_{sym} . Table II presents the Pearson linear correlation coefficients C between each bulk property

of nuclear matter at saturation density and the E_{CEN} of each GR: the isoscalar giant monopole resonance (ISGMR), isoscalar giant dipole resonance (ISGDR), isoscalar giant quadrupole resonance (ISGQR), isoscalar giant octupole resonance (ISGOR), isovector giant monopole resonance (IVGMR), isovector giant dipole resonance (IVGDR), isovector giant quadrupole resonance (IVGQR) and isovector giant octupole resonance (IVGOR). Note that it is seen from Table II that, in particular, there exist strong correlations between E_{CEN} of the ISGMR and the incompressibility coefficient, between E_{CEN} and the effective mass m^*/m for the ISGQR and between E_{CEN} of the IVGDR and the enhancement coefficient κ for the IVGDR energy weighted sum rule (EWSR) and, surprisingly, very weak correlations between E_{CEN} and the symmetry energy J or its first and second derivative, for the IVGDR. By comparing with available experimental data on E_{CEN} of GRs we obtained the following constraints on the values of : K_{NM} = 210-240 MeV, m^*/m = 0.7-0.9, and κ = 0.25-0.70.

Table II. Pearson linear correlation coefficients between the centroid energy ECEN of each giant resonance and each nuclear matter property at saturation density.

	K_{NM}	J	L	K_{sym}	m^*/m	κ
ISGMR	0.87	-0.10	0.25	0.45	-0.51	0.13
ISGDR	0.52	-0.10	0.13	0.36	-0.88	0.55
ISGQR	0.41	-0.09	0.15	0.41	-0.93	0.54
ISGOR	0.42	-0.10	0.15	0.43	-0.96	0.56
IVGMR	0.23	-0.26	-0.12	0.00	-0.70	0.86
IVGDR	0.05	-0.37	-0.42	-0.30	-0.60	0.84
IVGQR	0.18	-0.35	-0.29	-0.13	-0.74	0.80
IVGOR	0.25	-0.32	-0.19	0.02	-0.83	0.81

[1] S. Shlomo**,** and A.I. Sanzhur, Nucl. Phys. Atomic Energy **21(2)**, 113 (2020).

[2] G. Bonasera, S. Shlomo, D.H. Youngblood, Y.–W. Lui, J. Button, and X. Chen, Nucl. Phys. **A1010**, 122159 (2021).

[3] G. Bonasera, S. Shlomo, D.H. Youngblood, Y.–W. Lui, Krishichayan, and J. Button, Nucl. Phys. **A992**, 121612 (2019).

[4] G. Bonasera, M.R. Anders, and S. Shlomo, Phys. Rev. C **98**, 054316 (2018).

Beam-energy dependence of the production of light nuclei in Au + Au collision

Wenbin Zhao,[1,2,3,4] Chun Sen,[5,6] Che Ming Ko, Quangshen Liu,[1,2] and Huichao Song[1,2,3]

[1]*Department of Physics and State Key Laboratory of Nuclear Physics and Technology, Peking University, Beijing 100871, China*

[2]*Collaborative Innovation Center of Quantum Matter, Beijing 100871, China*

[3]*Center for High Energy Physics, Peking University, Beijing 100871, China*

[4]*Institute of Particle Physics, Key Laboratory of Quark and Lepton Physics (MOE), Central China Normal University, Wuhan, Hubei 430079, China*

[5]*Department of Physics and Astronomy, Wayne State University, Detroit, Michigan 48201, USA*

[6]*RIKEN BNL Research Center, Brookhaven National Laboratory, Upton, New York 11973, USA*

We have used the nucleon coalescence model to study light-nuclei production in the most central Au + Au collisions at $\sqrt{s_{NN}}$ = 7.7, 11.5, 19.6, 27, 39, 62.4, and 200 GeV [1]. The input phase-space distributions of protons and neutrons at kinetic freeze-out for the coalescence calculations are generated from the iEBE-MUSIC hybrid model [2] using three-dimensional dynamical initial conditions and a crossover equation of state. These comprehensive simulations can nicely reproduce the measured p_T spectra of pions, kaons, and (anti-)protons in Au + Au collisions at $\sqrt{s_{NN}} = 7 - 200$ GeV. We have found that the coalescence model calculations can reproduce the measured p_T spectra and dN/dy of (anti-)deuterons and (anti-)tritons and the particle ratio t/p within 10% of accuracy. However, the deviations between the calculated and measured particle ratios of d/p, $\bar{d}/\bar{p}$, and t/d increase to 15%, 20%, and 10%, respectively. Although the coalescence model reasonably describes the p_T spectra and yields of light nuclei at various collision energies, the predicted coalescence parameters of (anti-)deuterons and tritons, $B_2(d)$, $B_2(\bar{d})$, and $\sqrt{B_3(t)}$ decrease monotonically with increasing collision energy (left window of Fig.1),

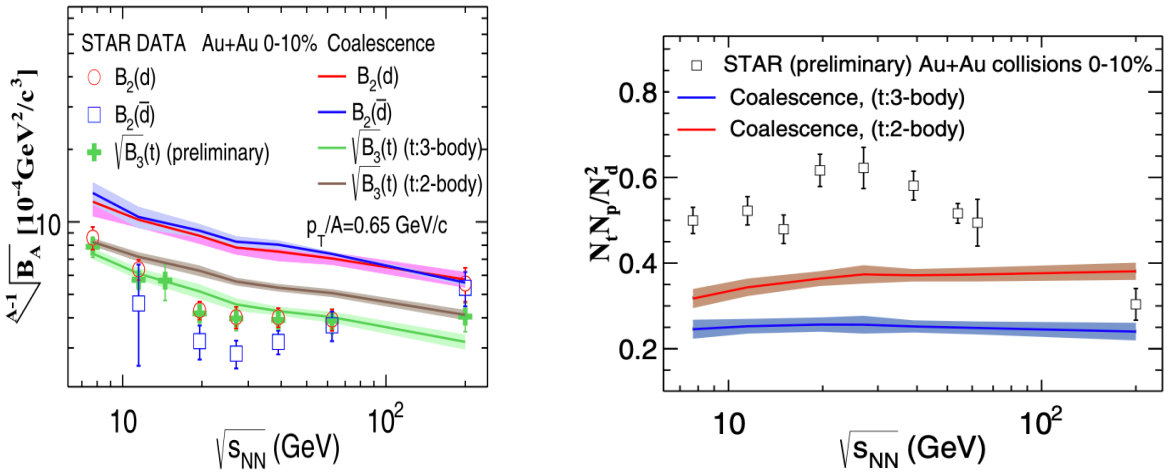

Fig. 1. Collision energy dependence of the coalescence parameters $B_2(d)$, $B_2(\bar{d})$, and $\sqrt{B_3(t)}$ at p_T/A = 0.65 GeV (left window) and the yield ratio $NtNp/N_d^2$ in 0-10% Au + Au collisions, calculated by the coalescence model. Data are taken from Refs. [3,4].

[1] W.B. Zhao, C. Sen, C.M. Ko, G.S. Liu, and H.C. Song, Phys. Rev. C **102**, 072301 (2020).
[2] G.S. Denicol, C. Gale, S. Jeon, A. Monnai, B. Schenke, and C. Shen, Phys. Rev. C **98**, 034916 (2018).
[3] D. Zhang (STAR Collaboration), in *Proceedings of 13th International Conference on Nucleus-Nucleus Collisions, Omiya (Saitama), Japan, 2019* (JPS, Tokyo 2019).
[4] J. Adam *et al.* (STAR Collaboration), Phys. Rev. C **99**, 064905 (2019).
[5] K.-J. Sun, L.-W. Chen, C.M. Ko, and Z. Xu, Phys. Lett. B **774**, 103 (2017).
[6] K.-J. Sun, L.-W. Chen, C.M. Ko, J. Pu, and Z. Xu, Phys. Lett. B **781**, 499 (2018).

Charmed hadron chemistry in relativistic heavy-ion collisions

Shanshan Cao,[1] Kai-Jia Sun, Shu-Qing Li,[2] Shuai Y.F. Liu, Wen-Jing Xing,[3]
Guang-You Qin,[3] and Che Ming Ko
[1]*Department of Physics and Astronomy, Wayne State University, Detroit, MI, 48201, USA*
[2]*Department of Physics and Information Engineering, Jining University, Qufu, Shandong, 273155, China*
[3]*Institute of Particle Physics and Key Laboratory of Quark and Lepton Physics (MOE), Central China Normal University, Wuhan, Hubei, 430079, China*

We have developed a comprehensive coalescence-fragmentation approach for studying heavy quark hadronization in heavy-ion collisions [1]. Both *s* and *p*-wave charmed hadron states, which are sufficient to cover all major charmed hadron states reported in PDG, have been included in our coalescence model. We have found that the inclusion of *p*-wave states enhances the total coalescence probability of charm quarks. It is also necessary for a full 3-dimensional calculation to normalize the charm-QGP coalescence probability at zero momentum using reasonable in-medium sizes for charmed hadrons. In our new coalescence model, a strict 4- momentum conservation has been implemented by first

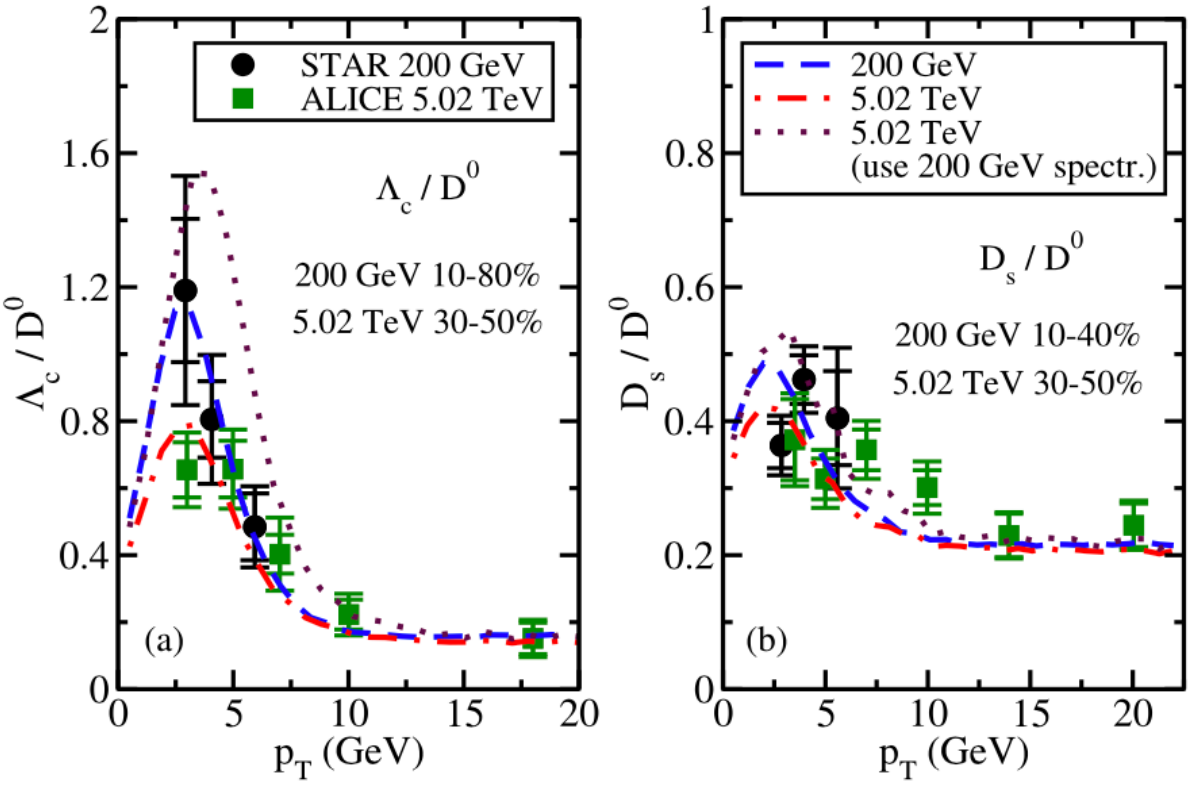

Fig. 1. $\boldsymbol{\Lambda_c/D^0}$ and $\boldsymbol{D_s/D^0}$ ratios in 200 GeV Au-Au collisions at RHIC [2] and 5.02 TeV Pb-Pb collisions at the LHC [3].

forming the off-shell excited hadron states and then letting them decay into the ground state charmed hadrons, which guarantees the boost invariance of the coalescence probabilities for producing charmed hadrons and the thermal limit of their energy spectra. By combining our new hadronization approach with the up-to-date FONLL+EPPS16 initial spectra of charm quarks and their nuclear modification through the advanced Langevin-hydrodynamics model, our state-of-the-art calculation has provided a simultaneous description of the p_{T}-integrated and differential Λ_c/D^0 and D_s/D^0ratios at both RHIC and the LHC as shown in Fig. 1. We have also found that the interplay between the QGP flow and the charm quark transverse momentum spectrum is essential for describing the final charmed hadron chemistry in heavy-ion collisions, especially the puzzling observation of a larger Λ_c/D^0 ratio at RHIC than at the LHC. Our study has further suggested that the sizes of charmed hadrons should be larger in medium than in vacuum, which is qualitatively consistent with the findings in Ref. [4] and may be further tested by hadronic model calculations in the future.

[1] S. Cao, K.J. Sun, S.Q. Li, S. Y.F. Liu, W. J. Xing, G.Y. Qin, and C.M. Ko, Phys. Lett. B **807**, 135561 (2020).

[2] J. Adam *et al.* (STAR Collaboration), Phys. Rev. Lett. **124**, 172301 (2020).

[3] L. Vermunt (ALICE Collaboration), arXiv:1910.11738, 2019.

[4] S. Shi, J. Zhao, and P. Zhuang, Chin. Phys. C **44**, 084101 (2020).

Constraining the in-medium nucleon-nucleon cross section from the width of nuclear giant dipole resonance

Rui Wang,[1,2] Zhen Zhang,[3] Lie-Wen Chen,[4] Che Ming Ko, and Yu-Gang Ma[1,2]

[1]*Key Laboratory of Nuclear Physics and Ion-beam Application (MOE), Institute of Modern Physics, Fudan University, Shanghai 200433, China*

[2]*Shanghai Institute of Applied Physics, Chinese Academy of Sciences, Shanghai 201800, China*

[3]*Sino-French Institute of Nuclear Engineering and Technology, Sun Yat-Sen University, Zhuhai 519082, China*

[4]*School of Physics and Astronomy and Shanghai Key Laboratory for Particle Physics and Cosmology, Shanghai Jiao Tong University, Shanghai 200240, China*

We have used the lattice Hamiltonian (LH) method to solve the Boltzmann-Uheling-Ulenbeck (BUU) transport equation with the binary collisions in the collision term treated via the stochastic approach [1]. By incorporating the stochastic NN collision term into the previous lattice-Hamiltonian Vlasov (LHV) framework [2], we have solved the BUU equation with nuclear mean field obtained from the N3LO Skyrme pseudopotential through the LH method. With the use of a sufficiently large number of

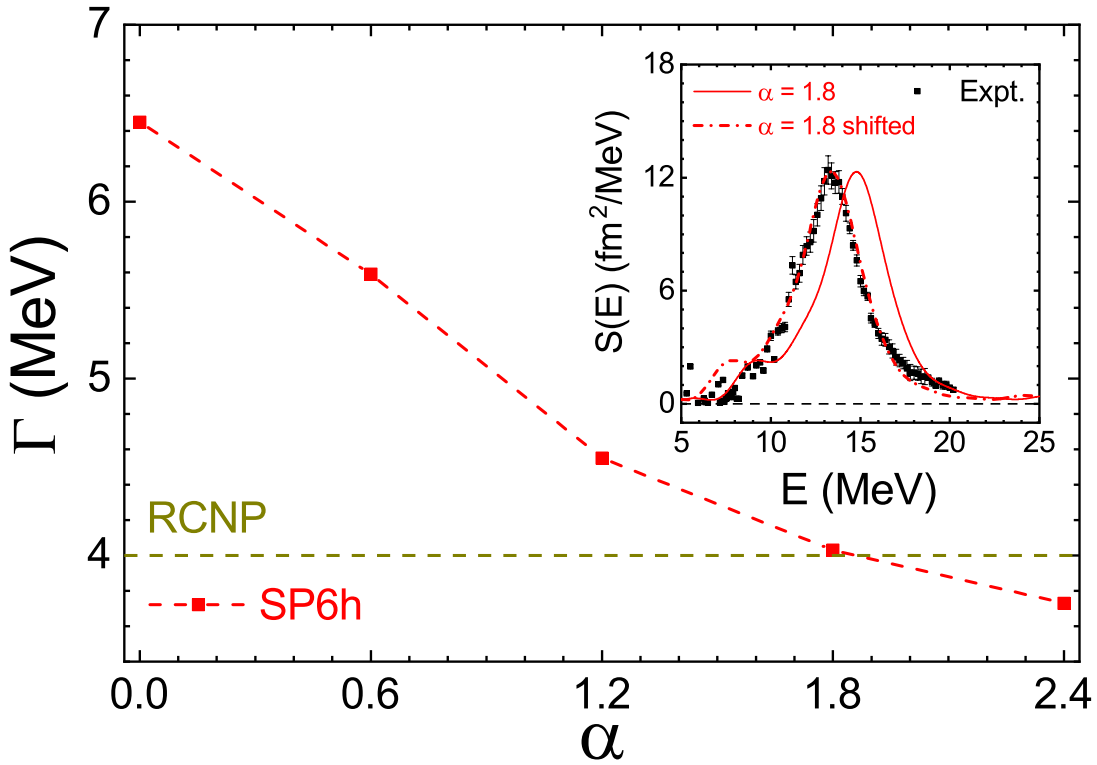

Fig. 1. The GDR width of ^{208}Pb from LBUU calculations for different values of $\boldsymbol{\alpha}$ in $\boldsymbol{\sigma^{*}_{NN}} = \boldsymbol{\sigma^{free}_{NN}} \exp\left[-\alpha \frac{\rho/\rho_0}{1+(T_{c.m.}/T_0)^2}\right]$. The horizontal line represents the RCNP experimental value of 4.0 MeV [3]. The inset shows the strength function with $\boldsymbol{\alpha}$ =1.8 (solid line) and the shifted one (dash-dotted line) to match the experimental GDR peak energy.

test particles, the present lattice-Hamiltonian BUU (LBUU) method treats the Pauli blocking in the collision term of BUU equation with very high precision and thus significantly increases the accuracy in solving the BUU equation. From the accurately calculated giant dipole resonance (GDR) width of ^{208}Pb, we have found that it depends strongly on the magnitude of the in-medium NN cross section σ_{NN}^{*}, and the experimentally measured GDR width of ^{208}Pb from the ^{208}Pb$(\vec{p},\overrightarrow{p'})$ reaction at RCNP [3] can only be reproduced with a NN cross section that is significantly reduced in nuclear medium as shown in Fig.1. The large medium reduction of the free-space NN scattering cross section $\sigma_{NN}^{\mathrm{free}}$ raises challenges to microscopic calculations based on realistic NN interactions. Also, the effects of such a large medium reduction of $\sigma_{NN}^{\mathrm{free}}$ on the widths of other modes of giant resonances in nuclei and on the dynamics of HICs need to be studied as it may significantly affect the extracted information on the properties of nuclear matter at various densities.

[1] R. Wang, Z. Zhang, L.W. Chen, C.M. Ko, and Y.G. Ma, Phys. Lett. B **807**, 135532 (2020).
[2] R. Wang, L.-W. Chen, Z. Zhang, Phys. Rev. C **99**, 044609 (2019).
[3] A. Tamii *et. al.*, Phys. Rev. Lett. **107**, 062502 (2011).

Effects of QCD critical point on light nuclei production

Kai-Jia Sun, Che Ming Ko, and Feng Li[1]
[1]*School of Physical Science and Technology, Lanzhou University, Lanzhou, Gansu, 073000, China*

Based on the nucleon coalescence model, we have obtained an explicit expression that relates the yield ratio $N_t N_p / N_d^2$ to the nucleon density correlation length ξ in the hadronic matter produced in heavy-ion collisions, which could be appreciable if the produced matter is initially close to the critical end point (CEP) in the QCD phase diagram. This ratio is found to increase monotonically with the dimensionless quantity ξ/σ where $\sigma \approx 2$ fm denotes the size of deuteron or triton. This enhancement is in addition to that due to the large neutron density fluctuation that could be developed during a first-order quark-gluon plasma to hadronic matter phase transition as previously studied in Refs. [2,3,4]. Consequently, the collision energy dependence of this ratio is expected to have a double-peak or a broad one-peak structure depending on the closeness between the signal of the CEP and that of the first-order phase transition. Such a non-monotonic behavior in the collision energy dependence of $N_t N_p / N_d^2$ has indeed been seen in the preliminary data from the STAR Collaboration [5]. Our study has thus led to the possibility of extracting the information of the CEP and the phase boundary of QCD phase diagram from comparing the precisely measured data on the yields of light nuclei in heavy-ion collisions with those from theoretical models based on the transport approach and the various hydrodynamic approaches.

[1] K.J. Sun, C.M. Ko, and F. Li, Phys. Lett. B **816**, 136258 (2021).
[2] K.-J. Sun, L.-W. Chen, C.M. Ko, and Z. Xu, Phys. Lett. B **774**, 103 (2017).
[3] K.-J. Sun, L.-W. Chen, C.M. Ko, J. Pu, and Z. Xu, Phys. Lett. B **781**, 499 (2018).
[4] E. Shuryak and J.M. Torres-Rincon, Phys. Rev. C **100**, 024904 (2019).
[5] D. Zhang, STAR, Nucl. Phys. **A1005**, 121825 (2021).

Enhanced production of strange baryons in high-energy nuclear collisions from a multiphase transport model

Tianhao Shao,[1] Jinhui Chen,[2] Che Ming Ko, and Zi-Wei Lin[3]

[1]*Shanghai Institute of Applied Physics, Chinese Academy of Science, Shanghai 201800, China and University of Chinese Academy of Science, Beijing 100049, China*

[2]*Key Laboratory of Nuclear Physics and Ion-beam Application (MOE), Institute of Modern Physics, Fudan University, Shanghai 200433, China*

[3]*Department of Physics, East Carolina University, Greenville, North Carolina 27858,*

We have introduced additional coalescence factors for strange baryons in the string melting version of the AMPT model to improve its description of multi-strange hadron production in heavy-ion

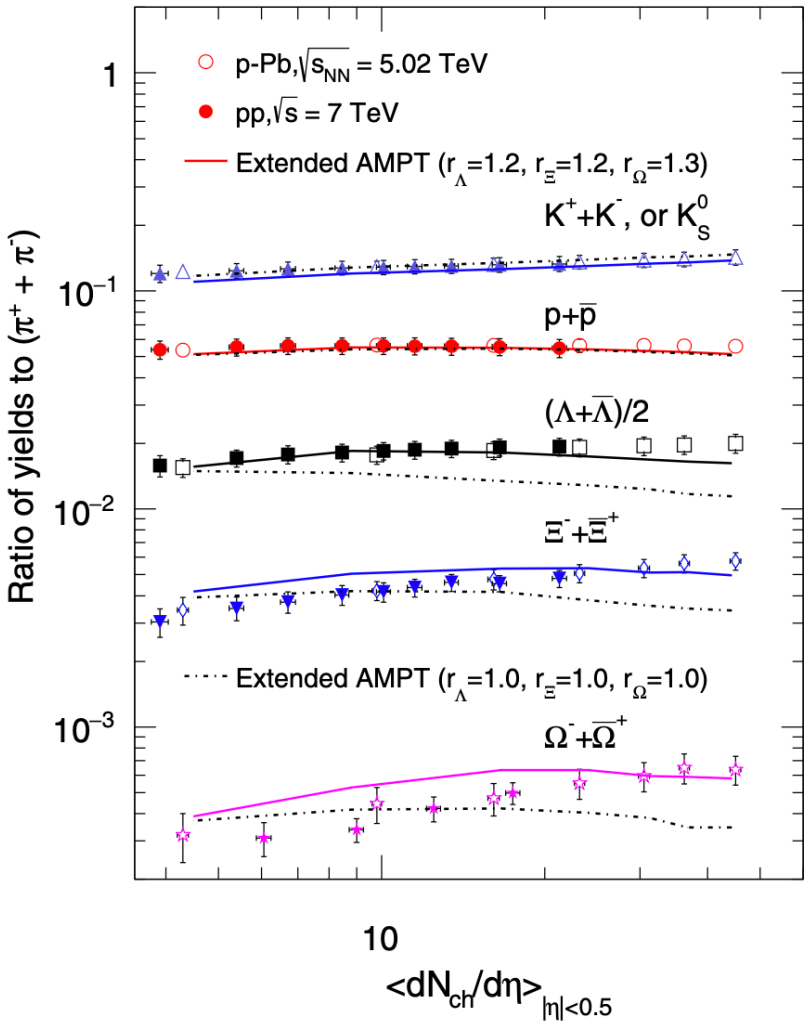

Fig. 1. The midrapidity yield ratios of kaon, proton, Λ, Ξ, and Ω to pion in *pp* collisions at $\sqrt{s_{NN}} = 7$ TeV and in *p*-Pb collisions at $\sqrt{s_{NN}}$ =5.02 TeV. Results from experiments [2,3,4] are shown by open symbols for *p*-Pb collisions and filled symbols for *pp* collisions, and the lines are AMPT results for *p*-Pb collisions with (solid) or without (dot-dashed) the extra hyperon enhancement r_Y factors.

collisions at both the LHC and RHIC energies [1]. This extended AMPT model is shown to describe reasonably well the hyperon p_T spectra in central Pb + Pb collisions at the LHC energy and Au + Au collisions at the top RHIC energy. It can also qualitatively describe the multiplicity dependence of strangeness enhancement in high multiplicity *pp* and *p*-Pb collisions at LHC energies. We find that the coalescence factors depend on the system size but not much on where the system is produced from and using multiplicity-dependent coalescence factors improves the description of the centrality dependence of particle production in Au + Au collisions as shown in Fig. 1. The current study provides a convenient way to model the mechanism underlying the strangeness enhancement observed in both small and large systems from nuclear collisions at the LHC, and it could also be relevant for the study of the QCD phase diagram in the Beam Energy Scan Program at RHIC via strange baryon production [5,6].

[1] T. Shao, J. Chen, C.M. Ko, and Z. Lin, Phys. Rev. C **102**, 014906 (2020).
[2] J. Adam *et al.* (ALICE Collaboration), Nat. Phys. **13**, 535 (2017).
[3] J. Adam *et al.* (ALICE Collaboration), Phys. Lett. B **758**, 389 (2016).
[4] B.B. Abelev *et al.* (ALICE Collaboration), Phys. Lett. B **728**, 25 (2014).
[5] T. Shao, J. Chen, C.M. Ko, and K.-J. Sun, Phys. Lett. B **801**, 135177 (2020).
[6] T. Shao, J. Chen, C.M. Ko, K.-J. Sun, and Z. Xu, Chin. Phys. C **44**, 114001 (2020).

Probing the partonic degrees of freedom in high multiplicity p-Pb collisions at $\sqrt{s_{NN}}$ = 5.02 TeV

Wenbin Zhao,[1,2] Che Ming Ko, Yuying Liu,[1,2,3] Guangyou Chen,[4,5] and Huichao Song[1,2,3]

[1]*Department of Physics and State Key Laboratory of Nuclear Physics and Technology, Peking University, Beijing 100871, China*

[2]*Collaborative Innovation Center of Quantum Matter, Beijing 100871, China*

[3]*Center for High Energy Physics, Peking University, Beijing 100871, China*

[4]*Institute of Particle Physics and Key Laboratory of Quark and Lepton Physics (MOE), Central China Normal University, Wuhan, Hubei 430079, China*

[5]*Nuclear Science Division, Lawrence Berkeley National Laboratory, Berkeley, California 94270*

We have carried out the first quantitative and timely study [1] of the number of constituent quark (NCQ) scaling of elliptic flow v_2 of pions, kaons and protons at intermediate p_T in high multiplicity p-Pb collisions at $\sqrt{s_{NN}} = 5.02$ TeV via the coalescence of soft thermal partons from the VISH2+1 hydrodynamics [2] and hard partons from the energy loss LBT model [3]. As shown in Fig. 1, adding low p_T hadrons from the hydrodynamically expanding fluid and high p_T hadrons from jet fragmentation to these intermediate p_T hadrons from quark coalescence, our Hydro-Coal-Frag hybrid model can simultaneously describe the p_T spectra (left window) and differential elliptic flow $v_2(p_T)$ (middle window) of identified hadrons over the p_T range from 0 to 6 GeV. We have also demonstrated that the inclusion of the quark coalescence contribution to the production of hadrons is essential in reproducing the measured $v_2(p_T)$ of these identified hadrons and their observed approximate NCQ scaling at intermediate p_T (right widow). Results from the present study thus provides a strong indication for the existence of the partonic degrees of freedom and the possible formation of the QGP in high multiplicity p-Pb collisions at $\sqrt{s_{NN}} =$ 5.02 TeV.

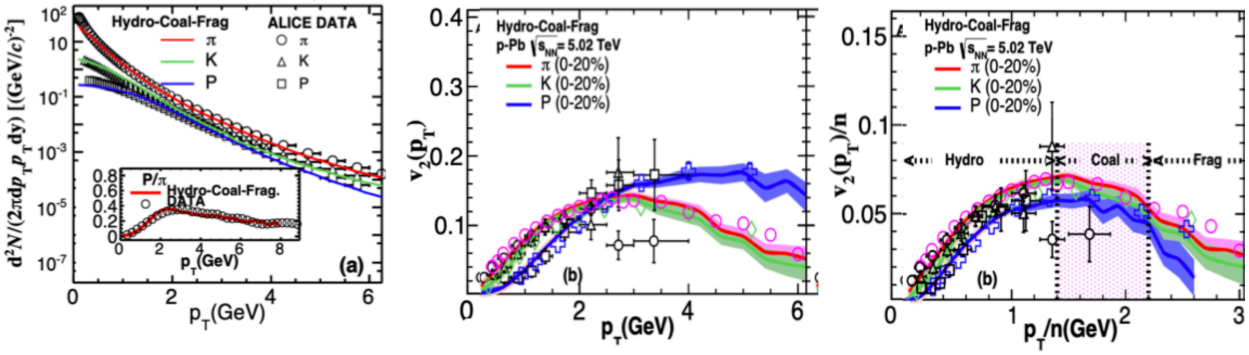

Fig. 1. Transverse momentum p_T spectra (left window), elliptic flow v_2 (middle window) and NCQ scaled elliptic flow (right window) of pions, kaons and protons in 0-20% p-Pb at $\sqrt{s_{NN}} = 5.02$ TeV. ALICE data on p_T spectra are from Ref.[4], and ALICE, CMS, and ATLAS data on elliptic flow are from Refs.[5], [6], and [7], respectively.

[1] W.B. Zhao, C.M. Ko, Y. X. Liu, G.Y. Chen, and H.C. Song, Phys. Rev. Lett. **125**, 072301 (2020).

[2] H. Song and U.W. Heinz, Phys. Rev. C **77**, 064901 (2008); Phys. Lett. B **658**, 279 (2008).

[3] X.N. Wang and Y. Zhu, Phys. Rev. Lett. **111**, 062301 (2013).

[4] J. Adam *et al.* (ALICE Collaboration), Phys. Lett. B **760,** 720 (2016).
[5] B.B. Abelev *et al.* (ALICE Collaboration), Phys. Lett. B **726**, 164 (2013).
[6] A.M. Sirunyan *et al*. (CMS Collaboration), Phys. Rev. Lett. **121**, 082301 (2018).
[**7**] M. Aaboud *et al.* (ATLAS Collaboration), Phys. Rev. C **96**, 024908 (2017).

Spin polarizations in a covariant angular momentum conserved chiral transport model

Shuai Y.F. Liu,[1,2] Yifeng Sun,[3] and Che-Ming Ko

[1]*Quark Matter Research Center, Institute of Modern Physics, Chinese Academy of Sciences, Lanzhou, Gansu, 073000, China*

[2]*University of Chinese Academy of Sciences, Beijing, 100049, China*

[3]*Laboratori Nazionali del Sud, INFN-LNS, Via S. Sofia 62, I-95123 Catania, Ita*

Based on the side-jump formalism for the scattering of chiral fermions, we have constructed a transport model that conserves the total angular momentum of the quark matter created in relativistic heavy-ion collisions [1]. Via the introduction of a covariant angular momentum tensor, the spin polarization of massless quarks then has both spin and orbital contributions. In the case of an expanding

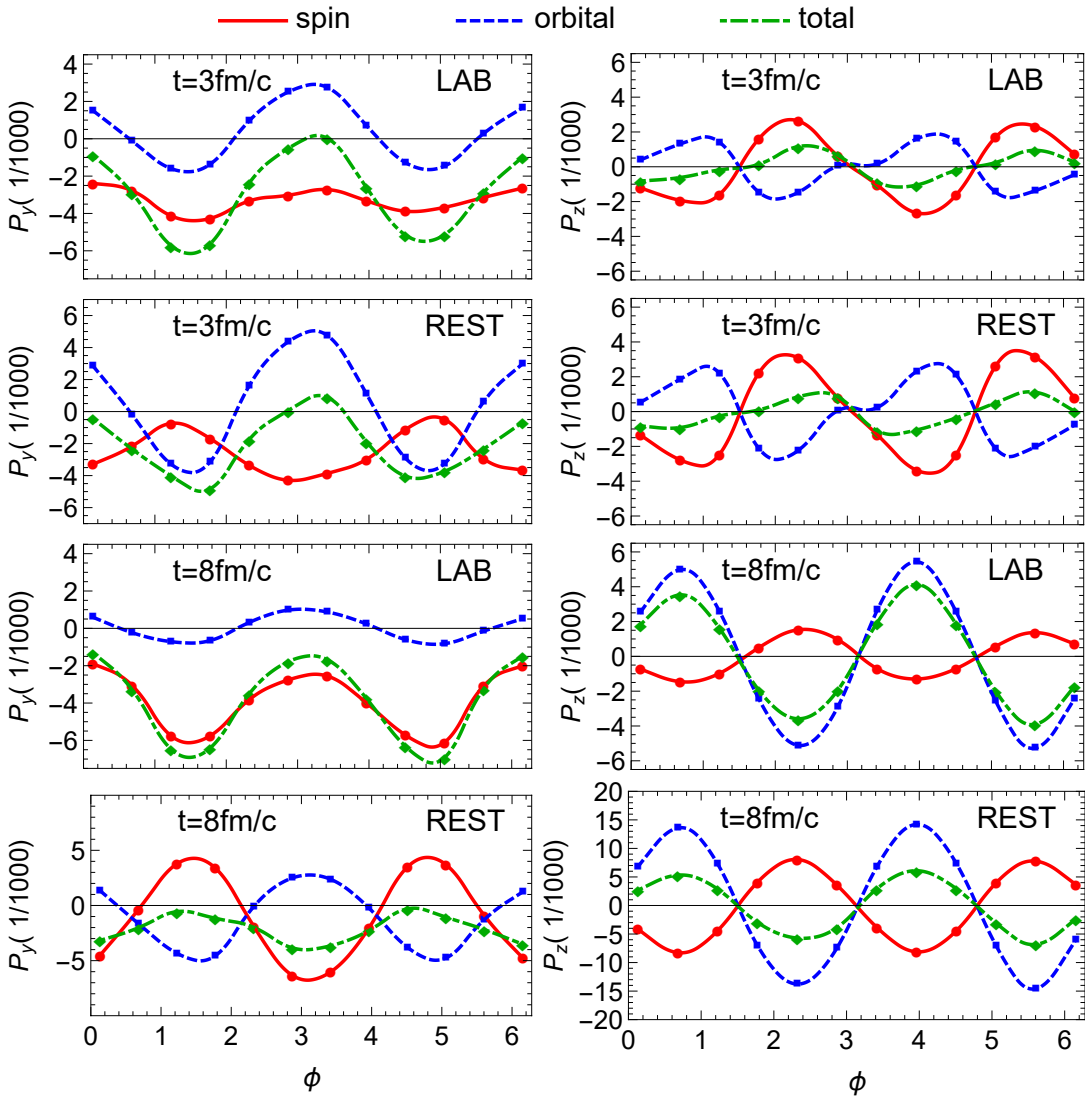

Fig. 1. Azimuthal angle φ dependence of spin polarizations P_y in the transverse plane and P_z along the beam-direction in the LAB and medium rest (REST) frame of a heavy ion collision at times t = 3 and 8 fm/c.

box with a given vorticity field, we have found that the final quark spin polarization is consistent with that expected from the thermal model. For the case of a heavy ion collision using initial conditions from the realistic AMPT model [2], the chiral vortical effect is found to lead to a redistribution of the axial charges in the produced quark matter, resulting in the appearance of dipole and quadrupole structures in the transverse plane of heavy ion collisions. As shown in Fig. 1, including both the spin and orbital contributions of these redistributed quarks to the quark local spin polarizations, we have found that their azimuthal angle dependence along the transverse (P_y) and longitudinal (P_z) directions in the medium rest frame are similar to those obtained from the chiral kinetic theory [3] and also of Lambda hyperons measureed in experiments [4].

[1] S.Y.F. Liu, Y.F. Sun, and C.M. Ko, Phys. Rev. Lett. **125**, 062301 (2020).
[2] Z.-W. Lin, C.M. Ko, B.-A. Li, B. Zhang, and S. Pal, Phys. Rev. C **72**, 064901 (2005).
[3] Y. Sun and C.M. Ko, Phys. Rev. C **99**, 011903 (2019).
[4] J. Adam *et al.* (STAR Collaboration), Phys. Rev. Lett. **123**, 132301 (2019).

The QCD critical point from the Nambu-Jona-Lasinio model with a scalar-vector interaction

Kai-Jia Sun, Che Ming Ko, Shanshan Cao,[1] and Feng Li[2]

[1]*Department of Physics and Astronomy, Wayne State University, Detroit, MI, 48201, USA*

[2]*School of Physical Science and Technology, Lanzhou University, Lanzhou, Gansu, 073000, China*

Based on the NJL model with both two flavors and three flavors as well as with the inclusion of the Polyakov loop (PNJL), we have studied the effect of the eight-fermion scalar-vector coupled interaction, which has no effects on the QCD vacuum properties, on the critical endpoint of the first-order QCD phase transition line in the QCD phase diagram [1]. We have found that the location of the critical point in the temperature and baryon chemical potential plane is sensitive to the strength of this interaction and can be easily shifted by changing its value as shown in Fig.1 by the dashed and dash-dotted lines in

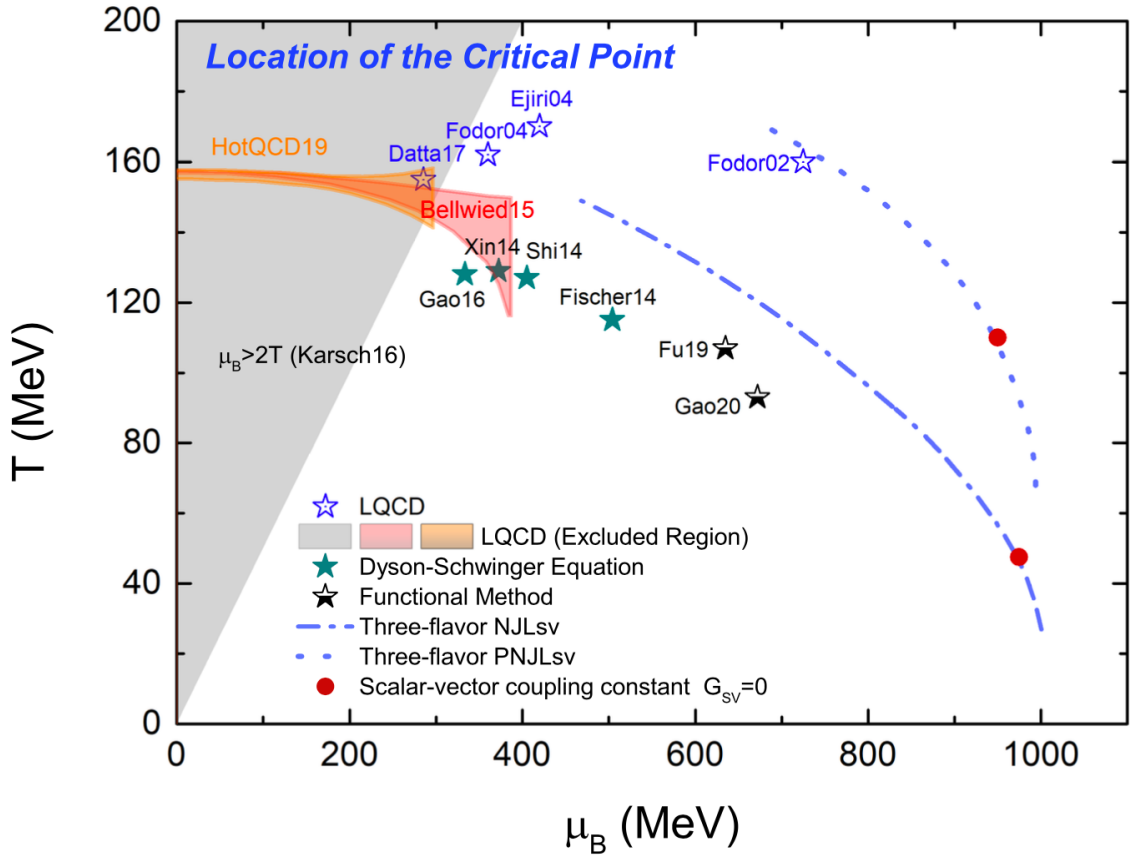

Fig. 1. Comparison of the location of the critical point in the plane of temperature T versus baryon chemical potential μ_B from the three-flavor NJL (dash line) and PNJL (dotted line) models by varying the value of the scalar-vector coupling constant G_{SV}, with red solid circles denoting that obtained with G_{SV} = 0, with predictions from other theoretical models.

Fig. 1 for the NJL and the PNJL models, respectively. This flexible dependence of the quark equation of state due to the quark scalar-vector coupled interaction is very useful for locating the phase boundary in

QCD phase diagram by comparing the experimental data with results from transport model simulations or hydrodynamic calculations based on equations of states from such generalized NJL and PNJL models.

[1] K.J. Sun, C.M. Ko, S.S. Cao, and F. Li, Phys. Rev. D **103**, 014006 (2021).

Yield ratio of hypertriton to light nuclei in heavy-ion collisions from $\sqrt{s_{NN}}$ = 4.9 GeV to 2.76 TeV

Tian-Hao Shao,[1,2,3] Jin-Hui Chen,[1,2] Che Ming Ko, Kai-Jia Sun, and Zhang-Bu Xu[4]

[1]*Key Laboratory of Nuclear Physics and Ion-beam Application (MOE), Institute of Modern Physics, Fudan University, Shanghai 200433, China*

[2]*Shanghai Institute of Applied Physics, Chinese Academy of Science, Shanghai 201800, China*

[3]*University of Chinese Academy of Science, Beijing 100049, China*

[4]*Brookhaven National Laboratory, Upton, New York 11973, USA*

We have argued that both the ratio S_2 and the ratio S_2/B_2, where S_2 and B_2 are, respectively, the coalescence parameters for the production of hypertriton from Λ and a deuteron, and of a deuteron from a proton and a neutron, are more sensitive observables than the previously proposed ratio $S_3 = N_{^3_\Lambda He}/N_\Lambda/\left(N_{^3He}/N_\mathrm{p}\right)$ for studying the local baryon-strangeness correlation in the matter produced in relativistic heavy-ion collisions. This argument is substantiated by a study in the framework of baryon coalescence, which demonstrates that the correlation coefficient $\alpha_{\Lambda d}$ between Λ and deuteron density fluctuations extracted from measured S_2/B_2 shows a stronger dependence on the energy of heavy-ion collisions than the correlation coefficients $\alpha_{\Lambda p} + \alpha_{\Lambda n}$ between Λ and nucleon density fluctuations extracted from the measured S_3 as shown in Fig. 1. Although the results in the present study are obtained without including the feed-down contribution to nucleons from Δ resonances, they will not be qualitatively affected because of the low kinetic freeze-out temperature of about 100 MeV, which only contributes about 20% to the nucleon yield. Experimental measurements of the ratio S_2/B_2 are expected to provide a promising way to study the strangeness and baryon correlation in the matter produced from

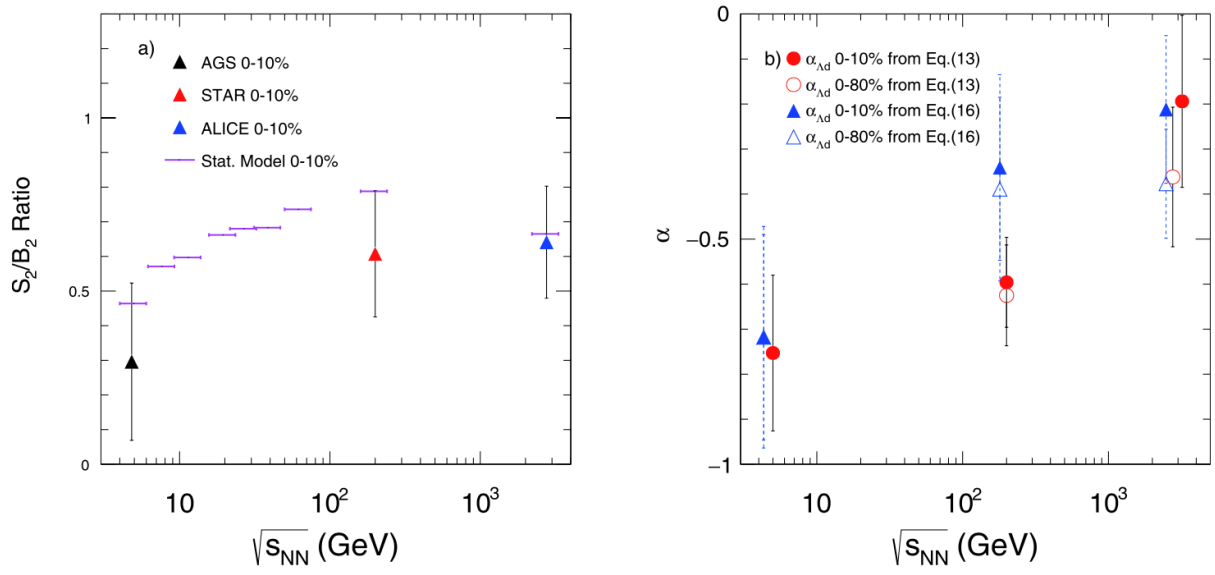

Fig. 1. Left: The S_2/B_2 ratio extracted from experimental data (solid triangles) and predicted by the statistical model (solid horizontal bars) for collision at the 0-10% centrality [2,3]. Right: Values of $\alpha_{\Lambda d}$ extracted from experimental results on S_2 (Eq. (13)) and S_2/B_2 (Eq. (16)).

heavy-ion collisions as the collision energy or the baryon chemical potential of produced matter is varied, which in turn can shed light on the properties of the QGP to hadronic matter phase transition during the collisions.

[1] T. Shao, J. Chen, C.M. Ko, K.-J. Sun, and Z. Xu, Chin. Phys. C **44**, 114001 (2020).
[2] J. Adam *et al*., Phys. Rev. C, **93**, 024917 (2016).
[3] J. Adam *et al*., Phys. Rev. C, **99**, 064905 (2019).

Nuclear theory – Nuclear astrophysics

J.W. Holt

Introduction:

The structure, phases, and dynamics of nuclear matter are crucial to understand stellar explosions, the origin of the elements, patterns in observed gravitational waves, and the composition of the densest observable matter in the universe. The appropriate tool to study strongly interacting matter at the typical scales relevant in nuclear astrophysics (well below the scale of chiral symmetry breaking $\Lambda_\chi \approx 1$ GeV) is chiral effective field theory [WEI79, EPE09, MAC11]. In recent years, chiral effective field theory has become a cornerstone of the modern approach to nuclear many-body dynamics that provides a systematic framework for describing realistic microphysics, such as multi-pion exchange processes and three-body forces, within a well-defined organizational hierarchy. The long and intermediate-range parts of the nuclear potential result from one- and two-pion exchange processes, while short-distance dynamics, not resolved at the wavelengths corresponding to typical nuclear Fermi momenta, are introduced as contact interactions between nucleons. Chiral effective field theory is unique in its multichannel methods for quantifying uncertainties and especially in its ability to estimate the importance of missing physics.

Radius and equation of state constraints from massive neutron stars and GW190814

In June 2020, the LIGO/Virgo Collaboration reported measurements [ABB20] of gravitational waves resulting from a $2.50 - 2.67 M_\odot$ "mass-gap" object in binary coalescence with a heavy $22.2 - 24.3 M_\odot$ companion black hole. Taken at face value, the mass-gap secondary object in the observation represents the discovery of either the heaviest known neutron star (NS) or the lightest known black hole (BH). Motivated by the unknown nature of the $2.50 - 2.67 M_\odot$ compact object in the binary merger event GW190814, we have studied [LIM20] the maximum neutron star mass based on constraints from low-energy nuclear physics, neutron star tidal deformabilities from GW170817, and simultaneous mass-radius measurements of PSR J0030+045 from NICER. Our prior distribution is based on a combination of nuclear modeling valid in the vicinity of normal nuclear densities together with the assumption of a maximally stiff equation of state at high densities, a choice that enables us to probe the connection between observed heavy neutron stars and the transition density at which conventional nuclear physics models must break down. We have demonstrated that a modification of the highly uncertain supra-saturation density equation of state beyond 2.64 times normal nuclear density is required in order for chiral effective field theory models to be consistent with current neutron star observations and the existence of $2.6 M_\odot$ neutron stars. We have also shown that the existence of very massive neutron stars strongly impacts the radii of $\sim 2.0 M_\odot$ neutron stars. In Fig. 1 we show the critical density n_t beyond which traditional nuclear physics modeling must break down in order to support neutron stars with mass $M_{\rm max}$.

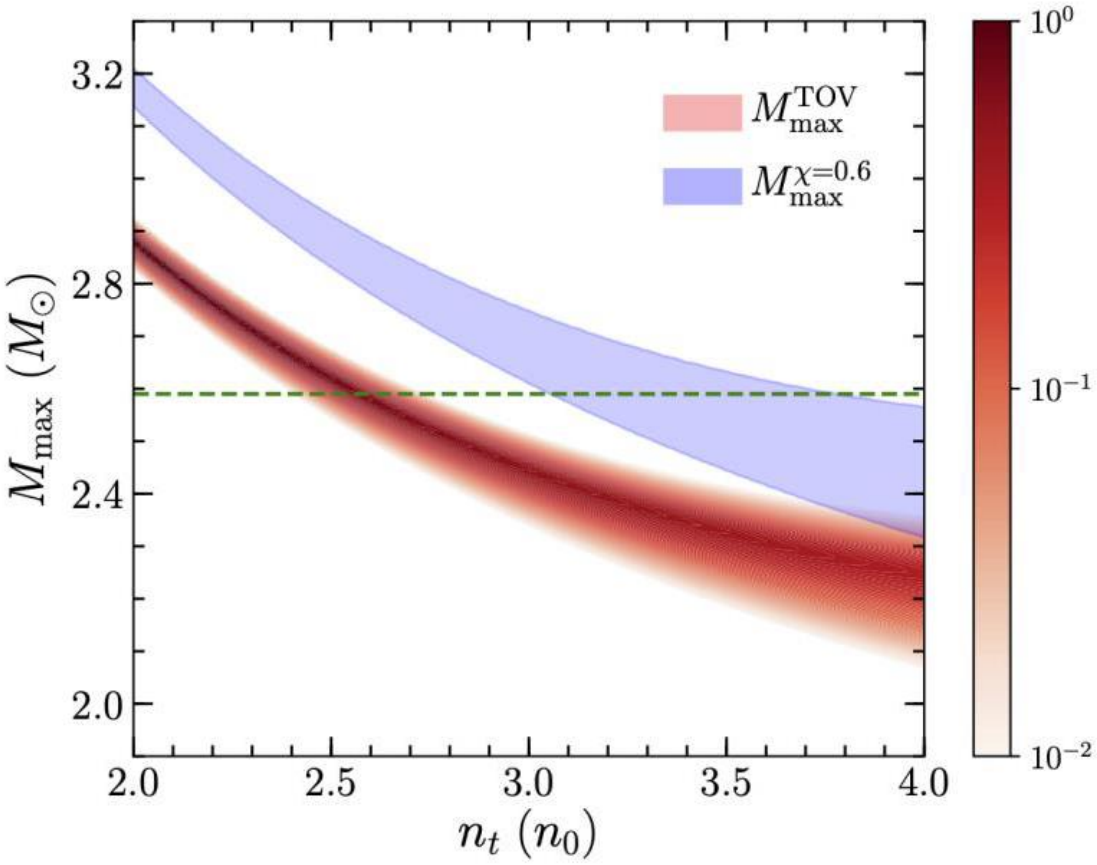

Fig. 1. Minimum transition density $\boldsymbol{n_t}$ at which traditional nuclear physics models break down in order to support massive $\boldsymbol{M}_{\rm max}$ neutron stars. Shown also is the same quantity in the case of rapidly rotating neutron stars with spin $\boldsymbol{\chi = 0.6}$.

Microscopic global optical potential from chiral effective field theory

Numerical simulations of r-process nucleosynthesis are essential for identifying the astrophysical site of the r-process, the primary candidates being the wind-driven ejecta from accretion disks surrounding binary neutron-star mergers or collapsars as well as the neutrino-driven winds of core-collapse supernovae. Neutron-capture rates on exotic neutron-rich isotopes are particularly important during the non-equilibrium freeze-out phase of r-process nucleosynthesis, but direct experimental studies at rare-isotope facilities remain unfeasible. The large uncertainties in these capture rates, due in part to difficulties in extrapolating phenomenological optical model potentials far from the valley of stability, limit the precision of predicted heavy-element abundances. Previously we have computed proton-nucleus and neutron-nucleus optical potentials [WHI19,WHI20] by combining the improved local density approximation with chiral effective field theory calculations of the nucleon self energy in homogeneous nuclear matter. Differential elastic scattering cross sections on calcium isotopes were found to be in quite good agreement with experimental data for projectile energies up to 150 MeV.

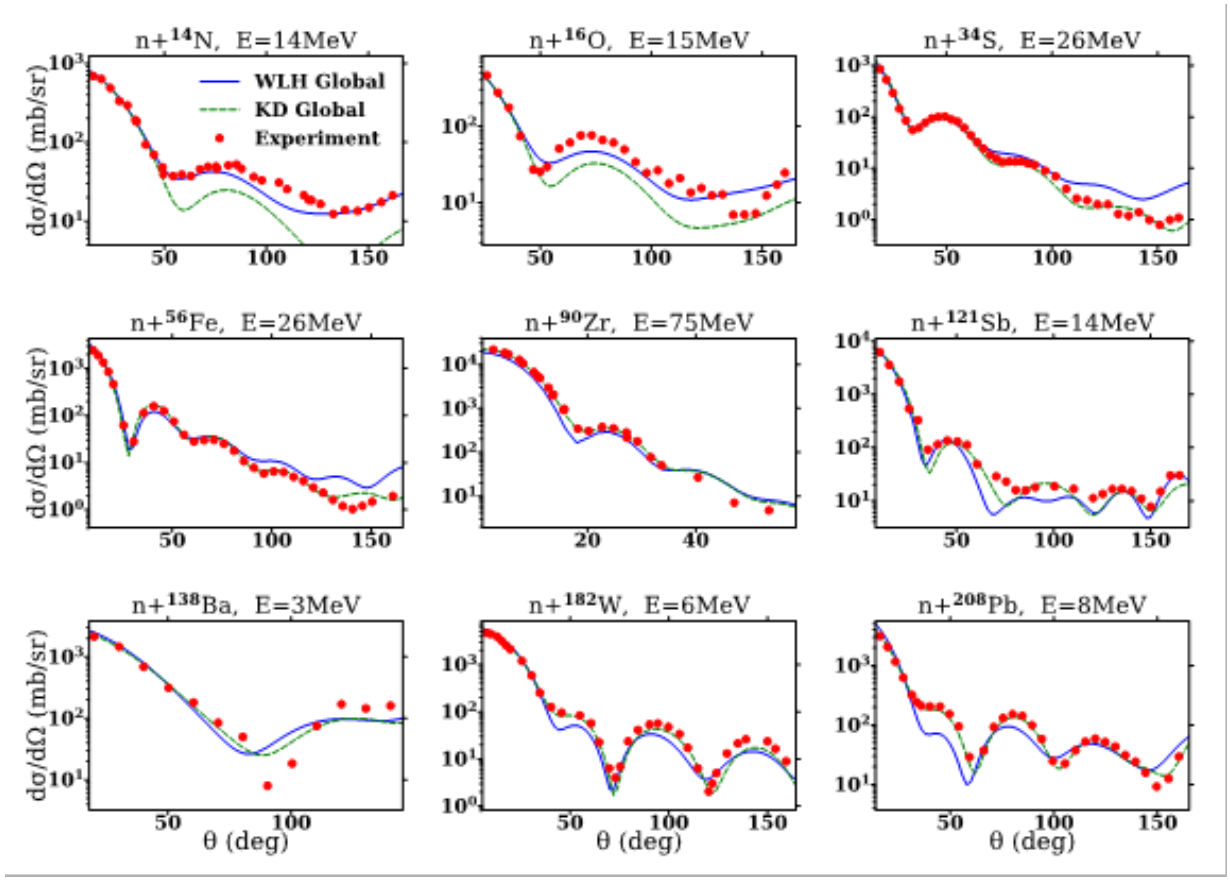

Fig. 2. Neutron elastic differential scattering cross sections from the microscopic global optical potential of Ref. [WHI21] (blue) compared to experimental data (red dots) and the Koning-Delaroche phenomenological optical potential (green dashed).

Recently, we have constructed from chiral effective field theory two- and three-body forces a microscopic global nucleon-nucleus optical potential suitable for reactions involving radioactive isotopes. Within the improved local density approximation and without any adjustable parameters, we have computed local proton and neutron optical potentials for 1800 target nuclei in the mass range $12 < A < 242$ and for energies between $0\ \text{MeV} < E < 200\ \text{MeV}$. We then constructed a global optical potential parametrization that depends smoothly on the projectile energy as well as the target nucleus mass number and isospin asymmetry. Elastic scattering observables calculated from the global optical potential were found to be in good agreement with available experimental data for a wide range of projectile energies and target nuclei. In Fig. 2 we show the predicted neutron elastic differential scattering cross sections for a range of isotopes and energies from the microscopic global optical potential of Ref. [WHI21] compared to experimental data and the results from the Koning-Delaroche phenomenological optical potential [KON03].

Constraining the nonanalytic terms in the isospin-asymmetry expansion of the nuclear equation of state

The equation of state of nuclear matter at arbitrary proton fraction and density is crucial for understanding the structure and dynamics of neutron stars, the properties of neutron-rich nuclei, and data from terrestrial heavy-ion collision experiments. We have extracted [WEN21] from chiral two- and three-body forces the high-order symmetry energy coefficients that consist of both normal terms (occurring with even powers of the isospin asymmetry δ) and terms involving the logarithm of the isospin asymmetry that are formally nonanalytic around the expansion point of isospin-symmetric nuclear matter:

$$\bar{E}(n,\delta) = A_0(n) + A_2(n)\delta^2 + \sum_{i>1}\left(A_{2i}(n) + A_{2i,l}(n)\log|\delta|\right)\delta^{2i}.$$

The coefficients were extracted from numerically precise perturbation theory calculations of the equation of state coupled with a new set of finite difference formulas that achieve stability by explicitly removing the effects of higher-order terms in the expansion. We have found that the coefficients of the logarithmic terms are generically larger in magnitude than those of the normal terms from second-order perturbation theory diagrams, but overall the normal terms give larger contributions to the ground state energy. We have also observed that high-order isospin-asymmetry terms are especially relevant at large densities where they effect the proton fraction in beta-equilibrium matter. In Fig. 3 we plot the density dependence of the coefficients A_4, A_6, A_{4l}, A_{6l} in the modified isospin-asymmetry expansion of the nuclear EOS arising at second-order in perturbation theory. We consider as an estimate of the theoretical uncertainty five different chiral potentials and include three-body forces throughout.

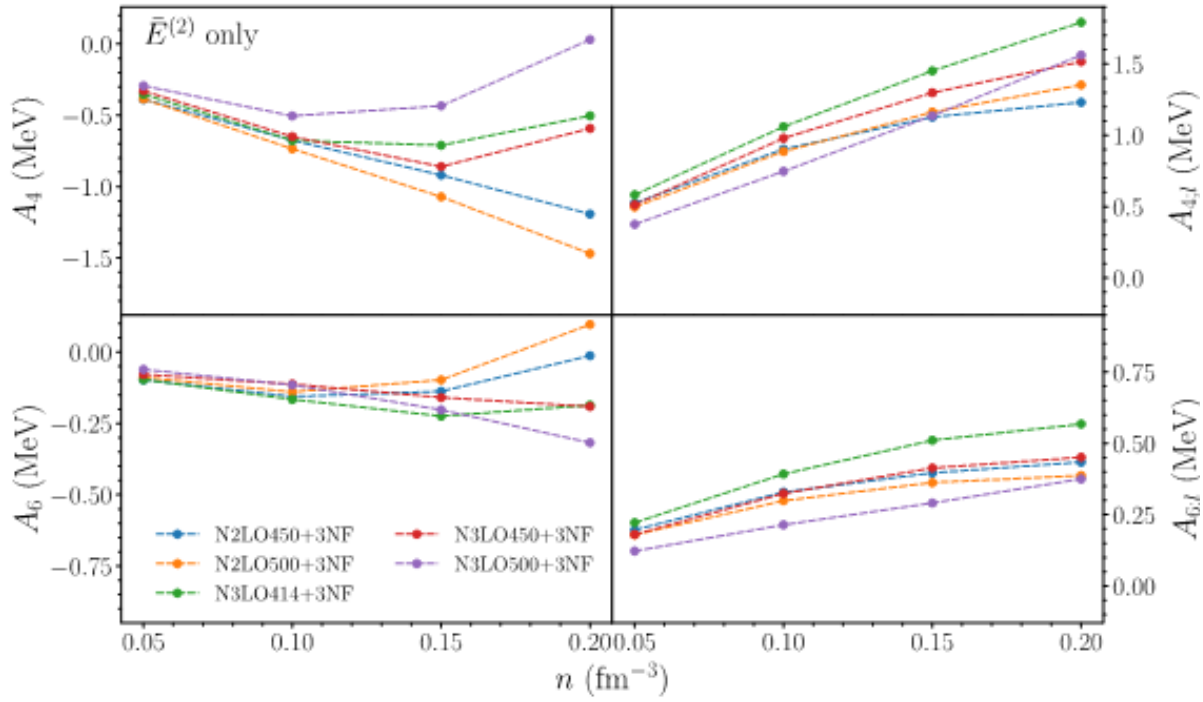

Fig. 3. Density dependence of the high-order normal and logarithmic contributions to the isospin-asymmetry dependence of the nuclear equation of state from chiral effective field theory two-body and three-body forces.

[1] S. Weinberg, Physica A **96**, 327 (1979).
[2] E. Epelbaum, H.-W. Hammer and U.-G. Meissner, Rev. Mod. Phys. **81**, 1773 (2009).
[3] R. Machleidt and D. R. Entem, Phys. Rept. **503**, 1 (2011).
[4] R. Abbott *et al.* (LIGO Scientific Collaboration and Virgo Collaboration) Astrophys. J. Lett. **896** (2020) L44.
[5] Y. Lim, A. Bhattacharya, J.W. Holt, and D. Pati, arXiv:2007.0652.
[6] T.R. Whitehead, Y. Lim, and J.W. Holt, Phys. Rev. C **100**, 014601 (2019).
[7] T.R. Whitehead, Y. Lim, and J.W. Holt, Phys. Rev. C **101**, 064613 (2020).
[8] T.R. Whitehead, Y. Lim, and J.W. Holt, arXiv:2009.08436.
[9] A.J. Koning and J.P. Delaroche, Nucl. Phys. **A713**, 231 (2003).
[10] P. Wen and J.W. Holt, Phys. Rev. C **103**, 064002 (2021).

Astrophysical S-factor for the $^{3}He(\alpha, \gamma)^{7}Be$ reaction via the asymptotic normalization coefficient (ANC) method

G.G. Kissa, M. La Cognata, C. Spitaleri, R. Yarmukhamedov, I. Wiedenhöver, L.T. Baby, S. Cherubini, A. Cvetinovic, G. D'Agatab, P. Figuera, G.L. Guardo, M. Gulino, S. Hayakawa, I. Indelicato, L. Lamiab, M. Lattuada, F. Mudò, S. Palmerini, R.G. Pizzone, G.G. Rapisarda, S. Romano, M.L. Sergi, R. Spartà, O. Trippella, A. Tumino, M. Anastasiou, S.A. Kuvin, N. Rijal, B. Schmidt, S.B. Igamov, S.B. Sakuta, K.I. Tursunmakhatov, Zs. Fülöp, Gy. Gyürky, T. Szücs, Z. Halász, E. Somorjai, Z. Hons, J. Mrázek, R.E. Tribble, and A.M. Mukhamedzhanov

The detection of the neutrinos produced in the p−p chain and in the CNO cycle can be used to test the Standard Solar Model. The $^{3}He(\alpha,\gamma)^{7}Be$ reaction is the first reaction of the 2nd and 3rd branch of the p−p chain, therefore, the uncertainty of its cross section sensitively influences the prediction of the ^{7}Be and ^{8}B neutrino fluxes. Despite its importance and the large number of experimental and theoretical works devoted to this reaction, the knowledge on the reaction cross section at energies characterizing the core of the Sun (15 keV - 30 keV) is limited and further experimental efforts are needed to reach the desired (≈ 3%) accuracy. The precise knowledge on the external capture contribution to the $^{3}He(\alpha,\gamma)^{7}Be$ reaction cross section is crucial for the theoretical description of the reaction mechanism. In the present work the indirect measurement of this external capture contribution using the Asymptotic Normalization Coefficient (ANC) technique is reported. To extract the ANC, the angular distributions of deuterons emitted in the $^{6}Li(^{3}He,d)^{7}Be$ α-transfer reaction were measured with high precision at the projectile energies of 3.0 MeV and 5.0 MeV. The ANCs were then extracted from comparison of DWBA calculations to the measured data and the zero energy astrophysical S-factor for $^{3}He(\alpha,\gamma)^{7}Be$ reaction was found to be 0.534 ± 0.025 keVb.

The work was published in Phys. Lett. B **807**, 135606 (2020).

One-center close-coupling approach to two-center rearrangement collisions

I.B. Abdurakhmanov, C. Plowman, A.S. Kadyrov, I. Bray, and A.M. Mukhamedzhanov

Calculations of ionization and electron-capture cross sections in ion-atom collisions usually require solving the Schrödinger equation governing the collision system by expanding the total scattering wave function in a basis of target- and projectile-centered pseudostates. This approach leads to the two-center close-coupling equations which in some cases may become ill-conditioned due to the non-orthogonality of the underlying combined basis. Here we develop a technique which allows to accurately extract the necessary collision information, including that for the rearrangement channels, from the computationally more convenient one-center close-coupling equations which are built from only target-centered pseudostates. The robustness of the method is demonstrated by considering the proton-hydrogen scattering problem across a wide incident energy range. The developed method is then applied to study proton scattering on multielectron target of lithium. The obtained results for the 2s→2p excitation and the total electron-capture cross sections are in good agreement with corresponding experimental data. It is concluded that the presented technique could be a simpler alternative when integrated cross sections are required.

The work was published in J. Phys. B: At. Mol. Opt. Phys. **53**, 145201 (2020).

Status on $^{12}C + ^{12}C$ fusion at deep sub-barrier energies: impact of resonances on astrophysical S* -factors

C. Beck, A.M. Mukhamedzhanov, and X. Tang

Since the discovery of molecular resonances in $^{12}C+^{12}C$ in the early sixties a great deal of research work has been undertaken to study α-clustering and resonant effect of the fusion process at sub-Coulomb barrier energies. The modified astrophysical S*- factors of $^{12}C +^{12}C$ fusion have been extracted from direct fusion measurements at deep sub-barrier energies near the Gamow window. They were also obtained by the indirect Trojan horse method (THM). A comparison of direct measurements and the THM, which elucidates problems in the analysis of the THM, is discussed in this research. The work was published in Eur. Phys. J. A **56**, 87 (2020), Letter to Editor.

The $^{3}He+^{5}He \rightarrow ^{4}He+^{4}H$ reaction below the Coulomb barrier via the Trojan Horse Method

C. Spitaleri, S. Typel, C.A. Bertulani, A.M. Mukhamedzhanov, T. Kajino, M. Lattuad, A.Cvetinović, S. Messina, G.L. Guardo, N. Soić, Milin, S.S. Perrotta, Chengbo Li, P. Čolović, G. D'Agata, D. Dell'Aquila, C.G. Fatuzzo, M.Gulino, S.Q. Hou, M. La Cognata, D. Lattuada, D. Nurki´c, R. Popočovski, N. Skuka, S. Szilner, O. Trippella1, M. Uroić, and N. Vukman

For the first time in an application to nuclear astrophysics, a process induced by the unstable ^{5}He= (4He-n) nucleus, the $^{3}He+^{5}He \rightarrow 2\alpha$ reaction, has been studied through the Trojan Horse Method (THM). For that purpose, the quasi-free (QF) contribution of the $^{9}Be(^{3}He,\alpha\alpha)^{4}He$ reaction was selected at ^{3}He incident energy of 4 MeV. The reaction was studied in a kinematic complete experiment following our recent publication, where for the quasi free contribution the momentum distribution between α and ^{5}He particle cluster in the ^{9}Be nucleus in the ground state have been extracted. The angular distribution of the QF $^{3}He+^{5}He \rightarrow 2\alpha$ reaction was measured at θ_{cm} = 78◦ - 115◦. The energy dependence of the differential cross section of the $^{3}He+^{5}He \rightarrow 2\alpha$ virtual reaction was extracted in the energy range E_{cm} = 0 - 650 keV. The total cross section obtained from the Trojan-horse method was normalised to absolute cross sections from a theoretical calculation in the energy range E_{cm} = 300 - 620keV.

The paper was published in Eur. Phys. J. A **57**, 20 (2021).

Trojan horse method as an indirect approach to study resonant reactions in nuclear astrophysics

A.M. Mukhamedzhanov, A.S. Kadyrov, and D.Y. Pang

The primary goal of the Trojan horse method (THM) is to analyze resonant rearrangement reactions when the density of the resonance levels is low and statistical models cannot be applied. The main difficulty of the analysis is related with the facts that in the final state the THM reaction involves three particles and that the intermediate particle, which is transferred from the Trojan horse particle to the target nucleus to form a resonance state, is virtual. Another difficulty is associated with the Coulomb interaction between the particles, especially, taking into account that the goal of the THM is to study resonant rearrangement reactions at very low energies important for nuclear astrophysics. The exact theory of such reactions with three charged particles is very complicated and is not available. This is why different approximations are used to analyze THM reactions. In this review paper we describe a new approach based on a few-body formalism that provides a solid basis for deriving the THM reaction amplitude taking into account rescattering of the particles in the initial, intermediate and final states of the THM reaction. Since the THM uses a two-step reaction in which the first step is the transfer reaction populating a resonance state, we address the theory of the transfer reactions. The theory is based on the surface-integral approach and R-matrix formalism. We also discuss application of the THM to resonant reactions populating both resonances located on the second energy sheet and subthreshold resonances, which are subthreshold bound states located at negative energies close to thresholds. We consider the application of the THM to determine the astrophysical factors of resonant radiative capture reactions at energies so low that direct measurements can hardly be performed due to the negligibly small penetrability factor in the entry channel of the reaction. We elucidated the main ideas of the THM and outline necessary conditions to perform the THM experiments.

The work was published as an invited review paper in Eur. Phys. J. A **56**, 233 (2020).

$^{12}C+^{12}C$ sub-barrier fusion cross section in an imaginary time-dependent mean field theory

A. Bonasera[1,2] and J.B. Natowitz[1]

[1]*Cyclotron Institute, Texas A&M University, College Station, Texas 77843*
[2]*Laboratori Nazionali del Sud-INFN, v. Santa Sofia 64, 95123 Catania, Italy*.

The $^{12}C+^{12}C$ sub-barrier fusion cross section is calculated within the framework of a Time Dependent Hartree-Fock (TDHF) based classical model using the Feynman Path Integral Method. The modified astrophysical S*-factor is compared to direct and indirect experimental results, see Fig. 1. A reasonable agreement with the direct data is found. In the lower energy region, where recent analyses of experimental data obtained with the Trojan Horse Method (THM) lead to contrasting results, the model predicts an S* factor half-way between those results. Low energy resonances revealed in the THM data are added to the calculation and the relative reaction rate in the Gamow region is calculated. The role of different resonances is discussed in detail and their influence on the reaction rate at temperatures relevant to stellar evolution is investigated.

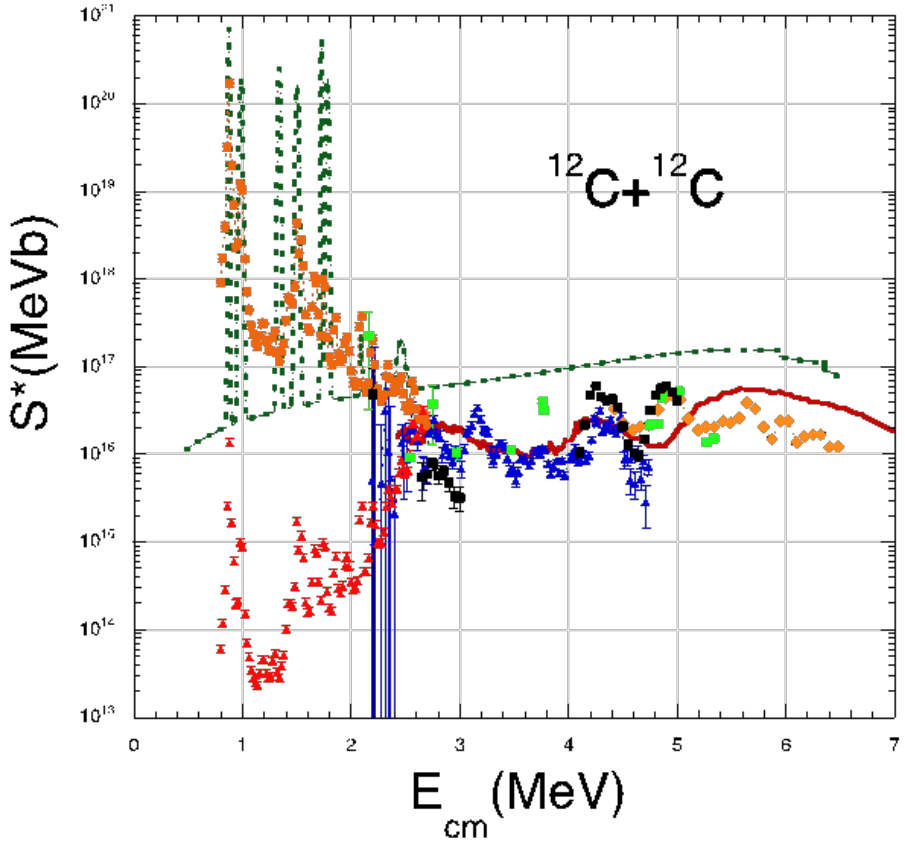

Fig. 1. Modified Astrophysical S*-factor as function of E_{cm}. The full line is the result from the Neck Model and the dashed line from the Vlasov equation in imaginary times, symbols are data from different experiments [1-2].

[1] A. Bonasera and J.B. Natowitz, Phys. Rev. C **102**, 061602(**R**) (2020).
[2] A. Bonasera, HINPw6 contribution, in press (2021).

Coulomb field correction due to virtual e^+e^- production in heavy ion collisions

Thomas Settlemyre, Samuel Brown, Hua Zheng, and Aldo Bonasera

The correction to the Coulomb energy due to virtual production of e+e- pairs [1], which is on the order of one percent of the Coulomb energy at nuclear scales is discussed. The effects of including a pair-production term in the semi-empirical mass formula and the correction to the Coulomb barrier for a handful of nuclear collisions using the Bass [2] and Coulomb potentials are studied. With an eye toward future work using Constrained Molecular Dynamics (CoMD) model [3], we also calculate the correction to the Coulomb energy and force between protons after folding with a Gaussian spatial distribution.

For distances less than the electron Compton wavelength $\boldsymbol{\lambda}$ = 386 fm, the vacuum polarization correction to the Coulomb potential between charges Z_1 and Z_2 is approximately [1]

$$V_{e+e-} = -\frac{2\alpha}{3\pi}\frac{Z_1 Z_2 e^2}{r}\left(\ln\frac{r}{\lambda} + 1.41\right). \qquad \text{Eq. (1)}$$

When folded with a Gaussian spatial distribution, the resulting potential is a complicated function involving derivatives of the confluent hypergeometric function [4]. The folding softens the 1/r singularity, as seen in Fig. 1.

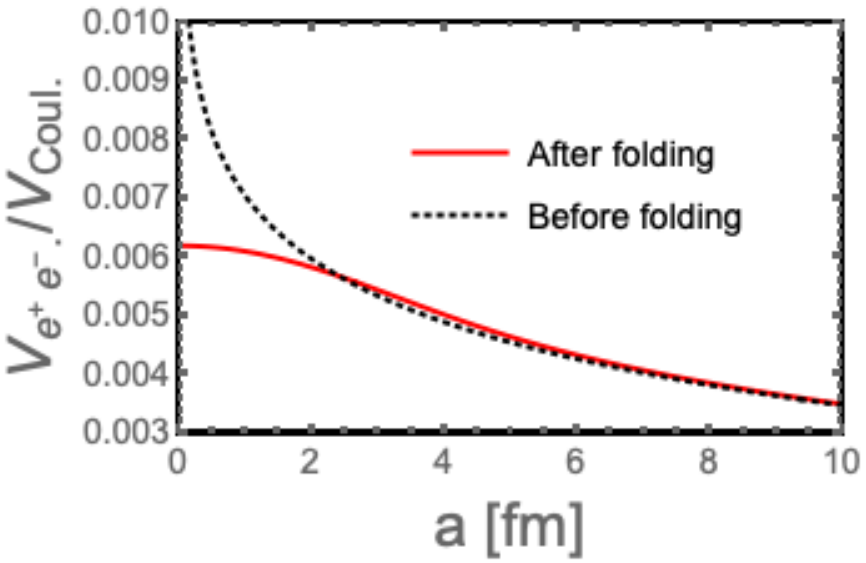

Fig. 1. The fractional change of the Coulomb energy of two protons separated by a distance a before folding (black, dotted), and after folding (red). (Note the vertical scale.) After folding, the correction is never more than about 0.6%.

The vacuum polarization correction was found to decrease the theoretical cross section of fusion in the $^{12}C+^{12}C$ system by as much as 15% for lower energies (Fig. 2????).

Currently, we are working to find e+e- production rates in ion collisions by solving the Dirac equation [5] coupled to the Coulomb trajectory of two heavy ions.

[1] E. Uehling, Phys. Rev. **48** 55 (1935).

[2] R. Bass, Phys. Rev. Lett. **39** 265 (1977).

[3] M. Papa, T. Maruyama, and A. Bonasera, Phys. Rev. C **64** 024612 (2001).

[4] T. Settlemyre, H. Aheng and A. Bonasera, Nucl. Phys. A (in press).

[5] I.A. Maltsev, V.M. Shabaev, I.I. Tupitsyn, A.I. Bondarev, Y.S. Kozhedub, G. Plunien, and Th. Stöhlker, Phys. Rev. A **91**, 032708 (2015).

Pseudorapidity distributions of charged particles in pp($\bar{p}$), p(d)A and AA collisions using Tsallis thermodynamics

J.Q. Tao,[1] M. Wang,[1] H. Zheng,[1] W.C. Zhang,[1] L.L. Zhu,[2] and A. Bonasera
[1]*School of Physics and Information Technology, Shaanxi Normal University, Xi'an 710119, China*
[2]*Department of Physics, Sichuan University, Chengdu 610064, China*

The pseudorapidity distributions of charged particles measured in p+p($\bar{p}$) collisions for energies ranging from $\sqrt{S_{NN}}$=23.6 GeV to 13 TeV and A+A collisions at RHIC and LHC are investigated in the fireball model with Tsallis thermodynamics [1]. We assume that the rapidity axis is populated with fireballs following q-Gaussian distribution and the charged particles follow the Tsallis distribution in the fireball. We also extend the fireball model to asymmetric collision systems, i.e., d+Au collisions at $\sqrt{S_{NN}}$=200 GeV and p+Pb collisions at $\sqrt{S_{NN}}$= 5.02 TeV, by taking into account the asymmetric geometry configuration. The model can fit well the experimental data for all the collision systems and centralities investigated. The collision energy and centrality dependence of the model parameters for the symmetric (asymmetric) collision system, i.e., the central position y_0 (y_{0a}, y_{0A}) and its width σ (σ_a, σ_A) of the fireball distribution, are also investigated and discussed. The results suggest that the fireball model with Tsallis thermodynamics can be used as a universal framework for the pseudorapidity distributions of charged particles in high energy collisions at RHIC and LHC.

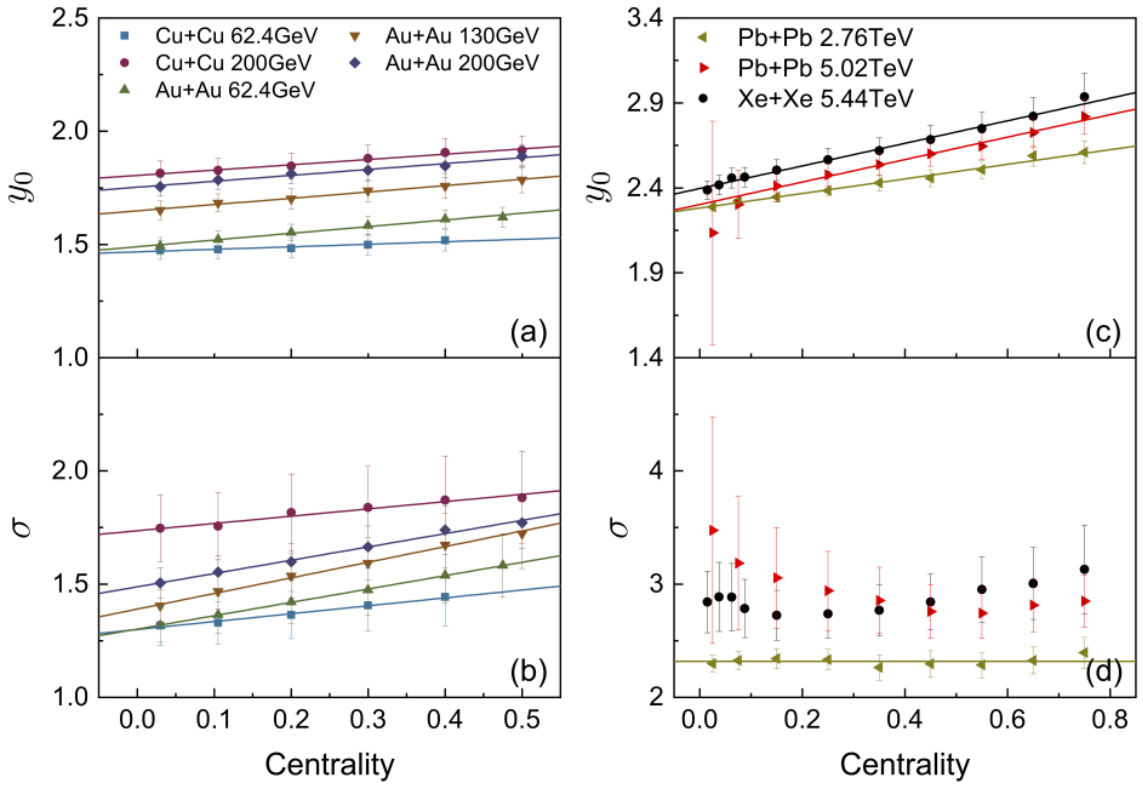

Fig. 1. (Color online) The centrality (0 represents the most central collisions) dependence of the y_0 and **σ** in Cu+Cu collisions at $\sqrt{S_{NN}}$=62.4, 200 GeV, Au+Au collisions at $\sqrt{S_{NN}}$=62.4, 130, 200 GeV, Pb+Pb collisions at $\sqrt{S_{NN}}$=2.76, 5.02 TeV and Xe+Xe collisions at $\sqrt{S_{NN}}$=5.44 TeV. The lines are the linear fitting results.

In Fig. 1, the centrality dependence of the y_0 and σ are shown for A+A collisions at $\sqrt{S_{NN}}$>60 GeV. A nice linear relation between y_0 and centrality is found. We performed linear fits shown with the lines in Fig. 1(a) and (c). The positive slope indicates that the stopping power is decreasing from central to peripheral collisions because there are more collisions and dissipation processes at central collisions comparing with peripheral collisions. The linear behavior of the width σ versus centrality is also observed at RHIC. The fitting results are shown by the lines in Fig. 1(b) and (d). For the collisions at LHC, σ shows different dependence on centrality. For Pb+Pb collisions at $\sqrt{S_{NN}}$=2.76 TeV, σ tends to be a constant for all the centralities and a constant line is plotted. While the collision energy goes up, i.e., Pb+Pb collisions at $\sqrt{S_{NN}}$=5.02 TeV and Xe+Xe at $\sqrt{S_{NN}}$=5.44 TeV, σ can only be roughly a constant within errors but it can not be conclusive. This is because the relatively limited η acceptance respect to the extremely high collision energies at LHC and the model parameter σ are not well constrained by the experimental data and show large errors.

In Fig. 2, the centrality dependence of the $y_{0a(A)}$ and $\sigma_{a(A)}$ are shown for p(d)+A collisions. The linear relation between $y_{0a(A)}$ ($\sigma_{a(A)}$) and the centrality can be seen. We also performed the linear fits shown with lines. Different from both the p+p and A+A collisions, negative slopes of the lines of $y_{0a(A)}$ ($\sigma_{a(A)}$) are found in the direction of the heavy nucleus beam. This may indicate the different dynamics in p+A collisions from the symmetric collisions because of the asymmetric configuration.

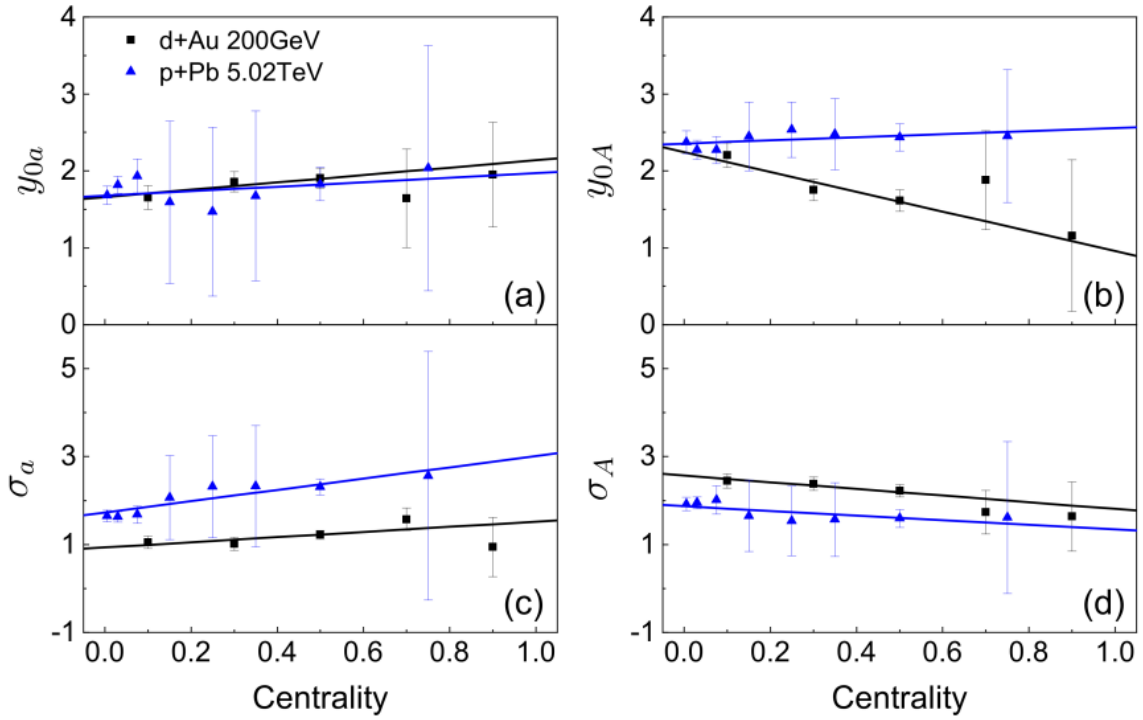

Fig. 2. (Color online) The centrality (0 represents the most central collisions) dependence of the y_{0a}, y_{0A},and $\boldsymbol{\sigma_a}$ and $\boldsymbol{\sigma_A}$ in d+Au collisions at $\sqrt{\boldsymbol{S_{NN}}}$=200 GeV, and p+Pb collisions at $\sqrt{\boldsymbol{S_{NN}}}$=5.02 TeV. The lines are the linear fitting results.

[1] J.Q. Tao, M. Wang, H. Zheng. W.C. Zhang, L.L. Zhu and A. Bonasera, 2021 J. Phys. G: Nucl. Part. Phys. https://doi.org/10.1088/1361-6471/ac1393 [arXiv: 2011.05026].

Baryonic sources of thermal photons

Nathan Holt and Ralf Rapp

Electromagnetic radiation from high-energy heavy-ion collisions is an excellent observable to investigate the microscopic properties of QCD matter produced in these reactions (e.g., the in-medium spectral functions of vector mesons, revealing a transition to quark-gluon degrees of freedom, and mechanisms of chiral-symmetry restoration) as well as the bulk properties of the expanding fireball (such as its temperature, lifetime and collective behavior) [1]. Since leptons and photons traverse the fireball without significant re-interactions, they can probe the conditions deep inside the hot and dense medium. The emission from the hadronic phase plays an essential role in the finally observed spectra. In particular, baryons and anti-baryons have been found to be strong catalysts for electromagnetic radiation, even at collider energies where the baryon chemical potential is small [2,3] but both baryons and anti-baryons are rather abundant.

In the present work, we have conducted a systematic analysis of π- and ω-meson-induced reactions off a large set of baryon states (ca. 30 nucleon, Δ and hyperon states). The interaction vertices are based on effective hadronic Lagrangians where the parameters are quantitatively constrained by empirical information from vacuum decay branchings (both hadronic and radiative) and scattering data (including πN scattering and nuclear photoabsorption); gauge invariance is maintained by suitable regularization procedures. The thermal emission rates are computed using kinetic theory but can be directly compared to previous calculations using hadronic many-body theory, see Fig. 1.

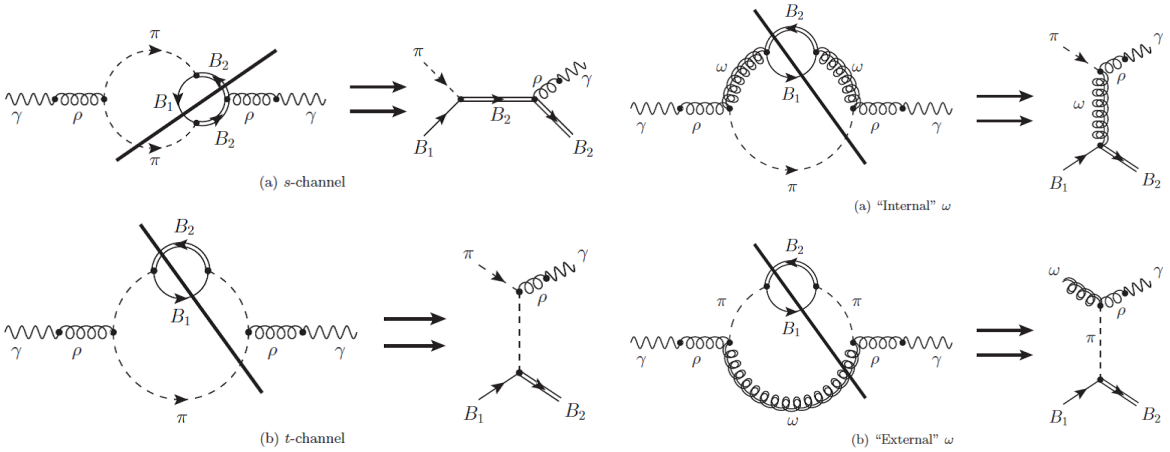

Fig. 1. Examples of the Feynman diagrams for photon production processes involving baryons considered in this work and their relation to cuts of the ρ-meson selfenergy; Left panel: pion-induced; right panels: processes involving the πρω vertex.

Our results for pion-indued processes (cf. Fig. 2) show that the emissions rates at photon energies below ~1 GeV are dominated by P-wave processes, with the largest individual contributions stemming from the N(939) and Δ(1232) couplings. At higher energies, D-wave processes take over, in particular NN(1520) and ΔΔ(1620) couplings. We also find that a previously used approximation for the ρ -

selfenergy, where only N and Δ couplings were considered but with an effective upscaled baryon density (nucleon density plus half the density of all excited states) [4], appears to be a fair approximation to the explicitly calculated rates.

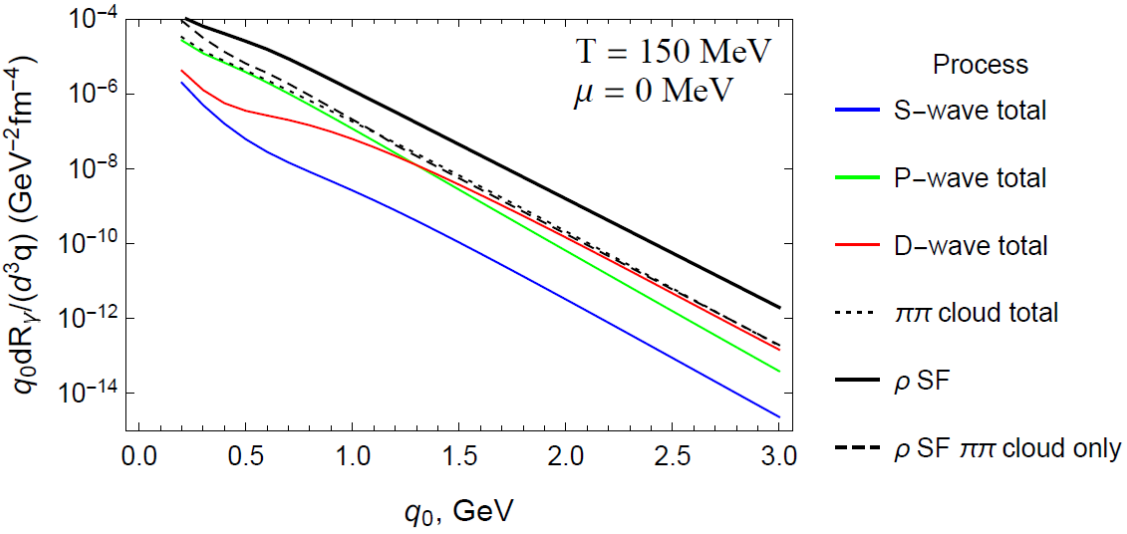

Fig. 2. Thermal photon rates from $\pi + B_1 \rightarrow \gamma + B_2$ reactions with pion exchange calculated in this work in the S-wave (blue line), P-wave (green line) and D-wave (red line) channels, and their sum (black dotted line), compared to the pion cloud contribution from the ρ SF [25] including only N and Δ states but using an effective nucleon density (black dashed line), and the total rate from the ρ spectral function (black solid line).

The second part of our study was devoted to processes with ω-meson-baryon couplings, most of which constitute novel sources of thermal photon production. These turn out to be significant relative to the pion cloud contributions for photon energies of around 1 GeV (several tens of percent), and exceed those for energies above ~1.5 GeV, cf. Fig. 3; ω-induced rates also have a potential for additional

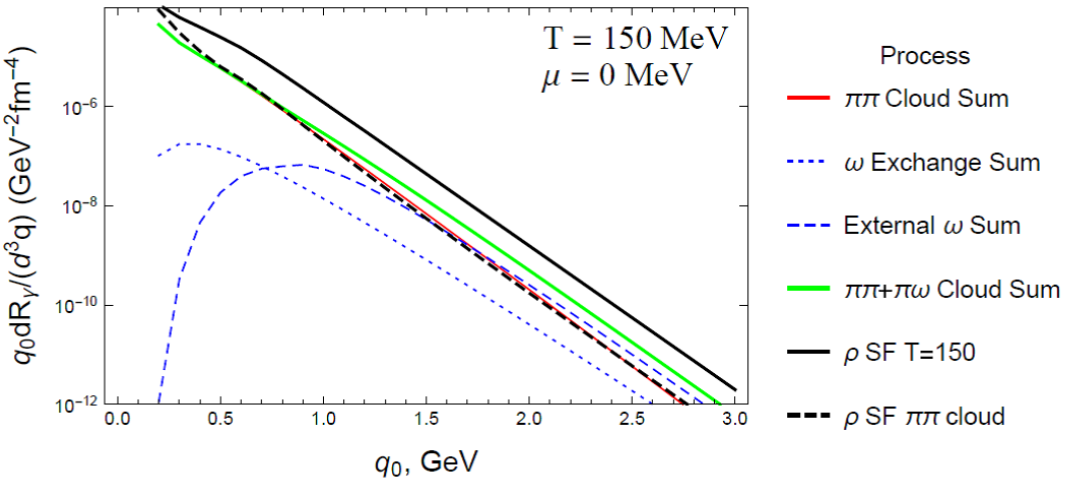

Fig. 3. Total thermal photon rates at T = 150MeV and vanishing baryon chemical potential calculated in this work from the ππ cloud (red line) and the πω cloud (blue dotted and dash-dotted lines); their sum (green solid line) is compared to the total rate from the in-medium ρ SF [4] (solid black line) as well as its ππ cloud component only (black dashed line).

contributions, as many of their manifestations in baryon decay branchings are not well established or not known at all to date. The additional sources found here may help to mitigate some of the tension that currently exists between theoretical calculations of thermal photon spectra and experimental data, especially at RHIC energies [5,6].

[1] R. Rapp and H. van Hees, Eur. Phys. J. A **52**, 257 (2016).
[2] R. Rapp, Phys. Rev. C **63**, 054907 (2001).
[3] S. Turbide, R. Rapp, and C. Gale, Phys. Rev. C **69**, 014903 (2004).
[4] R. Rapp and J. Wambach, Eur Phys. J. A **6**, 415 (1999).
[5] A. Adare *et al.* (PHENIX Collaboration), Phys. Rev. C **94**, 064901 (2016).
[6] S. Acharya *et al.* (ALICE Collaboration), Phys. Lett. B **789**, 308 (2019.

Dilepton signature of a 1st-order phase transition

F. Seck, T. Galatyuk, A. Mukherjee, R. Rapp, J. Steinheimer, and J. Stroth

At high temperatures and vanishing baryon chemical potential, μ_B=0, QCD matter undergoes a smooth cross-over transition from a hadronic phase with spontaneously broken chiral symmetry to a chirally restored plasma of quarks and gluons. It is conjectured that the hadron-quark transition develops a second order endpoint with a first-order transition line attached toward higher μ_B and smaller temperatures (which may occur, e.g., in the interior of neutron stars). In heavy-ion collisions a large region of the phase diagram can be probed by lowering the collision energies from the ultra-relativistic regime at RHIC and the LHC down to a few GeV per nucleon pair in the center of mass. However, clear evidence for a 1st-order transition remains elusive to date, but sustained efforts to explore the QCD phase diagram continue.

In the present work [1] we investigate dilepton radiation from the hot and dense fireballs created in Au-Au collisions at projectile energies of 1-2 AGeV for potential signatures of a 1st-order transition. Toward this end, we employ hydrodynamic simulations with a different equation of state (EoS), with and without a phase transition. The latter is constrained by susceptibilities computed in lattice-QCD at μ_B=0, as well as by neutron star properties [2], while the former is implemented via modifications of the mean fields in the quark phase. The resulting time evolutions of temperature and baryon density are shown in Fig. 1, indicating higher values for both quantities in the 1st-order case due the softer EoS compared to the crossover scenario. In addition, a significantly longer fireball lifetime is observed for the 1st-order EoS. These features are not unexpected but are notoriously difficult to discern using hadronic final-state observables.

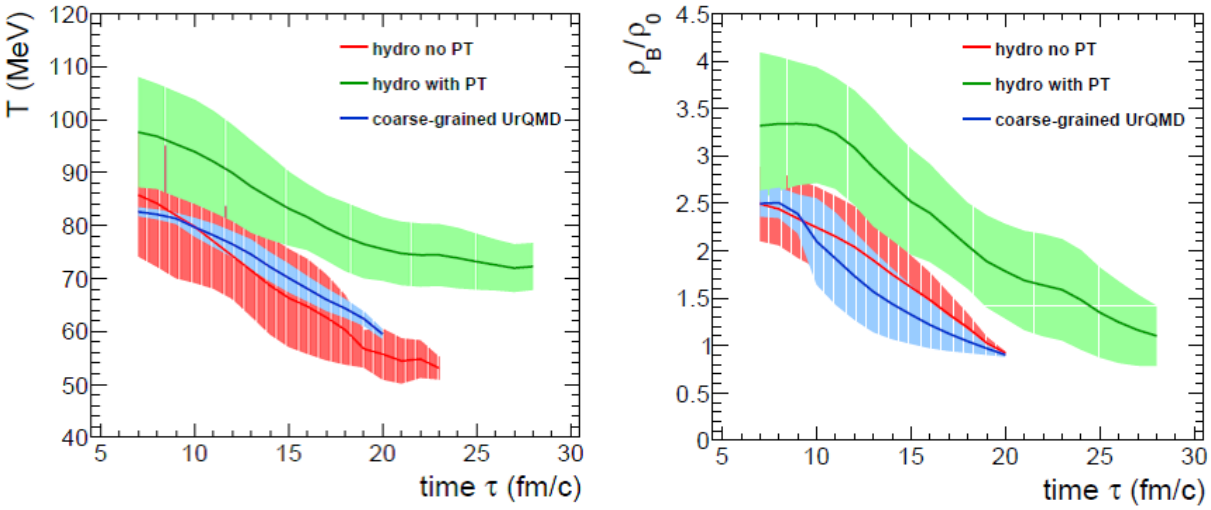

Fig. 1. Time evolution of average temperature (T, left panel) and baryon density (ρ_B, right panel) in hydrodynamic simulations of central Au+Au (1.23AGeV) collisions employing an EoS with (green lines) and without (red lines) a 1st-order phase transition (PT). For comparison, the coarse-graining results of hadronic transport calculations [3] are also shown (blue lines). The bands correspond to the second moment of the distributions in T and ρ_B.

This motivated us to search for signatures of a 1st-order transition in the spectra of electromagnetic radiation, which is emitted throughout the entire 4-volume of the fireball evolution. For the invariant-mass spectra of dileptons (e^+e^- pairs) one has

$$dN_{ee}/dM = \int (M/q_0)\, d^3q\, d^3x\, dt\, R_{ee} \ ,$$

where the integration is over space-time and 3-momentum, and R_{ee} is the 8-differential thermal production rate (with $M^2 = q_0^2 - \mathbf{q}^2$). We have employed hadronic emission rates including in-medium vector-meson spectral functions which have been well tested in heavy-ion collisions at the SPS and RHIC [4]. The invariant-mass spectra obtained from integrating the rates over the hydrodynamic simulations of central Au+Au collision at a lab energy of 1.23 AGeV are shown in Fig. 2. The main result is that the 1st-order scenario indeed produces significantly larger radiation yields than the cross-over one, by about a factor of 2 over most of the invariant-mass range from 0-1.5 GeV. At low masses, M < 1 GeV, this is mostly due to the longer lifetime, while at higher masses the larger temperatures also play an important role. We also show results from our previous work using coarse-grained hadronic transport calculations for the convolution with thermal dilepton rates [3]. The pertinent temperature and density evolution (Fig. 1), and the resulting dilepton spectra are quite similar to the hydrodynamic results without phase transition, which essentially reflects the systematic uncertainty in describing the medium evolution within the limits of small (hydrodynamics) and large (transport) mean-free-path approximations.

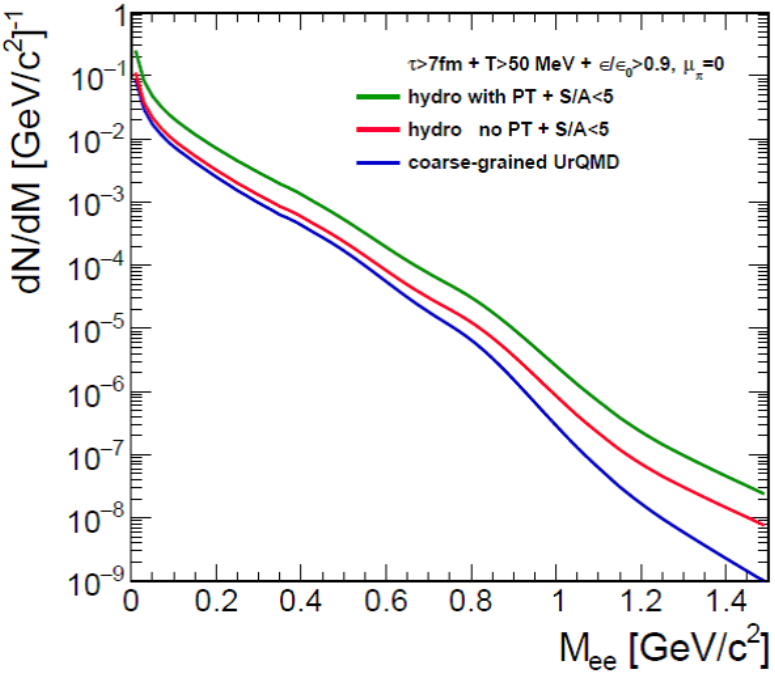

Fig. 2. Thermal dilepton spectra calculated for central Au+Au (1.23AGeV) collisions using hydrodynamic medium evolutions with an equation of state with 1st-order phase transition (green line) or with a cross-over transition (red line), as well as for a coarse-grained hadronic transport simulation using the UrQMD model (blue line).

[1] F. Seck, T. Galatyuk, A. Mukherjee, R. Rapp, J. Steinheimer, and J. Stroth, e-print arXiv:2010.04614.
[2] J. Steinheimer, S. Schramm, and H. Stöcker, Phys. Rev. C **84**, 045208 (2011); A. Mukherjee, J. Steinheimer, and S. Schramm, Phys. Rev. C **96**, 025205 (2017).
[3] R. Rapp and J. Wambach, Eur. Phys. J. A **6**, 415 (1999); H. van Hees and R. Rapp, Nucl. Phys. A **806**, 339 (2008); R. Rapp, Adv. High Energy Phys. **201**3, 148253 (2013).
[4] T. Galatyuk, P.M. Hohler, R. Rapp, F. Seck, and J. Stroth, Eur. Phys. J. A **52**, 131 (2016).

Hard probes 2020: A major nuclear physics conference, moved online

R.J. Fries, Michael Kordell, Arjun Sengupta, and collaborators

R.J. Fries was a co-chair of the 10th International Conference on Hard and Electromagnetic Probes of High-Energy Nuclear Collisions (Hard Probes 2020). The Conference took place June 1-5, 2020, with a student day preceding the conference on May 31. Hard Probes is one of the largest conferences in high energy nuclear physics, focusing on electroweak probes, jets and high-momentum hadrons, heavy flavor probes, quarkonia, and initial state physics in ultra-relativistic nucleus-nucleus collisions and related systems. It was originally planned as an in-person conference to showcase the vibrant and successful groups at Texas &M University and other universities in Texas (Rice University, the University of Houston and UT Austin were partners in organizing the conference). However, it turned out to be one of the first large conferences to be affected by the COVID-19 crisis. With just enough time to spare the co-chairs worked successfully to convert the full conference schedule to an online format. A decision was made to move the entire conference to Zoom, keeping the original dates. CERN graciously provided technical support (licenses and manpower) to manage the online aspects. A session format was designed with two lead persons per session, a session manager and a session chair, which allowed a separation of technical and scientific aspects of the session. Detailed manuals for chairs, managers and speakers as well as training sessions for session managers were devised. The poster session was organized with one Zoom room per poster. All rooms could be accessed easily from a hub on the conference Indico website. Poster presenters were allowed to upload a 3-minute teaser video before the session, leading to a surprisingly creative array of videos.

By all measures the conference was a success with more than 400 regular participants in the plenary sessions, more than in previous in-person editions of this conference series. The student day reached an unprecedented number of students and was attended by more than 200 participants from around the world.

Scientifically, Hard Probes 2020 featured a number of new results in heavy ion physics from the experimental collaborations at both RHIC and LHC as well as new insights from a diverse field of theory contributions. The online format was optimized to allow, over a period of 5 days, for participation across many time zones with daily plenary and parallel sessions. In total 37 plenary, 152 parallel, and 67 poster presentations were scheduled. The spotlight was shone on the next generation of scientists who were given an opportunity to present their award winning posters in 8 flash talks.

Quark recombination effects from small to large systems

R.J. Fries, Michael Kordell, Arjun Sengupta, and collaborators

One of the most amusing features of the strong force is the confinement principle: Free quarks and gluons cannot exist in vacuum, they need to form color singlet bound states. In recent years R. J. Fries and collaborators have developed the Hybrid Hadronization model to describe the process of quarks and gluons turning into hadrons in high energy collisions that produce such particles. The model interpolates between string fragmentation, which successfully describes hadronization in dilute systems such as e+e- or p+p collisions, and quark recombination, which seems to be active in nuclear collisions where phase space is occupied by an abundant number of quarks and gluons.

The goal of Hybrid Hadronization is a smooth, comprehensive description of hadronization across all systems, dilute or dense. The JETSCAPE framework [1] contains a module that implements Hybrid Hadronization for systems of quarks and gluons. This module has been described in previous reports. In a nutshell, for quark-antiquark pairs and (anti)quark-triplets the recombination probabilities into mesons and (anti)baryons, respectively, are computed and recombination is carried out using Monte Carlo methods. Remaining quarks and gluons form strings. Those partons tend to be far away from each other in phase space.

In the current reporting period we have carried out a systematic analysis of medium effect in Hybrid Hadronization [2]. To this end partons of different energies (simulating QCD jets) were shot through boxes of quark-gluon plasma of different length and with different collective flow velocities. This setup simulates the various situations in which QCD jets evolve and hadronize in high energy nuclear collisions. For example, in small systems a significant part of the jet shower develops outside of the system, i.e. most of the jet simply punches through the quark gluon plasma. The JETSCAPE framework was used to carry out this study.

We have found that below 10 GeV of momentum there are significant effects from thermal partons from the quark-gluon plasma recombining with partons from the jet shower. Two signature effects were found that are typically associated with recombination: an enhancement of the ratio of baryons vs mesons produced, and an overall enhancement of the number of hadrons with a flow “push” if the medium is given a collective flow velocity along the jet axis. Fig. 1 shows the enhancement of hadrons at low momentum from recombination and the flow “bump” that develops if thermal parton are given a collective velocity.

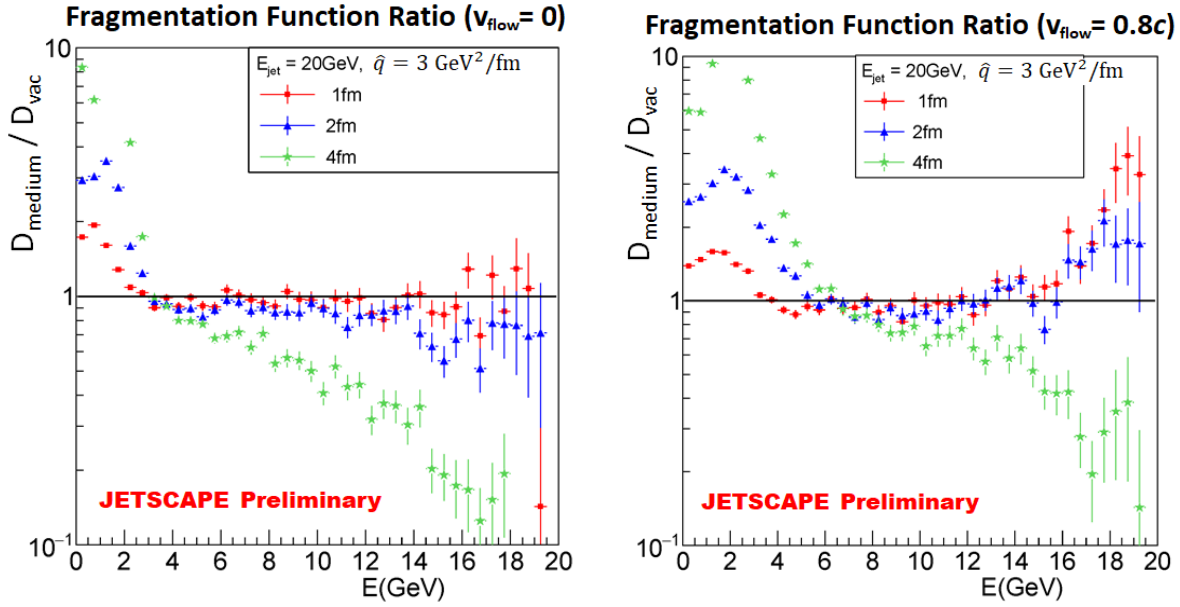

Fig. 1. Ratio of charged hadrons produced by a 20 GeV quark in medium vs vacuum as a function of hadron energy. Different medium lengths (1, 2, 4 fm are shown). Left panel: no collective motion of thermal partons. Right panel: collective velocity of 0.8 c along the jet axis for thermal partons. The suppression at large hadron energy is caused by jet quenching and is more pronounced in larger systems

[1] The JETSCAPE 3.0 package, https://github.com/JETSCAPE

[2] M. Kordell *et al.*, arXiv: 2009.03512 [nucl-th].

The JETSCAPE collaboration: X-scape and a year of first physics result

R.J. Fries, Fabian Garza, Michael Kordell, and JETSCAPE collaborators

In previous versions of this report we have discussed the inception and successful launch of the JETSCAPE collaboration and their product, a flexible and modular event generator that simulates collisions of nuclei at very high energies [1]. JETSCAPE stands for *Jet Energy-loss Tomography with a Statistically and Computationally Advanced Program Envelope*. Its initial funding consisted of $3.6M from the *Software Infrastructure for Sustained Innovation* (SI2) program of the U.S. National Science Foundation. The collaboration involves theoretical and experimental physicists, computer scientists, and statisticians at various institutions around the U.S. R. J. Fries has been a PI on this project from the first minute.

We are happy to report that in 2020 the NSF has approved the *X-Scape* project as the follow-up project for the JETSCAPE collaboration. Funded with $4M, the X-Scape project will build on the existing software framework and make it more comprehensive and powerful. The new project will allow users to simulate lower energy nuclear collisions as well as proton-nucleus and electron-nucleus collisions. Thus X-Scape will offer much needed capabilities to support experiments at the Electron-Ion Collider, the next-generation nuclear physics experiment planned by D.o.E. at Brookhaven National Laboratory for 2030 and beyond. The new project has also added more institutions and PIs to the project. Fig. 1 shows a schematic flow diagram for the X-Scape framework.

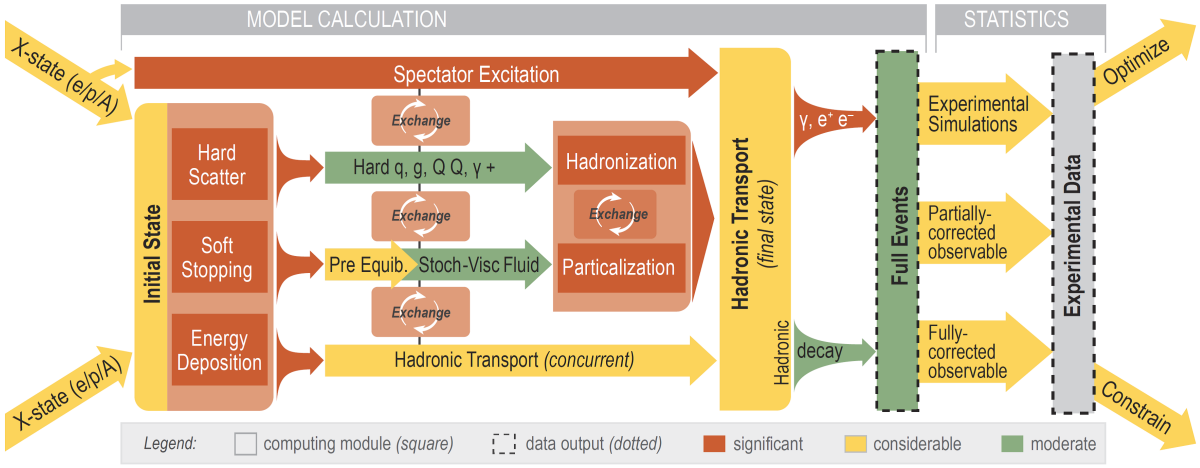

Fig. 1. Schematic Flow Diagram of the X-Scape event generator that will be able to simulate p+p, p+A, A+A, e+p and e+A collisions at high energies.

The current reporting year was also the first year where several science studies were successfully carried out by the JETSCAPE collaboration using the finished JETSCAPE framework. A comprehensive study of jets and hadrons at high momenta in p+p collisions was the first science paper published by JETSCAPE, and significant contributions were made by members of the Texas A&M group. The results have been published in 2020 [2]. Subsequently, two papers were published by JETSCAPE in Phys. Rev.

C and Phys. Rev. Lett. carrying out the most sophisticated study to date to extract parameters of the quark gluon plasma formed in high energy nuclear collisions from low-momentum experimental data, in particular the shear and bulk viscosities of quark gluon plasma [3,34. The analysis uses advanced statistical tools and also includes an estimate of uncertainties from modelling unknown details of the physical processes. Finally, JETSCAPE also published a paper with a Bayesian analysis of the jet transport parameter $\hat{q}$ [5]. This parameter determines the quenching of jet and high momentum particles in quark gluon plasma and is a major focus point of the nuclear physics programs at both the Large Hadron Collider (LHC) and the Relativistic Heavy Ion Collider (RHIC).

[1] The JETSCAPE 3.0 package, https://github.com/JETSCAPE.
[2] A. Kumar *et al.* (JETSCAPE Collaboration), Phys. Rev. C **102**, 054906 (2020).
[3] D. Everett *et al.* (JETSCAPE Collaboration), Phys. Rev. Lett. **12**6, 242301 (2021).
[4] D. Everett et al. (JETSCAPE Collaboration, Phys. Rev. C **103**, 054904 (2021).
[5] S. Cao *et al.* (JETSCAPE Collaborationi, arXiv: 2102.11337 [nucl-th]; Phys. Rev. C (accepted).

SECTION IV

RADIOCHEMISTRY

Development of a radiochronometric analysis for a radium pigment sample

J.R. Garcia[1,2] and C.M. Folden III[1,2]
[1]*Cyclotron Institute, Texas A&M University, College Station, Texas 77843*
[2]*Department of Chemistry, Texas A&M University, College Station, Texas 77843*

Radium pigments and paints were used in the early 1900s for household and military applications due to their attractive, self-luminescent properties [1-3]. Today, radium pigment and paints are no longer used because of the known biological and environmental hazards they pose [1, 3, 4]. The International Atomic Energy Agency (IAEA) has identified ^{226}Ra, the main component of activity in these samples, as a potential danger in the event of a nuclear terrorism attack [4, 5]. While no such events have been reported [5], the detonation of a radiological dispersive device (RDD) is concerning for national security. Preparatory work has been completed for a radium pigment sample to be analyzed using a nuclear forensic approach to establish a signature database for ^{226}Ra-containing samples. This will help to improve national security, as there are no such studies in the literature today.

Age determination procedures using radiochronometric techniques has been developed for this project thus far; the major goals for the radiochronometric analysis are to measure relevant chronometers using gamma spectrometry, alpha spectrometry, and ICP-MS. For this work, the ^{210}Pb/^{226}Ra and ^{210}Po/^{226}Ra chronometers were chosen, and the activity ratios were modelled over time using the Bateman equation (see Fig. 1). This preliminary model will be used in determining that age of the sample from the measured activity ratios.

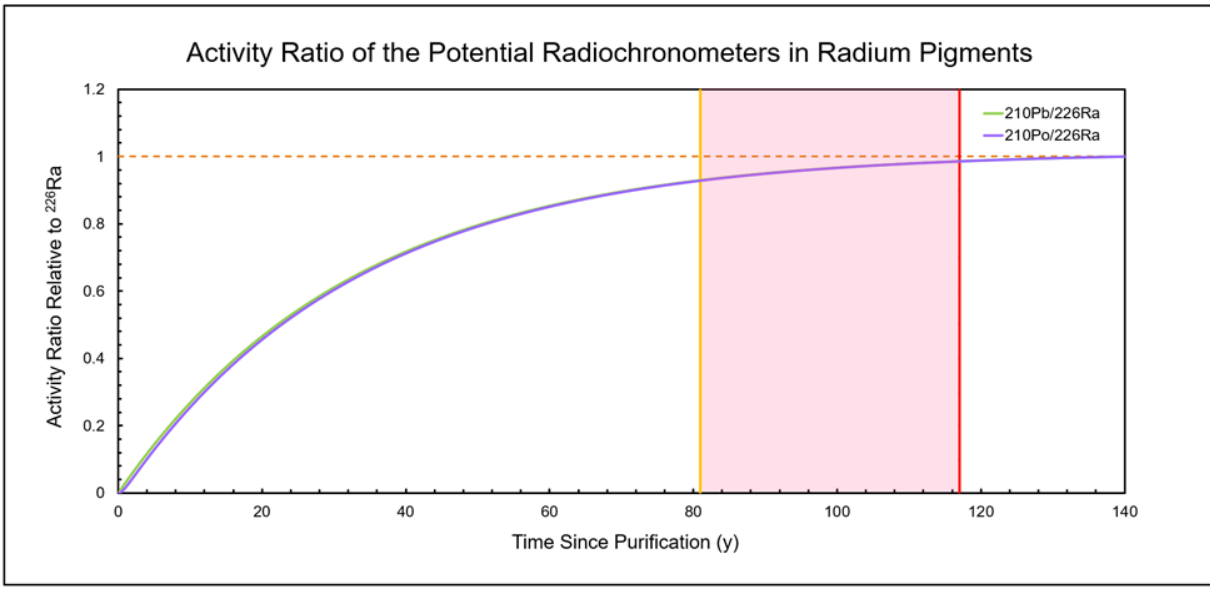

Fig. 1. Activity ratio of the potential chronometers ^{210}Po/^{226}Ra and ^{210}Pb/^{226}Ra. The red, vertical line indicates the model activity ratio of the oldest radium paint sample first patented in 1904 [6]. The orange, vertical line indiacates the model activity ratios of youngest samples (assumed to be 1940 [7]). Theoretically, every ^{226}Ra containing pigment and paint should fall within these lines (pink region).

A gamma spectrum will be collected using a high-resolution, high-purity germanium (HPGe) γ-ray spectrometer. Relevant gamma lines for this analysis correspond to the chronometer measured, ^{210}Pb/^{226}Ra (46.5 keV/186.2 keV). Similarly, alpha spectrometry can be utilized to measure the ^{210}Po/^{226}Ra chronometer. This analysis requires dissolution of the sample followed by dilution and evaporation on an aluminum planchette. Using a Canberra PIPS detector in a model 7401 single-channel alpha spectrometer, the alpha spectrum will be collected; alpha peaks of interest fall at 4.784 MeV and 5.304 MeV (^{226}Ra and ^{210}Po respectively). The measured activity ratios will be used with the model to determine the time since purification.

The number of atoms of the ^{210}Pb/^{226}Ra chronometer can be measured directly using ICP-MS. This analysis requires a separation procedure to isolate fractions of ^{210}Pb and ^{226}Ra using liquid chromatographic techniques. Dissolution of the sample has been challenging because of the contradicting chemical properties of the composition of the radium pigment [<1% RaX_2 (X=Cl or Br) and >99% ZnS]. In addition, there is no literature on the separation of RaX_2 from ZnS; however, phosphonium salts have shown promise in the dissolution of Zn and Pb sulfides under moderate conditions [8]. A mixture of tetrakis(hydroxymethyl)-phosphonium sulfate and ammonium chloride with stirring and heat (85 °C) should successfully dissolve the sample in preparation for liquid chromatography. The retention factors (k') for Ra, Ba, Pb, Po, Bi, and Zn in the mentioned liquid phase have not been published for any resin type, and thus these values will be measured and applied for separation. The measured atom ratio of ^{210}Pb/^{226}Ra can be used to determine activty and then applied to the model to determine the time since purification.

The procedure has been developed and will be tested beginning with the dissolution and determination of k' values for elements mentioned above in various resins. Once the basic foundations are developed for this project, the work will proceed with radiochronometric analysis of the radium pigment sample.

[1] D.I. Harvie, Endeavour **23**, 100 (1999). doi:10.1016/S0160-9327(99)01201-6
[2] H.A. Taylor, Sci. Am. **137**, 430 (1927).
[3] R.G.M. Crockett and G.K. Gillmore, Geol. Soc. Spec. Publ. **451**, 49 (2018). doi:10.1144/sp451.4
[4] D.G. Kelly and T. Mumby, Health Phys. **117**, 278 (2019). doi:10.1097/hp.0000000000001099
[5] S. Friedrich, R. Stan, and Z. Lyudmila, AIP Conf. Proc. **1034**, 3 (2008). doi:10.1063/1.2991254
[6] G.F. Kunz, (1905). U.S. patent number:789811
[7] M. Vobecký, Czechoslov. J. Phys. **49**, 35 (1999). doi:10.1007/s10582-999-0004-9
[8] A. Hussein and H. Mohamed, Int. J. Corros. Scale Inhib. **6**, 349 (2017). doi:10.17675/2305-6894-2017-6-3-9

Iridium and rhodium adsorption on functionalized silicon chips for the future study of meitnerium chemistry

Vira Zakusilova,[1,2] Evgeny E. Tereshatov,[2] and C.M. Folden III[2,3]
[1]*Université de Strasbourg, CNRS, IPHC, UMR 7178, F-67000 Strasbourg, France*
[2]*Cyclotron Institute, Texas A&M University, College Station, Texas 77843*
[3]*Department of Chemistry, Texas A&M University, College Station, Texas 77843*

One of the first attempts to coat silicon detectors with gold was reported during the chemical characterization of element 112, Cn. This resulted in better chemical sorption of this heavy element on the modified surfaces rather than on a non-modified surface [1]. However, element 113, Nh, showed an enhanced reactivity towards gold, which prevented the proper chemical characterization of this element [2]. Therefore, a need for new chemically modified silicon detectors has emerged. Such detectors should selectively bind the atoms of interest but with weaker interactions.

The formation of thiolate self-assembled monolayers (SAMs) on gold is a well-known approach to the functionalization of gold surfaces. SAMs are arrangements of molecules that can be spontaneously adsorbed on solid surfaces from a solution or a vapor phase [3]. In this work, the functionalization of gold-coated silicon chips with 1-(11-Mercaptoundecyl)imidazole (Im-C_{11}-SH) SAMs has been

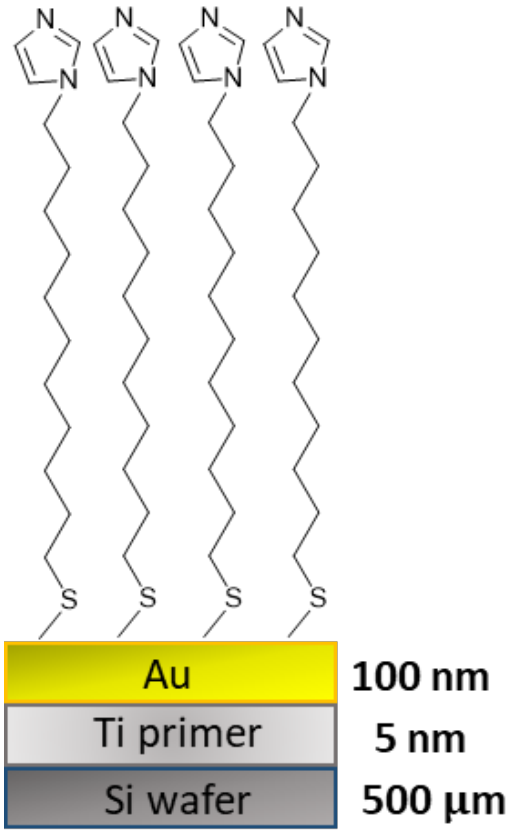

Fig. 1. Schematic diagram of the substrate investigated in this study.

investigated. This thiol is a commercially available compound and has already been used to form SAMs on gold surfaces [4]. The experiments were conducted on 1 cm^2 silicon chips covered with a 5 nm titanium adhesion layer and coated with 100 nm of gold. A schematic diagram of the corresponding substrate is shown in Fig. 1.

We are interested in studying the chemical properties of iridium and rhodium because it will help us better understand the chemistry of meitnerium which is believed to belong to Group 9 of the periodic table. Im-C_{11}-SH was chosen as the closest analogue of imidazolium-based ionic liquids that have already been used to extract metals, in particular iridium from hydrochloric acid solutions [5].

The functionalized surfaces were characterized using several techniques. Atomic force microscopy was used to evaluate the roughness of pure gold and substrates with SAMs. The average roughness of pure gold is on the order of 1-2 nm. The roughness remains in the same range after the SAMs deposition. The average surface coverage with Im-C_{11}-SH SAMs was measured using cluster secondary-ion mass spectrometry (SIMS). SAMs were found to cover up to 99.5% of the gold surface when being deposited from a 5 mM ethanolic thiol solution, which indicates quantitative adsorption. X-ray photoelectron spectroscopy was used to study the chemical state of SAMs. The sulfur 2p XPS spectrum of a fresh sample displayed in Fig. 2 contains primarily a spin-orbit split doublet with S $2p_{3/2}$

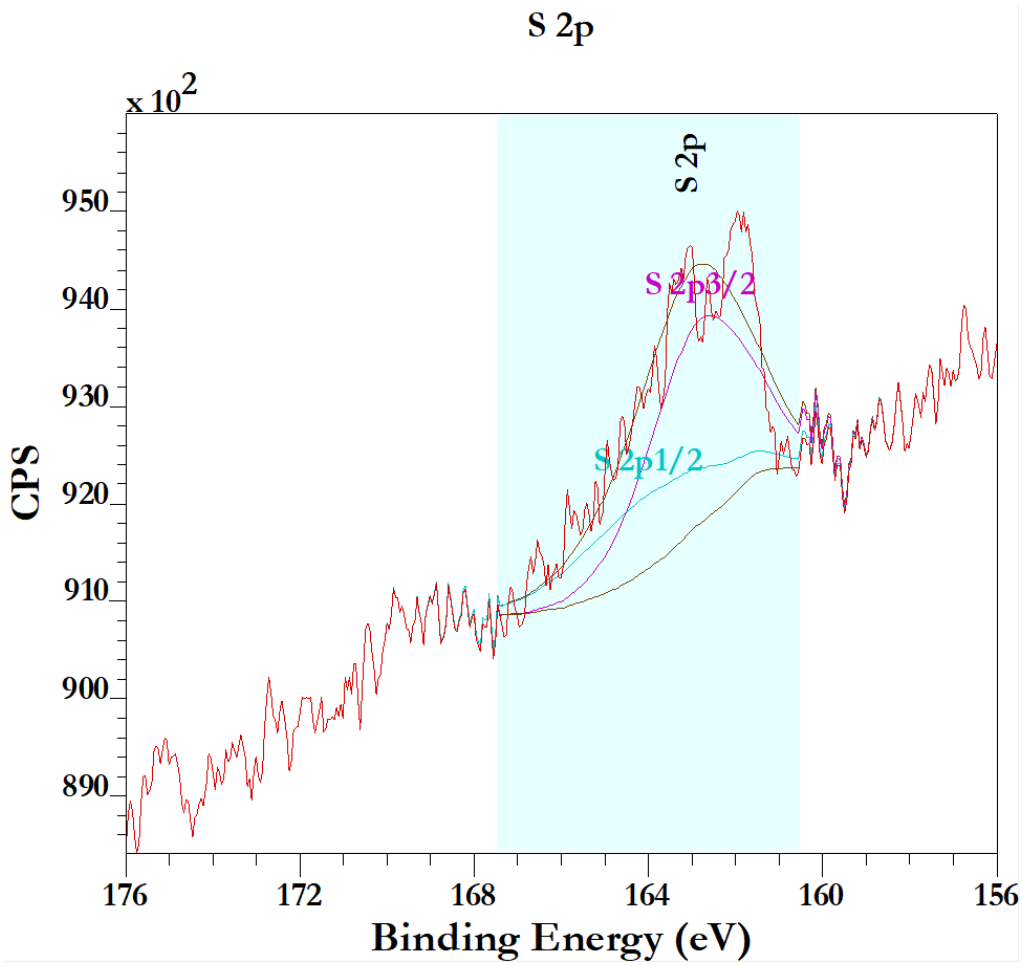

Fig. 2. XPS of S 2p region of Im-C_{11}-SH SAMs on gold.

component at 162.8 eV which corresponds to a thiol bound to gold [6]. H_2O_2-mediated liquid UV-light photooxidation treatment was employed to remove thiolate SAMs. The XPS spectra showed that peaks of S 2p and N 1s disappear after the removal of thiols. This means the gold-coated silicon chips can be reused. Also, the effect of aging was studied by recording XPS spectra over time. The results illustrated that SAM-functionalized surfaces remain stable for at least 1 week of sample storage in wafer carrier trays wrapped with aluminum foil under ambient laboratory conditions.

Ellipsometry was used to determine the thickness of SAMs, which was found to be 1.690±0.014 nm. This result indicates the presence of a single monolayer on the surface of gold and is in good agreement with the literature results obtained for similar films [7, 8]. Neutron activation analysis (NAA) showed that iridium can be adsorbed from 2% hydrochloric acid solution on functionalized gold-coated silicon chips with a sorption efficiency of approximately 77%. The results for rhodium are still being analyzed. SIMS was also employed to study which types of iridium and rhodium chloro-complexes are bound to Im-C_{11}-SH SAMs during the metal deposition. These results are still being analyzed.

A paper based on this project is under preparation and will be finalized after analyzing the NAA and SIMS data.

[1] R. Eichler *et al.*, Nature **447**, 72 (2007). doi:10.1038/nature05761

[2] S.N. Dmitriev *et al.*, Mendeleev Commun. **24**, 253 (2014). doi:10.1016/j.mencom.2014.09.001

[3] C. Vericat, M.E. Vela, G. Benitez, P. Carro, and R.C. Salvarezza, Chem. Soc. Rev. **39**, 1805 (2010). doi:10.1039/B907301A

[4] H.S. Kato, S. Yoshimoto, A. Ueda, S. Yamamoto, Y. Kanematsu, M. Tachikawa, H. Mori, J. Yoshinobu, and I. Matsuda, Langmuir **34**, 2189 (2018). doi:10.1021/acs.langmuir.7b03451

[5] N. Papaiconomou, I. Billardde, and E. Chaine, RSC Adv. **4**, 48260 (2014). doi:10.1039/c4ra06991a

[6] *XPS Reference Table Of Elements*, available at https://xpssimplified.com/elements/sulfur.php.

[7] D.A. Offord, S.B. Sachs, M.S. Ennis, T.A. Eberspacher, J.H. Griffin, C.E.D. Chidsey, and J.P. Collman, J. Am. Chem. Soc. **120**, 4478 (1998). doi:10.1021/ja9735281

[8] M. Prato, R. Moroni, F. Bisio, R. Rolandi, L. Mattera, O. Cavalleri, and M. Canepa, J. Phys. Chem. C **112**, 3899 (2008). doi:10.1021/jp711194

System improvements to produce astatine-211

L.A. McIntosh, G.C. Tabacaru, R. Burch, J.D. Burns, A. Hannaman, A. Hood, G. Kim, K.N. Lofton, B. Roeder, L.A. McCann, S. Schultz, E.E. Tereshatov, A. Vonder Haar, and S.J. Yennello

Astatine-211 shows promise for cancer treatments when connected to a targeting agent such as a monoclonal antibody, especially for non-localized cancers [1]. With the advent of such targeting agents, the major impediment to its use in clinical trials remains the availability of production and reliable separation chemistry [2]. We have made improvements to our ability to reliably produce ^{211}At at the Cyclotron Institute using the (α,2n) reaction at 28.8 MeV on a ^{209}Bi target. In the past year, we have added two graduate students to our team, expanded our collaborative footprint, improved the amount and stability of alpha beam available to produce astatine-211, made a detector to help monitor the beam current on target, experimented in target production methods (see McCann's contribution to this report), and improved detection methods to support a safe target extraction.

We produced astatine-211 on six occasions over the past year. A summary of the amount of beam available, length of irradiation, and total amount of astatine-211 produced during each of the runs is shown in Table I. The asterisk for the amount produced in December 2020 is because the target melted during this irradiation, and the amount of activity had to be estimated by a different means than the other runs. The targets were transferred to Radiochemical Lab 118 within the Cyclotron Institute, where the target was dissolved in HNO_3 and radiochemical experiments were carried out, which are described in reports by Burns and Tereshatov.

Table 1. Bombardments and amount of astatine-211 produced in each bombardment in the past year. The irradiations shaded blue occurred with the target 10 degrees from the beam, and the green rows occurred with the target at 80 degrees from the beam.

Irradiations	Highest Instantaneous Beam Current (pμA)	Average Beam Current (pμA)	Irradiation Length (h)	At-211 Activity at EoB (mCi)
June 2020	4.5	2.1 (Unstable)	9.4	8.0 ± 1.3
August 2020	2.6	2.4	9.6	21 ± 2
September 2020	7.4	5.1	7.3	22 ± 2
October 2020	5	4 .0	7.9	12 ± 1
November 2020	7.2	4.2	9.7	24 ± 2
December 2020	6.8	4.8	13.6	47 ± 5*

To investigate the uniformity of the beam at the target position, a segmented Faraday Cup-Viewer was assembled. The body is made of 3D-printed plastic, with 37 brass screws arranged at regular intervals, as shown in the right of Fig. 1. Each of these screws acts as a small Faraday Cup, from which

beam current can be read via a LabView program, as shown on the left in Figure 1. The body of the viewer was coated with adhesive and CdS, which caused it to phosphoresce in the presence of beam (right of Fig. 1). This gives a much more detailed view of where the beam is situated on the target. A more uniform beam on the target should lead to fewer melted targets.

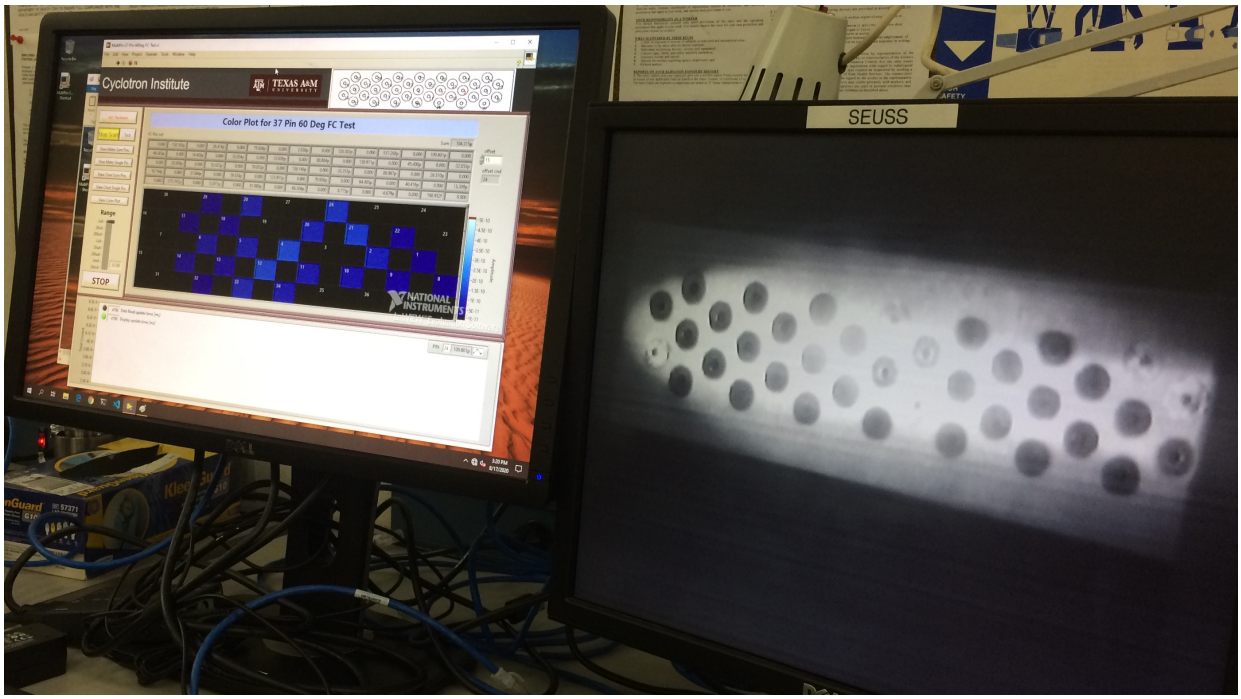

Fig. 1. Photograph of Segmented Faraday Cup-Viewer (SFCV) being used to tune the alpha beam. The SFCV is 3D printed, with 37 screws which are wired to read the beam current at each disparate position across the target position. The surface has material adhered to it which phosphoresces in the presence of the beam. On the right is a video feed of the SFCV with alpha beam on the target position. On the left is the LabView program reading in the beam current off of each of the disparate screws.

Another [illegible] ically [illegible] m the rest of the beamline, so th[illegible] an be [illegible] entire overnight irradiation. Thi[illegible] y Cups [illegible] w much beam is being delivere[illegible] get duri[illegible] target from the December 202[illegible] 2.

Anoth[illegible] isotope [illegible] ety of those who

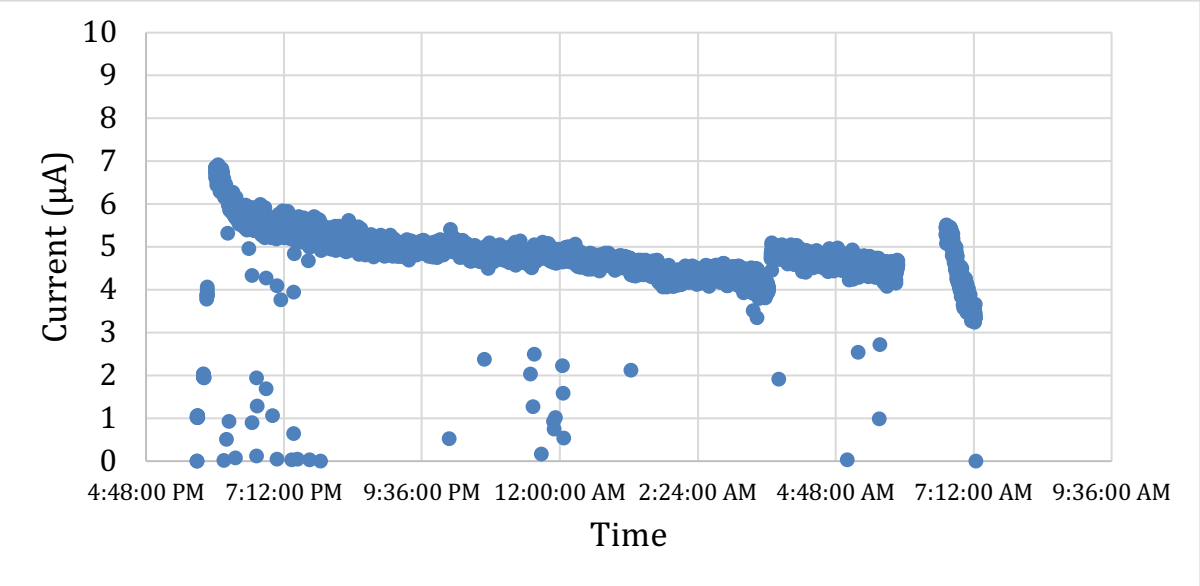

Fig. 2. Integrated alpha beam current on targetduring the overnight irradiation, December 2020.

Two High Purity Germanium (HPGe) detectors are used to measure the hundreds of liquid samples that are produced during the separation chemistry. A spectrum of one sample containing astatine-211 is shown in Fig. 4. Below 100 keV, there are many x-rays. The characteristic γ-ray of ^{211}At is pointed out at 687 keV. The two γ-rays of 211Po are also labeled at 569 and 897 keV. The other two γ-rays belong to unknown radiochemical species, which are separated out by the separation chemistry, but merit further investigation.

The astatine-211 team plans to build on this success and continue to expand our collaborations within TAMU and outside of the University in the next year.

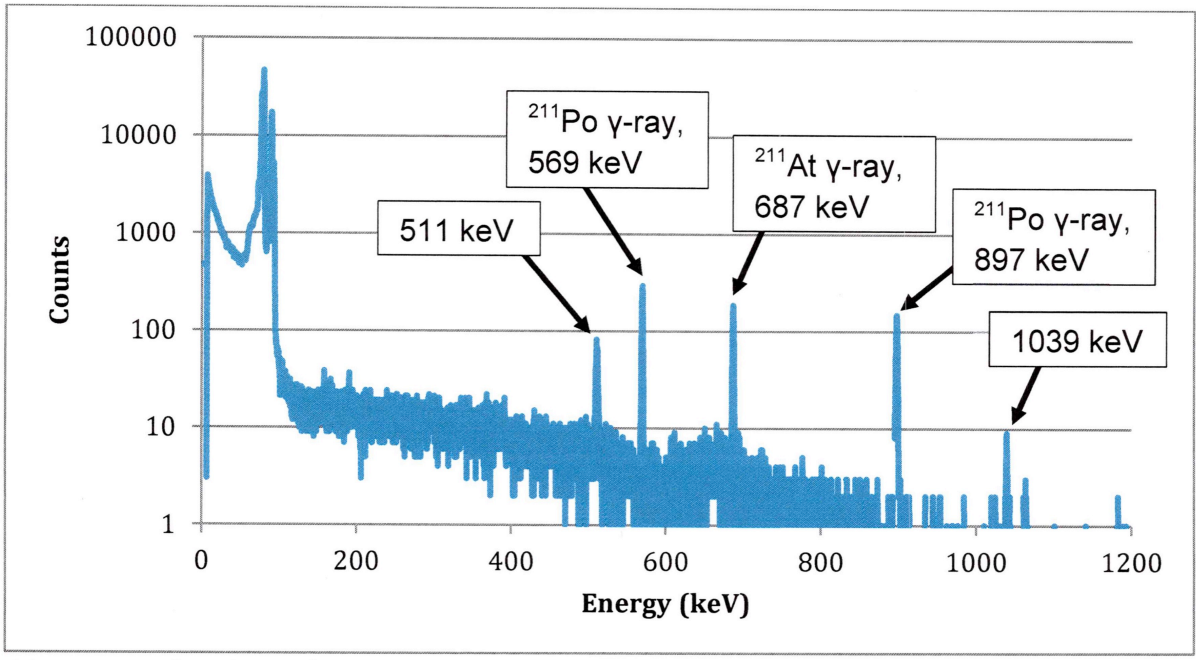

Fig. 4. HPGe spectrum of an aliquot of target dissolved solution, containing the characteristic gamma-rays from astatine-211 and its decay daughter polonium-211. The gamma-rays at 511 and 1039 keV are contributed to by gallium-66.

[1] J. Elgqvist, S. Frost, J. Pouget, and P. Albertsson, Frontiers in Oncology **3**, 1 (2014).

[2] M.R. Zalutsky and M. Pruszynski, Current Radiopharmaceuticals **4**, 177 (2011).

.

Astatine chemistry: Separation, purification, and fundamental science

J.D. Burns, E.E. Tereshatov, K.J. Glennon, A. Hannaman, K.N. Lofton, L.A. McCann, L.A. McIntosh, S.J. Schultz, G.C. Tabacaru, A.L. Vonder Haar, and S.J. Yennello

Targeted alpha therapy (TAT) drugs [1-11] have gained a large amount of interest following the success of Xofigo® [12], based on the α-emitting $^{223}RaCl_2$, in treating metastatic castration-resistant prostate cancer. The promising performance of Xofigo® has illustrated the need to expand the catalog of α-emitting radionuclides available for use [9]. One such isotope which has drawn a great deal of attention is ^{211}At, having well-suited decay properties for clinical settings, with a moderately-short half-life of 7.2 h and a quantitative α-emission from a simple decay scheme [13]. Roughly 30 cyclotrons possessing the ability to generate usable quantities world-wide. Only seven of them are located in the US, only one of which is currently a supplier for the US Department of Energy's Isotope Program [8], so the supply of ^{211}At remains limited. Bombardment of natural Bi targets with an α-particle beam in the energy range of 28.5–31 MeV has been adopted as the standard for generating usable quantities of ^{211}At via the ^{209}Bi(α,2n)^{211}At nuclear reaction [13-17]. Despite the low availability, ^{211}At has been used in a number of clinical trials investigating the treatment of malignant brain tumors [18], ovarian cancer [10], and a current study treating advanced hematopoietic malignancies [2].

The near quantitative separation, purification, and recovery of ^{211}At has been demonstrated at Texas A&M University's Cyclotron Institute through an extraction chromatography process which utilizes porous beads impregnated with 3-octanone, resulting in an elution yield of 92–95% (see Fig. 1) [19]. Moreover, the rapid nature of this process, less than 20 min, was achieved after dissolution of a Bi

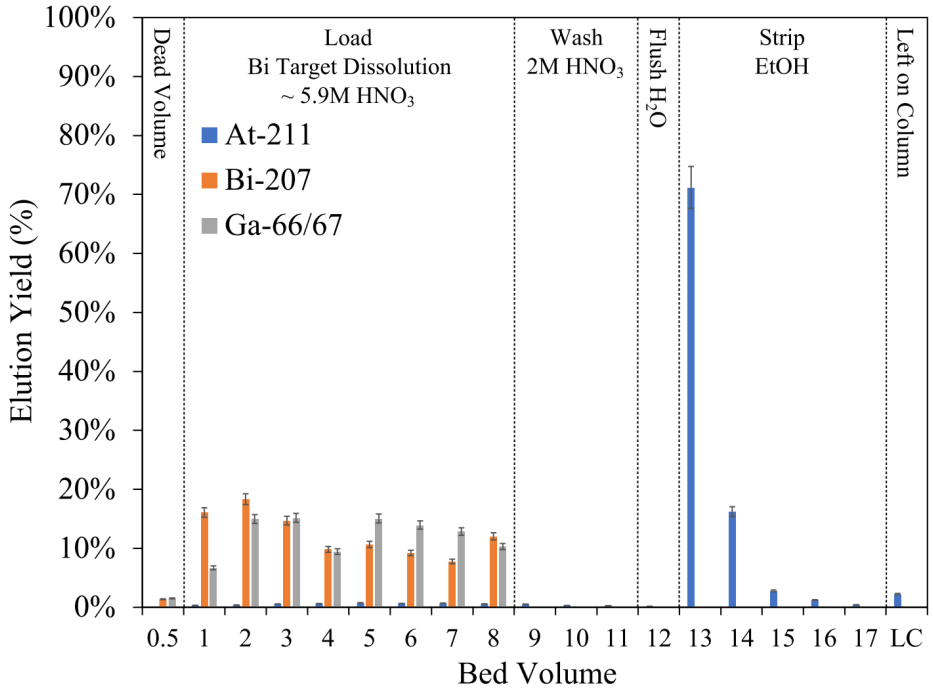

Fig. 1. Chromatogram of a dissolved bombarded target solution with a 3-octanone impregnated Amberchrom® CG300M resin bed (0.5-mL BV, 7 mm ID × 13 mm height). Adapted from Burns *et al*. [19].

metal target in HNO_3 following retrieval from the beamline after α-particle bombardment. The solution was directly loaded onto the column with no volume or acidity adjustment. The column was washed with HNO_3 and H_2O, and ^{211}At was eluted with ethanol, collecting roughly 87–93% in 1 mL. This process of recovering high purity ^{211}At, in near quantitative yields, represents a significant advance in At separations and purification.

The development of the efficient extraction chromatography process was based on gaining a fundamental understanding of how the At behaves in nitric acid systems. Through a collaboration with Michael Hall in the Department of Chemistry experimental data was coupled with theoretic computational chemistry to develop new insights into At chemistry. These studies showed that At exists in the trivalent oxidation state as the AtO^+ species in aqueous nitric acid system. The heavy-element nature of At, and the induced spin-orbit coupling, has a significant effect on the electronic structure of the AtO^+ molecular cation, which assumes a pseudo-closed-shell electronic configuration. This closed-shell configuration leads to an enhanced interaction with ketone molecules through a slightly covalent interaction between the sp^2 hybrid lone pair of the carbonyl oxygen and the lowest unoccupied molecular orbital (LUMO), a non-degenerate π* orbital, of the AtO^+, as shown in Fig. 2 [17].

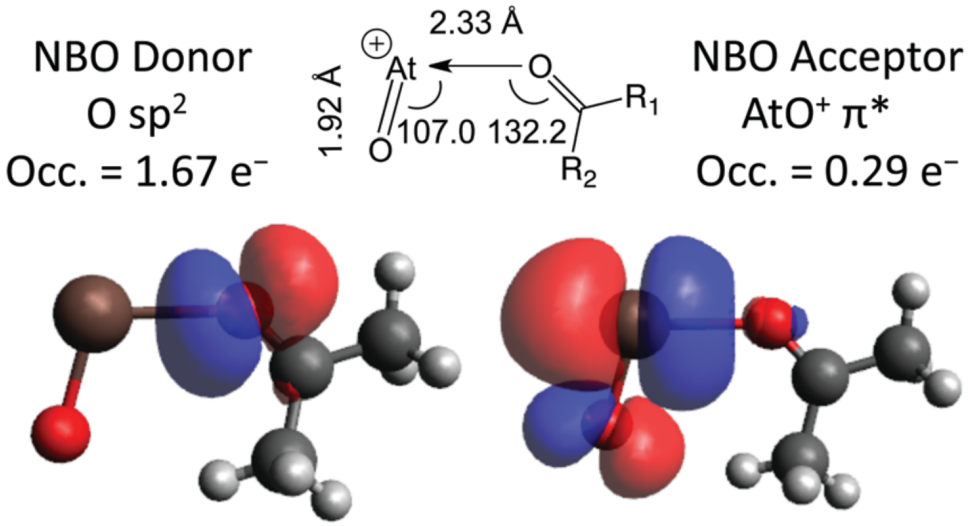

Fig. 2. The DFT geometry for the singlet state of the AtO^+ acetone complex (top center) shows a strongly bent structure that suggests an At–O bond formed from the donation of a lone pair (sp^2) into the π* orbital of AtO^+. The natural bond orbital (NBO) analysis of this AtO^+ acetone complex confirms a donor–acceptor bond in which ~0.3 electrons are donated from the lone pair (left) to the previously empty AtO^+ π*orbital (right). Adapted from Burns *et al*. [17].

Forward looking, efforts will continue to investigate the AtO^+ interaction with the ketone functionality more thoroughly to further enhance the separation and purification of ^{211}At. This should lead to a better understanding of the fundamental properties of AtO^+, which, in turn, will expand the currently limited knowledgebase of At chemistry. Broader impacts of this work include, not only enhancing basic understanding of At chemistry, but also contributing to an increase in the availability of this important isotope.

[1] M. Makvandi, E. Dupis, J.W. Engle, F.M. Nortier, M.E. Fassbender, S. Simon, E.R. Birnbaum, R.W. Atcher, R.K.D. John, O. Rixe, and J.P. Norenberg, Target. Oncol. **13**, 189. (2018).

[2] Y. Li, D.K. Hamlin, M.-K. Chyan, R. Wong, E.F. Dorman, R.C. Emery, D.R. Woodle, R.L.Manger, M. Nartea, A.L. Kenoyer, J.J. Orozco, D.J. Green, O.W. Press, R. Storb, B.M. Sandmaier, and D.S. Wilbur, PLoS One **13**, e0205135 (2018).

[3] R.M. Lambrecht and S. Mirzadeh, Int. J. Appl. Radiat. Isot. **36**, 443 (1985).

[4] E.L.L. Johnson, T.G.G. Turkington, R.J.J. Jaszczak, D.R.R. Gilland, G. Vaidyanathan, K.L.L. Greer, R.E.E. Coleman, and M.R.R. Zalutsky, Nucl. Med. Biol. **22**, 45 (1995).

[5] Y. Dekempeneer, M. Keyaerts, A. Krasniqi, J. Puttemans, S. Muyldermans, T. Lahoutte, M. D'huyvetter, and N. Devoogdt, Expert Opin. Biol. Ther. **16**, 1035 (2016).

[6] F. Kraeber-Bodéré, C. Rousseau, C. Bodet-Milin, C. Mathieu, F. Guérard, E. Frampas, T. Carlier, N. Chouin, F. Haddad, J.-F. Chatal, A. Faivre-Chauvet, M. Chérel, and J. Barbet, Int. J. Mol. Sci. **16**, 3932 (2015).

[7] J. Elgqvist, S. Frost, J.-P. Pouget, and P. Albertsson, Front. Oncol **3**. 324 (2014).

[8] M.R. Zalutsky and M. Pruszynski, Curr. Radiopharm. **4**, 177 (2011).

[9] D.S. Wilbur, Curr. Radiopharm. **4**, 214 (2011).

[10] H. Andersson, E. Cederkrantz, T. Back, C. Divgi, J. Elgqvist, J. Himmelman, G. Horvath, L. Jacobsson, H. Jensen, S. Lindegren, S. Palm, and R. Hultborn, J. Nucl. Med. **50**, 1153 (2009).

[11] M.R. McDevitt, G. Sgouros, R.D. Finn, J.L.Humm, J.G. Jurcic, S.M. Larson, and D.A. Scheinberg, Eur. J. Nucl. Med. Mol. Imaging **25**, 1341 (1998).

[12] P.G. Kluetz, W. Pierce, V.E. Maher, H. Zhang, S. Tang, P. Song, Q. Liu, M.T. Haber, E.E. Leutzinger, A. Al-Hakim, W. Chen, T. Palmby, E. Alebachew, R. Sridhara, A. Ibrahim, R. Justice, and R. Pazdur,. Clin. Cancer Res. **20**, 9 (2014).

[13**]** M.R. Zalutsky, D.A. Reardon, O.R. Pozzi, G. Vaidyanathan,and D.D. Bigner, Nucl. Med. Biol. **34**, 779 (2007).

[14] J.D. Stickler and K.J. Hofstetter, Phys. Rev. C **9**, 1064 (1974).

[15] D. Wilbur, Curr. Radiopharm. **1**, 144 (2008).

[16] G. Lucignani, Eur. J. Nucl. Med. Mol. Imaging **35**, 1729 (2008).

[17] J.D. Burns, E.E. Tereshatov, M.A. McCarthy, L.A. McIntosh,G.C. Tabacaru, X. Yang, M.B. Hall, and S.J. Yennello, Chem. Commun. **56**, 9004 (2020).

[18] M.R. Zalutsky, D.A. Reardon, G. Akabani, R.E. Coleman, A.H. Friedman, H.S. Friedman, R.E. McLendon, T.Z. Wong, and D.D. Bigner, J. Nucl. Med. **49**, 30 (2008).

[19] J.D. Burns, E.E. Tereshatov, G. Avila, K.J. Glennon, A. Hannaman, K.N. Lofton, L. McCann, M.A. McCarthy, L.A. McIntosh,S.J. Schultz, G.C. Tabacaru, A.L. Vonder Haar, and S.J. Yennello, Sep. Purif. Technol. **256**, 117794 (2021).

Natural bismuth target production and characterization to produce astatine-211

L.A. McCann, K.N. Lofton, F. Abegglen, J.D. Burns, L.A. McIntosh, H. Peeler,
S. Schultz, G.C. Tabacaru, E.E. Tereshatov and S.J. Yennello

Targeted alpha therapy (TAT) is an emerging field in cancer treatment research due to the ability to directly target cancer cells while minimizing damage to surrounding healthy cells. Several radioisotopes have been identified as showing great promise for this research. Astatine-211 is a promising candidate because of its simple alpha decay chain and short 7.2-hour half-life, ideal for biological systems. It is primarily produced via the $^{209}Bi(\alpha,2n)^{211}At$ reaction using a 28.8 MeV alpha beam [1]. Keeping the bismuth target intact poses one of the greatest challenges for astatine production. Bismuth has a relatively low melting point—only 270°C—which means the energy deposited by the beam can melt the target during irradiation [1]. This melting process alters the geometry of the irradiated bismuth (reducing total astatine production) and can cause the astatine to volatilized. To prevent melting of the bismuth targets, we have made significant advancements in the cooling of the bismuth target during irradiation by removing interfaces between the chilled water and the target. The current design uses a single jet, chilled water system flowing directly on the back of the target frame. Additionally, many efforts are being made to produce the optimal targets for irradiation and subsequently characterize them for integrity and impurities.

Bismuth targets are produced in-house by astatine production facilities and are made by a variety of facility-dependent methods. In an effort to develop a target-making procedure compatible with our

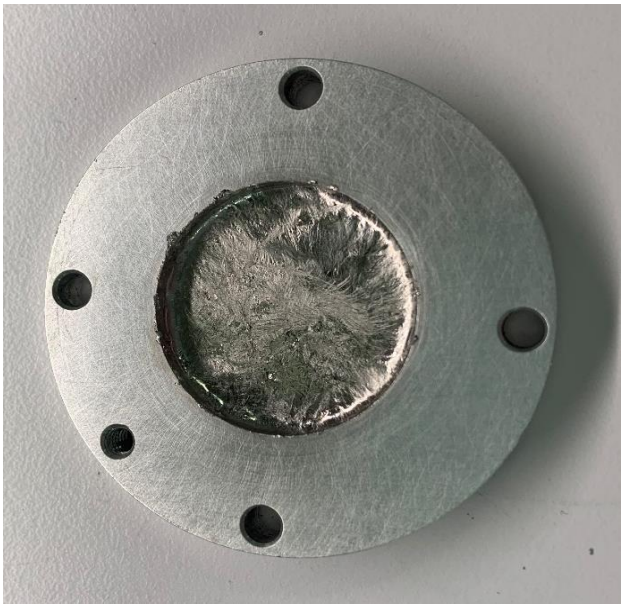

Fig. 1. Bismuth target produced by melting bismuth pellets into the aluminum frame at 310°C and spread with a ceramic spatula to evenly cover the surface. This is a thicker target, with a mass of 2.425 g of bismuth and an average thickness of 625 microns. This target was not used for irradiation.

facility, bismuth was molten into a solder pot (initially containing flux to aid in the melting. The flux was eventually discontinued due to potential impurities) and then pressed into the target frame with a machine press. Additional bismuth was removed through machining the surface of the target. While the use of a solder pot to melt bismuth and the use of the machine press to flatten the targets is still being explored, alternate methods based on procedures in use at other programs were also attempted.

In accordance with the procedure used at the University of Washington [2], another target-making process involved the melting of bismuth metal on a thin aluminum target frame on a hot plate. The bismuth is then spread evenly around the frame using a ceramic spatula (completed target shown in Fig. 1).

Another method attempted was adapted from the procedure used at the University of Pennsylvania [3], in which a heated block is pressed onto the molten bismuth to spread it into the target frame on the hot plate, rather than spread with a ceramic spatula. This method resulted in very uneven targets with a bismuth oxide crystalline surface when it was attempted at our facility (shown in Fig. 2).

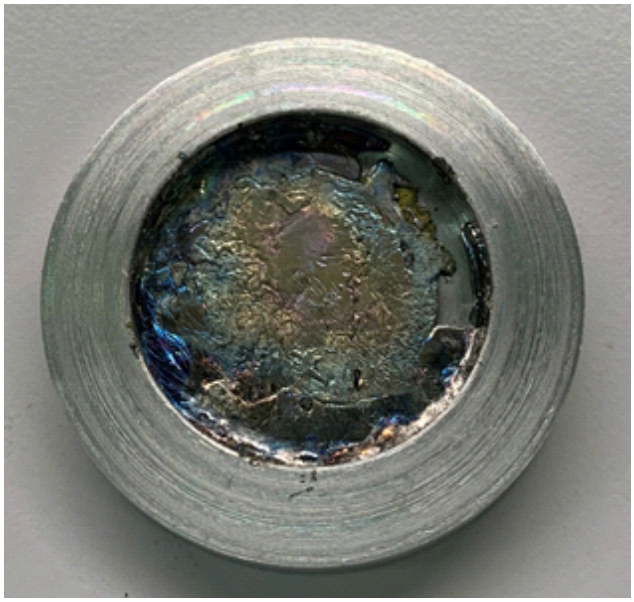

Fig. 2. Bismuth target produced by melting bismuth pellets into the aluminum frame at 310°C and pressed with a heated stainless-steel weight with aluminum foil in between the weight and melted bismuth. The weight and foil were removed while the target was still hot, to prevent adhesion to the surface. The bismuth did not spread fully over the surface, and a colorful bismuth oxide crystalline layer formed on the surface. The total mass of bismuth is 2.649 g, with an average thickness of 210 microns. This target was not used for irradiation.

To increase the surface interaction and conductivity between the bismuth and aluminum interface, an ultrasonic soldering iron (S-Bonder SB-9210, *S-Bond Technologies, LLC, Hatfield, PA 19440*) was used in addition to the hot plate. This method resulted in a noticeably stronger adhesion of the bismuth to the aluminum surface and allowed thinner targets, on the order of 50-100 microns, to be produced (shown

in Fig. 3). Since the alpha particles only have enough energy to produce astatine in the first 70 μm of the bismuth, targets thicker than this are absorbing the alpha energy as heat, further contributing to melting. The thinner targets produced by the ultrasonic soldering iron show promise for maximum production as well as decreased melting due to the strong bismuth-aluminum interface and 70 μm target depth.

Fig. 3. Bismuth target produced by melting bismuth pellets on a hot plate at 300°C and spreading the bismuth using an ultrasonic soldering iron. The surface is mostly smooth with some ridges and valleys. It has a mass of 0.258 g of bismuth and an average thickness of 66 microns. This target was not used for irradiation.

The presence of air bubbles and holes throughout the bismuth targets is another potential initiator of the melting process, as they can create hot pockets within the target when irradiated. Additionally, the presence of any impurities with lower melting points may also lead to melting of the target. To identify some of these imperfections, characterization of the targets via scanning electron microscopy coupled with energy dispersive x-ray spectroscopy (SEM-EDS) was performed. Figures 4a and 4b show some of the topographical imperfections in the target surface taken via SEM imaging. These images demonstrate the variability in the target surface within the same target. A subsequent EDS analysis indicates primarily the presence of oxygen, carbon, bismuth, and aluminum on the target. The most important of these elements is oxygen, which could indicate the presence of bismuth or aluminum oxide within the target. This oxide is particularly unwanted due to the nuclear reaction of oxygen with the alpha particles, resulting in the production of fluorine-18. These oxide impurities will likely be reduced through the use of the ultrasonic soldering iron.

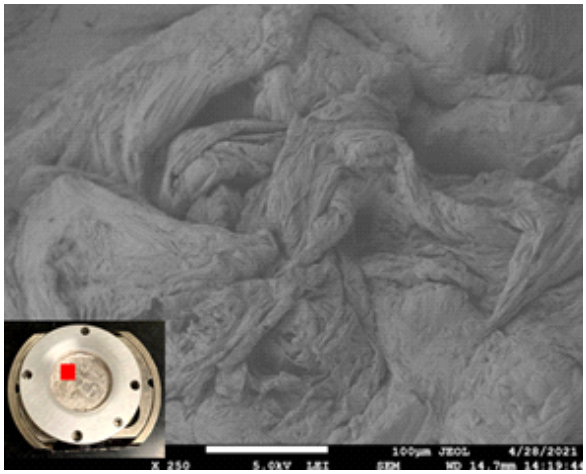

Fig. 4a. SEM image of part of the surface of a target produced by the spatula spreading method. The ridges and nonuniformities in the target surface from spatula spreading can be seen clearly.

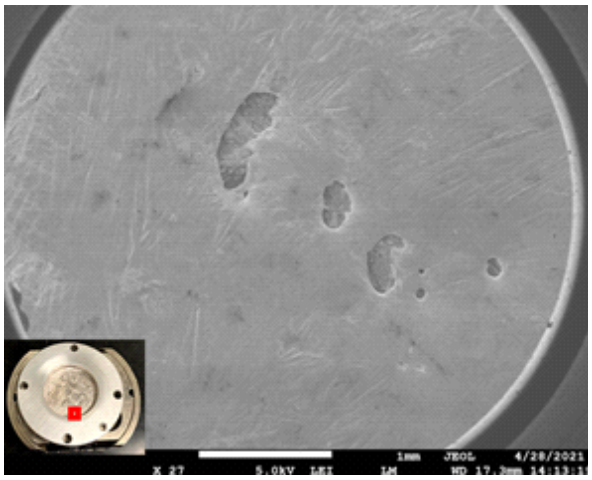

Fig. 4b. SEM image of another part of the surface of the same target produced by the spatula spreading method. A clear image of holes in the target surface that cannot be seen with visual inspection.

Many advancements in target production and characterization have been made to increase the total production of astatine-211. To combat the melting of bismuth targets, many improvements to the cooling and the integrity of the targets have already been made. The targets and the production process are continually being studied and optimized to forward the isotope production capabilities of the Cyclotron Institute.

[1] M.R. Zalutsky and M. Pruszynski, Curr. Radiopharm. **4**, 177 (2011).
[2] K. Gagnon *et al.,* J. Labelled Compd. Radiopharm. **55**, 436 (2012).
[3] University of Pennsylvania, personal communication.

.

Separation of astatine and bismuth upon extraction into conventional solvents

Evgeny E. Tereshatov, Jonathan D. Burns, Amy L. Vonder Haar, Lauren A. McIntosh, Gabriel C. Tabacaru, Laura A. McCann, Steven J. Schultz, Geoffrey Avila, Andrew Hannaman, Mallory A. McCarthy, Kylie N. Lofton, and Sherry J. Yennello

Astatine is one of the least chemically studied elements of the periodic table. Chemical knowledge about fundamental properties of this element is limited due to absence of any stable astatine isotopes. The longest half-lives are 8.3 h and 7.2 h for ^{210}At and ^{211}At, respectively. It should be mentioned that ^{211}At also attracts attention of chemical and medical communities because of its convenient decay mode for α-emitting therapy. The main route to produce medically relevant amounts of astatine-211 activity is the ^{209}Bi(α, 2n)^{211}At reaction [1]. The energy of the α-beam must be carefully controlled near 28 MeV, leading to 0.9 barn of ^{211}At cross section, to avoid production of radiotoxic ^{210}At [2].

Here we focus on the astatine behavior of the nitric media. Usually, Bi target dissolution is performed at ~10 M HNO_3. Based on current understanding of astatine behavior in this solution, there is a mixture of at least two cationic species, monovalent At^+ and trivalent AtO^+ [3, 4]. The vast majority of organic molecules have been applied to extract astatine like alkanes (including chloro-derivatives) and oxygen containing solvents (ether, alcohol, and ketone) [5-8]. The goal of this work is to study fundamental behavior of both astatine and bismuth upon transfer from nitric acid media to conventional solvents, 1-octanol and methyl anthranilate.

The bismuth extraction from nitric acid media to 1-octanol has been studied in experiments utilizing liquid-liquid extraction technique. Fig. 1 shows dependency of Bi distribution ratio values on the aqueous equilibrium concentration of nitric acid. It can be seen that despite the fact that all D-values are below 0.1, there is a clear increasing trend with increase of acidity. To understand the mechanism of Bi

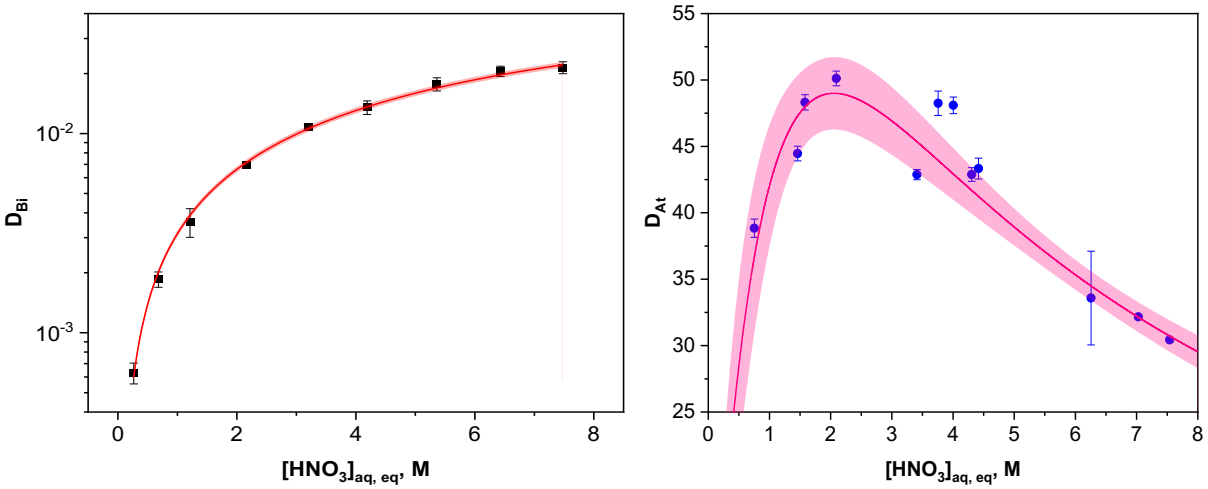

Fig. 1. Distribution ratio values of Bi (left) and At (right) as a function of aqueous equilibrium nitric acid concentration upon extraction into 1-octanol. Lines are fit according to a distribution ratio definition. Shade represents 95% confidence interval.

extraction and as a result to fit experimental data in Fig.1, a mathematical model must be developed. This model is based on a definition of distribution ratio value and Bi speciation in the nitric acid media.

Only one species in the aqueous, namely $Bi(NO_3)_3$, can be extracted into 1-octanol in order to maintain the charge balance of the system. The function $D_{Bi} = f([NO_3^-])$ based on the distribution ratio definition contains some parameters, namely Bi extraction and stability constants. The latter can be found in the literature and the former one can be estimated by fitting experimental data in Fig. 1 resulting in $K_{ext\_Bi} = 0.234 \pm 0.003$.

The extraction behavior of astatine from nitric acid media into 1-octanol was then studied. In contrast to bismuth, the astatine D-values are much higher, >30 over the HNO_3 range studied. Also, the astatine data trend is significantly different. The treatment previously discussed for bismuth is used to model the At behavior. In this particular case the $D_{At} = f([NO_3^-])$ function contains three unknown thermodynamic constants (extraction of At, complex formation with NO_3^-, and potentially reduction of At) and they can be estimated by means of mathematical treatment of experimental data. The corresponding parameters are found to be $K_{ext\_At} = 126 \pm 32$, $K_1 = 0.62 \pm 0.27$, and $K_{redox} = 0.237 \pm 0.033$. The value K_1 was previously estimated [9] at a level of 1.35 (no uncertainty provided) and is in agreement with the current findings.

Bismuth extraction into methyl anthranilate was studied by analogy with its extraction into 1-octanol. It can be seen in the left panel of Fig. 2, as with 1-octanol, the extraction efficiency also increases with an increase of acidity; however, the distribution ratio values are much greater with methyl anthranilate, almost reaching 1 at 2.5 M HNO_3. The methyl anthranilate solubility in the aqueous phase increases with increased nitric acid concentration and this limits the studied acidity range. More importantly, the rise in extraction as a function of acidity is much steeper for methyl anthranilate compared to 1-octanol (D_{Bi} at 2.5 M HNO_3 upon extraction to 1-octanol is ~0.01). This, along with high D-values, indicates a stronger interaction between Bi and methyl anthranilate compared to Bi and 1-octanol, resulting in the higher extractability of the metal. Analysis of experimental data indicates bismuth

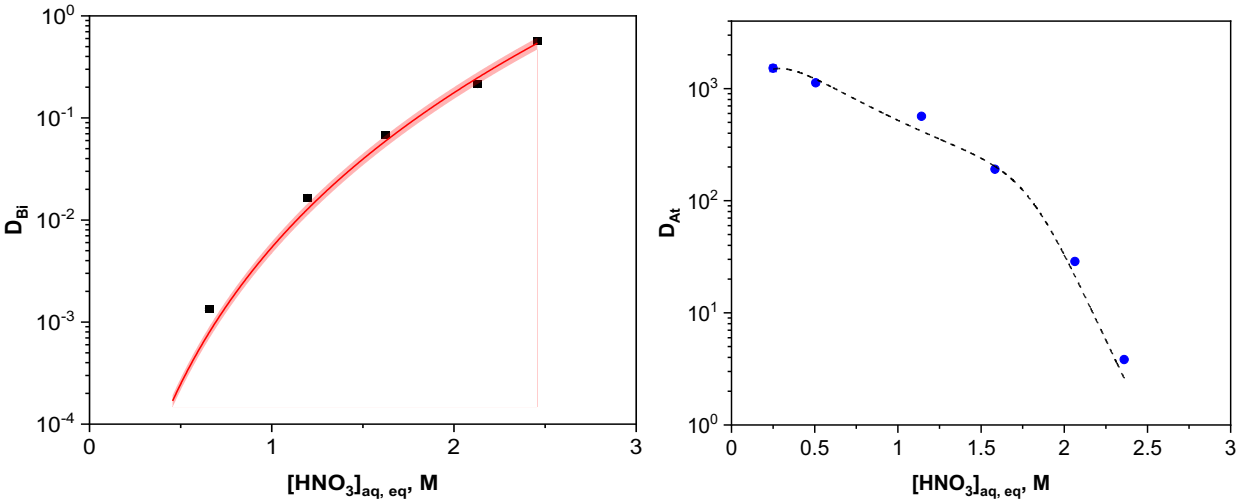

Fig. 2. Bi (left) and At (right) extraction into methyl anthranilate from nitric acid solutions. Solid line is calculated based on a definition of a distribution ratio. Shade represents 95 % confidence interval. D value uncertainties are less than the symbols shown.

is extracted in the form of $Bi(NO_3)_3 \cdot 4RNH_2$ with the extraction constant $K_{ext\_Bi\_MA} = 0.94 \pm 0.05$.

The astatine distribution ratio values at low acidity, ≤0.5 M HNO_3, (shown on the right of Fig. 2) deserve attention due to very high numbers exceeding 1,000. This makes methyl anthranilate one of the most efficient astatine extractants. There is a slight decrease in extraction as the acidity is increased to 1.5 M, after which point there is a sharp decline leading to a very small D-value of 4 at 2.4 M HNO_3. This is most likely a result of the protonation of the amine group on the methyl anthranilate, preventing the strong interaction between the AtO^+ species and the ligand. It is unclear at this point what the exact source of this diminished interaction is. Overall, this trend indicates that there is also an interaction between the At and methyl anthranilate. However, contrary to Bi behavior this interaction does not facilitate astatine extraction because the D_{At} values monotonically decrease with an increase of acidity.

[1] S. Lindegren, P. Albertsson, T. Back, H. Jensen, S. Palm, and E. Aneheim, Cancer Biother. Radiopharm. **35**, 425 (2020).

[2] M.R. Zalutsky and M. Pruszynski, Curr. Radiopharm. **4**, 177 (2011).

[3] E.H. Appelman, The radiochemistry of astatine, National Academies, 1960.

[4] J. Champion, C. Alliot, E. Renault, B. Mokili, M. Chérel, N. Galland, and G. Montavon, J. Phys. Chem. A **114**, 576 (2010).

[5] C. Alliot, M. Chérel, J. Barbet, T. Sauvage, and G. Montavon, Radiochim. Acta **97**, 161 (2009).

[6] C. Ekberg, H. Jensen, S.P. Mezyk, B.J. Mincher, G. Skarnemark, and J. Radioanal. Nucl. Chem. **314**, 235 (2017).

[7] J.D. Burns, E.E. Tereshatov, M.A. McCarthy, L.A. McIntosh, G.C. Tabacaru, X. Yang, M.B. Hall, and S.J. Yennello, Chem. Commun. **56**, 9004 (2020).

[8] G.W.M. Visser, and E.L. Diemer, Radiochim. Acta **33**, 145 (1983).

[9] D.K. Tyung, I.V. Dudova, and V.A. Khalkin, Sov. Radiochem. (Engl. Transl.) **15**, 552 (1973).

A novel approach to medical radioisotope production using inverse kinematics

M.R.D. Rodrigues,[1] G.A. Souliotis,[2] A. Bonasera,[1,3] V.E. Iacob,[1] N. Nica,[1] B. Roeder,[1]
G. Tabacaru,[1] and J.Mabiala[4]
[1]*Cyclotron Institute, Texas A&M University, College Station, Texas,*
[2]*Laboratory of Physical Chemistry, National and Kapodistrian University of Athens, Greece,*
[3]*Laboratori Nazionali del Sud, INFN, Italy,*
[4]*Praire View A&M University, Praire, Texas*

A novel approach to produce medically important radionuclides using inverse kinematics has been developed at the Cyclotron Institute at Texas A&M University. A heavy-ion beam is accelerated at an appropriate energy and focused on a light gas target. A foil catcher is positioned after the target to collect the isotopes of interest, typically focused along with the beam direction. Secondary emitted particles such as neutrons from the primary nuclear reaction can be used to irradiate other targets for further radionuclide production. As the quantity of material required to prepare heavy-ion beam is less than that used in the standard solid target approach, material costs are expected to be considerably reduced through this methodology. A detailed discussion about the methodology can be found in [1-3]. A successful test of this concept was performed with the production of the theranostic radionuclide ^{67}Cu ($T_{1/2}$ = 62 h) through the reaction of a ^{70}Zn beam at 15 MeV/nucleon with a hydrogen gas target [1]. The ^{67}Cu radionuclide alongside other coproduced isotopes, was collected after the gas target on an aluminum catcher foil, them their γ-activity was measured off-line. The main radioimpurity in the Al catcher coming from the ^{70}Zn + p reaction was ^{69m}Zn ($T_{1/2}$=13.8 h).

The activities at the end of bombardment (A_{EOB}) as well as the activities considering a beam intensity of 1pnA and an irradiation time of 1h, the so-called 1pnA-1h activity (H_{EOB}) were obtained. The average cross section ⟨σ⟩ and the respective average energy ⟨E⟩ were determined. In addition, the thick target yield in inverse kinematics extracted from the experimental activities and beam current TTY_{inv}^{exp}, and its conversion to forward kinematics TTY_{for}^{exp} were also obtained. Details of the analysis and the results can be found at [3]. Table I presents all these experimental results in comparison with the thick

Table 1. Experimental results for ^{67}Cu and ^{69m}Zn: activities, average cross sections and respective average energies, thick target yield in inverse kinematics and its conversion to forward kinematics. The thick target yield calculated from cross section and stopping power and the integral yield recommended by IEAE [4] are shown for comparison.

	A_{EOB} (kBq)	H_{EOB} $\left(\frac{kBq}{pnA.h}\right)$	$\langle\sigma\rangle$ (mb)	TTY_{inv}^{calc} (GBq/C)	TTY_{inv}^{exp} (GBq/C)	TTY_{for}^{exp} (GBq/C)	$Y(E_{max}) - Y(E_{min})$ (GBq/C)
^{67}Cu	2.16(12)	1.8(5)	7.7(21)	0.0161(16)	0.021(5)	0.38(10)	0.314
^{69m}Zn	2.55(26)	2.2(6)	4.6(13)	0.0214(21)	0.027(7)	0.50(14)	

target yield in inverse kinematics determined from cross section and stopping power TTY_{inv}^{calc} and the integral yield, $Y(E_{max}) - Y(E_{min})$ recommended by IAEA [4]

The results for ^{67}Cu production are in good agreement with experimental cross section from Kastleiner *et al*. [5]. For ^{69m}Zn, the average cross section describes well the experimental values from Levkovskij *et al*. [6]. The TTY_{inv}^{calc} predicted and the TTY_{inv}^{exp} experimentally determined are consistent considering the uncertainties. The experimental TTY converted to forward kinematics, for the ^{67}Cu, are also in good agreement with the integral yields recommended by IAEA [4], $Y(E_{max}) - Y(E_{min})$ as seen in Table I.

A test using the forward-focused neutrons from the primary reaction to irradiate ^{nat}Zn in order to produce ^{67}Cu was also performed. A block of twenty 25.4 × 25.4 mm^2 foils of ^{nat}Zn with 1 mm thickness was placed behind the Al catcher. Although, the tests showed promising results [3], more detailed experimental investigation is needed.

The present successful test indicates the possibility of producing important non-standard radionuclides of high radionuclide purity with the approach of inverse kinematics. The main requirement necessary to achieve the production of activities appropriate for preclinical studies is the availability of high-intensity (particle μA) heavy-ion primary beams.

[1] G.A. Souliotis *et al.,* Appl. Radiat. Isotopes **149**, 89 (2019).

[2] J. Mabiala *et al*., HINPw6 proceedings, EPJ-woc proceedings (article 08003 to be published).

[3] M.R.D. Rodrigues *et al*., HINPw6 proceedings, EPJ-woc proceedings (to be published).

[4] INTERNATIONAL ATOMIC ENERGY AGENCY, Technical Reports Series No. **473**, IAEA, Vienna (2012).

[5] S. Kastleiner *et al*., Radiochim. Acta **84**, 107 (1999).

[6] V.N. Levkovskij, Data file EXFOR A0510.070 dated 2016- 02-16 compare Levkovskij, Act. Cs. by Protons and Alphas, Moscow (1999). EXFOR data retrieved from IAEA Nuclear Data Section, Vienna.

Enhanced production of ^{99}Mo in inverse kinematics heavy ion reactions

J. Mabiala,[1] M.R.D. Rodrigues,[2] G.A. Souliotis,[3] A. Bonasera,[2,4] V.E. Iacob,[2] N. Nica,[2]
B. Roeder,[2] G. Tabacaru,[2] K. Wang,[2] and J. Romo[2]
[1]*Prairie View A&M University - Prairie View, Texas*
[2]*Cyclotron Institute, Texas A&M University, College Station, Texas*
[3]*Laboratory of Physical Chemistry, National and Kapodistrian University of Athens, Greece,*
[4]*Laboratori Nazionali del Sud, INFN, Italy*

Today, radioisotopes are commonly used in medicine, both in diagnosis and therapy [1, 2]. A novel method for the production of important medical radioisotopes has been developed at the Cyclotron Institute at Texas A&M University. After a successful test of the production of the theranostic radionuclide ^{67}Cu ($T_{1/2}$ = 62 h) through the reaction of a ^{70}Zn beam at 15 MeV/nucleon with a hydrogen gas target [3], the production routes were studied for the formation of medically interesting ^{99}Mo with the

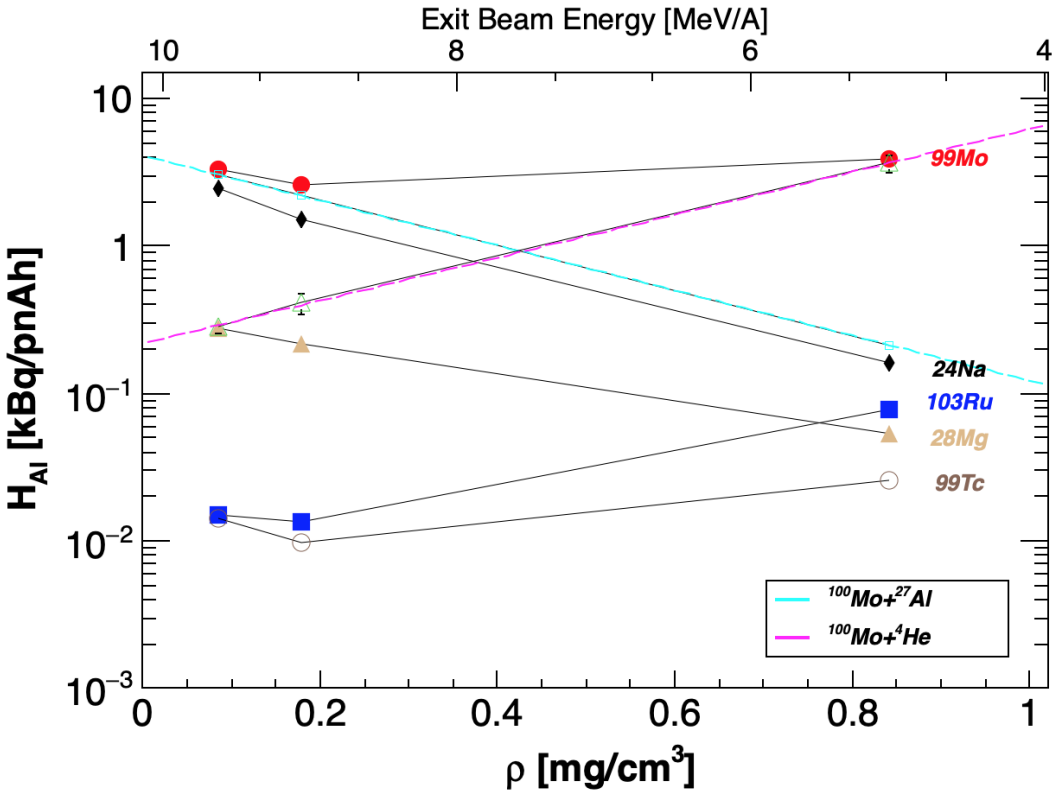

Fig. 1. Experimental activities (full symbols) for the isotopes indicated in the insets. The open symbols refer to ^{99}Mo contributions (open squares) coming from the Al catcher, low gas target density- high beam energy impinging on Al. The difference between the experimental points (solid circles) and the estimated Al contribution (open squares) gives the contributions due to the He gas target (open triangles). The exponential decay slope was estimated from the ^{24}Na production (full diamonds) and the ^{28}Mg production (full triangles) obviously coming from reactions in the Al target. Assuming binary reactions, the partner of ^{28}Mg is ^{99}Tc whose activity for this particular channel can be estimated and is given by the open circles.

use of cyclotrons. The ^{99}Mo was produced with a primary beam of ^{100}Mo accelerated by the K500 with an

energy of 12 MeV/nucleon impinging on a ^{4}He-gas cell target cooled at 77K. Three different runs were performed: a very low gas pressure (102 torr), low beam intensity (I_b=0.067 pnA) and irradiation time t_b=11h35 (source 1); a low gas pressure (213 torr), I_b=0.21pnA and t_b=10h28 (source 2) and a high gas pressure (1008 torr), I_b=0.172 pnA and t_b=7h52 (source 3). The ^{99}Mo alongside other coproduced isotopes were collected after the gas target on an aluminum catcher foil and their respective radioactivities were measured by off-line γ-ray analysis. Fig. 1 presents the activities for different isotopes of interest (full symbols), which were identified using their strongest and independent γ-lines.

[1] S. Takács, Z. Szűcs, and F. Tárkányi *et al.*, J. Radioanal. Nucl. Chem. **257**, 195 (2003); https://doi.org/10.1023/A:1024790520036

[2] S.M. Qaim, Radiat. Phys. Chem. **71**, 917 (2004).

[3] G.A. Souliotis, M.R.D. Rodrigues, K. Wang, V. Iacob, N. Nica, B. Roeder, G. Tabacaru, M. Yu, P. Zanotti-Fregonara, and A. Bonasera, Appl. Radiat. and Isot. **149**, 89 (2019).

.

SECTION V

SUPERCONDUCTING CYCLOTRON, INSTRUMENTATION AND RIB UPGRADE

K500 operations and development

D.P. May, G.J. Kim, B.T. Roeder, H.L. Clark, G. Tabacaru, and F.P. Abegglen

Introduction

During the 2020-2021 reporting period a total of 28 different beams, including 16 newly developed beams, were used for experiments, and there were a total of 36 beam tunings for these experiments. The SEE program and the radioactive-beam effort are treated separately in this progress report.

Ion Sources

In August 2020 osmium was sputtered into the ECR1 ion source in order to develop a beam for an experiment. A single dowel of osmium was introduced radially with a linear feed-through. Using oxygen as a support gas proved to be problematic as more and more gas has to be introduced to support the plasma. After removing the osmium, the source had to be cleaned and flushed several times before the oxygen pressure could be maintained. Since osmium oxidizes so easily into the dioxide or tetroxide form, it may be advisable in the future to use nitrogen or neon as a support gas. Also, since osmium tetroxide, a heavy gas at room temperature is, highly toxic, special precautions need to be made in cleaning the source after running. Indeed, because of contamination and toxicity it is advisable that osmium not be run again.

In early November 2020 the ECR1 ion source catastrophically failed. The source developed a leak that was eventually traced to the interior of the aluminum plasma chamber. Glue was placed over several suspicious spots on the wall, and the source was able to pump down confirming that the chamber was now unrecoverable. The most likely spot is the one that has been under scrutiny for several years as the measured magnetic field strength at a position aligned with a joint between two NdFeB blocks has slowly decreased over several years. A new plasma chamber had already been assembled, so more permanent magnets were ordered for a new hexapole.

From early November to the end-of-the-calendar-year shutdown the 14.5 GHz ECR3 ion source was repurposed from charge-breeding to injection of noble gas beams into the K500 exclusively for the SEE program. Even with the lack of a biased disk ECR3 was able to supply the low intensities of $^{40}Ar^{11+}$, $^{84}Kr^{23+}$ and $^{129}Xe^{31+}$ sufficient for SEE. In early March of 2021 after the shutdown the new 6.4 GHz ECR4, described elsewhere in this progress report, became available for K500 injection.

Cyclotron Beams

New beams of ^{21}Ne at 28 and 40 AMeV, ^{94}Zr at 13 AMeV, ^{129}Xe at 6.3 AMeV, and ^{192}Os at 6.3 AMeV were developed for experiments. The majority of experiments used the 2A line devoted to the recoil spectrometer MARS.

Operations

For the period April 1, 2020 through March 31, 2021, the operational time is summarized in Table I, while Table II lists how the scheduled time was divided. Unscheduled maintenance time increased substantially partly due to restrictions on access to the lab during the pandemic. In addition later in the reporting period much time was spent on issues with the radio-frequency system, the major problem being that the lower frequencies became impossible to obtain. During the shutdown several repairs to seals and the replacement of a cracked insulator on the upper "B" resonator successfully resolved the issues. Beam development for this period mainly involved the repurposing of ECR3 and developing tunes for its injection line in November and then developing tunes for the new ECR4injection line in March. Scheduled time for outsider users, exclusively SEE customers remained about the same as in the last reporting period.

Table I. 2020-2021 Operational Time.

Time	**Hrs**	**%Time**
Beam on Target	4129	47.3
Beam Development	1391	15.9
Scheduled Maintenance	1672	19.1
Unscheduled Maintenance	1544	17.7
Total	8736	100

Table II. 2020-2021 Scheduled Beam Time.

Time	**Hrs**	**%Time**
Nuclear Physics	296	5.4
Nuclear Chemistry	680	12.3
Outside Collaboration	0	0
Outside Users	3153	57.1
Beam Development	1391	25.2
Total	5520	100

K150 operations and development

G.J. Kim, B.T. Roeder, F. Abegglen, H.L. Clark, L. Gathings, D.P. May, and H. Peeler

We had a busy year operating the K150 cyclotron in the midst of pandemic. For the reporting period we logged over 3767 hours of beam-on-target and 2337 hours for beam developments. Included in the beam-on-target time was 3123 hours (2424 for physics and 699 for chemistry) for in-house science experiments and 644 hours for the SEE tests (see Table I).

. **Table I**. 2020-2021 operational time.

Time	Hours	% Time
Beam on target	3767	43.1
Beam development	2337	26.7
Scheduled maintenance	2416	27.7
Unscheduled maintenance	216	2.5
Total	8736	100

The large beam development hours reflect our time spent on trying to extend the list of 15 and 9.4 MeV/u SEE beams. Other big users of the K150 beams were: the SEE tests using both the proton and heavy ion beams, the Yennello group, and the Rogachev group, which used mainly ^{7}Li and ^{12}C beams from 1.3 to 10.3 MeV/u.

Our beam development work to extend the 15 MeV/u heavy ion beams for the SEE tests continued from last year. This year we were able to add $^{51}V^{18+}$ and $^{78}Kr^{27+}$, to the list of 15 MeV/u beams that we had developed so far: $^{4}He^{2+}$, $^{14}N^{5+}$, $^{20}Ne^{7+}$, $^{40}Ar^{14+}$, and $^{63}Cu^{22+}$. Four separate groups came to use the 15 MeV/u heavy ion beams for their SEE testing in 2020. The $^{78}Kr^{27+}$ beam was difficult to produce, it required lots of power on the source, and high voltages on the RF dee and also on the deflector. Even then the resulting beam intensity was so small that we had to verify the beam with a total energy detector. It also helped to identify two contaminants, namely $^{26}Mg^{9+}$ and $^{52}Cr^{18+}$, and to steer around them to provide over 90% pure krypton beam for the users. In addition, using 0.275 charge-to-mass ions, we have been developing a list of 9.4 MeV/u beams for SEE testing, which includes: $^{22}Ne^{6+}$, $^{40}Ar^{11+}$, $^{51}V^{14+}$, $^{65}Cu^{18+}$, $^{84}Kr^{23+}$, $^{92}Mo^{25+}$, and $^{107}Ag^{29+}$. We are working to add $^{124}Xe^{34+}$ beam to this list.

Since last year we started to develop a few proton beams extracted through the deflector, instead of strip extraction through a foil, and this year we have pushed the energy of the proton beam up to 45 MeV, which required 71 kV on the deflector E1. For those uses which do not need a lot of beam or those that need both proton and heavy ion beams in quick succession, this is a convenient way to produce the proton beams.

The astatine-211 production from bismuth-209 targets requires a very intense 29 MeV ^{4}He beam. We started out accelerating $^{4}He^{2+}$ ions at 710 A on the main magnet, and our best intensity out of the

cyclotron was 5 pμA. In the effort to increase the beam intensity, we switched from $^{4}He^{2+}$ to $^{4}He^{1+}$ ions in 2020. The new beam required 1930 A on the main magnet, also higher dee and higher deflector voltages, but it was much easier to produce high currents of $^{4}He^{1+}$ from the source to inject into the cyclotron. Almost immediately we were able to more than double the previous intensity up to 12 pμA and then up to 16 pμA later in 2020. However, using higher dee and deflector voltages meant that they were more prone to sparking, and the beam became was less stable at times. Also, injecting more than 200 μA of light $^{4}He^{1+}$ along with a substantial component of $^{16}O^{4+}$, at the charge-to-mass of 0.25, required more re-tunings of the injection line for each higher current from the source. The internal transmission averaged 70 to 80% with typical cyclotron vacuum of $1x10^{-6}$ torr, and the extraction efficiency was about 50% with 60 to 65 kV on the deflector. However the excessive sparking of the deflector with the beam on has been problems at times. At present, we can produce up to 8 pμA of 7.2 MeV/u $^{4}He^{1+}$ beam reliably, we hope to extend that to 10 pμA and more.

Texas A&M Cyclotron radiation effects facility
April 1, 2020 – March 31, 2021

H.L. Clark, G. Avila, V. Horvat, B. Hyman, M. Kennas, H.I. Park,
B. Roeder, and G. Tabacaru

Usage of the Radiation Effects Facility (REF) decreased largely due to COVID-19 pandemic travel restrictions however it was still the 5th highest ever. In this reporting period, the facility was used for 3,300 hours, which is a 17% decrease over the record setting 3,981 hours used in the 2019-2020 reporting period. Users of the facility (and hours used) over the past year were: Northrop Grumman (402.5), Texas Instruments (353), MDA (278.5), RTS (216.5), Renesas (205), NASA JPL (161.5), Boeing Corp

Table I. Radiation Effects Facility usage by commercial and government customers for this and previous reporting years.

Reporting Year	Total Hours	Commercial Hours (%)	Government Hours (%)
2020-2021	3,300	2,435 (74%)	865 (26%)
2019-2020	3,982	2,862 (72%)	1120 (28%)
2018-2019	3,678	2,939 (80%)	739 (20%)
2017-2018	3,681	2,622 (71%)	1,059 (29%)
2016-2017	3,355	2,501 (75%)	854 (25%)
2015-2016	3,042	2,326 (76%)	716 (24%)
2014-2015	3,024	1,975 (65%)	1,049 (35%)
2013-2014	2,399	1,517 (63%)	882 (37%)
2012-2013	2,626	1,856 (71%)	770 (29%)
2011-2012	2,673	1,630 (61%)	1,043 (39%)
2010-2011	3,042	1,922 (63%)	1,121 (37%)
2009-2010	2,551	1,692 (66%)	859 (34%)
2008-2009	2,600	1,828 (70%)	772 (30%)
2007-2008	2,373	1,482 (62%)	891 (38%)
2006-2007	2,498	1,608 (64%)	890 (36%)
2005-2006	2,314	1,314 (57%)	1,000 (43%)
2004-2005	2,012	1,421 (71%)	591 (29%)
2003-2004	1,474	785 (53%)	689 (47%)
2002-2003	1,851	1,242 (67%)	609 (33%)
2001-2002	1,327	757 (57%)	570 (43%)
2000-2001	1,500	941 (63%)	559 (37%)
1999-2000	548	418 (76%)	131 (24%)
1998-1999	389	171 (44%)	218 (56%)
1997-1998	434	210 (48%)	224 (52%)
1996-1997	560	276 (49%)	284 (51%)
1995-1996	141	58 (41%)	83 (59%)

(144.5), SEAKR (128), Sandia Nat Lab (125), VPT Inc (125), Honeywell (112), Intuitive Machines (111), Blue Origin (104), Raytheon (80), Fifth Gait (77), NAVSEA (72), Cobham (64), SMU (56), Troxel Engineering (55), Lockheed Martin (48), AFRL (47), Space X (35), Aria Labs (31), Innoflight (24), Johns Hopkins (24), Millennium (24), Space R2 (24), Crane AE (20), GSI Technology (20), NASA GSFC (20), BAE Systems (16), MOOG (16), Semi Zabala (16), T2 Research (16), Vorago Tech (15), mPower Tech (13), Collins Aerospace (8), Microchip (8), and TAMU Physics (4). New users included Intuitive Machines, Fifth Gait Space R2, MOOG Semi Zabala, Vorago Tech, mPower Tech and Collins Aerospace.

Table I compares the facility usage by commercial and government customers. While commercial hours still dominate, the ratio from this reporting year (74% to 26%) is similar to usage from previous reporting periods (see Fig 1). Commercial usage decreased by 15% but was the fifth highest commercial usage ever. Government usage decreased by 23% and was the tenth highest usage ever. 15 MeV/u ions were the most utilized and especially 15 MeV/u Au, until the ECR1 ion source and the K500 cyclotron RF system had failures. Then 24.8 MeV/u Xe was the highest ion in demand. No new beams were added to the K500 cyclotron SEELine users list, however 15 MeV/u V and Zr were developed for the K150 cyclotron SEELine users list. Much of the testing conducted at the facility continues to be for defense systems by both government and commercial agencies. We had no foreign users at the facility due to COVID-19 travel restrictions.

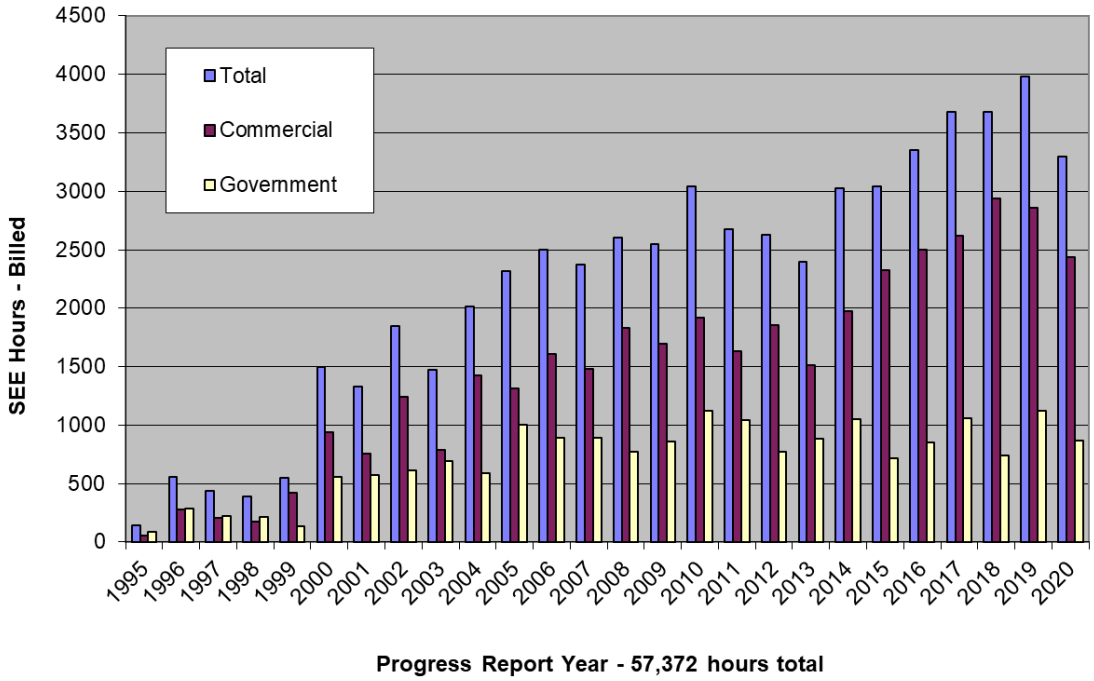

Fig. 1. Radiation Effects Facility usage by commercial and government customers for this and previous reporting years. While commercial hours still dominate, the ratio from this reporting year (74% to 26%) is similar compared to usage from prior reporting period. Usage hours decreased but largely due to COVID-19 pandemic travel restrictions however it was still the 5th highest ever. 57,372 hours provided since the start of the project in 1995.

Installation and commissioning of the ECR4 ion source

D.P. May, B.T. Roeder, F.P. Abegglen, S. Molitor, H. Peeler, and R. Olsen

The final construction, installation and commissioning of the new 6.4 GHz ECR4 ion source gained increased urgency in November of 2020 when the ECR1 ion source failed abruptly due to an unrepairable vacuum leak in the thin aluminum wall of the plasma chamber.

In early February of 2021 ECR4 and its injection beam-line were ready for commissioning (Fig. 1). The axial-coil currents were initially set using the currents calculated using the program POISSON. The design of the axial magnet field structure for ECR4, specifically the fields at the injection and extraction ends of the plasma chamber as well as the central minimum, aimed to match the axial field of ECR1 for its most successful beams, but using fewer axial coils and a more compact steel yoke.

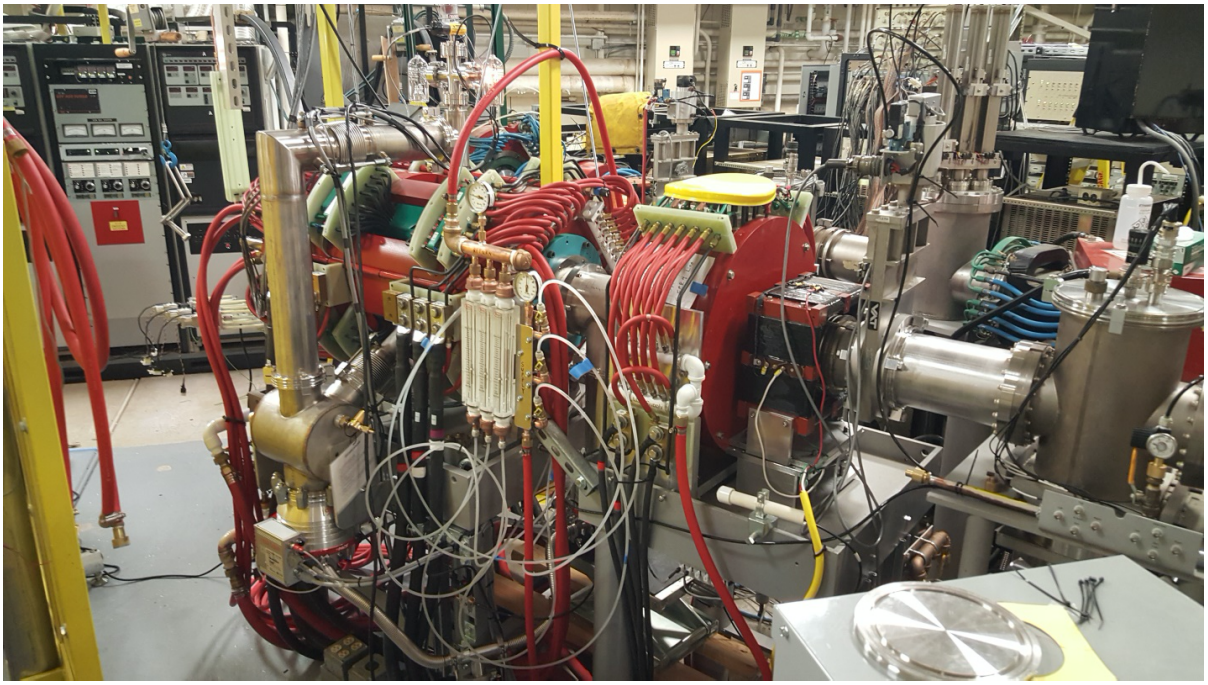

Fig. 1. ECR4 installed for K500 injection.

After power-up of the coils and of the microwave transmitter and after some trouble-shooting, the source was opened to show that the plasma "stars" on the opposite ends of the plasma chamber were thin and properly aligned (Fig. 2). Finally initial charge-state scans were obtained which enabled some tuning of the source. The axial-coil currents required for best performance were close to those obtained for ECR1. Differences could be ascribed to the inaccuracy of the ECR1 coil power supplies or to differences between ECR1 and ECR4 in the magnetic properties of their steel yokes and plugs. The exception was that the ideal central-field minimum for ECR4 seemed to be much lower than that calculated for ECR1. This was most certainly due to the fact that a high central-field minimum is required for the highest performance, but since this produces a higher plasma electron temperature more conditioning is required. This explanation seemed to be correct since raising this minimum initially produced more outgassing, but as this decreased raising the minimum gradually through several days produced the best performance.

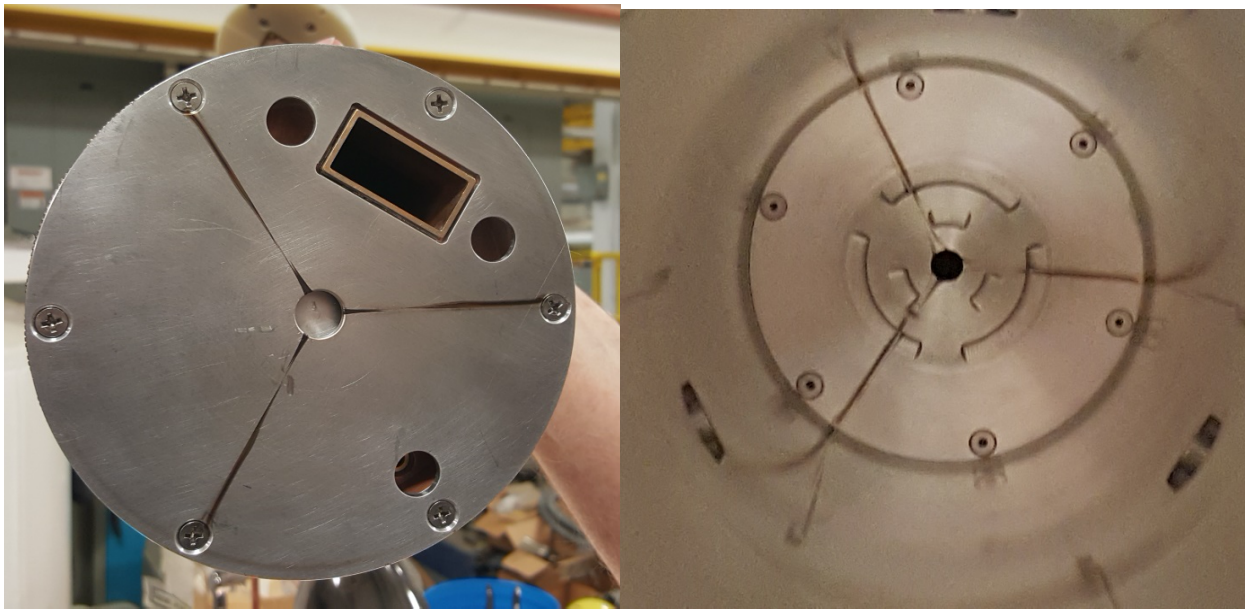

Fig. 2. The plasma "star" at the injection and extraction ends of the plasma chamber.

The performance of ECR4, as demonstrated by charge-state scans of argon beams, improved at a faster rate than the performance of the upgraded ECR1 in 1995. Ultimate performance could not be investigated, however, since ECR4 was urgently needed for K500 operation. The sputter targets were mounted in ECR4, and injection into the cyclotron began in March. Fig. 3 shows a scan of a silver beam from a sputter target.

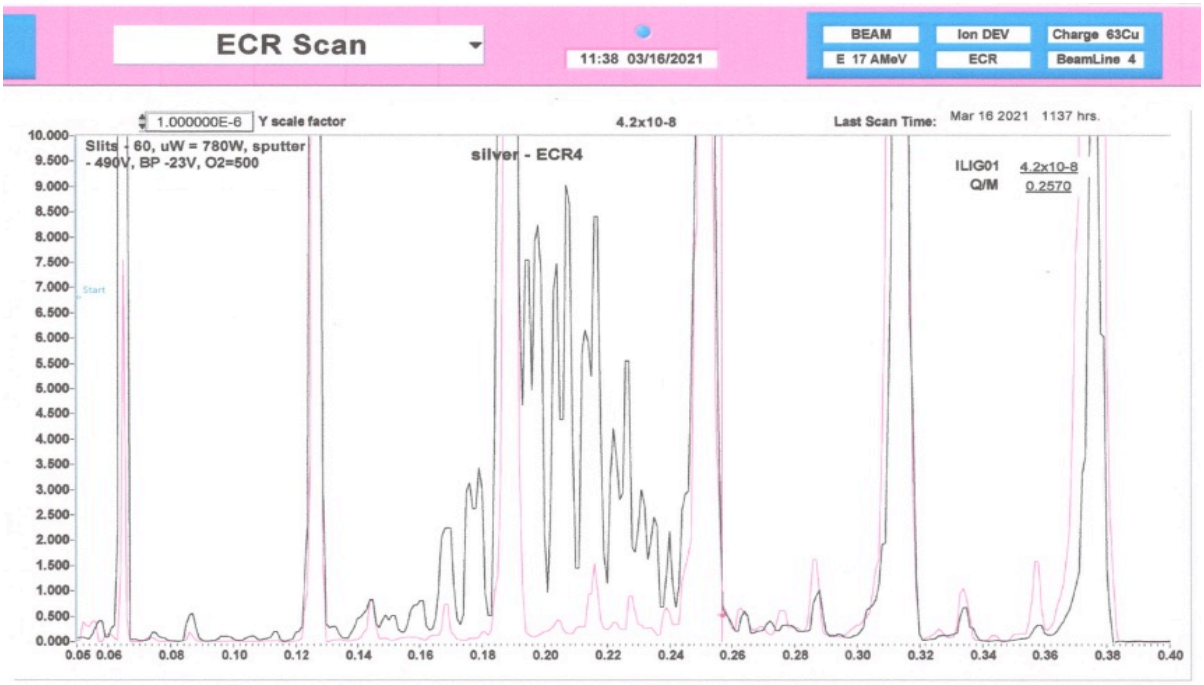

Fig. 3. ECR4 charge-state scan of silver beam.

Recent progress on the light ion guide project

G. Tabacaru, J. Ärje, D.P. May, A. Saastamoinen, F.P. Abegglen, L.N. Gathings, G.J. Kim, V. Kolhinen, S. Molitor, and B.T. Roeder

The Light Ion Guide project entered a new set-up phase in the last year [1]. Two new aluminum chambers were fabricated by Nor-Cal Products, Inc, according to our design and instructions. The chambers accommodate the new 2.5 m long SPIG, the support platform, and the vacuum barriers. The two boxes are electrically isolated through a commercially available 160 ISO ceramic break. The new SPIG has four sections and is constructed using commercially available flat aluminum extruded bars with two rounded edges. The choice of using flat bars was based on reducing the machining time, consequently reducing the machining imprecision and improving the straightness of the bars as well as the sturdiness of the whole SPIG assembly. The rounded tip of the bars has a diameter of 4.76 mm (3/16") and the inscribed circle has a radius of 4.23 mm. The current dimensions are based on the calculations presented in the paper [2] and the references therein.

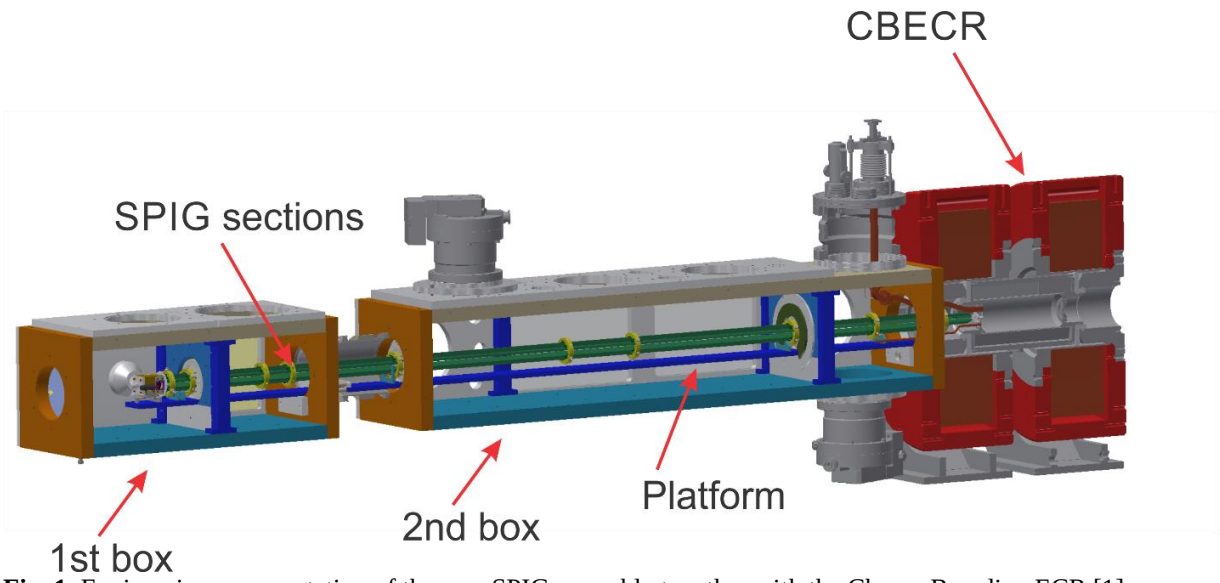

Fig. 1. Engineering representation of the new SPIG assembly together with the Charge Breeding ECR [1].

The transport efficiency of the two different geometry systems rods vs. bars has been tested offline using three different heated alkali sources (Fig. 2) (rubidium, cesium, and potassium) fitted with an extractor, and connected directly to the front-end of the SPIG. We did not notice any change in the transport efficiency, both versions of the SPIG performed in the same way.

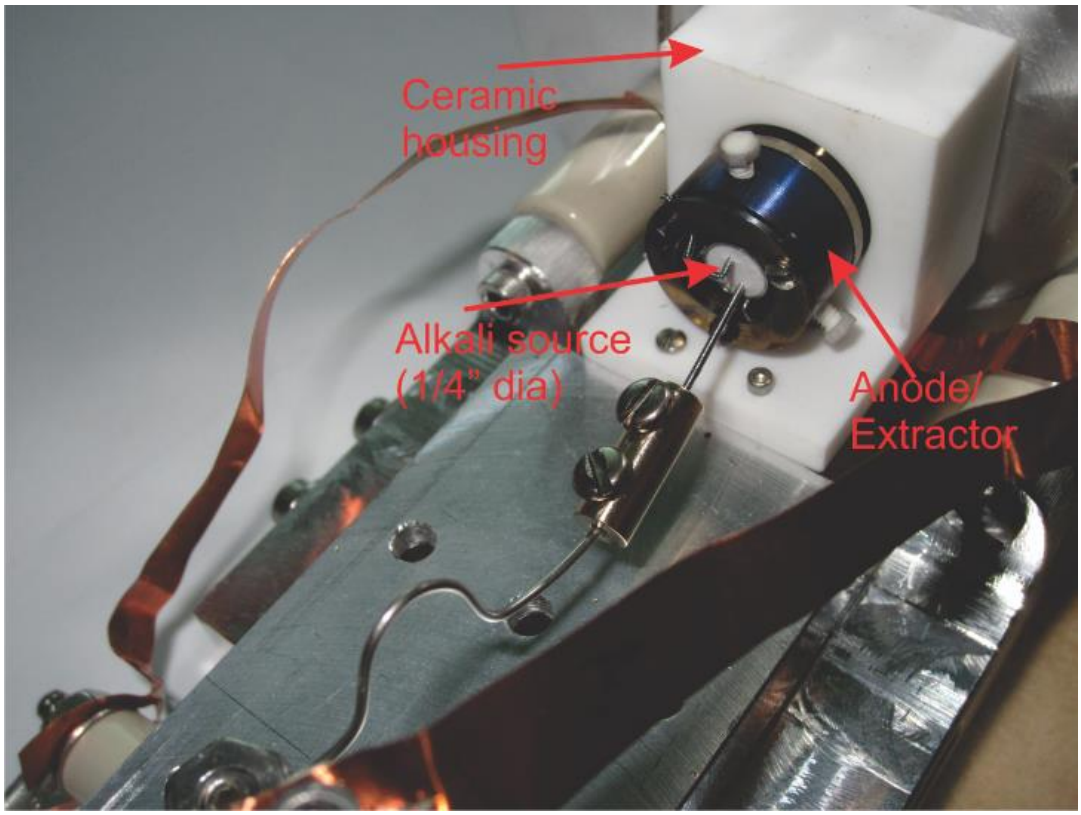

Fig. 2. Picture of the alkali source used in the off-line testing.

The charge breeding efficiency was tested using only the rubidium heated alkali source. The 2.5 m long SPIG was not very difficult to install and align inside the two boxes, pointing into the CB-ECRIS injection aperture. Fig. 3 shows a screenshot of one of the charge distribution spectra. The efficiency of the charge breeding was not calculated due to the contradictory numbers, but it is assumed to be greater than 30%-40%. With this setupit is difficult to measure the injected 1+ rubidium ion beam intensity. The 1+ injected beam can be measured at a very low anode voltage, between 5 V to 7 V, using the plasma chamber as a faraday cup, resulting in an unrealistic very low current. Consequently, the charge breeding efficiency is larger than 100%, which is not possible.

In conclusion, the new setup proved to be easier to work with and less challenging to align. The performance of the new SPIG/CB-ECRIS assembly appears to be very good with a charge breeding efficiency greater than 40%. In the future, we're going to restart the production of the radioactive ion beams and the charge breeding of its products.

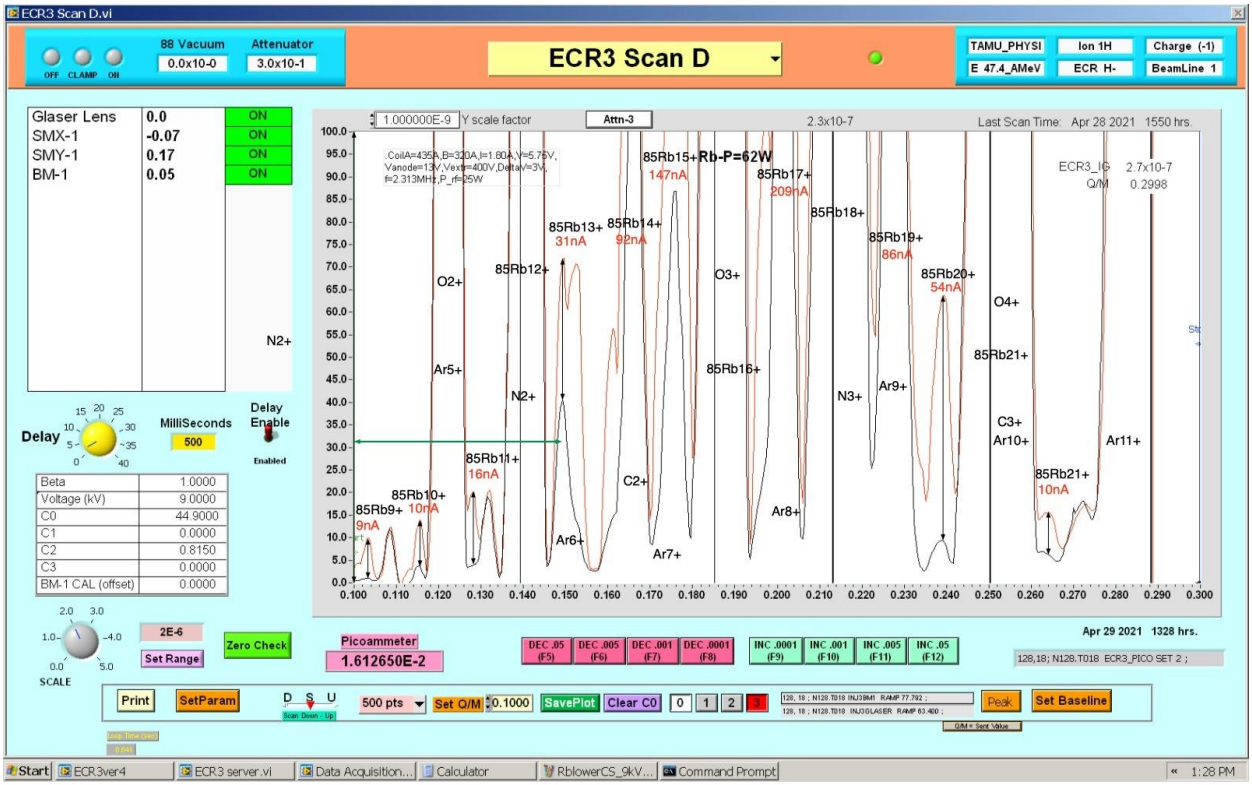

Fig. 3. Charge states distribution for the rubidium charge breeding.

[1] G. Tabacaru *et al.*, *Progress in Research*, Cyclotron Institute, Texas A&M University (2018-2019), p. IV-11

[2] T. Brunner *et al.*, Int. J. Mass Spectrom. **379**, 110 (2015).

Computing at the cyclotron institute

R. Burch, K. Hagel, J. Gauthier, and Y.-W. Lui

During the winter, an upgrade has been performed on the slave nodes of the GR group cluster. The group users were running out of space in the HDFS file system and the cluster was very unstable since the drives were getting full. We took the decision to remove all the 2TB drives from the height nodes and replace them with 2x14TB drives per node to increase the cluster total storage capacity to 224TB. We also installed 500GB SSD drives as system drives on each node and did a clean OS install, replacing Scientific Linux 7 with CentOS 7. The operation was successful and the cluster is now stable and running without issues.

The configuration of the Linux cluster was changed during the past year. Scientific Linux 6, the work-horse of our computing effort officially went end-of-life on 14-Nov-2020. To allow systems to have proper security updates, we upgraded the entire cluster to CentOS-8. As noted, this allowed us to continue to receive security updates. But in addition, the new compilers included in CentOS-8 allow for the use of root 6, whereas old compilers had prevented the upgrade to root 6, and so we had continued with root 5.

Ansible, a system we have been bringing online for some time, was brought to full utilization during this upgrade. Once we settled on the system configuration appropriate scripts were added to ansible. The upgrade process using this system consisted of bringing up a minimal system using PXE. After that, the scripts executed by ansible configured the system to the running configuration in a very short period of time. In addition, many systems could be upgraded in parallel. Whenever a system configuration needs to be changed from now on, the change is added to ansible and then the configuration change is performed through ansible on all cluster machines.

We also added significant computing capability to our cluster as we were beneficiaries of the decommissioning of the Brazos Cluster and acquired 26 SuperMicro compute servers as well as 6 file servers. We were able to implement these computers by installing CentOS-8 using ansible in a short period of time. All of the newly commissioned computers were immediately completely loaded to capacity by various jobs from various groups in the Institute.

In addition, we rearranged the racks in the computer room to make room for the three racks from the Ada Cluster that were awarded to us as a result of a proposal for its acquisition upon its planned decommissioning.

.

Development of an electron cyclotron emission imaging system

L.E. Henderson, H. Clark, C.A. Gagliardi, and D. May

Despite the logistical challenges of the past year, we were able to proceed with the fabrication of the electronically variable reflective surface (EVRS) prototypes and the construction of an anechoic chamber for characterizing microwave optical components. (See Fig. 1.) Final assembly and testing of EVRS prototypes will occur this summer, after which the full electron cyclotron emission (ECE) imaging system can be constructed and installed on one of the Cyclotron Institute's electron cyclotron resonance ion sources (ECRIS).

The anechoic chamber houses a 17-45 GHz scalar network analyzer: A tracking generator with an up-converter drives a fixed position low-gain microwave transmitter horn, and a moveable high-gain microwave receiver horn is connected through a down-converter to a spectrum analyzer. The receiver horn and device-under-test (DUT) are mounted onto concentric turntables, allowing the microwave antenna horns and DUT to be positioned at arbitrary relative angles. The reflectivity and transmissivity of microwave optical elements for the final ECE imaging system can therefore be characterized at all important angles of incidence over the K- and Ka-bands.

Fig. 1. View into anechoic chamber with calibration plate DUT.

A number of refinements to the anechoic chamber were made to ensure that microwave components behave like conventional optical elements. The combination of antenna gains adheres to the basic assumptions of geometric optics while still maintaining good angular resolution at the receiver. 3D-printed PLA posts, frames and clamps have been developed for mounting all microwave antennas, lenses, and DUTs. This plastic hardware demonstrated minimal reflectivity, as expected, while still being strong enough to replace metal mounting hardware. Off-the-shelf carbon-loaded foam panels along the walls of the anechoic chamber were found to be sufficient for absorbing stray microwave signals and dampening unwanted reflections. The only remaining optical issue to be addressed is the potential for standing waves to develop along the optical axis, which should be resolved by introducing the proper thickness of a carbon-film attenuator into the optics.

Some issues were found with the electronics themselves, including unwanted intermediate frequency (IF) feedthrough and standing waves developing on the longer coaxial cables, but those issues were addressed with an additional filter and additional attenuators. Neither off-axis coupling of the antennas nor the location of the electronics inside the anechoic chamber appear to contribute appreciably to noise levels.

Minor design revisions were made to the EVRS printed circuit boards (PCBs) in order to fit with available materials and manufacturing capabilities, but the revisions did not change the overall concept of operation or intended usage in the final detector. The revisions chiefly enabled PCB finishing operations to be carried out in-house. Facilities to perform those finishing operations – screenprinting carbon ink and electrical component mounting – have been built over the past year as well.

The EVRS test program planned for this summer will use the anechoic chamber to characterize and compare bare copper arrays, arrays with carbon traces, fully assembled PCBs, and several array design permutations. This test program will both verify the operation of components needed for the final ECE imaging system and validate the EVRS design principles inferred from simulations.

If the EVRS operate as expected, assembly of the ECE imaging system will be straightforward and will proceed immediately. However, before installation, the microwave lenses and waveguides needed to transport the ECE signal out of the ECRIS will also be characterized using the same anechoic chamber built for the EVRS. Like the tests of the EVRS prototypes, the measurements of these other optical components will test the results of design simulations and provide calibration curves for the final instrument.

.

A novel technique for the production of robust actinide targets

S. Dede,[1,2] G. Christian,[1,3] K. Manukyan,[2] and A. Aprahamian[2]
[1]*Cyclotron Institute, Texas A&M University, College Station, TX 77843*
[2]*Department of Physics, University of Notre Dame, Notre Dame, IN 46556*
[3]*Department of Astronomy & Physics, Saint Mary's University, Halifax, NS B3H 3C3, Canada*

The success of accelerator experiments is highly influenced by the availability of targets with specific and well-defined properties. Actinide targets in particular are in high demand due to the importance they hold for stockpile stewardship as well as nuclear science. The main goal of this project is the development of revolutionary new approaches in the preparation of actinide targets that are isotopically pure, cost efficient, reliable, robust, and highly uniform with controlled thicknesses and dimensions (Stewardship Science Academic Alliances Program Topic Research Area # 3: Radiochemistry). The actinides will be provided by the Actinide Center of Excellence in Research in the Engineering College at the University of Notre Dame.Leading up to the experiment, I. Richardson participated in the $^{54}Fe+^{58}Ni$ beam production experiment with the Momentum Acromat Recoil Separator (MARS) [1]. For that experiment, a $^{54}Fe^{18+}$ beam at 36 MeV/u from the K500 cyclotron impinged on a natural nickel target 50 μm thick. Analysis of this data for production rates is ongoing.

The method used to produce these targets is electrospray deposition of chemically reactive layers that can be converted to actinide oxides by simple heat treatments. The experimental setup used consists of the following components as shown in Fig. 1:

Fig. 1. The Electrospraying setup. The components are marked as follow.

a. Ozone cleaner, for the preparation of substrates before the spraying.
b. Syringe pump – Syringe – Capillary nozzle.
c. Distance regulator between the tip of the nozzle and the substrate.
d. Copper base,
e. Hot plate,
f. High voltage power supply,
g. furnace

The first step was investigating the different combinations of parameters that will produce the best possible targets with respect of uniformity, thickness, and robustness (see Figs. 2 and 3). The surface treatment of both the aluminum and carbon substrates prior to spraying is where the investigation started, by determining the best treatment in order to have a thin target layer and not just droplets on the surface. Following that, the investigation turned to the parameters of the spraying itself. More specifically, the spraying time (from 15min to 2hr), the Uranium concentration (from 0.1 M to 1M) in the solution, the flow rate (from 3μl/h to 30μl/h) , the heat treatment temperature (from 350oC to 550oC) as well as the stability and robustness of the targets under irradiation with an Argon beam (from 2×10^{16} to 1.3×10^{17} ions/cm^2).

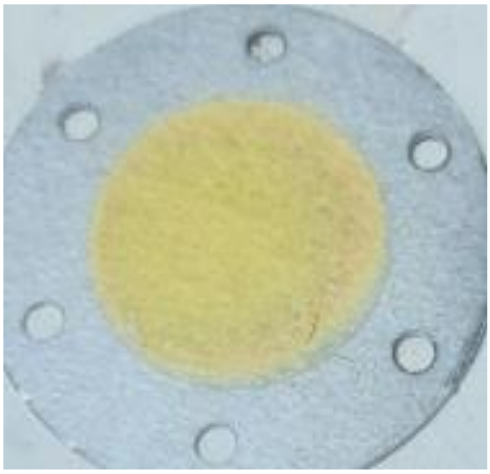

Fig. 2. UO_2 target on pure Al substrate.

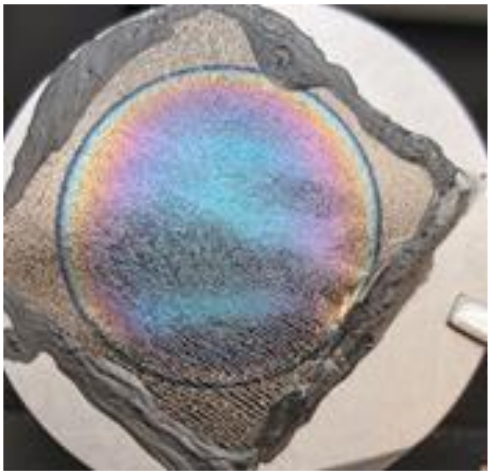

Fig. 3. UO_2 target on thin Carbon substrate.

In order to fully characterize these targets, alpha spectroscopy (thickness), X-Ray Fluorescence (XRF) analysis (uniformity), Transmission Electron Microscopy (TEM) analysis (crystal structure), Scanning Electron Microscopy (SEM) analysis (surface analysis) and X-Ray Photoelectron (XPS) analysis.(oxygen coefficient $k_0 = 2 + x$ and ionic (U^{4+}, U^{5+}, U^{6+}) composition of the UO_{2+x} layer) were used. Some of the results are presented below:

From the figures below as well as all the measurements we performed we can draw certain conclusions regarding our targets.

- The surface of our targets, (Fig 4) is smooth with minimum imperfections.
- The heat treatment temperature in-fluences the crystal structure of our deposited layer. Higher temperatures result in Mg leaking from the substrate into our UO_2 layer, thus obstructing the

crystallization of our layer and forming a MgO layer (Fig 5) inside our UO_2 layer. Otherwise, we have good crystallization of our target layer (Fig 6).

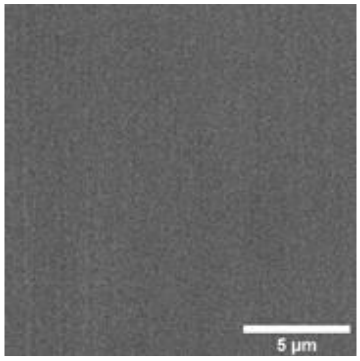

Fig. 4. SEM image of the surface after 350° C heat treatment and no irradiation.

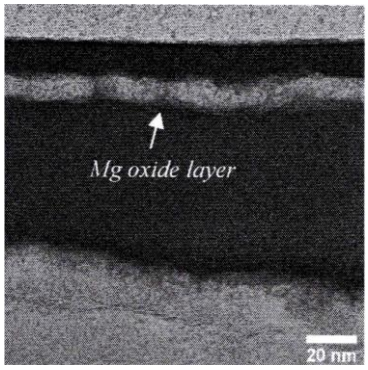

Fig. 5. TEM image of a target after heat treatment at 550° and irradiation with 7.7×10^{16} ions/cm^2

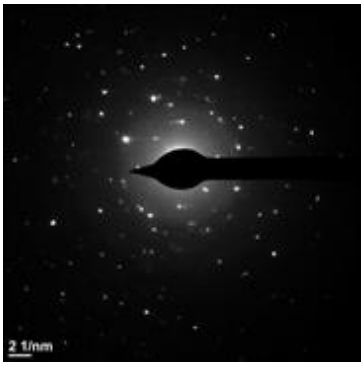

Fig. 6. Diffraction pattern of the UO_2 layer after heat treatment at 350ºC and irradiation with 2×10^{16} ions/cm^2.

- The amount of U in our target linearly depends on the duration of the spraying (Fig 7), which allows us to control the thickness of the target by varying the spraying duration.
- Higher fluence results in higher non uniformity of our targets, (Fig 8) but still less than 10%.
- The overall thickness of the targets does not change after the irradiation (Fig 9).

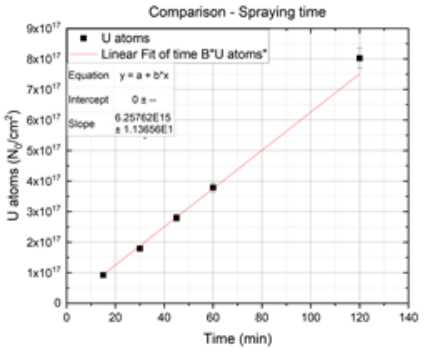

Fig. 7. Alpha spectroscopy results for targets with different spraying duration**.**

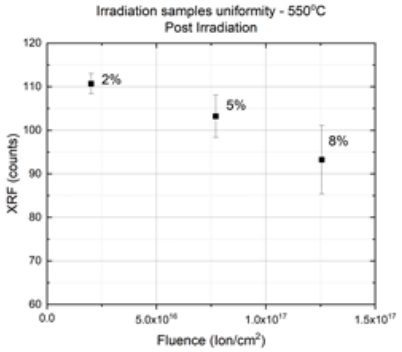

Fig. 8. XRF results for targets with different irradiation fluence and heat treatment at 550ºC.

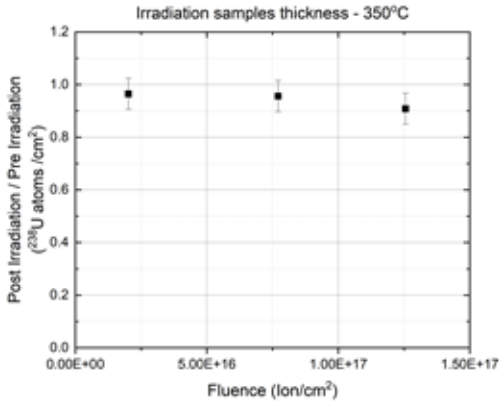

Fig. 9. Alpha spectroscopy results for target stability after irradiation and heat treatment at 350°C.

The next step in the project was to determine the robustness and purity of the targets under a neutron beam. For this investigation we utilized the neutron beam at the Los Alamos National Lab (LANL) using the DANCE detector array [1]. We used targets of varying thicknesses on both pure and alloy aluminum backings in order to determine the significance of the resulting γ-rays from the alloy's impurities in relation to the lines of interest from the uranium. The second aspect of the tests we performed at LANL was a measurement of the average total kinetic energy (TKE) of correlated fission fragments of ^{238}U as a function of incident neutron energy with a twin Frisch-gridded ionization chamber (FGIC) at WNR [2].

The data from the first experiment are currently being analyzed. Some preliminary results are presented below:

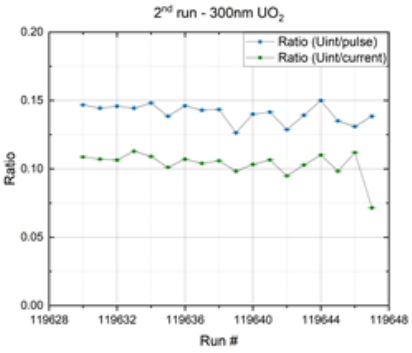

Fig. 10 Preliminary results of our targets stability under neutron beam.

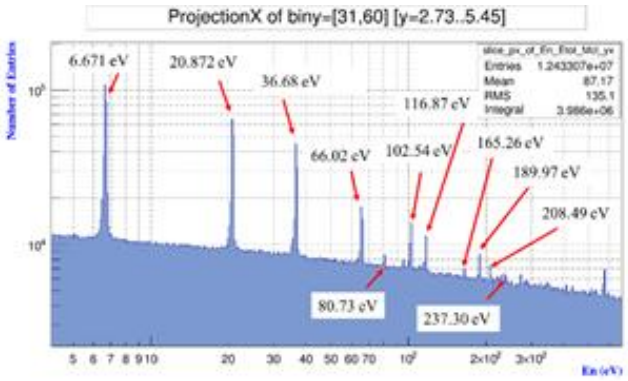

Fig. 11. Preliminary results of the ^{238}Uranium levels we are able to detect.

From the preliminary figures above, we can safely assume that our targets are fairly robust with no impurities that would interfere with our measurements.

Future work

Regarding future work, finalizing the results from the LANL experiment is the top priority. Analysis of our microscopy measurements are also being performed at the moment in order to fully understand our target's damage under the Ar beam, as well as the crystalizing mechanisms conditioning our targets.

Following that, we have started exploring the combustion properties of Eu as a surrogate for Am, which is going to be our next step in the actinide target production.

The final step would be a cross section measurement using the neutron beam that is being developed at University of Notre Dame in the following months.

[1] J.L. Ullmann, T. Kawano, T.A. Bredeweg, A. Couture, R.C. Haight, M. Jandel, J.M. O'Donnell, R.S. Rundberg, D.J. Vieira, J.B. Wilhelmy, J.A. Becker, A. Chyzh, C.Y. Wu, B. Baramsai, G.E. Mitchell, and M. Krtička, Phys. Rev. C **89**, 034603 (2014).

[2] D.L. Duke, F. Tovesson, A.B. Laptev, S. Mosby, F.J. Hambsch, T. Brys, and M. Vidali, Phys. Rev. C **94**, 054604 (2016).

Development of position and pulse shape discriminant neutron detector modules

D.P. Scriven,[1,2] G. Christian,[1-3] G.V. Rogachev,[1,2] C.E. Parker,[1] L. Sobotka,[4] S. Ahn,[1] S. Ota,[1]
E. Koshchiy,[1] E. Aboud,[3] J. Bishop,[1] N. Dronchi,[4] and A. Thomas[4]
[1]*Cyclotron Institute, Texas A&M University, College Station, Texas 77843*
[2]*Department of Physics and Astronomy, Texas A&M University, College Station, Texas 77843*
[3]*Department of Astronomy and Physics, Saint Mary's University, Halifax Nova Scotia, B3H 3C3, Canada*
[4]*Departments of Chemistry and Physics, Washington University, St. Louis, Missouri 63130*

There are many applications for fast neutron detectors including fundamental physics, astrophysics, and stewardship science [1,2]. Many conventional detectors with neutron/gamma discrimination capabilities use liquid scintillators that are dangerous due to toxicity and volatility and do not offer great position resolution. A push for more modern detectors with greater energy resolution and efficiency has driven the development of many new dense detector systems that use solid organic scintillators. One such detector array is being developed here at the Texas A&M University Cyclotron Institute (CI). The Texas Neutron detector, TexNeut, is being constructed here using novel pseudo-bar detector modules. In past annual reports, we presented simulations that guide R&D [3] and also the results of construction and characterization of these modules [3-5]. Each module was shown to offer 2 cm position discrimination (xD) with a reasonably low threshold, and the modules retain the exceptional pulse shape discrimination (PSD) capability of the *p*-terphenyl scintillator. During 2020-2021, we continued to characterize the detector modules, worked on optimization, and began the design of the TexNeut array using these neutron detector modules.

Because TexNeut will be operated in a time-of-flight (TOF) mode it is important to understand the timing resolution of the device. At the CI, analog electronics were setup to characterize the timing resolution of the pseudo-bar modules using a ^{22}Na source as shown in Fig. 1. The electronics setup consisted of a constant fraction discriminator (CFD), time-to-digital converter (TDC), and charge-to-digital converter (QDC) to record pulse times and energies. The ^{22}Na source produces β^+ which annihilate readily with electrons in the environment creating 511 keV γ-rays which are emitted at 180° from each other. Two cesium fluoride (CsF) detectors, which have sub-ns rise times, were positioned to detect the coincident gammas, with a single pseudo-bar module. One CsF (stop) was placed at the same location as the pseudo-bar, 20 cm from the ^{22}Na source. The other CsF (start) was placed 20 cm opposite the ^{22}Na source.

We used the QDC and TDC to record energy and timing information for all detectors. γ-Ray timing and energy information was recorded with the start and stop CsF. This information was used to understand the timing resolution of the CsF detectors. The timing resolution of the CsF detectors was found to be 364 ps FWHM. Using lead bricks, we collimated the γ-rays to expose each crystal in the pseudo-bar separately. This allowed us to measure the timing resolution all the way down to any threshold created in the electronics, even beyond the xD threshold established in [4] of 300 keVee.

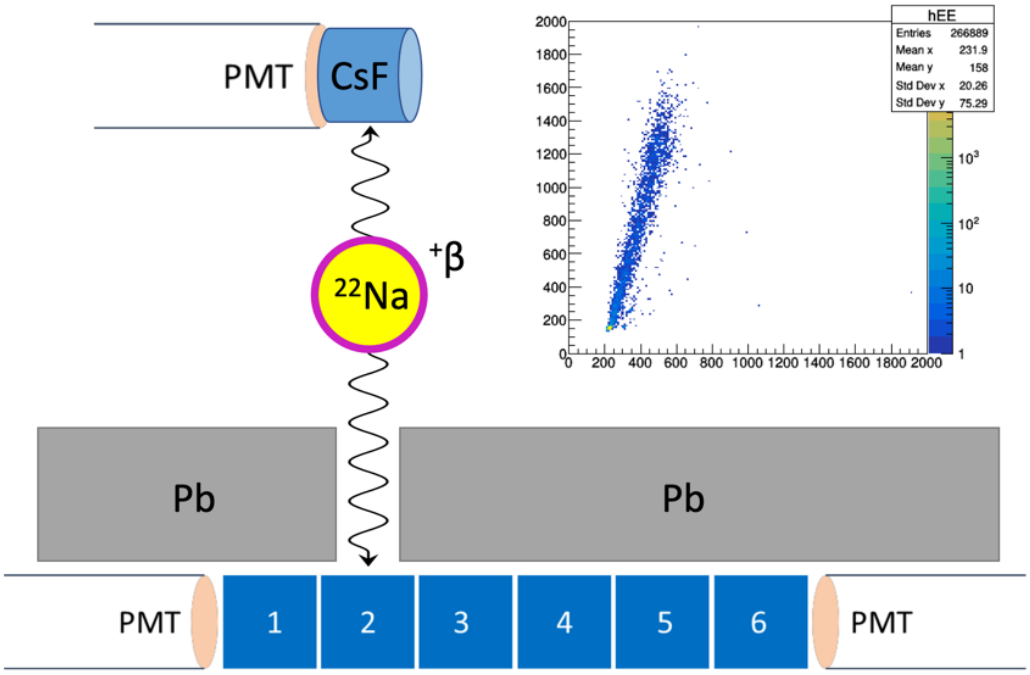

Fig. 1. Sketch of the CsF and pseudo-bar placement during the timing characterization experiments. The placement of the stop CsF detector is not shown here. The histogram inset shows the energy spectrum from both PMTs, E_{left} vs E_{right}, with γ-rays only being exposed to crystal-2 as shown in the diagram. Units in the inset histogram are ADC channel.

After deconvoluting the CsF timing contribution from each pseudo-bar timing spectrum we were able to extract the timing resolution for the pseudo-bar on its own. This was done for the entire data set, but also for events only above the 300 keVee xD threshold. Additionally, the timing information from both left and right PMTs was combined using a weighted average, to give optimal resolution. Two weighted averaging methods were used – a bulk weighted average of all events (labeled "W-Avg in Fig. 2), which gives the singles timing resolution, and an event-by-event weighted average ("E-by-E" in Fig. 2), which simulates the procedure used in a time-of-flight experiment. The single crystal timing as well as the results of both weighted average methods are shown in Fig. 2.

To conclude, between this work and [3-5], the relevant detector properties have been fully characterized, with a timing resolution of 400-700 ps FWHM. The results from this work, as well as [3-5] are currently under review for publication with *Nuclear Instrumentation and Methods A.* Moving forward we plan to construct the TexNeut array using these pseudo-bar modules and commision the detector in conjuction with TexAT [6], exploring the low-level structure of ^{10}Li by studying highly excited states in ^{10}Be that are isobaric analogues those low-level resonances in ^{10}Li.

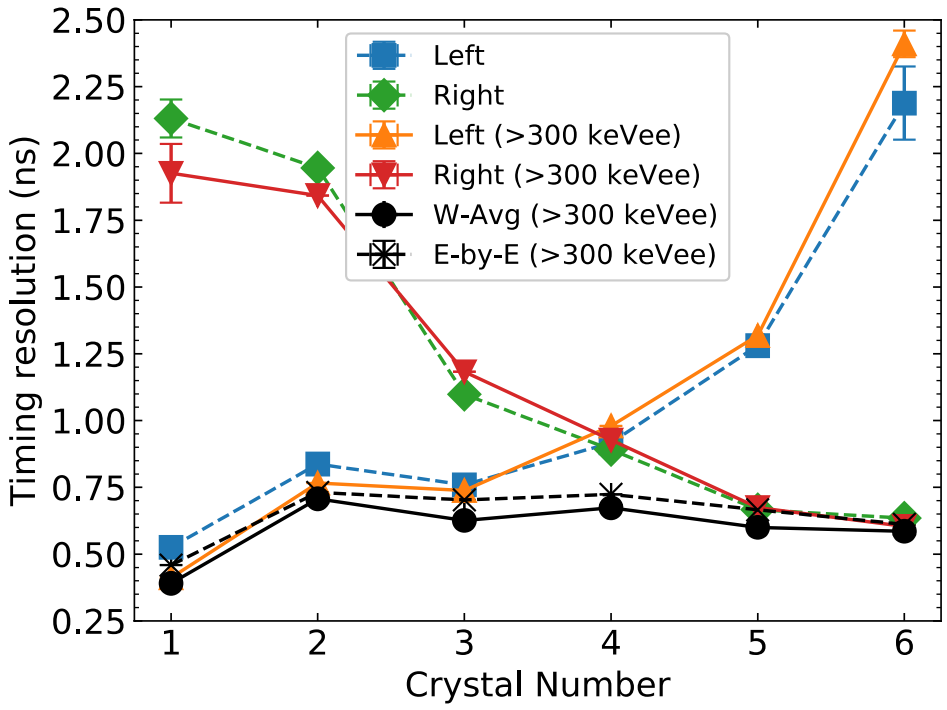

Fig. 2. The timing resolution measured for each crystal (colored polygons) as well as the timing found by using weighted averaging (black circle/x).

[1] E. Aboud *et al.*, *Progress in Research*, Cyclotron Institute, Texas A&M University (2019-2020), p. IV-121.

[2] E. Aboud *et al.*, *Progress in Research*, Cyclotron Institute, Texas A&M University (2018-2019), p. IV-39.

[3] D.P. Scriven *et al.*, *Progress in Research*, Cyclotron Institute, Texas A&M University (2018-2019), p. IV-55.

[4] D.P. Scriven *et al.*, *Progress in Research*, Cyclotron Institute, Texas A&M University (2019-2020), p. IV-112.

[5] C.E. Parker *et al.*, *Progress in Research*, Cyclotron Institute, Texas A&M University (2018-2019), p. IV-52.

[6] E. Koshchiy *et al.*, Nuclear Inst. and Methods in Phys. Res. **A957**, 163398 (2020).

.

Toward the understanding of the ^{10}Li system and the commissioning of the TexNeut array

D.P. Scriven,[1,2] G. Christian,[1-3] G.V. Rogachev,[1,2] C.E. Parker,[1] L. Sobotka,[4] S. Ahn,[1] S. Ota,[1]
E. Koshchiy,[1] E. Aboud,[3] J. Bishop,[1] N. Dronchi,[4] and A. Thomas[4]
[1]*Cyclotron Institute, Texas A&M University, College Station, Texas 77843*
[2]*Department of Physics and Astronomy, Texas A&M University, College Station, Texas 77843*
[3]*Department of Astronomy and Physics, Saint Mary's University, Halifax Nova Scotia, B3H 3C3, Canada*
[4]*Departments of Chemistry and Physics, Washington University, St. Louis, Missouri 63130*

Significant progress has been made in the last three years towards the construction of a state-of-the-art neutron detector at the Texas A&M University Cyclotron Institute (CI). The neutron detector array, TexNeut, will use novel neutron detector modules called pseudo-bars to reconstruct the kinetic energy of fast neutrons from experiments. These pseudo-bar modules are described and characterized in the works [1-3] and in this issue of *Progress in Research.* With a well-established understanding of the operating properties of these modules in the last year, we have started the construction of the TexNeut array.

For the commissioning run of TexNeut, we plan two experiments in conjunction with TexAT [4]. Using a ^{9}Li beam generated in MARS [5] we intend to populate states in the ^{10}Be system above the ^{9}Li + *p* and ^{9}Li + *n* thresholds. These states are expected to be T=2 isobaric analogue states (IAS) to the low-lying excited states of ^{10}Li. In the past, TexAT has been used for thick target inverse kinematics (TTIK) to populate IAS states of nuclear systems via proton elastic scattering. In our first experiment we use proton elastic scattering and TTIK to record the excitation function in the (*p*,*p*) channel. The second experiment uses TexAT with the addition of TexNeut outside of the target chamber to observe the excitation function in the (*p*,*n*) channel.

The IAS resonance corresponding to the s-wave ground state of ^{10}Li sits at 1.57 MeV center of mass (COM), and the first excited p-wave state is expected around 2.1 MeV COM. Shown in Fig. 1 are R-matrix predictions for the cross sections for both the (*p*,*p*) and (*p*,*n*) interactions around the COM energy regime of those T=2 states in ^{10}Be. One can see from these predictions that there is a strong reduction in the cross section in the resonance at 1.57 MeV in the (*p*,*p*) channel and a small enhancement expected at 2.1 MeV. The resonance at 2.1 MeV has a much stronger enhancement in the (*p*,*n*) channel. These features suggest that probing the ^{10}Li system will be aided by the addition of the TexNeut array.

The construction of TexNeut is ongoing with collaborators of the L. Sobotka group at Washington University in St. Louis. There, they are developing the data acquisition (DAQ) electronics which use ASIC chips [6] for signal processing and CFDs for accurate timing. We are currently benchmarking the DAQ to ensure the detector modules operate within nominal performance limits found during characterization using analog and digital DAQs. The Wash. U. group is also designing the structure for the detector which is carefully designed to be able to hold many detector modules in different arrangements that conform to experimental needs. In this way, TexNeut can be made thick or thin, wide or narrow, and sparse or dense.

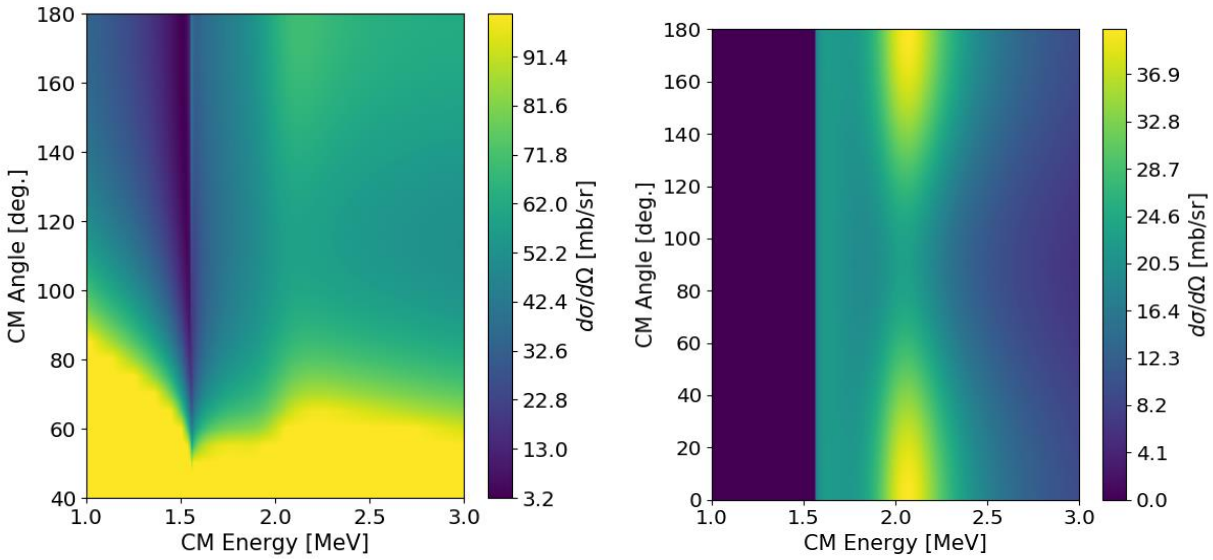

Fig. 1. Predicted cross sections for the ^{9}Li + p (left) and ^{9}Li(p,n)^{9}Be reaction (right) channels. Data is truncated on the left due to obscene enhancement in the cross section at low angles due to Rutherford scattering. The hard cutoff in the (p,n) channel is from the ^{9}Li(p,n)^{9}Be Q-value.

Some initial calculations and Geant4 simulations were performed to optimize the array arrangement for the ^{9}Li(*p*,*n*)^{9}Be experiment. The commissioning run will use a smaller prototype version of the TexNeut array that uses 48 detector modules rather than the 120 modules of the full array. The interlayer time-of-flight was calculated for neutrons with kinetic energies 0.5-5.0 MeV, which are

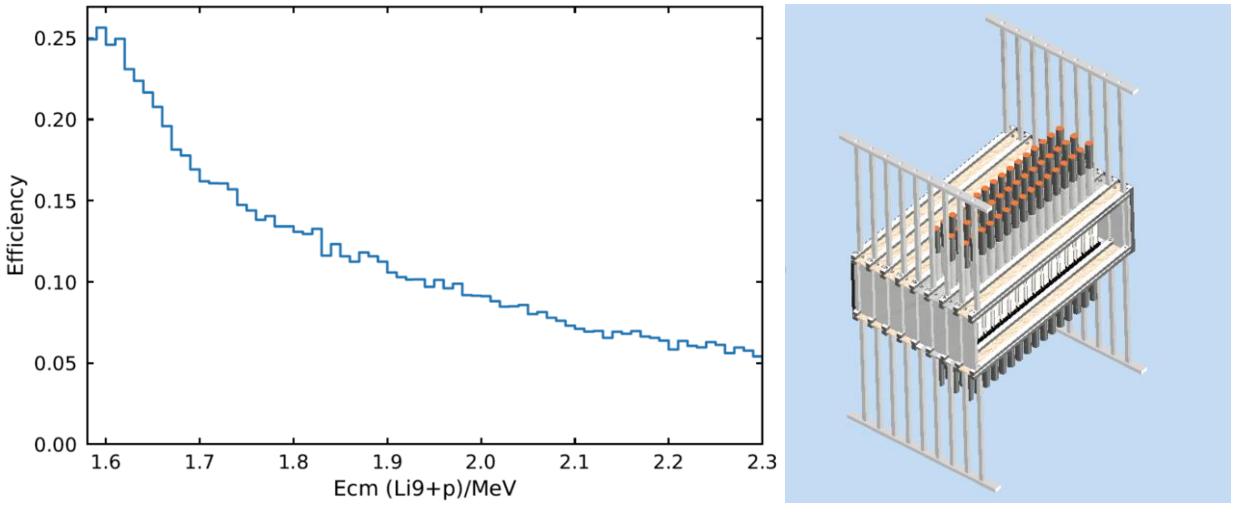

Fig. 2. The simulated efficiency of neutrons from ^{9}Li(p,n)^{9}Be (left) and a CAD drawing of TexNeut in the same configuration that was simulated and that is planned for deployment.

expected from the reaction kinematics. Based on the timing resolution of the detectors, individual layers should be separated by about 4 cm center-to-center to give time-resolved layer ID for causality cuts. Taking into account the predicted R-matrix scattering cross sections shown in Fig. 1, layer spacing, and

detector thresholds of [1-3], Geant4 simulations showed that the best use of the 48 modules was to arrange them in 3 layers, with 16 modules each. The simulated efficiency of this configuration is shown in Fig. 2 along with the most recent CAD drawing.

In October 2020, beam time was allocated to perform the ^{9}Li(*p*,*p*)^{9}Li study. This allowed us to spend time tuning MARS for optimal production of ^{9}Li and also to optimize many of the running parameters of the TexAT detector. It also allowed the (*p*,*p*) channel to be studied with TexAT optimized for the proton detection (in the (*p*,*n*) experiment, TexAT will be optimized for detecting breakup products of ^{9}Li$^{(gs)}$ isobaric analog). We are currently working to analyze this data. During this run several different nuclear species were produced in MARS with the same magnetic rigidity, $B\rho$ = 1.113 Tm. The primary beam constituents were ^{3}H, ^{6}He, and ^{9}Li. In our analysis we are able to successfully identify the beam particles based on their energy loss using the micromegas Detectors of TexAT. After calibration of the TexAT silicon array, we have start looking for the relevant ^{9}Li + *p* scattering events using coincidences with ^{9}Li beam, silicon detector energies, and energy loss found in the tracks of scattered particles. Micromegas tracks from one suspected ^{9}Li + *p* event can be seen in Fig. 3. Continued analysis is ongoing to produce the (*p*,*p*) excitation function. Completion of TexNeut is expected during 2021 with the commissioning run following by the end of the year.

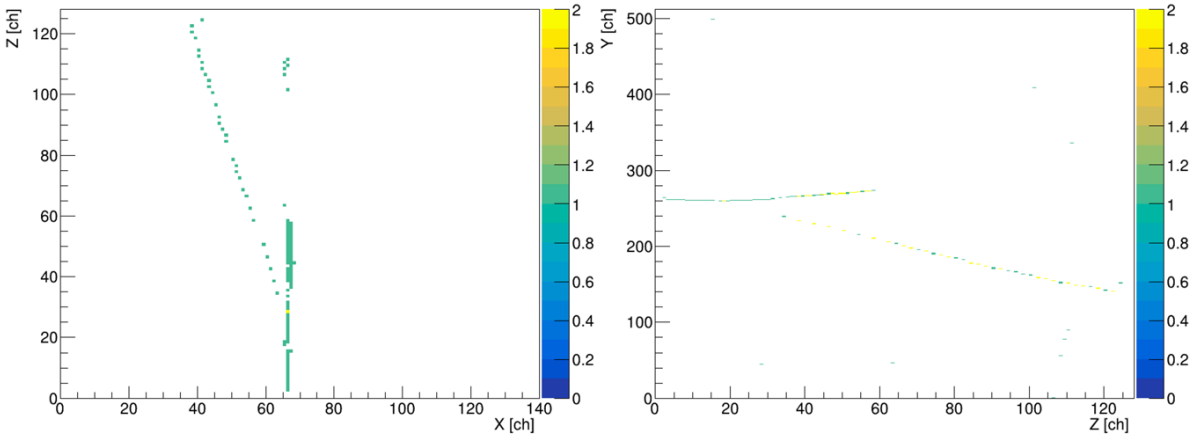

Fig. 3. Tracks recorded by the micromegas detectors in TexAT of a suspected ^{9}Li + p event. This event was selected by gating on the ^{9}Li beam events and on silicon events within the kinematically allowed energy. These are the X-Z (left) and the Z-Y (right) projections.

[1] D.P. Scriven *et al*., *Progress in Research*, Cyclotron Institute, Texas A&M University (2018-2019), p. IV-55.

[2] D.P. Scriven *et al*., *Progress in Research*, Cyclotron Institute, Texas A&M University (2019-2020), p. IV-112.

[3] C.E. Parker *et al*., *Progress in Research*, Cyclotron Institute, Texas A&M University (2018-2019), p. IV-52.

[4] E. Koshchiy *et al*., Nucl. Instrum. Methods Phys. Res. **A957**, 163398 (2020).

[5] R. Tribble, *et al.*, Nucl. Phys. **A701**, 278 (2002).

[6] G. Engel *et al.*, Nucl. Instrum. Methods Phys. Res. **A612** 161 (2009).

Assessment of suitability of an LBC-detector-based system for identification and quantification of radioactive nuclides in samples irradiated by cyclotron beams

V. Horvat, H. L. Clark, and B. Hyman

A gamma-spectroscopy apparatus was purchased from Berkeley Nucleonics Corporation (BNC) [1] in order to improve quality of radiation surveys of the devices irradiated at the TAMU Radiation Effects Facility [2]. All the devices under test (DUTs) must be surveyed upon beam exposure and only those that show activity at or below the typical background level can be released back to their owners immediately. Initial survey is normally done using a portable hand-held Geiger-Müller counter and most of the DUTs normally satisfy the above-mentioned criterion. Those that do not pass this test have to be kept and eventually surveyed at a later time in hope that the excess activity is short-lived and so these DUTs will pass the test then. Predicting that time is difficult without some kind of automation of the process.

Furthermore, DUTs irradiated with protons at a flux typical for the K150 cyclotron runs often show long-term activity. Those DUTs must be kept indefinitely or shipped back to the owner. The latter is preferable in order to prevent accumulation of radioactive material (RAM) at our facility. However, it is possible only if the owner is licensed to possess RAM and if the shipment has a declaration that specifies the radioactive nuclides present and their respective activities.

The new apparatus can address both of the above-mentioned problems, but first it has to be characterized in order to assess its capabilities and limitations. The characterization includes assessment of intrinsic background, energy scale, resolution as a function of energy, efficiency, and capabilities of the software for data acquisition and analysis.

Our system includes a lanthanum bromochloride (LBC) scintillation detector with a 2" diam. x 2" thick crystal, coupled to a photomultiplier tube (PMT) [3, 4]. The tube is plugged into the socket of a PMT base integrated with a power supply, an amplifier, an analog-to-digital converter, and a multichannel analyzer (MCA) with multichannel scaler (MCS) capability [5]. The data acquisition and analysis software [6] and a personal computer were purchased separately. The crystal and the PMT are encapsulated in 0.4 mm thick aluminum to protect the detector from ambient light and moisture and to reflect the scintillation light.

Scintillation material in our LBC detector is $LaBr_{2.85}Cl_{0.15}$:Ce. Its density is 4.90 g/cm^3, its photoelectron yield is about 1.30 times that of NaI, and its primary decay time is about 26 ns, which is an order of magnitude less compared to NaI. LBC detectors have superior mechanical strength and energy resolution compared to all other scintillation detectors. Typical energy resolution of an LBC detector is 3% FWHM at 662 keV. It is not as good as that of a typical semiconductor detector (0.2% for high-purity germanium), which limits complexity of a spectrum that can be effectively analyzed. However, an LBC detector is much cheaper, sturdier, and more versatile. Also, it does not require cooling by liquid nitrogen and is virtually maintenance-free.

Another limitation of the LBC detector usefulness comes from its relatively high intrinsic background, as illustrated in Figure 1, with about 200 counts per second (cps) total, and with about 100 cps between 33 keV and 220 keV for the 103 cm^3 crystal. Namely, natural lanthanum contains 99.911%

of stable ^{139}La and 0.089% of ^{138}La that has a half-life of 1.05×10^{11} y and undergoes β^- decay with 34.4% fraction and electron capture decay with 65.6% fraction, in each case emitting a single gamma-ray having energy of 789 keV and 1436 keV, respectively. The 1436 keV gamma-ray peak is prominent in the background spectrum (at 12 cps), while the 789 keV gamma ray peak blends with the 1436 keV gamma-ray Compton distribution. Because of the distributed nature of the source uniformly all over the crystal, the 1436 keV gamma-ray peak has a low-energy tail due to likely escape of scattered gamma rays and secondary x rays as well as a high-energy bump (stronger than the gamma-ray peak) due to coincidence summing with barium x rays. The 789 keV gamma-ray peak has a prominent high-energy tail because scintillations are produced by gamma and beta radiation combined (with beta end-point energy of about 255 keV) and because of coincidence summing with cerium x rays. Also prominent in the background spectrum are the overlapping peaks due to *K* x rays of barium and cerium, emitted following *K* electron capture and β^- decay of ^{138}La, respectively. Peak at 36 keV (50 cps) in Fig. 1 is predominantly due to Ba *K*β x rays. The Ba *K*α peak at 32 keV was cut off from the spectrum by setting a high discriminator lower level. Some lanthanum *K* x rays are expected to contribute to the spectrum as well, due to fluorescence by higher-energy gamma rays.

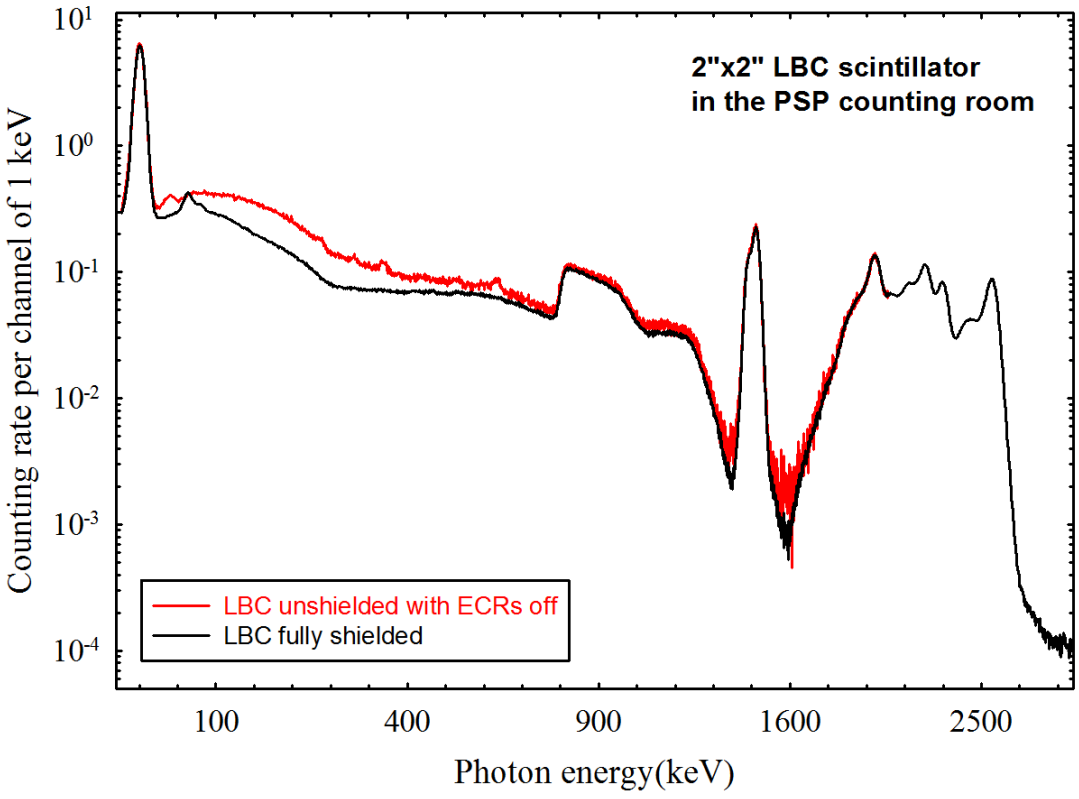

Fig. 1. Spectrum of the LBC detector background.

According to the manufacturer, the peak structure at energies from 1.6 MeV to 2.7 MeV (at about 32 cps) is predominantly "^{227}Ac-related" and possibly "^{235}U-related" (since ^{227}Ac is a progeny of ^{235}U), as these impurities are typically present is $LaBr_3$ and $LaCl_3$ raw materials [7]. Ac and La are homologous elements and therefore are extremely difficult to separate by chemical means, while the average number

of ^{227}Ac atoms per La atom is estimated to be on the order of 10^{-14} [8]. Hull *et al*. [9] reiterate that these peaks are due to alpha decays in the ^{227}Ac (^{235}U) series and demonstrate that their position in the spectrum varies depending on the composition of the scintillator, unrelated to the photon energy calibration. Major individual peaks in the structure are attributed to alpha decays of ^{227}Ac progenies, specifically those of ^{223}Ra (5716 keV), ^{211}Bi (6623 keV), ^{219}Rn (6819 keV), and ^{215}Po (7386 keV) [10].

The two curves in Figure 1 illustrate the effect of shielding the detector with a lead-brick structure built around it and the contribution from nearby sources of radiation at the measurement location (PSP counting room). Apparently, shielding is most effective in the energy range from 45 keV to 700 keV, although it gives rise to peaks due to *K* x rays of lead in the region between 70 keV and 90 keV. It should be noted that radiation levels in the lab increase significantly when the ion sources and the cyclotrons are in operation, resulting in a broad distribution in the background spectrum, extending up to about 250 keV and peaking at about 85 keV. Therefore, the setup normally should be shielded by at least one lead-brick wall. It was found that shielding the PMT is just as important as shielding the LBC crystal.

[1] https://www.berkeleynucleonics.com

[2] https://cyclotron.tamu.edu/see/

[3] https://www.berkeleynucleonics.com/lanthanum-bromochloride

[4] https://scionix.nl/high-resolution-lbc-scintillators/

[5] https://www.berkeleynucleonics.com/bmca-ethernet

[6] https://www.berkeleynucleonics.com/bgamma-software-package

[7] S. Petrak, M. Selle, P. Schotanus, E. Bodewits, and F. Quarati, Scintillation Properties of high-resolution $La(Br_x\ Cl_{1-x})_3$:Ce and high-sensitivity $CeBr_3$, 14th Int. Conference on Scintillating Materials and their Applications (SCINT), Chamonix, France, 2017.

[8] F. Quarati *et al*., Nucl. Instrum. Methods Phys. Res. **A729**, 596 (2013).

[9] G. Hull *et al.*, Nucl. Instrum. Methods Phys. Res. **A925**, 70 (2019).

[10] J.K. Hartwell and R.J. Gehrke, Applied Radiation and Isotopes **63**, 223 (2005).

.

Gamma-spectroscopy-based survey of the devices on a board activated by proton beams from the K150 cyclotron

V. Horvat

Devices on a board shown in Fig. 1 have been irradiated by proton beams from the K150 cyclotron. As a result, the devices (and parts of the board) have been activated above the background level, and the induced activity had to be analyzed before the board with the devices could be returned to the owner.

Fig. 1. Devices on a board irradiated by proton beams from the K150 cyclotron.

The survey was performed using an apparatus purchased from Berkeley Nucleonics Corporation (BNC) [1]. It includes a lanthanum bromochloride (LBC) scintillation detector with a 2" diam. x 2" thick crystal, coupled to a photomultiplier tube (PMT) [3, 4]. The tube is plugged into the socket of a PMT base

integrated with an amplifier, an analog-to-digital converter, and a multichannel analyzer (MCA) [5]. The data acquisition and analysis software [6] and a personal computer were purchased separately. The crystal and the PMT are encapsulated in 0.4 mm thick aluminum to protect the detector from ambient light and moisture and to reflect the scintillation light. The new apparatus has been well characterized in terms of its intrinsic background, efficiency, energy scale, and resolution as a function of energy.

Measurements and subsequent analysis were challenging because of the large size (9.5" x 7.5") and complicated (non-planar) geometry of the board and the devices on it. Ideally, the board should be measured from a distance much larger than the 30 cm length of its diagonal, so that the board could be regarded as a point-like source. However, this is neither practical (because there is not enough room in the lab for that) nor feasible. Namely, the maximum detector counting rate at the surface of the board is less than four times that of the background, and so at a large distance the contribution from the board is surely well below the background level and therefore not detectable.

Consequently, we opted to measure the activity at a distance of 30 cm from the board, as shown in Fig. 1, hoping to determine intensity of the strongest peak in the spectrum with good accuracy (on the order of a few percent). This is also justified by the fact that the detector solid angle is large (more than 2π). As a follow-up, we measured activity at the surface of each device in order to determine intensities of the weaker peaks relative to the strongest one and use that information to identify the active nuclides and their relative activities. Each measurement involving the board was immediately followed by a background measurement in the same configuration. Spectra measured at the distance of 30 cm are shown

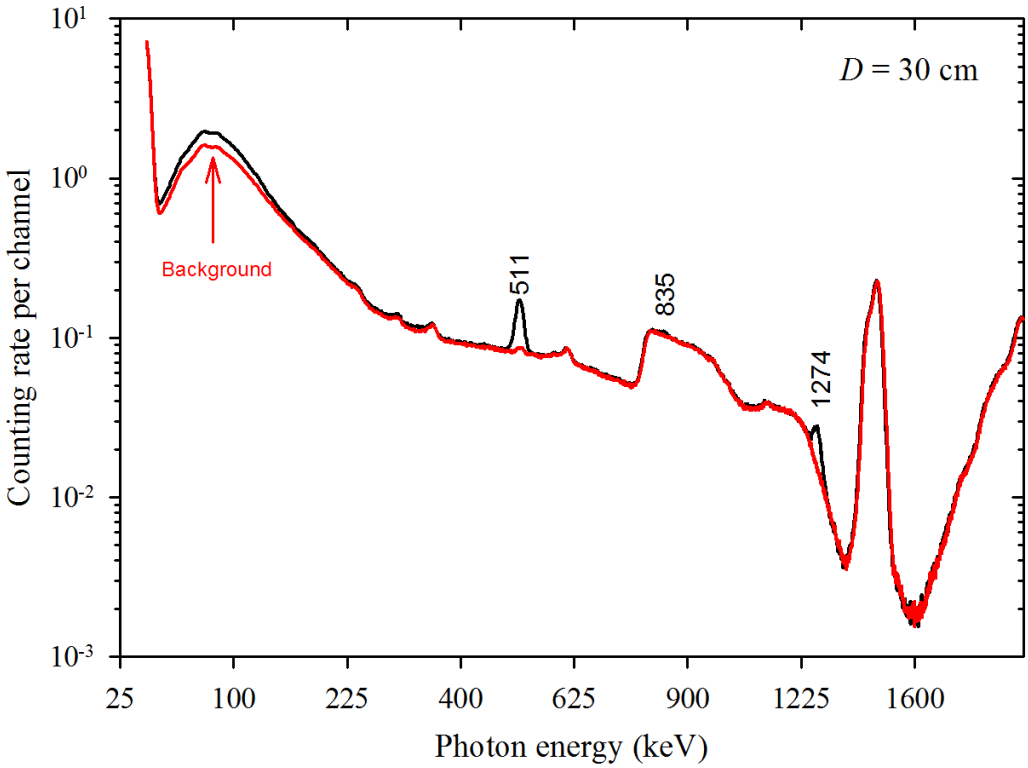

Fig. 2. Photon spectrum of the board taken at the distance of 30 cm (shown in black) and the corresponding background spectrum (shown in red).

in Fig. 2, while some of the spectra measured at the surfaces of the devices are shown in Fig. 3.

Fig. 2 shows very few peaks discernible above the background level, although there may be additional peaks in the regions where the background is high. The peak at 1274 keV is characteristic of Na-22 decay, as is the peak at 511 keV due to annihilation of the positrons emitted in the process. The peak at 835 keV is characteristic of Mn-54 decay. The structure between 789 keV and 1044 keV, the peaks at about 1450 keV, as well as the structure above 1600 keV are all attributed to the intrinsic background of the LBC detector [7-10]. The broad distribution centered at about 85 keV is due to the x-ray emissions from the nearby ECR sources. Intensity of that distribution varies over time depending on the source usage. Unfortunately, it was not practical to shield the detector from these x rays when the detector was 30 cm above the board. However, this was done very effectively for the subsequent measurements in which the detector was close to the board, by building a lead-brick structure around the setup. The small peaks that show up in both spectra shown in Fig. 2 are environmental, mostly due to radon and its descendants. Their intensity also varies over time.

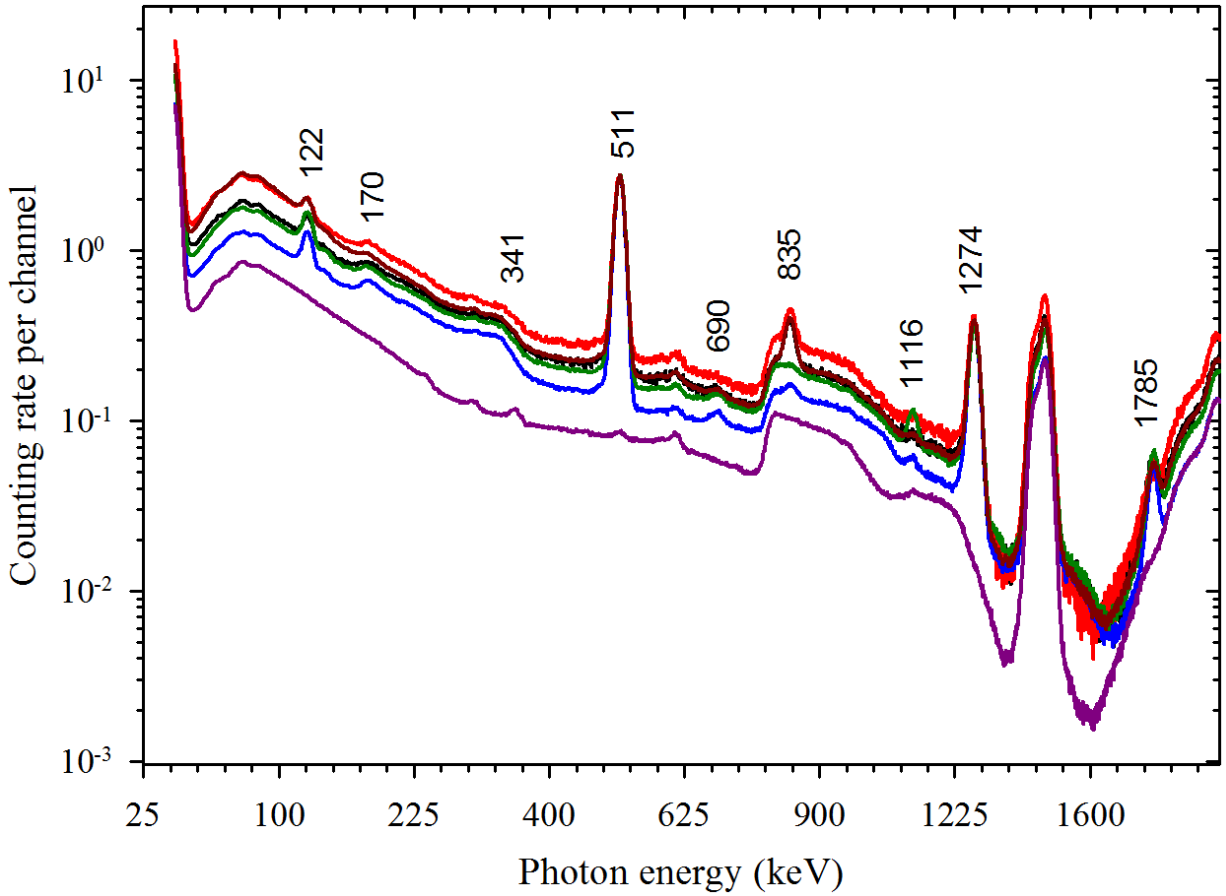

Fig. 3. Selected photon spectra measured at the surfaces of the devices, slightly renormalized to match the amplitude of the 511 keV peak in the spectrum shown in blue. The remaining measured spectra do not display any new features. The corresponding background spectrum is shown in purple.

Fig. 3 shows selected photon spectra measured at the surfaces of the devices. Compared to Fig. 2, new peaks have emerged due to the more favorable peak-to-background ratio and the increased counting rate. The ridges at 170 keV and 340 keV represent edges of the 511 keV peak's Compton distribution,

while the peak at 1785 keV is due to coincidence summing (511 keV + 1274 keV). The remaining three new peaks are at 122 keV (characteristic of Co-57 decay), at 1116 keV (characteristic of Zn-65 decay), and at 690 keV. Origin of the peak at 690 keV is not clear, but since the peak is very weak (comparable in intensity to the nearby environmental peak), its contribution to the overall activity of the sample can be ignored.

It should be noted that the spectra shown in Figs. 2 and 3 were measured about seven months after exposure of the board to the proton beam. Consequently, all the short-lived activity had decayed away, and the nuclides with half-lives on the order of one hundred days or more do not emit gamma rays outside of the energy region shown in the graphs. A few spectra were taken with photon energy range extended up to 3000 keV to confirm that assertion for the case at hand.

Peaks in the spectra were analyzed using bGamma software[11-12] that featured a National Nuclear Data Center (NNDC) photon-emission database NuDat [13-14], while the efficiency at the distance of 30 cm from the board was calculated using CYLTRAN, a Monte Carlo electron-and-photon transport code [15]. CYLTRAN was verified to produce accurate efficiency values in the previous measurements featuring various calibrated gamma-ray sources located at different distances from the detector and at different displacements from the detector axis. Unfortunately, the complex geometry of the board and the devices on it could not be modeled precisely in CYLTRAN. Therefore, we simplified the model to reflect the worst-case scenario (*i.e.*, the lowest possible efficiency). Two configurations were considered. In one configuration the board was modeled as a thin disc having diameter of 30 cm and having its radioactivity uniformly distributed on its surface. In the other configuration board was modeled as a thin disc having diameter of 1 cm and having its radioactivity uniformly distributed on its surface, but unlike in the previous case, it was displaced away from the detector axis, by as much as 14 cm. As expected, the efficiency turned out to be lower in the latter case and that set of values was used in the analysis. Nevertheless, the differences between the two sets of efficiencies were reassuringly small, ranging from 1.6% at 122 keV up to 6.3% at 1274 keV.

Analysis showed that the emission at 511 keV is almost entirely due to Na-22 decay and that the upper limit of activity associated with the peak at 691 keV is only 50 ± 8 decays per second (dps) or 1.3 ± 0.2 nCi and can be ignored. The report summary is presented in Table I below.

Table I. Activity of the nuclides from the board.

Nuclide	Half-life	Activity (dps)	Activity (nCi)
Na-22	2.60 y	1438 ± 26	38.8 ± 0.7
Mn-54	312 d	355 ± 6	9.6 ± 0.2
Zn-65	244 d	251 ± 8	6.8 ± 0.2
Co-57	272 d	133 ± 2	3.60 ± 0.06

[1] https://www.berkeleynucleonics.com
[2] https://cyclotron.tamu.edu/see/
[3] https://www.berkeleynucleonics.com/lanthanum-bromochloride
[4] https://scionix.nl/high-resolution-lbc-scintillators/

[5] https://www.berkeleynucleonics.com/bmca-ethernet
[6] https://www.berkeleynucleonics.com/bgamma-software-package
[7] S. Petrak, M. Selle, P. Schotanus, E. Bodewits, and F. Quarati, Scintillation Properties of high-resolution $La(Br_x\ Cl_{1-x})_3$:Ce and high-sensitivity CeBr3, 14^{th} Int. Conference on Scintillating Materials and their Applications (SCINT), Chamonix, France, 2017.
[8] F. Quarati *et al*., Nucl. Instrum. Methods Phys. Res. **A729**, 596 (2013).
[9] G. Hull *et al.*, Nucl. Instrum. Methods Phys. Res. **A925**, 70 (2019).
[10] J.K. Hartwell and R.J. Gehrke, Applied Radiation and Isotopes **63**, 223 (2005).
[11] http://www.brightspec.be/brightspec/index.php
[12] https://www.brightspec.be/brightspec/?q=node/42
[13] N. D. C. National, "NuDat V2," Brookhaven National Laboratory, USA, 2018.
[14] N. N. D. Center, " http://www.nndc.bnl.gov/nudat2/," BNL. [Online]. [Accessed Nov 2018].
[15] J.A. Halbleib and T.A. Mehlhorn, Nucl. Sci. Eng. 92, 338 (1986), J.A. Halbleib, R.P. Kensek, T.A. Mehlhorn, G.D. Valdez, S.M. Seltzer, and M.J. Berger, CYLTRAN 3.0, Sandia National Labs (Albuquerque, NM), Report SAND91-1634 (1992).

Optimization of performance and calibration of LBC detector

V. Horvat

A lanthanum bromochloride (LBC) scintillation detector [1-2] was acquired for gamma-ray spectroscopy of devices activated by cyclotron beams at the Radiation Testing Facility [3]. The detector is a 2" diam. x 2" crystal of $LaBr_{2.85}Cl_{0.15}$:Ce (density 4.90 g/cm^3), coupled to a photomultiplier tube (PMT). The tube is plugged into the socket of a PMT base integrated with a power supply, an amplifier, an analog-to-digital converter, and a multichannel analyzer (MCA) [4]. The crystal and the PMT are encapsulated in 0.4 mm thick aluminum to protect the detector from ambient light and moisture and to reflect the scintillation light.

Since there are no manual controls for the supporting electronics, everything has to be set with software. This can be done using a basic data-acquisition and analysis package that came with the detector [5] or with a more sophisticated program that was purchased separately [6]. However, neither the manufacturer nor the supplier provided the recommended settings for the LBC detector and so all the performance-affecting parameters had to be optimized using trial-and-error method. The only exception was the PMT bias, for which the manufacturer recommended the value of 700 V, but without any explanation of what happens if the detector is slightly under-biased or slightly over-biased. Unfortunately, at 700 V and at the lowest signal amplification the last channel in the spectrum corresponds to about 1250 keV, which severely limits usefulness of the apparatus. Consequently, we kept signal amplification at its minimum value and lowered the bias in order to increase the energy range. After it was verified that the bias-dependence of gamma-ray peak widths (measured in keV) is negligible, it was decided to conveniently set the bias to 643.7 V, so that on the 2048-channel full scale the channel width at the low-energy side of the spectrum corresponds to 1 keV. With the intrinsic non-linearity of the energy scale, *i.e.*, slightly reduced gain on the high-energy side of the spectrum, the resulting energy range was 2064 keV. Of course, the detector bias can be lowered even further if an increased energy range is needed.

Other parameters important to performance of the data-acquisition hardware include the lower-level discriminator (LLD), the digital threshold (DT), rise time (RT) of the signal and flat-top width (FTW) of the signal. LLD is set in channel units and results in a sharp cutoff on the low-energy side of the spectrum. It was set to channel 37 in order to avoid processing of the strong peaks due to $K\alpha$ x rays of barium, lanthanum and cerium (which are always present as a part of the detector's intrinsic background), while enabling detection of most of the corresponding $K\beta$ x rays (which are much weaker). Cutoff produced by DT is gradual. Consequently, DT was set to the channel value of 8, so that it has no effect on channels above 37.

RT and FTW are signal-shaping parameters that can have a substantial direct effect on resolution and dead time and an indirect effect on gain. Their values were varied independently and simultaneously in order to keep the resolution at the value specified by the manufacturer, while minimizing the dead time and maximizing the gain. This was done at the incoming counting rate (ICR) of about 10,000 events per

second (10 kcps). We found that the optimal values of RT and FTW were 1.56 μs and 0.48 μs, respectively, which resulted in the dead-time losses of about 4.7%.

Detection efficiency was determined in a series of measurements with calibrated (almost) point-like sources in order to establish its dependence on photon energy, source-to-detector distance, and displacement from the detector axis. The efficiency was also calculated using CYLTRAN, a Monte Carlo electron-and-photon transport code [7].

Detection efficiency as a function of photon energy was measured with sources of ^{109}Cd (4.62 μCi), ^{137}Cs (0.1 μCi), ^{60}Co (0.69 μCi), ^{133}Ba (1 μCi), ^{152}Eu (1.032 μCi), and ^{207}Bi (1 μCi) placed at the distance of 5 cm from the detector on the detector axis. The listed source activities refer to the date of their calibration. Nominal diameters of the sources were 3 mm. The results are shown in Fig. 1.

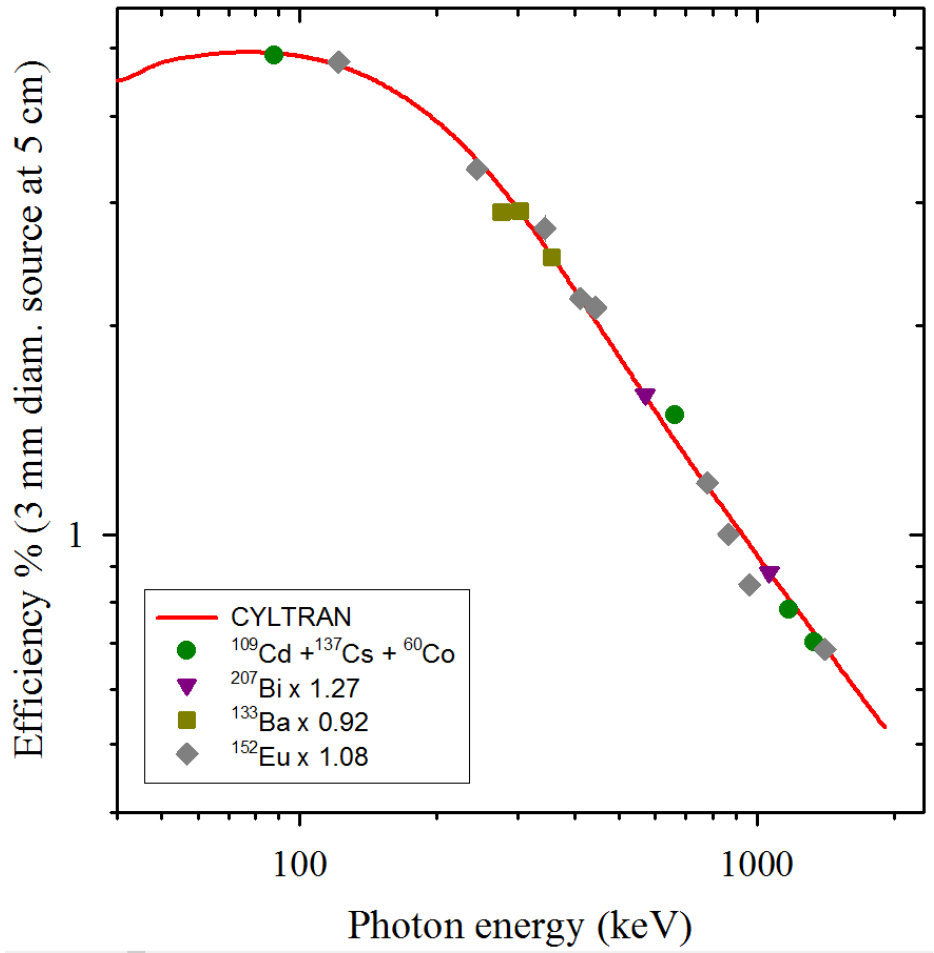

Fig. 1. Measured and calculated LBC detector efficiency as a function of photon energy.

Fig. 1 shows that CYLTRAN calculations are in excellent agreement on absolute scale with measurements involving the sources of ^{109}Cd, ^{137}Cs, and ^{60}Co. The results of the measurements with the remaining three sources had to be slightly scaled in order to agree with the calculations. This correction for ^{133}Ba and ^{152}Eu results was -8% and +8%, respectively, while the correction for ^{207}Bi results was

+27%. These corrections are not unexpected considering typical tolerances in activities of calibrated sources [8]. The larger correction for ^{207}Bi (an open source) results may also indicate that some of the radioactive material may have been removed over time.

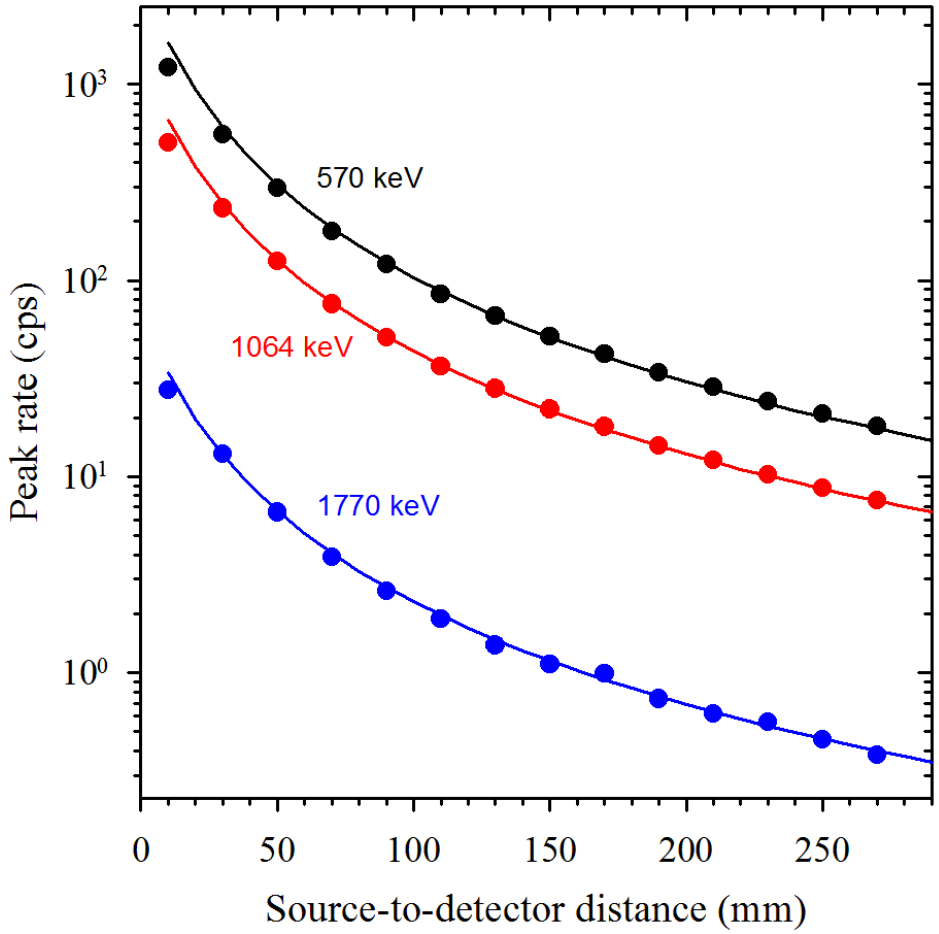

Fig. 2. Measured and calculated LBC detector efficiency as a function of source-to-detector distance.

Since it was established that CYLTRAN calculations are in excellent agreement with measurements on the absolute scale, the remaining calibration measurements and related calculations were compared by renormalizing one set of results relative to the other. Fig. 2 shows how the efficiency (which is proportional to the peak counting rate) depends on the source-to-detector distance. Again, the agreement between the measurements and the calculations is found to be excellent. Fig. 3 shows the efficiency dependence on the source offset from the detector axis for the same distance along the axis. The agreement between the measurements and the calculations is excellent in this case as well.

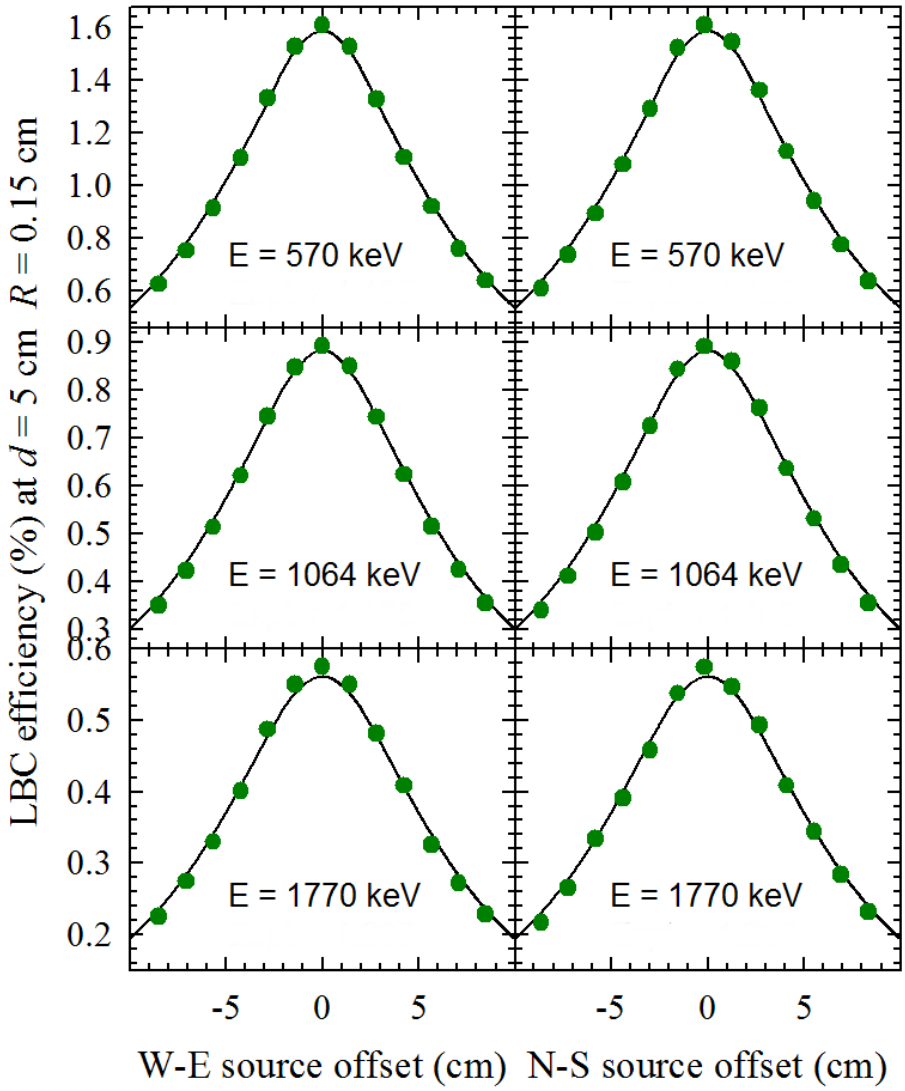

Fig. 3. Measured and calculated LBC detector efficiency as a function of source offset from the detector axis.

[1] https://www.berkeleynucleonics.com/lanthanum-bromochloride

[2] https://scionix.nl/high-resolution-lbc-scintillators/

[3] https://cyclotron.tamu.edu/see/

[4] https://www.berkeleynucleonics.com/bmca-ethernet

[5] https://www.berkeleynucleonics.com/basic-spectrometry-software

[6] https://www.berkeleynucleonics.com/bgamma-software-package

[7] J.A. Halbleib and T.A. Mehlhorn, Nucl. Sci. Eng. **92**, 338 (1986), J.A. Halbleib, R.P. Kensek, T.A. Mehlhorn, G.D. Valdez, S.M. Seltzer, and M.J. Berger, CYLTRAN 3.0, Sandia National Labs (Albuquerque, NM), Report SAND91-1634 (1992).

[8] https://www.gammadata.se/products/radiation-detection/radioactive-sources/beta-standards/conversion-electron-sources/

Design and testing of YAP:Ce array for DAPPER

A. Abbott, M. Sorensen, A.B. McIntosh, R. Wada, and S.J. Yennello

An array of cerium-doped yttrium aluminum perovskite (YAP:Ce) scintillators has been designed and tested for use in DAPPER (the **D**etector **A**rray for **P**hotons, **P**rotons, and **E**xotic **R**esidues) for the purpose of obtaining a TOF measurement to distinguish fusion events from interesting (d,p) products. DAPPER will measure photons emitted from excited ^{58}Fe nuclei from a ^{57}Fe(d,pγ)^{58}Fe reaction in inverse kinematics with future plans to measure the ^{59}Fe(d,pγ)^{60}Fe reaction. The target is CD_2 and fusion is possible with the carbon. The YAP:Ce array is positioned approximately 80 cm from the target position which would give a 3 ns separation in the flight time between the fusion and (d,p) centroids. YAP:Ce is a radiation hard, fast timing detector that has been shown to take up to 2.5E9 pps of ^{63}Cu for 10 minutes without a noticeable reduction in the rise time of the signals. The rise time is typically around 2-3 ns when coupled to a Hamamatsu 1924A photomultiplier tube (PMT). New active bases were constructed in order to improve the saturation rate for these detectors.

In a previous test run [1], the saturation rate of a YAP:Ce detector was tested using a beam of ^{84}Kr at 7.5 MeV/u. When placed at 0 degrees and using various bases coupled to a Hamamatsu 1355 PMT, the maximum rate achieved on the detector was 1.7E6 pps. This was achieved using the lowest resistance base and with the lowest operating voltage (-800 V). In order to improve performance, new bases were built using a template for active bases [2]. High (HR), mid (MR), and low (LR) resistance bases were constructed for the 1924A PMTs to be tested with a beam of ^{63}Cu at 7.5 MeV/u accelerated down the K150 SEE line. A temperature sensor made contact with the active base during the run in order to monitor the performance of the detector as temperatures increased.

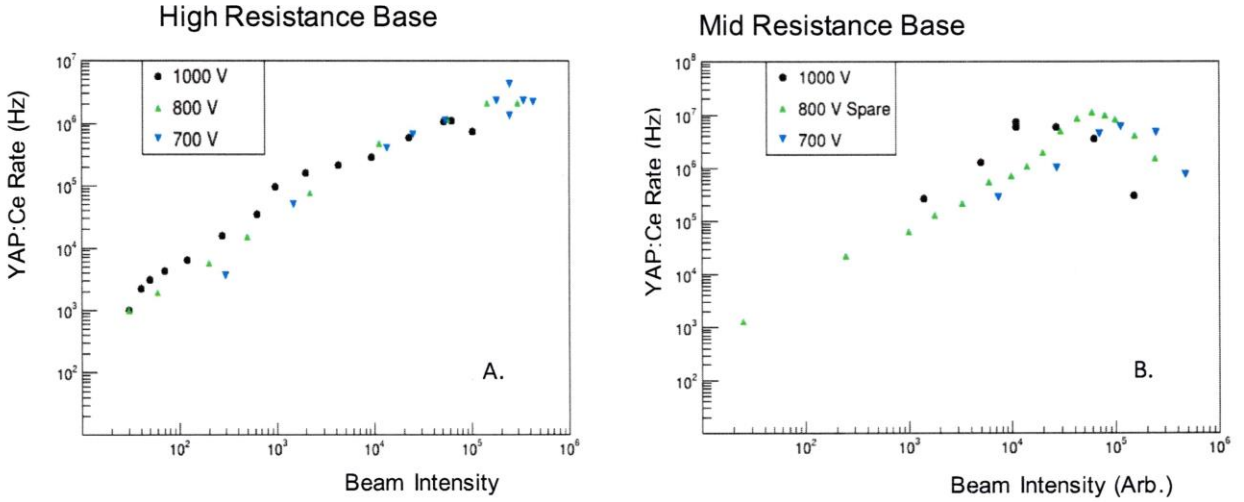

Fig. 1. The resulting YAP:Ce saturation rate as a function of the beam rate measured by a plastic scintillator for both the high (A) and mid (B) resistance bases at various voltages. The HR base achieved a maximum 1.2E6 pps at 700 V while the MR base achieves 1.0E7 pps around 800 V.

Fig. 1 shows the improved saturation rate achieved by the MR base compared to the HR. The LR base saturated around the same rate as the MR but generated more heat during the run. This higher heat

can damage the circuit and render the base unusable so the MR base was chosen for the array. During this test, the full beam of ^{63}Cu (2.5E9 pps) was delivered to the YAP:Ce detector for 10 minutes after which some damage was indicated by a shift in the integrated charge of the signals. However, within the resolution of the electronics, the rise time of the waveforms was unaffected indicating that the timing resolution was maintained.

The geometry of the array was determined given its collection efficiency for the beams. The ^{57}Fe beam is stable and the beam is quite symmetric when delivered through MARS. The radioactive ^{59}Fe beam has an asymmetric beam divergence which affects the spread of the reaction products. A simple toy model was built to look at the spread of the products for both the stable and radioactive beams and the resulting collection efficiency of the array for various geometries.

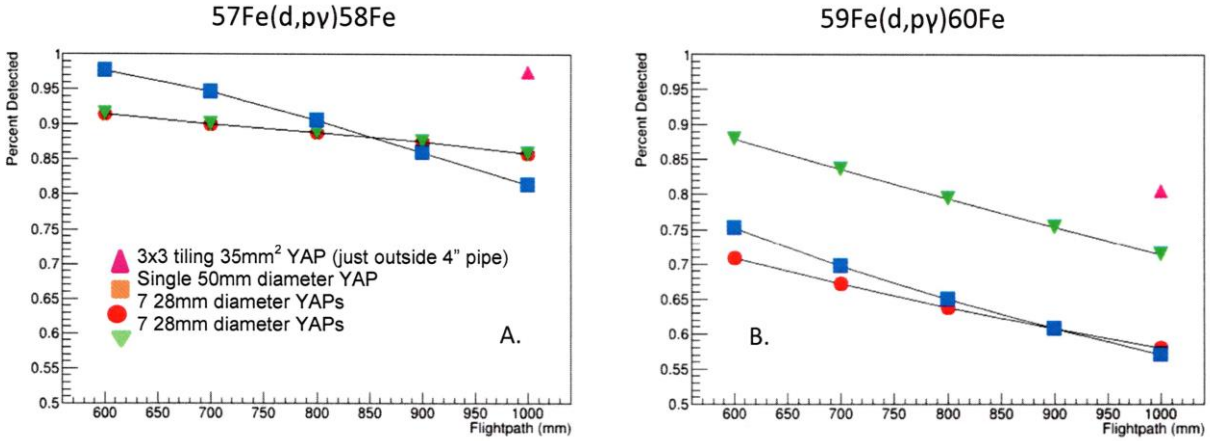

Fig. 2. Percent of residues collected given the geometry of the YAP:Ce array for the stable beam (A) and the radioactive beam (B) as a function of the distance of the array from the target position.

The geometry ultimately chosen (Fig. 3) gives flexibility in the distance from the target position as it can fit within the 4" beam pipe and can be oriented in such a way that improves the collection efficiency for the future radioactive beam experiment while not sacrificing efficiency for the stable beam.

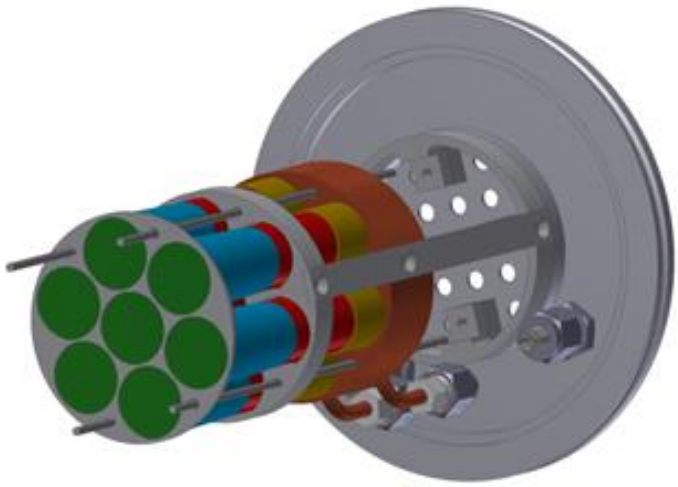

Fig. 3. CAD drawing of the YAP:Ce array. The green circles represent the YAP:Ce crystals, the blue cylinders are UVT light guides, the red cylinders are the 1924A Hamamatsu PMTs, and the gold pieces are the active bases. The bases are then slotted into an actively-cooled copper block (bronze).

[1] A.B. McIntosh and A. Abbott., *Progress in Research*, Cyclotron Institute, Texas A&M University (2019-2020), p. IV-72.

[2] P. Ren *et al*., Nucl. Sci. Tech. **28**, 145 (2017).

Establishing control over VO_2 phase transformations through radiation-induced defects

E.J. Braham, M. Sorensen, D. Zhao, D.A. Santos, K. Xie, and S. Banerjee

Background and introduction

Neuromorphic computing aims to emulate and surpass the energy-efficiency of the human brain but requires the design and experimental realization of an altogether new palette of neuron- and synapse-like materials. The metal–insulator transition (MIT) of VO_2 provides a sensitive and versatile vector for achieving the necessary conductance switching required to fashion the neuroemulative circuits necessary to fully realize brain-inspired computing. While the effect of point and planar defects on the transition characteristic of materials with an MIT has been recorded, several knowledge gaps exist.[1,2] In this work, we seek to elucidate the specific defects generated in VO_2 upon α-irradiation and how such defects modify their memristive response.

Methodology

Ge-doped VO_2 particles were prepared hydrothermally at 250°C through reduction of 8 mL 0.4 M vanadic acid by 3 mL isopropanol in the presence of 5—50 mg solid GeO_2 and 5 mL water followed an annealing at 550°C under Ar for 6 h. The as-prepared particles were affixed to either a silicon nitride, or silica glass membrane by drop casting which were then loaded onto an aluminum backing plate. The samples were irradiated by 3 MeV α-particle irradiation using a helium (4He) beam at a constant current under vacuum to avoid oxidation of VO2 to V_2O_5. Target irradiation doses from $9.46*10^{14}$ cm^{-2} to $6.44*10^{15}$ cm^{-2} were achieved by controlling exposure times (1 h – 10.5 h). The dynamical behavior the VO_2 particles was measured before and after irradiation exposure through differential scanning calorimetry (DSC) using a TA Instruments Q2000 instrument. Irradiation effects were imaged by transmission electron microscopy (TEM) using an FEI Tecnai TEM operated at 200 kV.

Results and discussion

Fig. 1 shows the heating and cooling transitions of Ge-doped VO_2 upon cycling at a heating and cooling rate of 10°C/min from 0°C to 100°C for the unirradiated samples (Figs. 1A and 1C) and from 0°C to 150°C for the irradiated samples (Figs. 1B and 1D). Fig. 1B ($9.46*10^{14}$ cm^{-2}) and 1D ($6.44*10^{15}$ cm^{-2}) show that the irradiation effects are manifested as a one-time depression of the heating transition temperature (Cycle 1, Figs. 1B and 1D). A return to the pre-irradiated transition temperature upon heating to 150°C is observed suggesting an annealing phenomenon which ‘heals’ the aforementioned irradiation damage (Cycle 2, Figs. 1B and 1D). Here, a shift in the cooling transition is not readily apparent. Moreover, the hysteresis width is not lowered which indicates that the effect of the induced damage is not easing the nucleation step of the phase transition in a way that has been previously observed for point defects

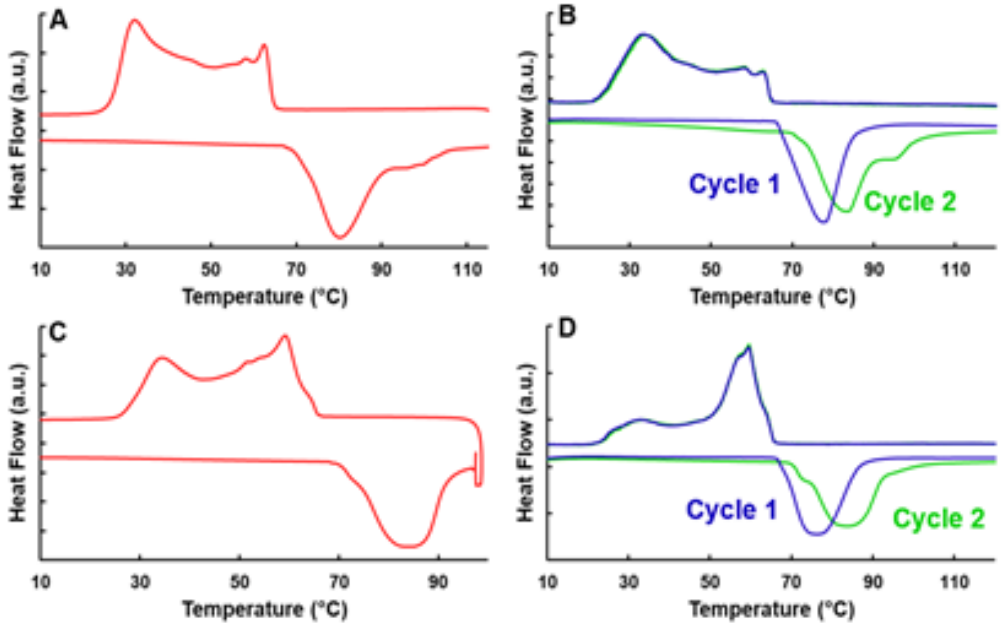

Fig. 1. DSC Cycles of Ge-Doped VO_2. A and C plot the thermograms of two independent Ge VO_2 samples prior to irradiation with alpha particles and B and D plot the same respective samples post irradiation. The Ge-Doped sample in A and B was irradiated with a dose of $9.46*10^{14}$ cm^{-2} over 1 hour and the sample in C and D was irradiated with a dose of $6.44*10^{15}$ cm^{-2} for 10.5 hours. To show the cycling behavior two cycles of the irradiated sample are shown in B and D with the first cycle in blue and the second cycle in green.

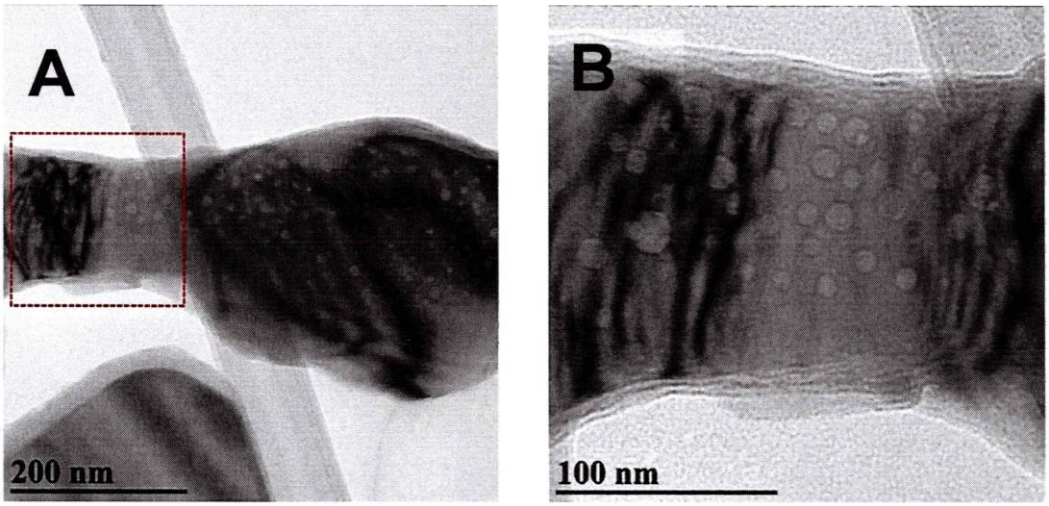

Fig. 2. (A) Voids formed inside of Ge-doped VO_2 nanoparticle after irradiation. (B) Shows a close-up view of the red boxed area in (A)

The TEM images shown in Figs. 2A and 2B reveal the formation of intraparticle voids which are likely caused by He bubble generation, (zoomed-in image of the boxed area (Fig. 2A, red) is shown in Fig. 2B. Here, the facets are most likely related to the crystallography of VO_2, wherein the atoms within

the most closely packed planes are preferentially displaced during irradiation. We postulate that the observed resetting of the heating transition temperature may result from a heat-induced evacuation of the observed He.The observations gleaned from DSC and TEM characterization suggest that while the effects of irradiation damage in Ge-doped VO_2 are significant, further experiments are required to elucidate the mechanism of their action on the MIT of this material.

[1] W. Fan, J. Cao, J. Seidel, Y. Gu, J.W. Yim, C. Barrett, K.M. Yu, J. Ji, R. Ramesh, L.Q. Chen and J. Wu, Phys. Rev. B **83**, 235102 (2011).

[2] H. Clarke, B.D. Carraway, D.G. Sellers, E.J. Braham, S. Banerjee, R. Arróyave, and P.J. Shamberger, Phys. Rev. Mater. **2**, 103402 (2018).

[3] S.H. Li, J.T. Li, and W.Z. Han, Materials (Basel) **12** (2019).

Integrator method for resistive dual-axis duo lateral position sensitive silicon detectors

A. Hannaman, A.B. McIntosh, K. Hagel, M.D. Youngs, A. Abbott, J. Gauthier, B. Harvey, Y.-W. Lui, L. McCann, L.A. McIntosh, S. Schultz, M. Sorensen, Z. Tobin, R. Wada, and S.J. Yennello

The Dual-Axis Duo-Lateral (DADL) detectors of the Forward Array Using Silicon Techbology (FAUST) are position sensitive silicon detectors that measure the position of incident particles through resistive charge splitting [1]. Vertical position information is obtained by measuring the charge collected on the contacts F1 (bottom) and F2 (top) while horizontal position information is obtained by measuring the charge collected on contacts B1 (left) and B2 (right) as shown in Fig. 1(a). Prior work has shown that conventional pulse processing methods yield position and energy non-linearities [2,3]. To this end, the summed trigger analysis method was developed to significantly reduce these distortions by measuring the charge for all contacts in a region of the pulse absent of distortion effects and over the same time interval as outlined in Fig 1(b) [4]. While this method provides excellent position and energy resolution, the requirement of writing out waveforms can be prohibitive due to immense data storage and event rate saturation. An upcoming experiment that will measure the 7-α breakup of ^{28}Si requires data collection rates unobtainable using this method. This work presents a new method that approximates the summed trigger analysis method using the eight integrators of the Struck SIS3316 waveform digitizer.

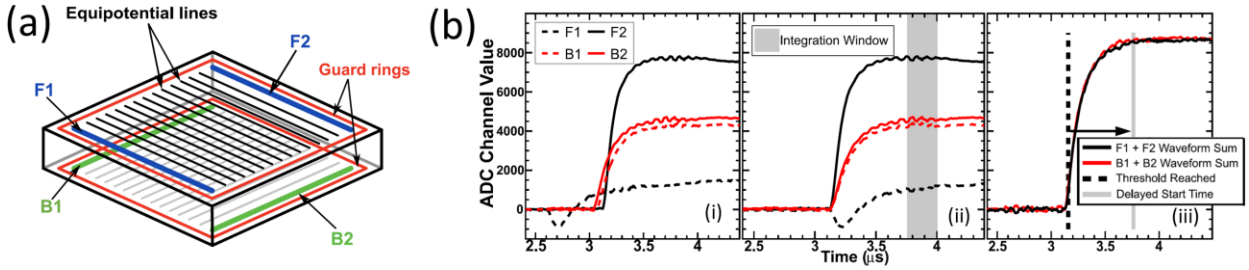

Fig. 1. (a) Schematic of a DADL detector. Charge is collected on the contacts F1 and F2 on the front face and B1 and B2 on the back face. The equipotential conductive lines help facilitate charge movement and the guard rings help to prevent charge bleeding. (b) Summed trigger analysis method. (i): Waveforms from the four contacts for a single event aligned based on their trigger time. (ii): Waveforms have been shifted in time based on the 3316 digitizer time stamp relative to F2. (iii): Sum of time shifted front (black) and back (red) waveforms. The time that the summed waveform reaches threshold (dashed line) is delayed by 0.6 μs (gray line) and is used as the integration start time in panel (ii). Reproduced from Ref [4].

The eight integrators of the 3316 have a start time that can be set relative to the internal trigger of each channel. One integrator is used to calculate the baseline of the waveform. In the summed trigger analysis method, the integration start time is found by applying a 0.6 μs delay to the time that the sum waveform for a given face (i.e., F1 + F2) reaches a threshold above noise. In Fig. 2(a), the F1 and F2 waveforms result from a particle incident near the top or bottom edge of the detector. The two waveforms are displayed based on when they trigger, where F1 triggers just as it deviates from baseline while the F2 trigger occurs roughly 0.5 μs past its deviation from baseline. For any given position, the waveform that triggers earliest in time will have less of the bimodal feature of F2 that causes late triggering. This gives a trigger time for F1 that will approximate well the summed waveform threshold time due to its sharp rise

and qualitatively same shape as the summed waveform. Therefore, an integrator that starts 0.6 μs after the internal trigger is used for the waveform that has the earlier trigger time, in this case F1. However, due to the later triggering of smaller, distorted pulses such as F2, this delayed integrator will begin integration later than it would using the summed trigger analysis method. To accommodate, the remaining integrators can be set to begin integration in 72 ns intervals before the first delayed integrator shown by the blue lines in Fig. 2(a). By comparing the trigger time between the two waveforms, the ideal integrator can be chosen for the smaller waveform.

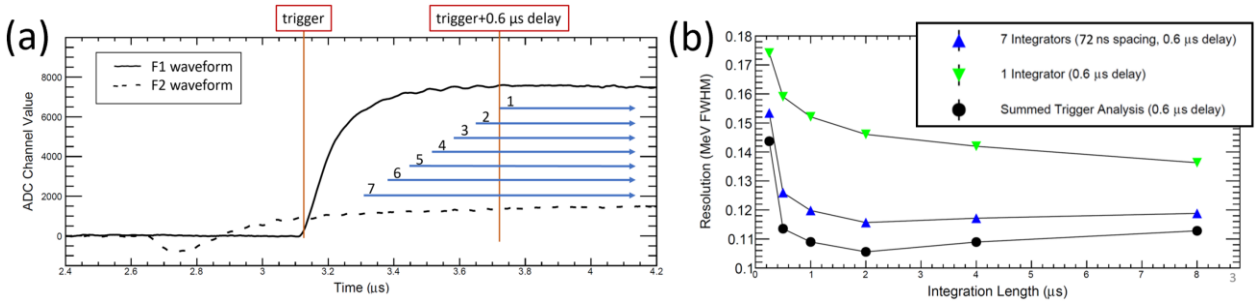

Fig. 2. (a) Integrator method: Waveforms from F1 and F2 for a single event displayed based on their trigger time. The trigger time and first delayed integrator are shown by the red vertical lines. The integration range of the seven integrators are shown as blue arrows. (b) Resolution (MeV FWHM) using a ^{228}Th source comparison between the integrator method, summed trigger analysis method, and a single integrator as a function of the integrator length. Statistical error bars are smaller than the data points.

^{228}Th source data on a DADL detector was used to compare the integrator method to the summed trigger analysis method, and to optimize the integration length for energy resolution as shown in Fig 2(b). A 2 μs integration length gives the best resolution (107 keV for the summed trigger analysis method, 117 keV for the integrator method). To observe the importance of integrating both waveforms over the same interval in time, the resolution obtained from only using one delayed integrator for all waveforms is shown in green. By incorporating additional integrators to compensate for differing pulse shapes and trigger times, the resolution is improved by roughly 50%. Additionally, the use of the integrators over the summed trigger analysis method has been found to have no observable effect on the quality of the position reconstruction. The small sacrifice in energy resolution is levied by the reduction in data storage and increase in data collection rates.

This integrator method was used with the two outermost rings of FAUST (D and E) to measure reaction products from ^{20}Ne on ^{12}C at 17 MeV/u to observe the quality in particle identification prior to full implementation. Isotopic resolution was achieved up through oxygen as seen in Fig. 3. Given the excellent quality in particle identification and retention of good position and energy resolution, this method will be used in an upcoming experiment scheduled that will measure the excitation function for the 7-α breakup of ^{28}Si in the search for high excitation resonance peaks that could possibly be attributed to toroidal nuclei.

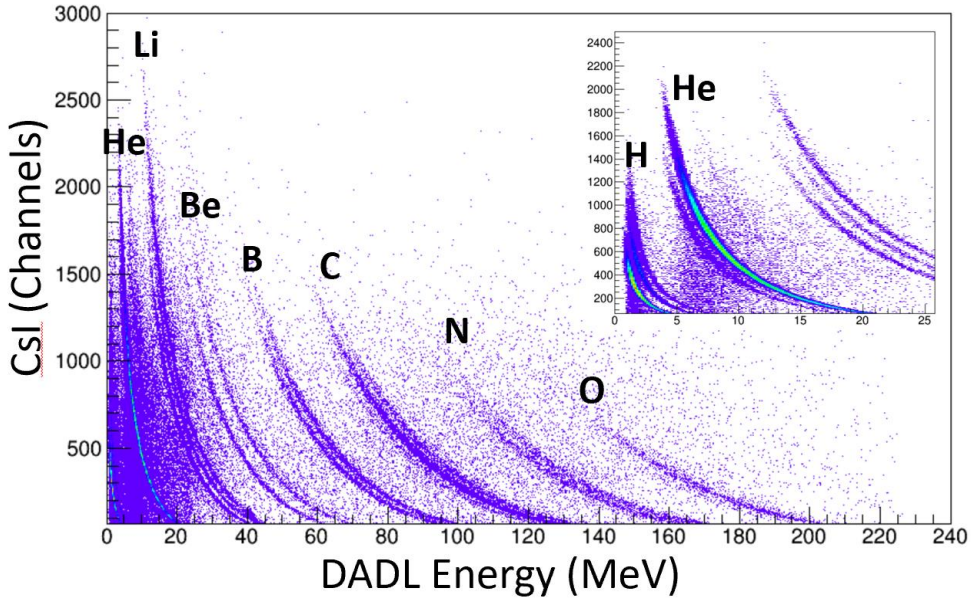

Fig. 3. DADL energy (MeV) as a function of CsI (Channels) for a single detector telescope in ring D of FAUST of reaction products from 17 MeV/u ^{20}Ne on ^{12}C. The inset shows a zoomed in view of H and He isotopes.

[1] S.N. Soisson *et al.,* Nucl. Instrum. Methods Phys. Res. **A613**, 240, (2010).

[2] L.A. Heilborn, PhD thesis, Texas A&M University, 2018, http://hdl.handle.net/1969.1/174435.

[3] L.A. McIntosh *et al.*, Nucl. Instrum. Methods Phys. Res. **A985**, 164642, (2021).

[4] M.W. Aslin, A. Hannaman, *et al.*, Nucl. Instrum. Methods Phys. Res. **A985**, 164674 (2021).

.

Light charged particle correlations in ^{78,86}Kr+^{12}C

A.B. McIntosh, L.A. McIntosh, K. Hagel, and S.J. Yennello

The experiment to measure the asymmetry dependence of the nuclear caloric curve using fusion reactions of ^{78,86}Kr + 12C @ 15, 25, 35 MeV/u is a rich data set and can allow for other analysis. Light charged particles are measured with good energy and position resolution over a large angular range, which allows correlation functions to be investigated. Correlation functions with the DADL-upgraded FAUST [1,2] were used to measure proton-proton correlation functions.

Here, investigation of LCP correlations in the Kr+C data set begins with alpha-alpha pairs. The upper left panel of Fig. 1 shows in black the relative momentum distribution of alpha-alpha pairs from the ^{86}Kr+^{12}C @ 35 MeV/u. For events with more than two alpha particles, all pair-wise combinations are used. The peaks at roughly 20, 50, and 100 MeV/c correspond to ^{8}Be(g.s.), ^{9}Be(2.43MeV) and ^{9}Be(3.03MeV), respectively. The uncorrelated background due primarily to sequential alpha particle emission is assessed using the mixed event technique. Alpha particles are randomly paired with the requirement that the two did not come from the same event or hit the same detector. Crucial in this is the accounting of the alpha particles: each time an alpha particle is used to add a count to the true relative momentum distribution, it must also be added to the list for generating mixed events. Thus for an event with four alpha particles, each of these alpha particles must be added to the list for mixing three times, not

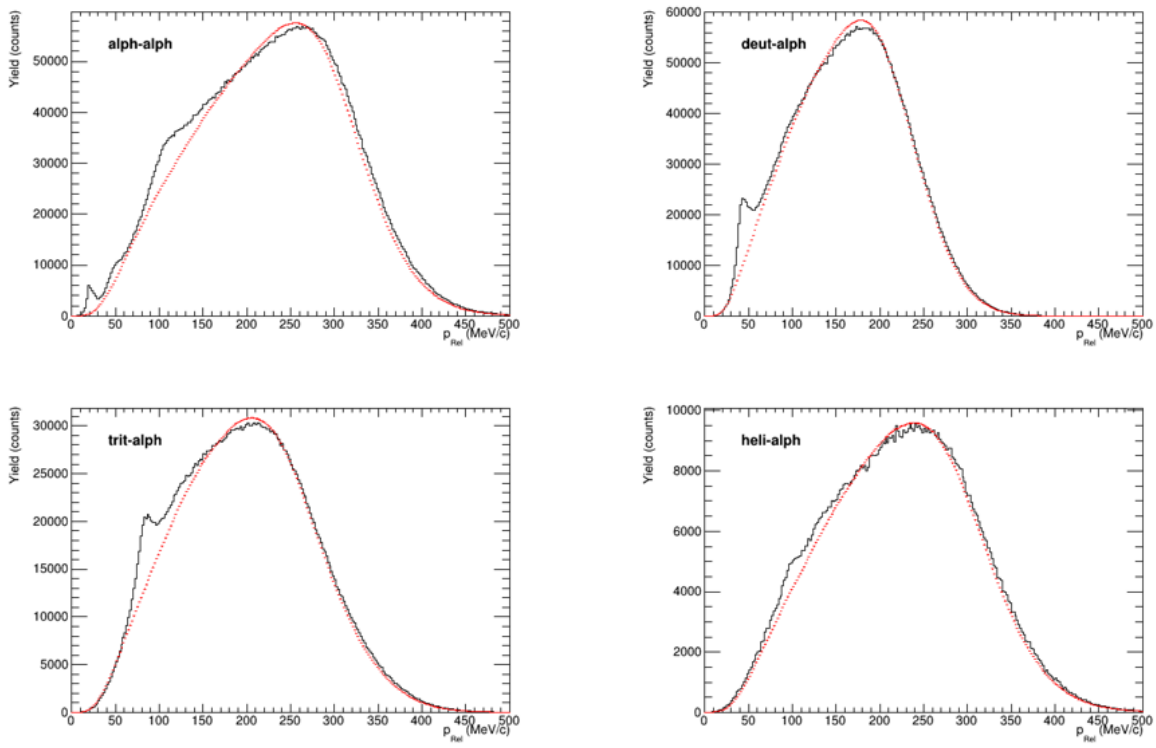

Fig. 1. Relative momentum distributions for four LCP pairs, and their mixed event background, for 86Kr+12C @ 35 MeV/u.

just one. Failure to account for the multiplicity in this way results in significant underprediction of the background at high relative momentum, and significant overprediction at low relative momentum, and is most severe for the lowest beam energies. The resulting mixed event background is shown in red. The three resonant states are clearly discernible over the mixed-event background. Fig. 1 also shows relative momentum distributions for other LCP pairs: d-a, t-a, and h-a. Each of these has a clear excess in yield at a known relative momentum [3]. These states are observed to somewhat lesser degrees as beam energy decreases. The yield of the ^{9}Be state is much reduced for the less neutron-rich beams. Resonant states can allow extraction of temperature through excited state populations (see e.g. [4] and references therein), or manifestation of tidal forces for short-lived states that decay in the field of the source that emitted them [5].

[1] L.A. McIntosh, Ph.D. Thesis, Texas A&M University, 2018.

[2] L.A. McIntosh, A.B. McIntosh, K. Hagel, M.D. Youngs, L.A. Bakhtiari, C.B. Lawrence, P. Cammarata, A. Jedele, L.W. May, A. Zarrella, and S.J. Yennello, Nucl. Instrum. Methods Phys. Res. **A985**, 164642 (2020).

[3] J. Pochodzalla, C.K. Gelbke, W.G. Lynch, M. Maier, D. Ardouin, H. Delagrange, H. Doubre, C. Grégoire, A. Kyanowski, W. Mittig, A. Péghaire, J. Péter, F. Saint-Laurent, B. Zwieglinski, G. Bizard, F. Lefèbvres, B. Tamain, J. Québert, Y. P. Viyogi, W.A. Friedman, and D.H. Boal, Phys. Rev. C **35**, 1695 (1987).

[4] H. Xi, W.G. Lynch, M.B. Tsang, W.A. Friedman, and D. Durand, Phys. Rev. C **59**, 1567 (1999).

[5] A.B. McIntosh, S. Hudan, C.J. Metelko, R.T. de Souza, R.J. Charity, L.G. Sobotka, W.G. Lynch, and M.B. Tsang, Phys. Rev. Lett. **99**, 132701 (2007).

Online calibration, particle ID, and analysis for FAUST and other large multi-detector arrays in nuclear physics

A.B. McIntosh, A. Hannaman, and K. Hagel

An experiment to measure products from ^{28}Si + ^{12}C collisions at 35MeV/u using the Forward Array Using Silicon Technology (FAUST) [1-3] was recently conducted. A new "multi-event" [4] readout was deployed to dramatically reduce deadtime and allow high counting rate. This readout required accurate time stamping of digitized data which must be subsequently time-matched. In principle, the observation of isotopic lines in the *ΔE-E* plots indicates that this is being achieved to some degree. But since the measurement was aimed at looking for the high-multiplicity 7-α breakup of excited "toroidal" states in ^{28}Si, data packet matching must be working correctly and very efficiently. To this end, I developed a new online calibration and particle ID toolset as additional verification early in the experiment that the data was being recorded as desired. This toolset can be adapted and deployed for other multi-detector arrays.

First, the energy calibration of the silicon detectors was established using a ^{229}Th source (any multi-line source would work). These are fit automatically with a multi-gaussian function which assumes all peaks have the same width, and that the spacing between the peaks given by the true energies, modified by the dead layers, is preserved modulo a gain and offset. All peak amplitudes are independent. Thus for N peaks the function has N+3 degrees of freedom. (I had recently built this functionality for the silicon detector of DAPPER). Fig. 1 shows a typical spectrum with resulting fit. The gain and offset from the fit constitutes the linear calibration of the silicon detector.

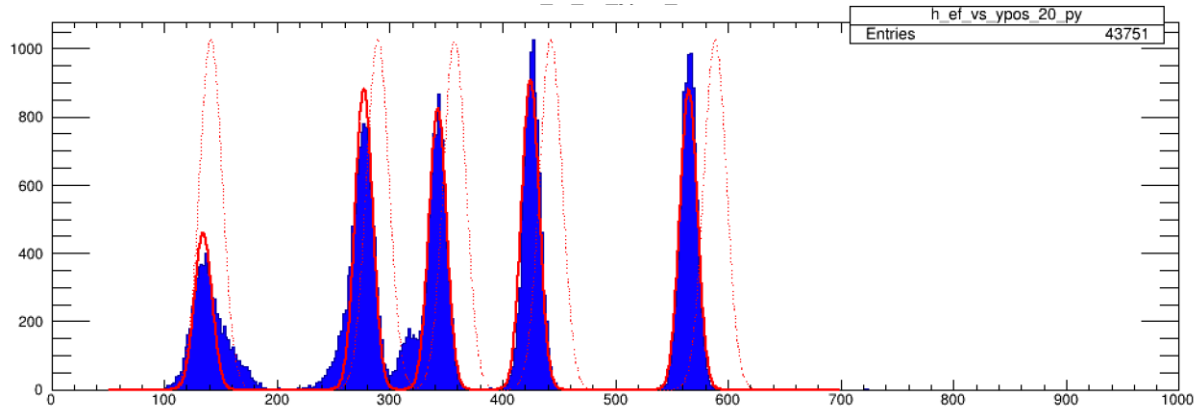

Fig. 1. ^{229}Th spectrum (blue), initialization of multi-gaussian function (dashed red) and resulting multi-gaussian fit (solid red); the last constitutes the online calibration.

Second, particle ID must be done, as the CsI cannot be accurately calibrated without it. Since the spectrum of ΔE vs E exhibits points along a locus described (approximately) by hyperbolas, plotting the data in log-log scale gives (approximately) straight lines. For our purposes, identification of alpha particles is most important and, fortunately, easiest. The log-log distribution is shown in Fig. 2 in black, the dominant yield is alpha particles. The profile, <log(ΔE)> vs log(E) is shown in blue and is fit with a line. A narrow selection around this line allows selection of alpha particles with some contamination,

mostly from 3He. Thus, sufficient particle ID is achieved for online high-multiplicity alpha particle analysis.

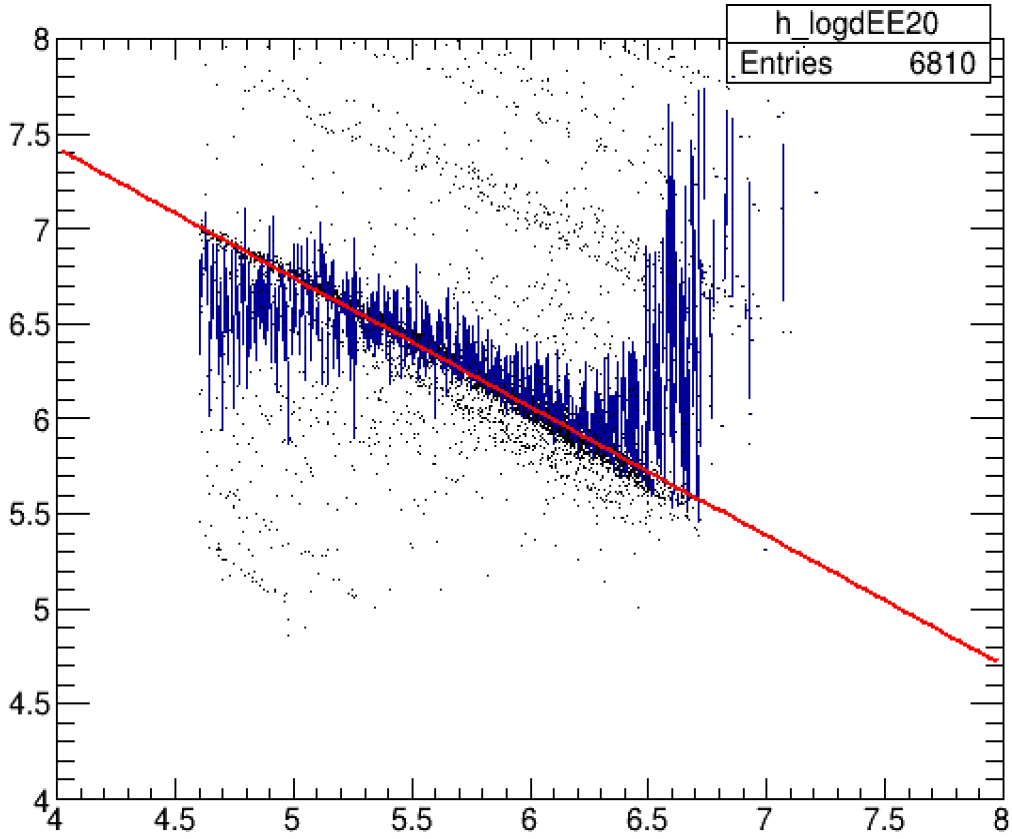

Fig. 2. log(ΔE) vs log(E) in black. The profile, <log(ΔE)> vs log(E) is shown in blue and fit with a linear function. The vertical distance to this function constitutes the particle ID parameter, and a gate of constant width around this red line selects only alpha particles (with some 3He contamination).

Next, the CsI detectors are calibrated using the known energy in the silicon, the thickness of the silicon, the particle type (just alpha particles) and energy loss calculations (using CycSrim [5,6]). The deduced energy deposited in the CsI is nearly linear as a function of the measured signals from the CsI detector, and a fit to this correlation comprises the CsI energy calibration.

The position of each particle is determined as in the previous FAUST-DADL experiments, using the known positions of the detectors, and the four signals from each silicon to establish the local position within each silicon detector [3]; the local scaling parameters were increased to adjust for the use of the long integration of the signals [7]. To check the position calibration, a precision slotted mask was placed between a collimated source and the detectors; stripes were observed across the global position projection as expected as shown in Fig. 3.

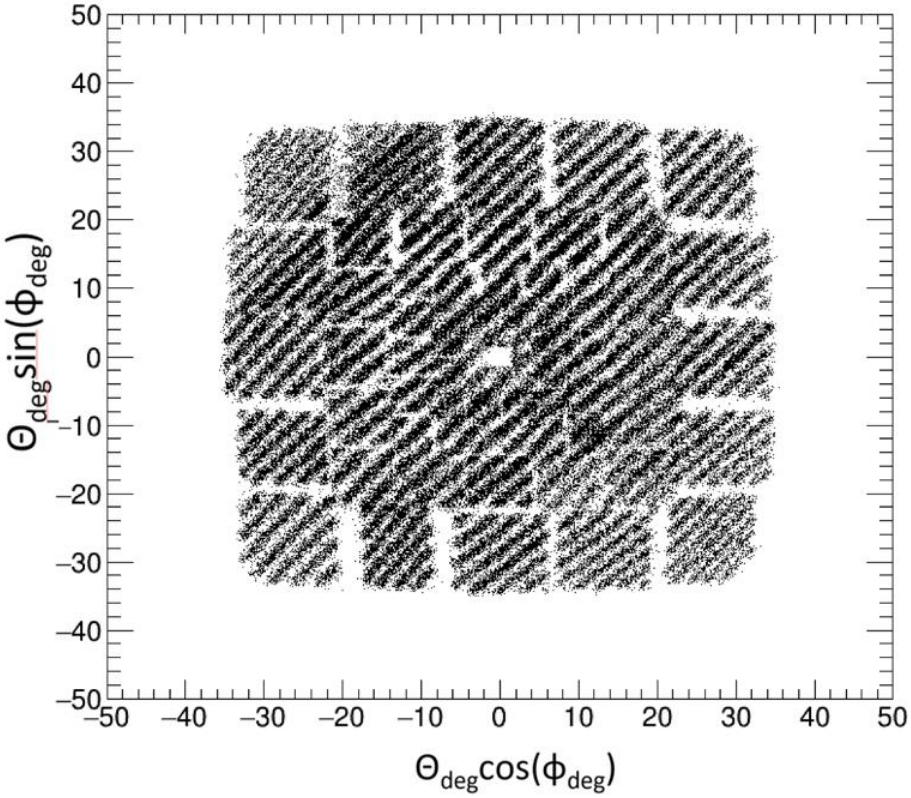

Fig. 3. Global position projection (φ sin(θ) vs φ cos(θ)) obtained from a collimated ^{229}Th source with the precision slotted mask.

This calibration allowed us see, online, ^{8}Be(gs,3.03), ^{9}Be(2.43MeV), and ^{12}C(7.6, 9.6) peaks in relative energy distributions shown in Fig. 4, and to verify that the relative energy distribution for 7-alpha

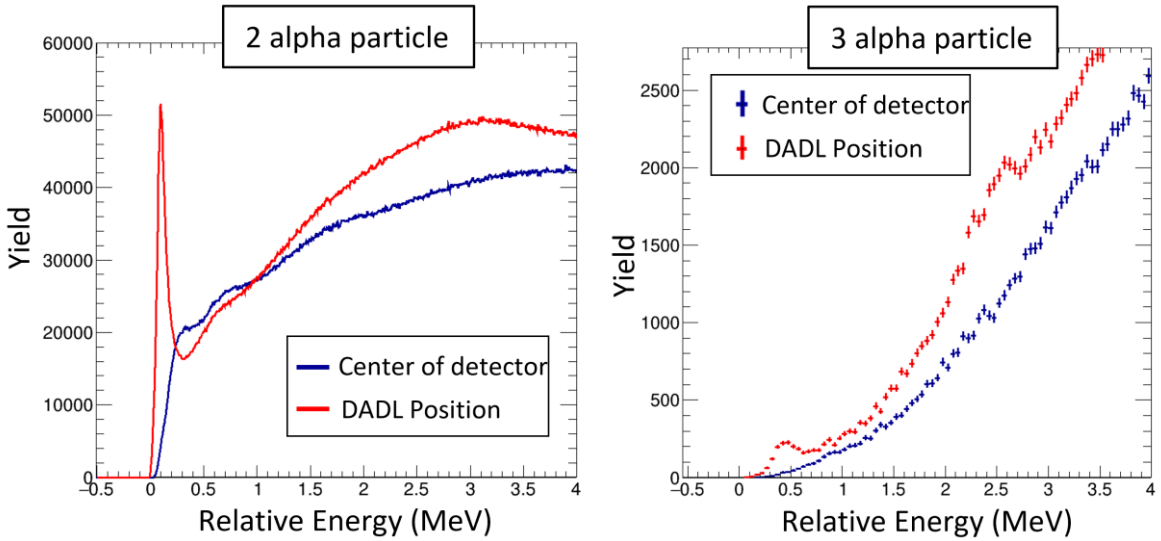

Fig. 4. Preliminary relative energy distributions for two alpha particles (left) and three alpha particles (right) for true events (red) and mixed events (blue) obtained with the quick online calibration and analysis toolkit.

events in fact covered a similar energy range as the previous NIMROD experiment in which possible signals of toroidal states were observed [8]. It also allowed us to see that for all alpha multiplicities, the energy per nucleon of the center of mass of all measured alpha particles (shown in Fig. 5) was peaked between 22-24 MeV, significantly damped from beam energy of 35 MeV/u, suggesting incomplete fusion as a significant reaction mechanism.

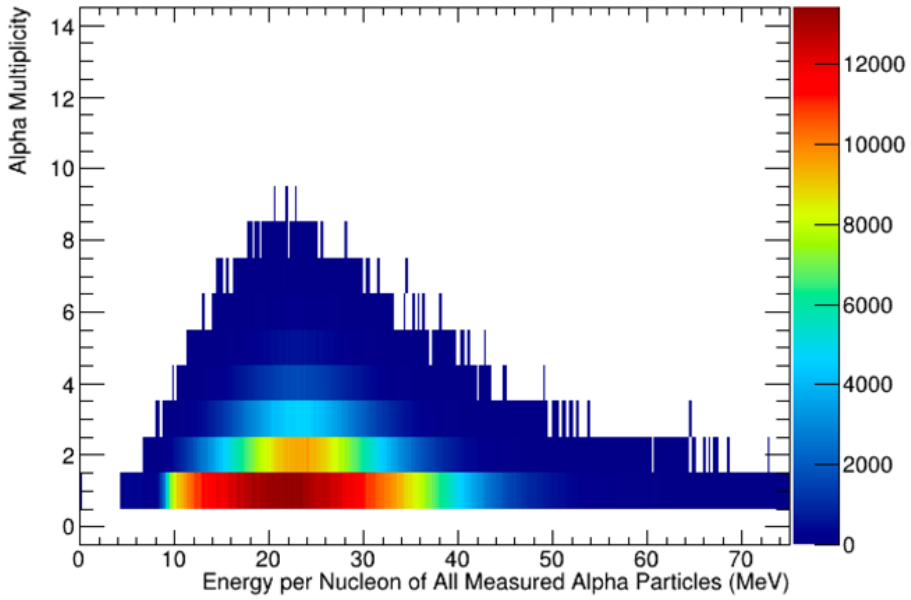

Fig. 5. Alpha multiplicity vs total energy per nucleon of all alpha measured particles. Significant damping from beam energy suggests incomplete fusion may be dominant.

Further development of online particle ID is the limiting step to a more complete online analysis, and investigation into an automated method of that is underway both for identification of Z and possibly A. At present, this online tool package has succeeded in indicating that the present high-rate data set obtained with multi-events does preserve the physical events, packaging them, at least to a large extent, into proper corresponding data events.

[1] F. Gimeno-Nogues, D.J. Rowland, E. Ramakrishnan, S. Ferro, S. Vasal, R.A. Gutierrez, R. Olsen, Y.-W. Lui, R. Laforest, H. Johnston, and S.J. Yennello, Nucl. Instrum. Methods Phys. Res. **A399**, 94 (1997).

[2] S.N. Soisson, B.C. Stein, L.W. May, R.Q. Dienhoffer, M. Jandel, G.A. Souliotis, D.V. Shetty, S. Galanopoulos, A.L. Keksis,S. Wuenschel, Z. Kohley,S.J. Yennello, M.A. Bullough, N.M. Greenwood, S.M. Walsh, and C.D. Wilburn, Nucl. Instrum. Methods Phys. Res. **A613**, 240 (2010).

[3] L.A. McIntosh, A.B. McIntosh, K. Hagel, M.D. Youngs, L.A. Bakhtiari, C.B. Lawrence, P. Cammarata, A. Jedele, L.W. May, A. Zarrella, and S.J. Yennello, Nucl. Instrum. Methods Phys. Res. **A985**, 164642 (2020).

[4] K. Hagel *et al.*, *Progress in Research*, Cyclotron Institute, Texas A&M University (2020-2021), p. V-58.
[5] L.C. Northcliffe and R.F. Schilling, Nucl. Data Tables **A7**, 233 (1970).
[6] F. Hubert, R. Bimbot, and H. Gauvin, At. Data Nucl. Data Tables, **46**, 1 (1990).
[7] M.W. Aslin, A. Hannaman, M.D.Youngs, A.B.McIntosh, A. Abbott, P.Adamson, J. Gauthier, K.Hagel, A.Jedele, Y.-W.Lui, L.A.McIntosh, M.Q.Sorensen, Z.N.Tobin, R.Wada, A.Wakhle, and S.J. Yennello, Nucl. Instrum. Methods Phys. Res. **A985**, 164674 (2020).
[8] X. G. Cao, E. J. Kim, K. Schmidt, K. Hagel, M. Barbui, J. Gauthier, S. Wuenschel, G. Giuliani, M. R. D. Rodriguez, S. Kowalski, H. Zheng, M. Huang, A. Bonasera, R. Wada, N. Blando, G. Q. Zhang, C. Y. Wong, A. Staszczak, Z. X. Ren, Y. K. Wang, S. Q. Zhang, J. Meng, and J. B. Natowitz, Phys. Rev. C **99**, 014606 (2019).

.

Testing a diamond detector for use in DAPPER

M. Sorensen, A. Abbott, A.B. McIntosh, Z. Tobin, K. Hagel, R. Wada, and S.J Yennello

As compared to silicon detectors diamond detectors have a higher displacement energy, which makes them more radiation hard, their signals have faster rise time, and their large band gap keeps their dark current low even at higher voltages. The combination of good energy resolution, excellent time resolution and improved radiation hardness make diamond detectors attractive as a potential ΔE detector for beam identification. Known disadvantages of diamond detectors are their higher cost, small single crystalline size and larger pulse height defect than their silicon counterparts [1]. Additionally, there is some evidence that diamond detectors' large radiation hardness as compared to silicon diminishes for lower energy beams [2-4].

If the diamond detector exhibits high radiation hardness along with sub 3% FWHM energy resolution for incident particle rates of 10^5 pps it would make an excellent beam purity detector for the DAPPER array (Detector Array for Photons Protons, and Exotic Residues). The measurement of the ^{60}Fe's photon strength function is hampered by the presence of cobalt contamination present in the ^{59}Fe secondary beam. A ΔE measurement of the beam before it reaches the CD_2 target would allow for the cobalt contamination to be gated out. The limited data on the performance of the diamond detectors at various rates of low energy heavy ion beams motivated this study to see if the detectors could operate in this capacity.

The diamond detectors were characterized using sources and then used in beam experiments consisting of both low and high rates of low energy heavy ions. The energy resolution of the detector was monitored closely, as a representative of the radiation hardness, as well as other effects like pulse-height defect and polarization.

In order to test the characteristics of diamond detectors at high beam rates, a test was done using a 4.5 mm x 4.5 mm 20 μm thick single crystalline chemical vapor deposited (sCVD) diamond detector supplied by Applied Diamond, Inc. A beam of ^{78}Kr accelerated to 7.5 MeV/u impinged the diamond detector and a ^{39}K beam contaminant was used as a calibration point. In this test, two preamps were used in order to monitor both the event rate and energy resolution of the detector. An Ortec 412 preamplifier was used to monitor the resolution of the detector via the alpha particles from a ^{228}Th source placed near the detector during low beam rates. In order to monitor the high ^{78}Kr beam rates on the detector, a Caen 1425 preamplifier was used due to the signals fast rise and fall times. The energy resolution and polarization effects at various applied voltages were investigated at low and high beam rates. After the ^{78}Kr beam test, a lab test was done using a ^{228}Th source, and a 300 μm Dual-Axis Duo-Lateral (DADL) detector in order to characterize the variance of the permanent damage across the area of the diamond detector.

When the diamond detector was subjected to a modest rate of ^{78}Kr it began to exhibit signs of polarization. This affect was previously demonstrated with a strong ^{90}Sr positron source in [5] with scCVD diamond detectors. This polarization effect has been shown to be reduced by increasing the electric field via the applied voltage on the detector. This relationship is shown in Fig. 1. At 430 pps on the diamond biased to 28 V (1.4 V/μm), there is a stable response of the ^{78}Kr peak position (shown by the

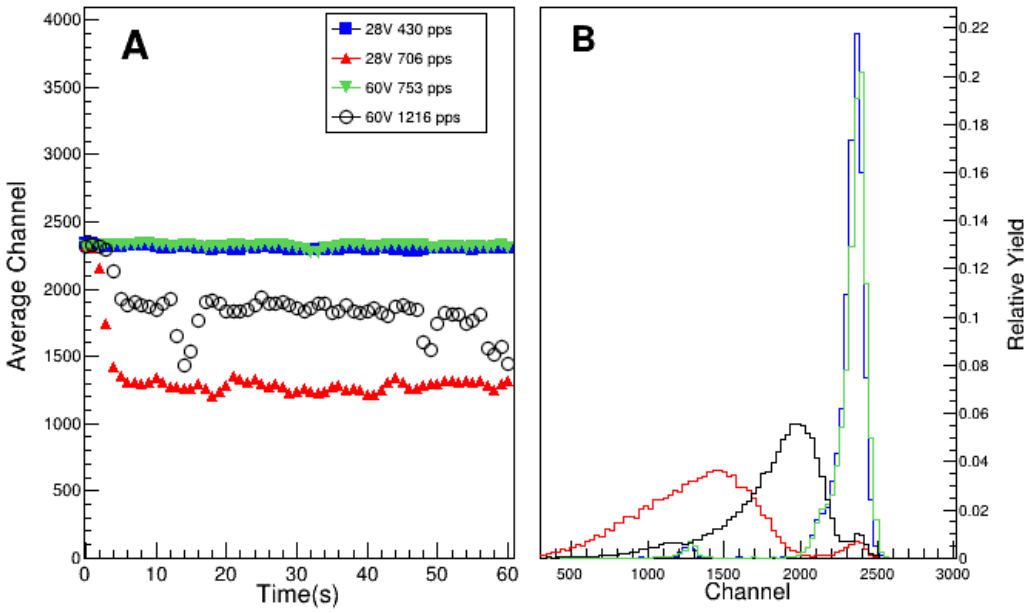

Fig. 1. The average channel number observed in the diamond detector as a function of time. At 28 V the diamond detector has a stable response at 430 pps (blue squares), but at 706 pps (red triangles) it shows a degradation in pulse height until it plateaus at a new equilibrium value, though with much larger fluctuations. Increasing the voltage to 60 V makes the diamond response stable again even at 753 pps (green point-down triangles). However, when the beam rate was subsequently increased to 1216 pps (black open circles), degradation in pulse height was seen again. B). The spectrum observed in the diamond for the same runs as in A). When the pulse height degraded, the energy resolution also suffered.

blue squares). When the beam rate is increased to 706 pps, the polarization effect begins to affect the electric field in the detector resulting in the degradation of the pulse height to a new equilibrium (red triangles) until the applied voltage is increased to 60 V (3 V/μm). At this higher voltage, the pulse height is stable even at 753 pps. However, once again an increase in the beam rate to 1216 pps (black circles) results in the polarization of the detector. When attempting to increase the voltage on the detector past this point, evidence of dielectric breakdown was observed.

After the completion of the high rate beam tests, the long term effects of the high rate on the performance of the sCVD diamond detector was investigated using a ^{228}Th source. Prior to the beam run, an alpha spectrum was taken at 4 V in order to get pristine data (Fig. 2 blue curve). After the ^{78}Kr beam an alpha spectrum was taken with the same detector and same electronics test at both 4 V and 40 V (green and black curves respectively). A significant decrease in energy resolution is observed in the alpha source data indicating permanent damage had been done to the detector, with the increase in voltage giving a modest improvement. The diamond DADL telescope test showed that this degradation in the energy

resolution is not primarily due to differences in the charge collection efficiency (CCE) across the area of the diamond.

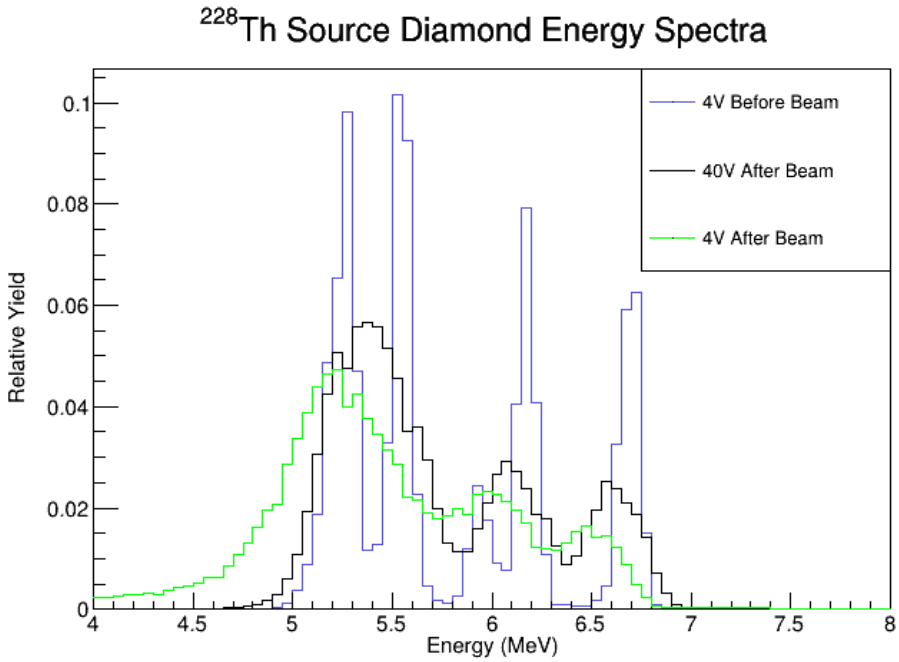

Fig. 2. ^{228}Th alpha spectra in Diamond-DADL telescope configuration. Black is the ^{228}Th spectra with the diamond biased to +40 V while in green it is biased at +4 V. In blue is the same detector biased at +4 V before the experiment.

sCVD diamond detectors have been shown to possess energy resolution sufficient for isotopic resolution up to magnesium [6]. In addition, they can simultaneously provide excellent energy resolution and timing resolution. However, they are small and expensive. Their radiation hardness appears to be superior to silicon detectors for minimally ionizing particles, however this advantage appears to diminish for higher Z beams. The strong polarization effects seen with the ^{78}Kr indicates that energy resolution quickly degrades somewhere in the 1000pps region, depending upon the voltage per micrometer that can safely be applied to the diamond detector. Diamond detectors appear to suffer from a similar issue to gas filled detectors when the rate of the charge put into them becomes too high. This means that the diamond detector will most likely perform poorly as a ΔE beam purity detector for high mass beams. This makes the diamond detector unsuitable for implementation into the DAPPER array.

[1] O. Beliuskina, A.O. Strekalovsky, A.A. Aleksandrov, I.A. Aleksandrova, H.M. Devaraja, C. Heinz, S. Heinz, S. Hofmann, S. Ilich, N. Imai, D.V. Kamanin, M. Kis, G.N. Knyazheva, C. Kozhuharov, E.A. Kuznetsova, J. Maurer, G.V. Mishinsky, M. Pomorski, Yu.V. Pyatkov, O.V. Strekalovsky, M. Träger, V.E. Zhuchko, Eur. Phys. J. A **53**, 32 (2017).
URL:https://doi.org/10.1140/epja/i2017-12223-8,doi:10.1140/epja/i2017-12223-8.

[2] A. Bhattacharya, T.A. Grotjohn, and A. Stolz, Diamond Relat. Mater. **70**, 124 (2016). URL:http://www.sciencedirect.com/science/article/pii/S0925963516305477;https://doi.org/10.1016/j.diamond.2016.10.009.

[3] W. de Boer, J. Bol, A. Furgeri, S. Müller, C. Sander, E. Berder-mann, M. Pomorski, M. Huhtinen, M., Physica Status Solidi **204**, 3004 (2007). https://doi.org/10.1002/pssa.200776327.

[4] I. Zamboni, Željko Pastuović, M. Jakšić, Diamond Relat. Materi. 31, 65 (2013). URL:http://www.sciencedirect.com/science/article/pii/S0925963512002142, doi:https://doi.org/10.1016/j.diamond.2012.11.002.

[5] Florian Robert Kassel, Ph.D. Thesis, CERN, 2017

[6] Zach Tobin *et al*. Progress in Research, Cyclotron Institute, Texas A&M University 92019-2020),p. IV-64.

.

Zero deadtime event readout for experiments at the Cyclotron Institute

K. Hagel, A. Hannaman, A.B. McIntosh, M. Sorensen, A. Abbott, A. Jedele,
M.K. Youngs, and A. Hood

Event readout in experiments at the Cyclotron Institute have historically suffered from deadtime issues resulting from the inability of the data acquisition system to acquire events while event readout is in progress. Many modern data acquisition modules, however, support multievent readout. Some modules allow the acquisition of a number of events. When the so called multievent capability is activated, the acquisition can benefit from fast streaming where larger readout lengths consisting of several events can be read out more efficiently than multiple readouts of single events with a shorter lengths. Other acquisition modules have multiple readout banks so that acquisition can occur at the same time as readout.

With experiments now exploiting the capabilities of waveform digitizers whose single event readout is relatively slow and the complexity of many experiments requiring significant numbers of waveform digitizers, the deadtime issue became untenable. Corrections for deadtime increased from the historically typical 10-20% to 95% or larger. In addition to the significant corrections required because of deadtime, statistics suffered as only a few percent of events could be accepted into the computer and the rest were ignored.

We therefore implemented a multievent readout into our data acquisition system. This required implementing new infrastructure into the data acquisition and analysis systems. Although the implementation of the multievent readout is designed to be general, the current focus is on the multievent readout of Struck 3316 waveform digitizers [1].

To implement multievent readout in the online data acquisition system, we changed the triggering from using the interrupt of the controller module to searching for the event threshold set on the waveform digitizers to be met on at least one channel of all digitizers used in the experiment. Once this threshold is reached, all events of all modules are read out. This is read into the data acquisition system as a traditional "event", but is tagged in the event header as a multievent. In that way event counters and rates are maintained. Events are written to disk as well as sampled to the online analysis monitor in the same way as was used for single event readout.

In the backend analysis, the multievent tag in the buffer header triggers a multievent decoding of the buffer. This decoding separates data from all of the channels into lists. The multievent flag then triggers an event building routine which builds events by comparing timestamp differences between the various events of the various channels. After the events are built, the traditional online analysis routines are called.

A similar operation occurs when preparing the raw data files for offline analysis. When the events are converted to root trees [2], the multievent flag triggers the same event building routine and the same infrastructure builds the events into the event data structure that is written into the root trees.

We have tested and then used the multievent readout in two experiments. The first was a NIMROD [3] experiment to test the new implementation. Employing 9 Struck digitizers [2] with single event readout limited our data rate to about 200 events per second with 90-95% deadtime. After

implementing the multievent readout described above, we achieved 4000 events per second with no deadtime using 100 multievents per readout. Increasing the beam rate above that did not yield more events because that was the point where the events were accumulating faster than they could be readout due to the limit of our data transfer rate.

Another experiment employed 18 Struck digitizers and 3 Mesytec Madc32 [4] peak sensing ADCs in two VME crates. In this experiment, we employed an external clock to synchronize the digitizers in the different crates as well as exploiting the multievent and external clock capability of the Mesytec ADCs. A test experiment leading to the one discussed here employed four digitizers using single event readout. That test experiment suffered significant deadtime and a limit of a few hundred events per second. We were able to achieve 2000+ events per second with the multievent readout of 18 digitizers and 3 Mesytec ADCs. The limit of 2000 events per second was driven by the limit of beam that could be used with the forward detectors rather than the data acquisition limit.

We note also that multievent readout can also be useful in experiments where single event readout is used. One example is the neutron ball (NBL) [5] readout. That readout has typically been done counting triggers from the PMT signals with a 100us gate that results from the experimental trigger to count signals from the reaction followed by a 100us gate to count signals from the background. We have tested the NBL readout with a fission source using digitizers with multievents. We used a single event trigger from the fission fragment to open a 200us gate which allowed all signals to be counted and timestamped during that 200us. Using this method, signals the first 100us as determined from the time stamp can be used to establish the signals from the reaction and from the second 100us to establish the background. This method can also be used in multievent readout as described above and the timestamps are used to match the NBL signals to each event with a 200us gate instead of the much smaller gate when, for example, CsI signals are matched to build an event.

Another application using multievents with single event readout and achieving zero deadtime involves studying decaying nuclei. If, for example, events do not need to be matched, a multievent number of, say 20, can be used to detect with zero deadtime all events that occur and the results can be analyzed according to timestamps even with single event readout. This technique was exploited in a recent study of multinucleon transfer [6] where alpha particles emitted from heavy products implanted in an active catcher were detected.

The primary benefit of multievent readout is that much more efficient readout of large parameter experiments can be achieved. This increases both the statistics accumulated in the experiment in addition to increasing the efficiency of Cyclotron usage given the significant demand of beamtime. In the future, the multievent capability of more acquisition modules will be implemented into the software. As we progress to ever more complex experiments, it may be necessary to split the data acquisition into parts and acquire each part using multievent capabilities in parallel and then implement true event building. This development will occur as the need arises.

[1] Struck Innovative Systems, https://struck.de/sis3316.html.
[2] R. Brun, F. Rademakers, Nucl. Instrum. Methods Phys. Res. **A389**, 81 (1997).
[3] S. Wuenschel *et al*., Nucl. Instrum. Methods Phys. Res. **A604,** 578 (2009).
[4] Mesytec, http://mesytec.com/products/nuclear-physics/MADC-32.html

[5] R.P. Schmitt *et al*., Nucl. Instrum. Methods Phys. Res. **A354**, 487 (1995).
[6] A. Hood, *Progress in Research* , Cyclotron Institute, Texas A&M University (2020-2021), p. II-1.

.

Measuring the photopeak efficiency of the TexCAAM detector using the ^{11}Be decay and the ^{60}Co gamma source

M. Barbui,[1] E. Aboud,[1,2] A. Ascione,[1,2] J. Bishop,[1] L. Jeffery,[1,2] E. Harris,[1] C.H. Hunt,[1] Z. Luo,[1] E. Koshchiy,[1] M. Roosa,[1,2] C.E. Parker,[1] A. Saastamoinen,[1] D. Scriven,[1,2] and G.V. Rogachev[1,2]

[1]*Cyclotron Institute, Texas A&M University, MS3366 College Station, TX*

[2]*Department of Physics & Astronomy, Texas A&M University, College Station, TX 77843*

The Texas CsI Array for Astrophysical Measurements, TexCAAM, was built and commissioned for charged-particle gamma coincidence experiments with radioactive beams with the focus on nuclear astrophysics. The absolute photopeak efficiency of the TexCAAM detector was measured in the energy range from 1 to 8 MeV. The β decay of ^{11}Be and the ^{60}Co source were used to obtain the experimental photopeak efficiency at various energies.

TexCAAM is an array of 32 CsI(Tl) scintillators read by pin diodes. It has nearly 4π coverage and a compact geometry allowing for good passive shielding from external gamma-rays. Each scintillator has an area of 5x5 cm^2 and a thickness of 4 cm. The detectors are arranged in a box geometry. The box is composed of four sections each made by 8 closely packed scintillators. For this experiment the four sections are placed at theta angles 146^o, 128^o, 93^o and 55^o from the center of a 1 mm thick silicon detector that is used as implantation target.

The ^{11}Be beam with energy 115 MeV was produced at the MARS spectrometer line of Cyclotron Institute and implanted in the Silicon detector. The beam was pulsed with a 30 s on, 30 s off frequency. Beta particles produced by the beta decay of ^{11}Be were detected in the silicon detector and provided the trigger for the acquisition system. Gamma rays from the deexcitation of ^{11}B were detected by the TexCAAM scintillators in coincidence with the beta particles. We note that two detectors were missing in this experiment: one in the section at 93^o and one in the section at 146^o. The measured efficiencies are not corrected to compensate for the missing detectors.

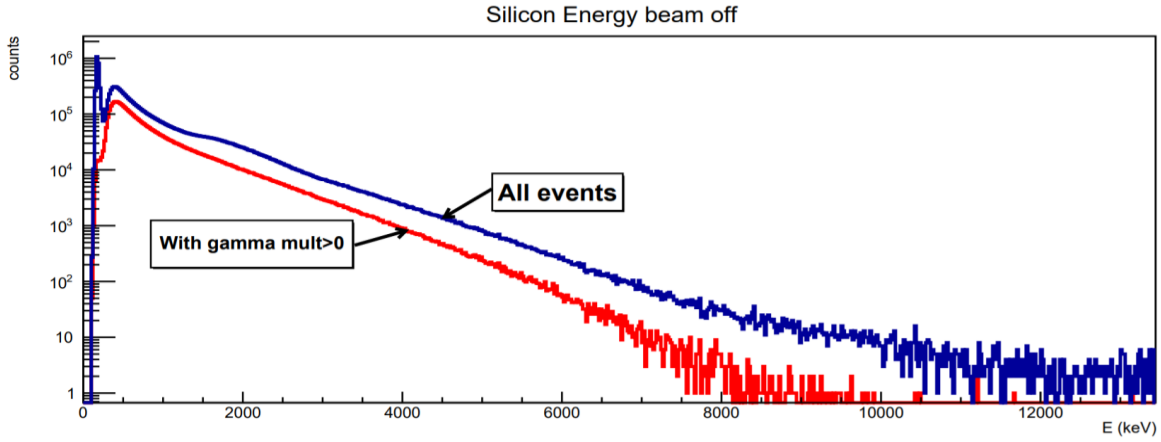

Fig. 1. Beta particle spectra measured in the beam off interval. Blue line all events, read line events with at least one gamma.

The beta particle spectrum measured in the Silicon detector during the beam off time is shown in Fig. 1, whereas the gamma spectra measured in the four sectors of the TexCAAM array are shown in Fig. 2.

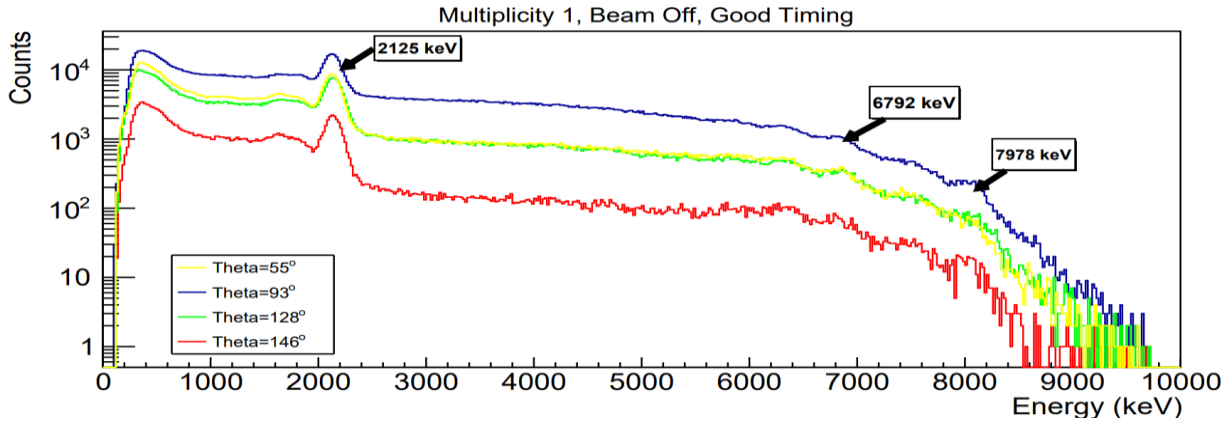

Fig. 2. Gamma spectra measured in the four sections of the TexCAAM array during beam off.

Integrating the beta spectrum from above the noise (267 keV) up to 10000 keV we measured a total of 9172520 beta decays. Looking at the gamma ray spectra in Figure 2, three peaks are clearly visible. These peaks correspond to the transitions from the excited states of ^{11}B at 2125, 6792 and 7978 keV to the ground state. After background subtraction, the integral of these peaks was used to obtain the experimental photopeak efficiency. The results are reported in Table I together with the branching ratios from ref. [1]. The efficiency obtained considering the photopeak and the first escape peak is also reported in Table I.

Table 1. Photopeak efficiency of the TexCAAM detector from 2 to 8 MeV. Branching ratios are from ref. [1].

Beta decay to ^{11}B state	Beta branching ratio %	Gamma branching ratio to the ground state %	Expected counts if 100% efficiency	Measured photopeak counts	Efficiency %	Measured photopeak + first escape peak	Efficiency %
2125 keV	31	100	2843481	211819	7.4	257850	9
6792 keV	6.5	68	405425	5464	1.3	11550	2.8
7978 keV	4	47	172443	2135	1.2	4806	2.8

A ^{60}Co gamma source was also used to measure the photopeak efficiency of TexCAAM at 1173 and 1332 keV. For this measurement the source was placed at the silicon detector position. The source spectrum obtained considering all the CsI detectors is shown in the left panel of Fig. 3. The photo-peaks were fitted with a two gaussians + linear background function to obtain the total number of counts in each peak (C_{1174} and C_{1332}). The right panel of Fig. 3 shows a two-dimensional plot of E1 vs. E2 for multiplicity two events. The energies are ordered so that the largest energy measured is always on the x axis. The integral in the 2-dimensional gate around the coincidence spot provides the number of coincidences with a 1173 keV and 1332 keV gamma, C_2. The efficiency at 1173 keV is $\varepsilon_{1332} = C_2/C_{1332}$ =24%. The efficiency at 1173 keV is $\varepsilon_{1173} = C_2/C_{1173}$ =20%. Fig. 4 shows the measured photopeak

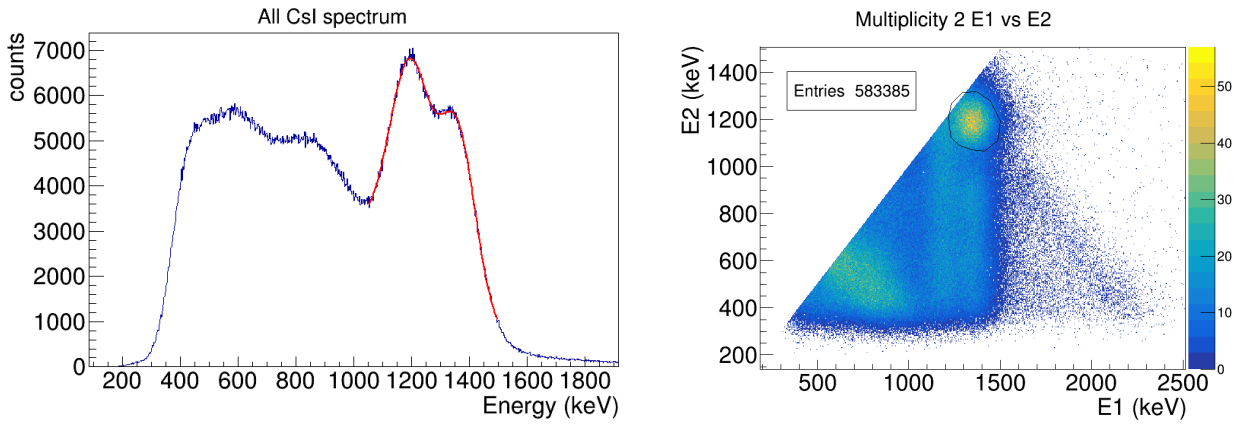

Fig. 3. Left panel: Spectrum of the ^{60}Co source. The red line shows the result of the fit with two gaussians and a linear background. Right panel: ^{60}Co source, multiplicity two events, E1 vs E2. A two-dimensional gate is plotted around the spot of 1173 keV and 1332 keV gamma ray coincidences.

efficiencies as a function of the gamma energy. The points are fitted with a simple power law function to interpolate the efficiency values in between the measured points. Fig. 4 also shows the energy resolution as a function of the gamma energy.

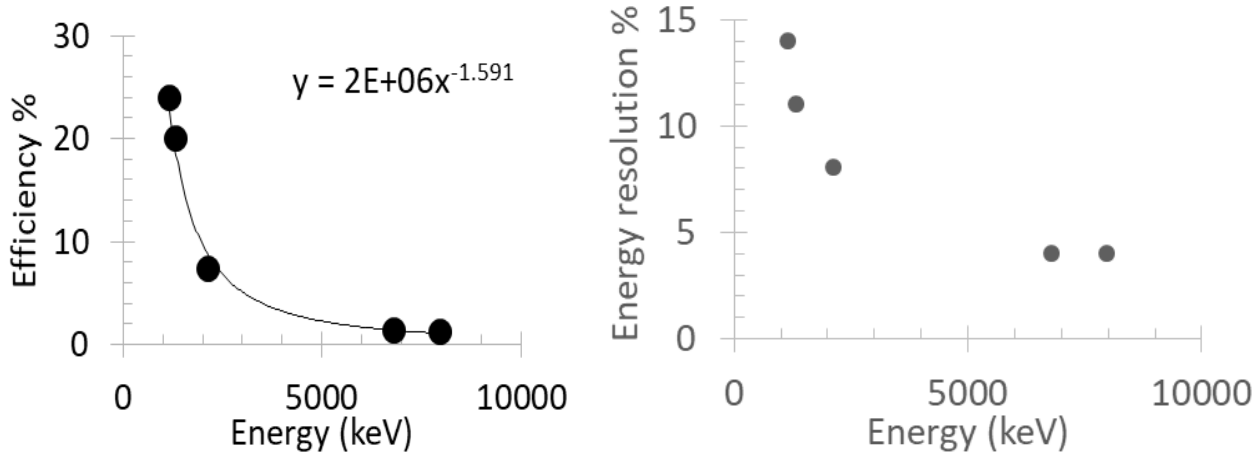

Fig. 4. Left panel: photopeak efficiency as a function of the gamma energy fitted with a power law. Right panel: Energy resolution as a function of the gamma energy.

The rather low absolute photopeak efficiency of the TexCAAM array at the highest energies makes the device not ideal for applications where high energy gamma rays needs to be detected. On the contrary, the efficiency of the assembly is high at energies below 2 MeV. This makes the detector suitable for experiments where gamma rays in the energy range from 400 to 2000 keV are produced. For example, TexCAAM could be used around an extended gas target to tag inelastic scattering events in (p, p') or (α, α') reactions. The segmentation of the detector can also provide a rough measurement of the location of the interaction point inside the gas target.

[1] D.J. Millener *et al.*, Phys. Rev. C **26**, 1167 (1982).

Design of a dual-purpose chamber for the gas cells of the *p*/He-LIG facility

P.D. Shidling, V.S. Kolhinen, G. Chubarian, V.E. Iacob, M. Nasser, D. Melconian, and G. Tabacaru

The low-energy RIBs for TAMUTRAP facility will be delivered by a new He-LIG facility. Last year, most of the effort was dedicated towards designing the gas cell chamber, its support structure and the extraction section, and detailed SIMION simulations of the He-LIG system to help design and optimize the LSTAR mass separator using the program COSY INFINITY. More details on simulations and designs of the He-LIG and mass separator are discussed in our other reports [1]. Here we describe in more detail the chamber to service the existing *p*-LIG system as well as the new He-LIG system.

The chamber is designed with the aim to: (a) have easy access to work around the chamber; (b) be compatible with the *p*-LIG and He-LIG facilities; (c) be able to easily and quickly switch between proton and ^{3}He modes of operation; and (d) provide a strong support structure for the gas cell chamber to allow precise alignment and ensure mechanical rigidity. Fig. 1 shows the assembled design of the *p*/He-LIG facility consisting of a gas cell chamber, extraction sides of *p*- and He-LIG facilities, and coupling of the K150 and beam-dump sides to the chamber.

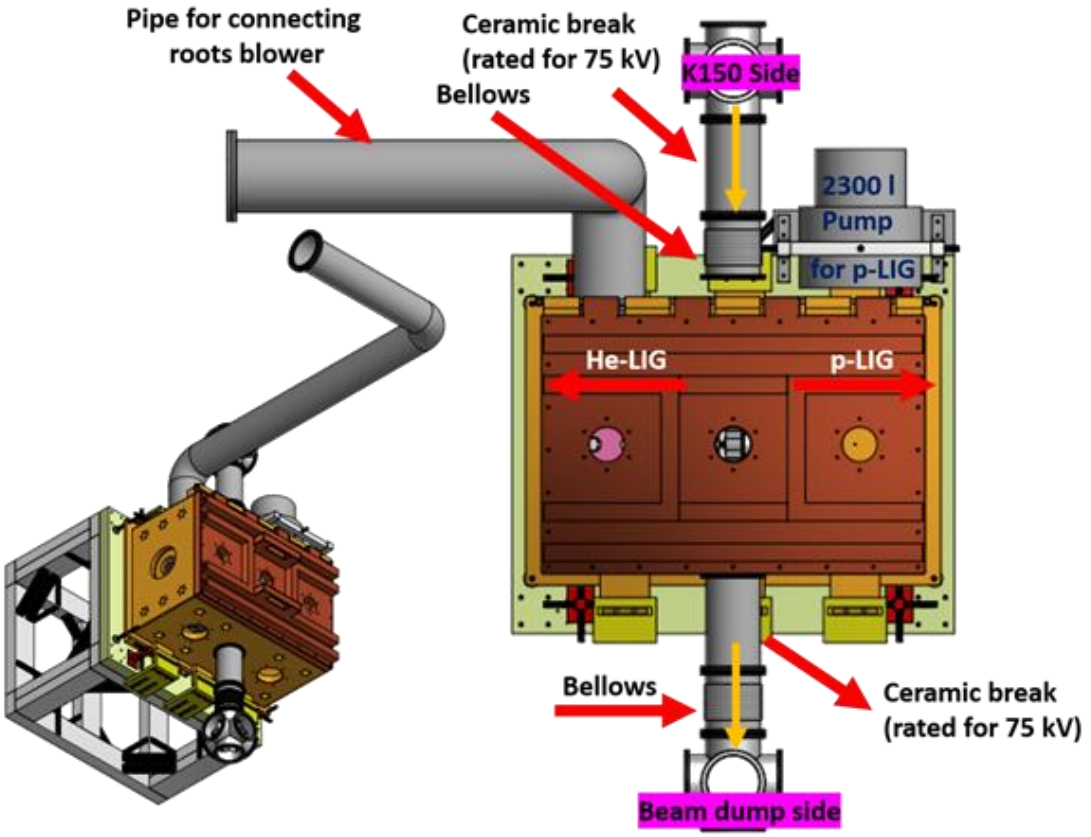

Fig. 1. The design of a gas cell chamber and coupling of the chamber to beam dump and K150 beam line.

The gas-cell chamber will be coupled to the K150 and beam dump beamlines using a combination of bellows and ceramic breaks which are rated for 75 kV. When operating in ^{3}He mode, the gas-cell chamber will be floated to a high voltage ranging between 50–70 kV, while in the proton mode it will only be floated to 10–15 kV. The roots blower and a turbo pump for the *p*-LIG will be connected to the chamber from the side (see Fig. 1) providing easy open access to the inside of the chamber from the top.

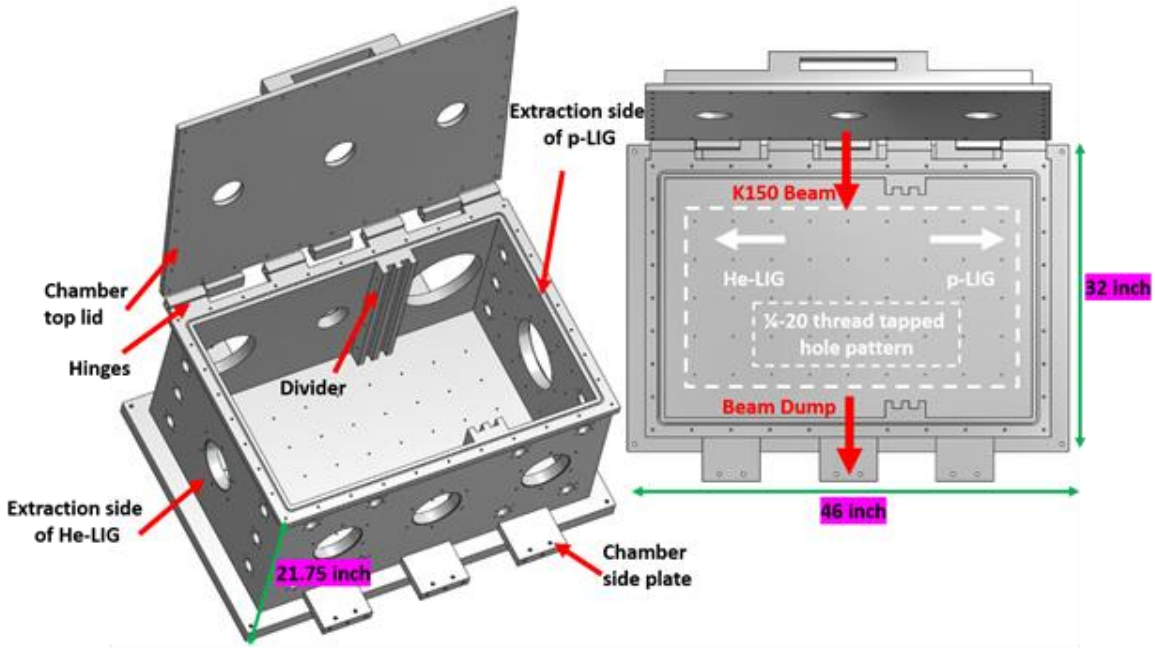

Fig. 2. The design of the gas-cell chamber for servicing both the proton and ^{3}He modes of operating the LIG facility.

Fig. 2 shows the design of the gas-cell chamber which will be fabricated out of aluminum in the coming year. It is a rather large rectangular chamber: 46”×32”×21.75”. The wall thickness of the chamber sides is 1.5” and the bottom plate has thickness of 1.75”. The bottom plate of consists of a ¼-20 tapped bolt pattern to mount the support structure for the gas cell. The beam entrance and exit ports consist of ISO 100 and ISO 160 type flanges, respectively. The *p*-LIG and He-LIG extraction sides consists of ISO 160 and ISO 200 type flanges, respectively. In total, the chamber consists of 4 ISO 100 ports, 4 ISO 160 ports, 2 ISO 200 ports, 1 ISO 250 type port, and 14 NW40 KF-type flanges. NW40 KF flanges will be used for feeding the UHP He gas to the gas cell and the electrical feedthroughs for the various electrostatic and electrodynamic components. The ISO 200 and ISO 250 ports will be used to connect the roots blower and HiPace 2300 l/s turbo pump, respectively. One of the critical parts of the chamber is the divider slot which will be used to install a plate with a differential pumping diaphragm for isolating the *p*-LIG section for better vacuum when extracting RIB to the right (proton mode), and vice-versa when extracting to the left (^{3}He mode). The chamber has side plates (see Fig. 2) to securely bolt the chamber to the support structure after it has been precisely aligned. The top lid and the gas chamber have

one complete side hinged. A stainless-steel threaded rod extends through an elongated slot in the hinge arm allowing to lift the top lid from one side. The chamber will be fabricated out of aluminum and all the sides of the chamber will be vacuum welded from the inside.

Apart from the design, a stress analysis of the chamber was performed to study the behavior of the assembled gas-cell chamber when exposed to atmospheric pressure (14.7 psi) using Autodesk inventor (2015 version). This study was used to determine the thickness of the chamber walls needed to keep deformations (in all three direction) from causing misalignment. Atmospheric pressure was applied to all sides of the chamber with the corners and tapped holes as fixed constraints, with Fig. 3 showing the output of the analysis. No significant deformation was observed, and the safety factor of the assembled chamber was as high as 15 (Fig. 3(d)). The maximum displacement of 0.08 mm was observed for the bottom flange.

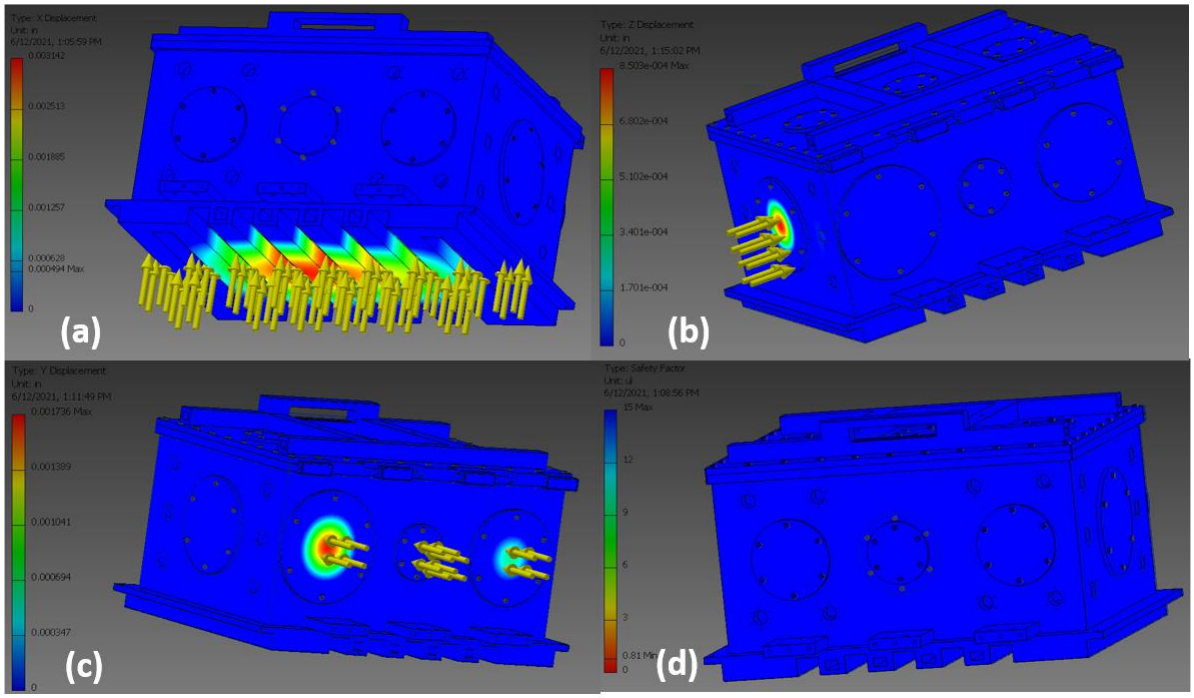

Fig. 3. Stress analysis of the gas cell chamber. (a), (b) and (c): Displacement observed on different sides of the chamber. (d) safety factor of the chamber.

The gas cell chamber support structure will be constructed from solid, double-quad 80/20 aluminum extrusions (6" in height and 3" in width). Fig. 4 shows the design of the support structure. The chamber will be bolted on swivel leveling mounts from all corners and the levelling mounts (red circle in the left image Fig. 4) will be used to adjust the height of the chamber and align it with respect to the beam axis. The left/right and front/back adjustment will be done using swivel-Tip set screws (blue circle on the right side of Fig. 4). After aligning, the chamber side plates will be bolted to the support structure using L-brackets (highlighted as a black circle in Fig. 4).

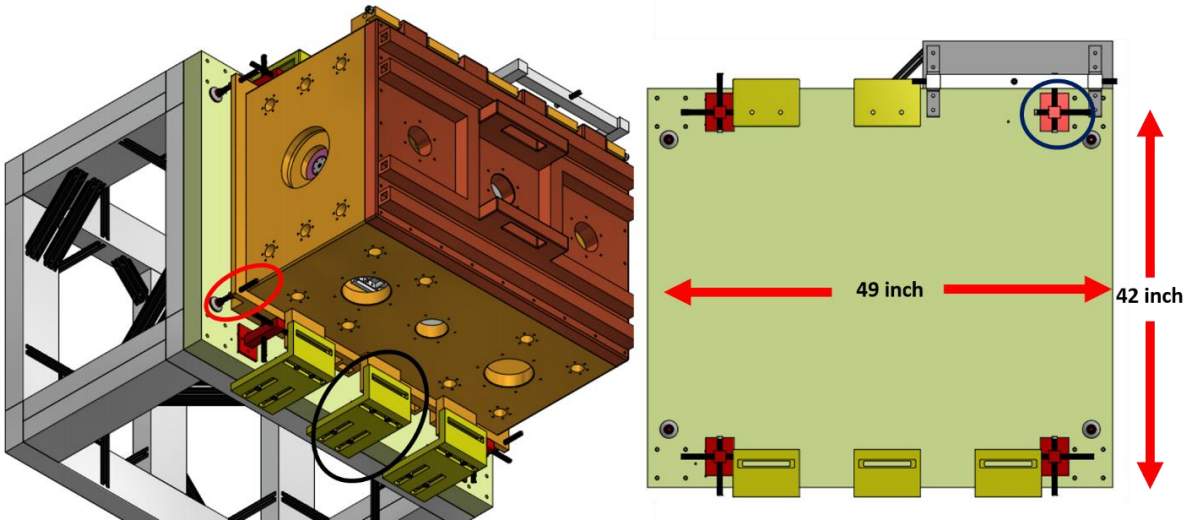

Fig. 4. Support structure for the dual-purpose chamber. Fine-tune adjustments in all three directions is possible with the threaded-rod feet on the corners (height adjustment) as well as threaded rods pressing against the chamber wall and side plates (horizontal adjustment).

The technical drawings are completed and we are in the process of soliciting bids to fabricate the chamber. The chamber will be installed and aligned in the fall of 2021.

[1] D. Melconian *et al.*, LSTAR facility, 2020-2021, *Progress in Research*, Cyclotron Institute, Texas A&M University (2020-2021), p. V-71.

.

Radio frequency quadrupole cooler buncher for ^{6}He CRES experiment

D. McClain, G. Chubarian, V. Iacob, V.S. Kolhinen, D. Melconian, M. Nasser, A. Ozmetin,
B. Schroeder, and P.D. Shidling

The ^{6}HeCRES collaboration uses the cyclotron radiation emission spectroscopy (CRES) technique developed by the Project-8 collaboration [1] to measure the β spectrum of ^{6}He from radiation emitted due to the cyclotron radiation as a charged particle precesses in a magnetic field. The cyclotron frequency, *f*, of an electron is dependent on the kinetic energy E_e of the electron according to

$$f = \frac{1}{2\pi}\frac{eB}{m_e + E_e},$$

where *e* is the electron charge, B is the magnetic field, and m_e is the rest mass of the electron. The incredible sensitivity of the CRES technique is this ability to use the frequency measurement to deduce the energy of the electron [2].

The experiment consists of a rectangular waveguide with a U-shape turn to read frequencies from either end to negate any Doppler shifts. The rectangular waveguide is split on one side of the U shape to include a circular waveguide that exists as a decay volume for the ^{6}He as shown in Fig. 1.

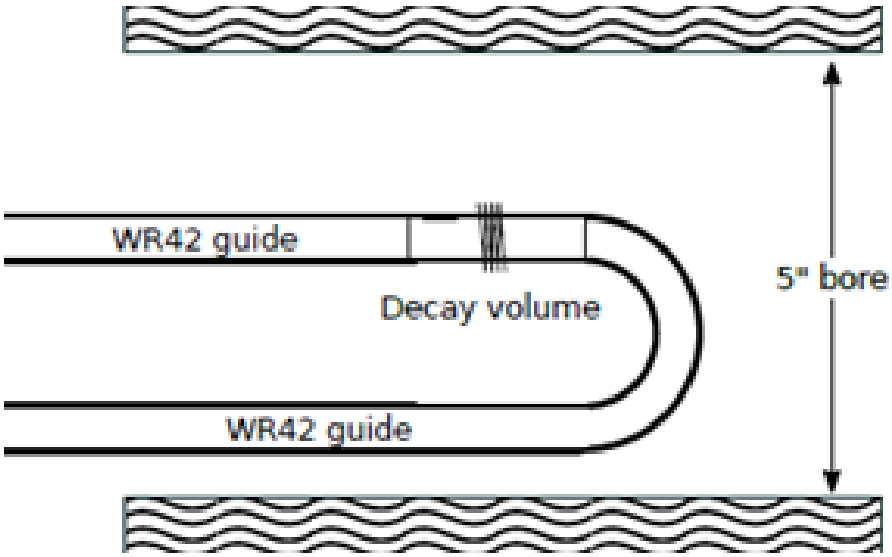

Fig. 1. Drawing of the U-shaped waveguide in the magnet.

The current phase of the project involves pumping ^{6}He gas into a decay volume via twenty-five holes along the side, each approximately 1-mm in diameter. The decay volume is ~10 cm in length and 1.156 cm in diameter. This radius propagates frequencies between 18–24 GHz well. The magnetic field can be varied from 0.5–7 T to shift our 18–24 GHz window to different energies and scan the whole β

spectrum. The decay volume also has a coil around it creating a magnetic trap. This setup allows ^{6}He atoms to freely move about within the decay volume. The emitted βs of the ^{6}He nuclei that are near the walls are lost, and because of an increasing cyclotron radius with higher energy, higher energy βs would be more likely to hit the wall as show in Fig. 2, resulting a bias toward lower energies in our energy spectrum. With this issue it is still expected to get the uncertainty of $b_{Fierz} < 10^{-3}$ [3].

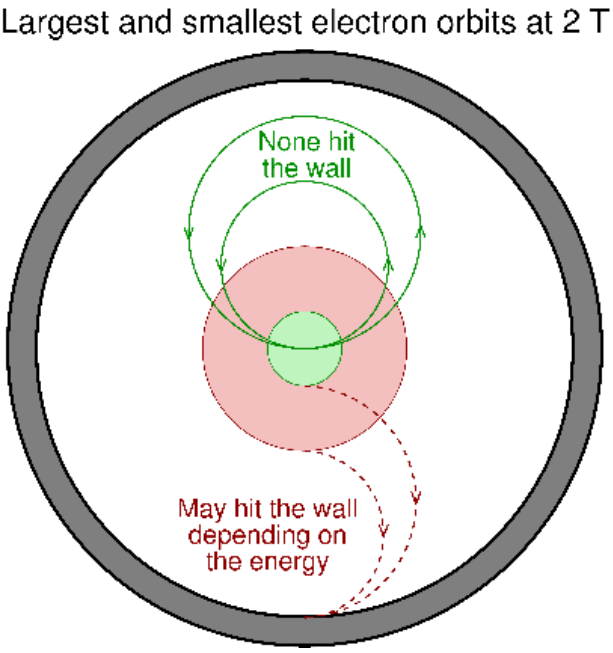

Fig. 2. The geometric effect of wall collisions in the case where there is no radial confinement of the ^{6}He.

The next phase of the experiment involves the implementation of an ion trap to radially confine the ^{6}He ions and eliminate wall collisions, effectively bringing our expected precision to 10^{-4}. This however requires more modifications to the experimental setup as we would no longer be able to pump in neutral ^{6}He into holes within the trap. The waveguide will need to be modified to have a hole that allows a beam of ^{6}He ions to flow in and to the Penning trap. We will also need to cool and bunch the ions for efficient transfer to the Penning trap.

In order to accomplish this, SimION was used to simulate the radiofrequency quadrupole trap (RFQ) in cooling ^{6}He ions. An RFQ's stability relies on the Mathieu parameter, q, to keep an ion of mass m contained while inside the RFQ:

$$q = \frac{4QV_{RF}}{mr_0^2\Omega^2}.$$

Here Q is the ion's charge, V_{RF} is the RF voltage applied to with a frequency Ω, and $2r_0$ is the distance between opposite electrodes of the RFQ. The ion's motion in the RFQ is stable for the Mathieu parameter between 0.4–0.6. Note that larger potential will correspond to an increased maximum rate that

the RFQ can handle. Our design for the 6He-CRES RFQ is largely a rescaled version of the TAMUTRAP RFQ [4], where we increased r_0 from 6 mm to 15 mm, which allows us to operate with V_{RF} = 200V, and frequencies between 0.5–1.5 MHz. These parameters in the simulation gives us a time spread of <1 μs and an energy spread of <3 eV which will help us plan the rest of the beamline after the RFQ. The RFQ design has been completed in Autodesk Inventor as shown in Fig. 3. The construction and first tests of the RFQ should be completed by the end of 2021.

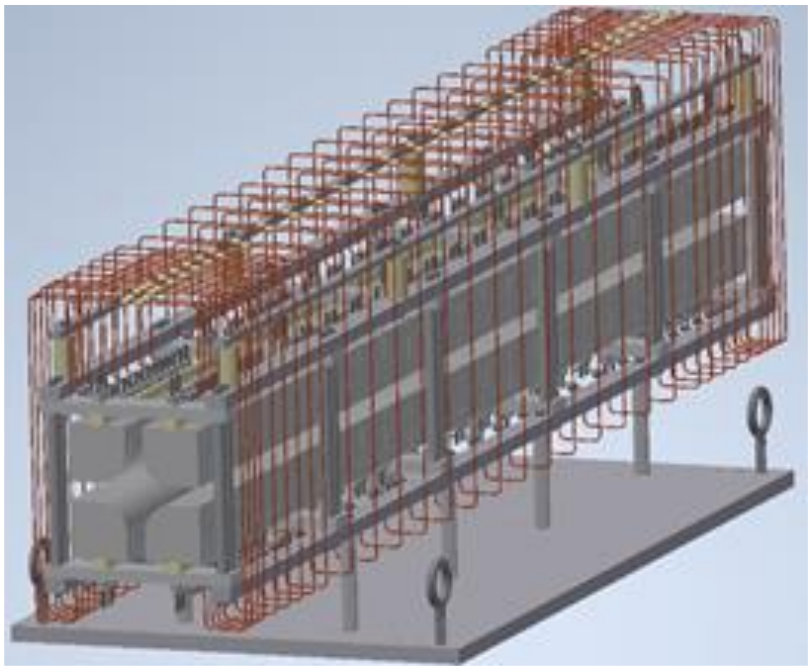

Fig. 3. The geometric effect of wall collisions in the case where there is no radial confinement of the ^{6}He.

[1] D.M. Asner *et al.*, Phys. Rev. Lett. **114**, 162501 (2015).

[2] A.A. Esfahani *et al.*, J. Phys. G **44**, 054004 (2017).

.

Update on LSTAR, the isobar separator for the He-LIG system

G. Chubarian, V.S. Kolhinen, D. Melconian, P.D. Shidling, G.P.A. Berg,[1] M. Couder,[1]
M. Brodeur,[1] and M. Wiesher[1]
[1]*University of Notre Dame, Notre Dame, Indiana*

As explained in last year's report [1], the **L**ight-ion guide **S**eparator for **T**exas **A**&M's K150 **R**adioactive beams (LSTAR) is needed to purify and transport radioactive ion beams from the new He-LIG [2] production system up to the TAMUTRAP facility.

TAMUTRAP's initial program will be measuring β-delayed proton transitions ^{20,21}Mg, ^{24,25}Si, ^{28,29}S, ^{32,33}Ar, ^{36,37}Ca (and possibly heavier Ti and Cr, depending on K150 upgrades) for test of fundamental symmetries. The unique β-*p* coincidence of our detectors will ensure a background-free measurement regardless of contaminants. However, the efficiency of transport and loading the RIB of interest will dramatically suffer if the background is orders of magnitude larger, with the bottleneck of $<10^5$ (perhaps as high a 10^6) ions/s for >10% efficiency of the gas-filled radiofrequency quadrupole (RFQ) cooler and buncher; once the RFQ gets saturated, the efficiently quickly goes to zero. The cross section for production of isobaric contaminants is 2-3 orders of magnitude larger in the odd *A*=21, 25, 29, 33 and 37 masses, and 3-5 orders larger in the superallowed *A*=20, 24, 28, 32, and 36 cases, so efficient *and* effective isobaric separation is critical.

The figure of merit for our design was initially the mass resolving power of the separator, however this definition is highly dependent on the initial beam emittance. Instead, to best determine the demands of LSTAR's performance, we used SimION [3] to provide realistic ion positions and trajectories upon exiting the SPIG of the He-LIG system, accelerated them to 65 keV, and then used that as input to a COSY INFINITY [4] calculation of the LSTAR design. The COSY calculation transports ions through the design (including fringe fields) and provides a spectrum of ions – both good and contaminant – at the focal plane of the exit of LSTAR, where we can see how many good ions got through and how many contaminants were vetoed. We included a 3.3 eV FWHM energy spread when tracing rays through COSY. We took the most difficult case and made our benchmarks compared to that. Of the RIBs of interest to TAMUTRAP listed above, ^{37}Ca has the closest contaminant, ^{37}K, produced with 1750x the cross section. With an estimated 2×10^4 ^{37}Ca/s produced via a ^{36}Ar(^{3}He,2*n*) fusion-evaporation reaction, the 3.5×10^7 pps of ^{37}K would overload the RFQ. However, if the separator removes 97% of the ^{37}K, the RFQ may be able to handle 10^6 ions/s. If LSTAR removed 99.75% of the ^{37}K, then only 10^5 ion/s would reach the RFQ which will certainly not overload it. The plots in Fig. 1 show the COSY calculations for two mass separations of good and contaminant ions (corresponding to ^{37}Ca/^{37}K and the easier 21Mg/21Na cases) and two values for the emittance of the ions exiting the SPIG (what SimION predicts, and twice as big). In the initial stages of the TAMUTRAP program, LSTAR will easily be able to completely purify the RIB and transport it from the He-LIG with near-perfect transmission. Even in the most difficult case, mass 37 with SimION underestimating the emittance by a factor of two (bottom right plot), LSTAR will veto >99% of the contaminants while still transporting >88% of the ions of interest through LSTAR.

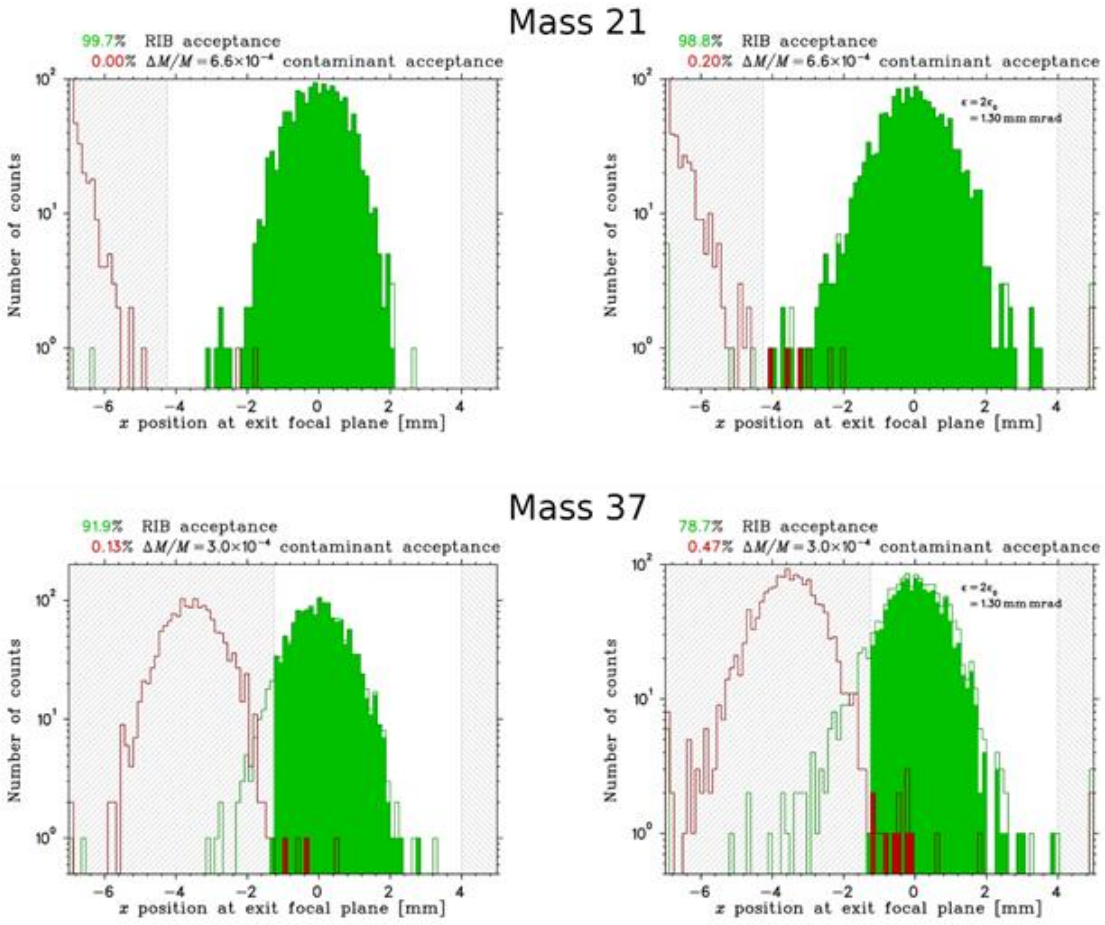

Fig. 1. Final positions of ions at the exit focal plane of LSTAR using the SimION-simulated initial emittance $\epsilon_0 = 0.652\ \text{mm} \cdot \text{mrad}$ (left) and twice as large (right). The unfilled histograms are the positions of all good (green) and $\Delta M/M$ = 3×10^{-4} contaminants (red), while the filled are the subset that successfully exit the final rectangular aperture, indicated by the grey hatched regions.

We submitted a proposal to fund the construction of LSTAR, which was fully funded by the Department of Energy, Office of Science for $0.78M. We are finalizing the technical document and plan to submit the bid request for building LSTAR before the fall of 2021.

[1] G. Chubarian *et al.*, *Progress in Research*, Cyclotron Institute, Texas A&M University (2019-2020), p. IV-94.

[2] P.D. Shidling *et al.*, *Progress in Research*, Cyclotron Institute, Texas A&M University (2019-2020), p. IV-95.

[3] SIMION 8.1 Ion optics simulation program. https://simion.com/.

[4] M. Berz and K. Makino, Department of Physics and Astronomy, Michigan State University, MSU Report MUSHEP 151103-rev (2017).

Upgrade of TRINAT's β telescopes

G. Chubarian and D. Melconian

As the analysis to measure the Fierz interference parameter from the last TRINAT wraps up, we are preparing for the next correlation measurement of polarized ^{37}K at TRIUMF. One of our limiting systematics is the performance of our current β detectors, which are made up of a 40 mm × 40 mm × 300 μm double-sided Si-strip (DSSD) ΔE detector backed by a BC408 plastic scintillator E detector (see the left schematic of Fig. 1). We are upgrading these telescopes to reduce the large (~100 keV) energy loss in the DSSD and the (back-) scattering it induces by replacing the ΔE with a multiwire proportional counter (MWPC). We will also replace the magnetic-field-sensitive PMT readout of the scintillator with Si photomultipliers (SiPMs). In order to avoid completely changing our overall system, we will use the same detection chamber and in particular the existing re-entrant flanges for the β telescopes. This constrains the dimensions of the new telescope.

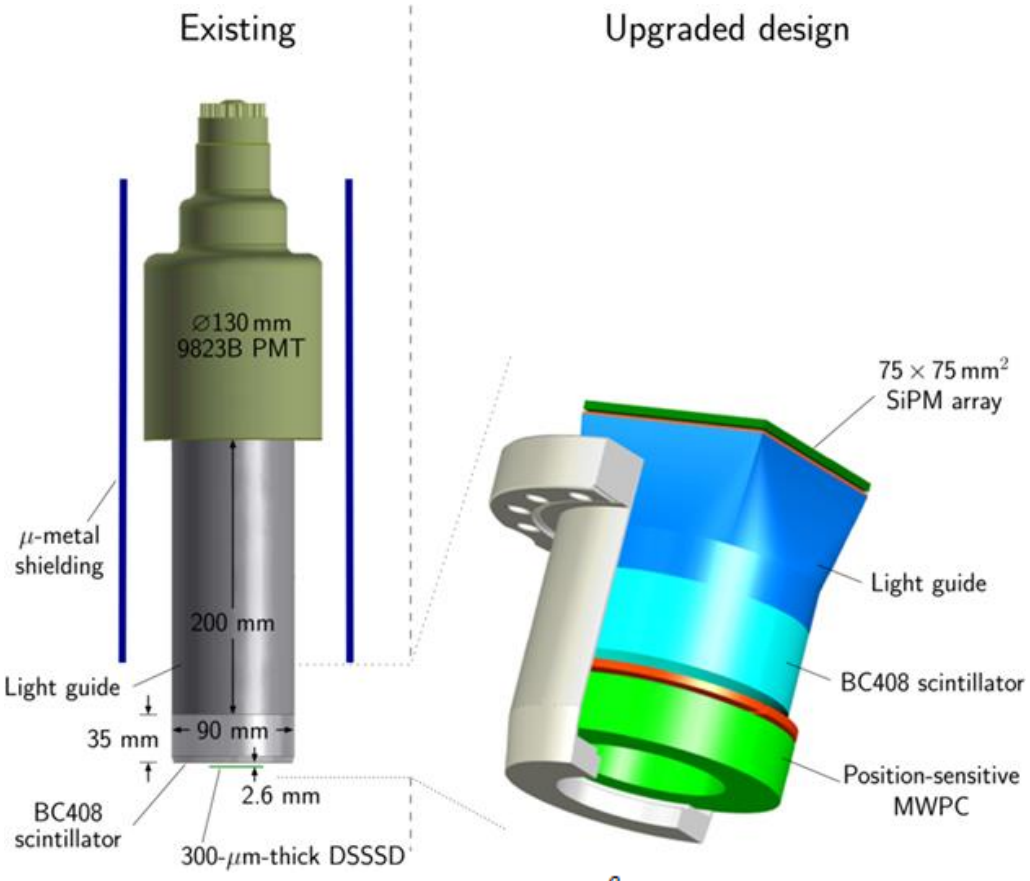

Fig. 1. Old (left) and new (right) design for TRINAT's β telescopes. The new design will be more compact, have much smaller energy loss and large-angle scattering in the ΔE, and be much less sensitive to the varying magnetic field used by TRINAT for trapping and polarizing neutral atoms.

The multiwire proportional chamber

The choice of the gas detector was defined by the main requirement to minimize the energy loss and angular scattering of the detected β particles, and to make it position sensitive. The MWPC consists of two mutually perpendicular wire planes with a wire-winding pitch of 1 mm. The wires of gold-plated beryllium-bronze with a diameter of 16 microns are connected in pairs, with better than 2 mm resolution obtainable based on the centre-of-gravity of ionization. The cathode is made of a thin (< 1 μm thick) double-sided aluminized-mylar foil situated in the middle between the wire planes. Such a design of the electrodes allows forming a uniform electric field throughout the entire volume of the detector. A fast-timing signal also will be taken from the central cathode.

The MWPC will be filled with P10 gas (a mixture of 90% argon and 10% methane) at a pressure slightly above atmospheric by a few Torr. The detector will be operated with a constant gas flow which simplifies the entire design of the gas system. The MWPCs windows are made of 5 μm-thick Kapton films. This choice of the film material and the thickness was made to avoid the use of a supporting grid. The active area of this cylindrical detector has a diameter of 58 mm, and the whole assembly has an outer diameter of 95 mm, which fits in the existing re-entrant flanges. Due to the severe lack of space for the wiring, electrical, and gas fittings, sophisticated multilayer PCBs have been designed.

The scintillation detector

After passing through the MWPCs, the bulk of the energy of the β particles will be detected using a BC408 plastic scintillator as before. The new ΔE requires us to replace the scintillators so we decided to also change the light readout from a PMT to SiPMs; this makes the overall length of the telescope much more compact, and removes the PMT's sensitivity to varying magnetic fields. The scintillator thickness is 40 mm, slightly longer than the previous 35 mm which was optimized for ^{37,38m}K which have 5 MeV Q-values; the extra 5 mm will contain βs with energies up to 8 MeV, extending the cases that can be studied at TRINAT. The diameter of the scintillator should be as large as possible for the given volume to maximize the solid angle and minimize the likelihood of a β escaping out the side before being stopped. In our case, to leave room for the MWPC's wiring and gas-flow plumbing, the scintillator's diameter can be 88 mm. A short light-guide will bring the light out of the re-entrant flange to an array of SiPMs, flaring out slightly and changing from cylindrical to square to match the 75×75 mm^2 area of the array (3×3 set of Hammamatsu S14161 series, each 25×25 mm^2).

We have completed our design and are in the process of constructing the telescopes. We expect to test and characterize them this Fall at the Cyclotron Institute and then install them in the TRINAT lab at TRIUMF early in 2022.

.

MARS status report for 2020-2021:
Tuning of rare isotope beams ^{7}Be, ^{9}Li, ^{20}F, ^{35}Ar, ^{11}Be, ^{95}Zr

B.T. Roeder and A. Saastamoinen

This year, we continued the program of providing rare isotope beams (RIBs) for the physics program at the Cyclotron Institute at Texas A&M University with the Momentum Achromat Recoil Separator (MARS) [1]. Despite the COVID-19 pandemic, the MARS beam line was utilized in 8 separate experimental runs for RIB development and various experiments. Beams developed in previous years that were employed in physics experiments this year are as follows. ^{11}Be beam, made with the ^{13}C+^{9}Be reaction at 30 MeV/u, was provided to Dr. Rogachev's research group for a commissioning run of the new TexCAAM detector. A production rate of 32 eV/nC was obtained with about 10% contamination from ^{8}Li. ^{7}Be and ^{9}Li secondary beams had been produced before, but this year we produced them at low energy for experiments with Dr. Rogachev's group and the TexAT detector. Details of these low energy RIBs are described in the following paragraphs.

Three new RIBs were developed this year: ^{20}F, ^{35}Ar, and an attempt to make ^{95}Zr. These new MARS tunes are also described in the following paragraphs.

The low energy ^{7}Be beam was requested by Dr. Rogachev's group to measure ^{7}Be+^{7}Li reactions with TexCAMM. ^{7}Be was produced using the p(^{7}Li,^{7}Be)n reaction at 3.5 MeV/u with beam from the K150 cyclotron. To obtain the lowest possible secondary beam energy for the ^{7}Be, while providing the needed beam intensity for the experiment, we used for the first time thinner HAVAR windows for the MARS gas target. The MARS gas target was configured with a 0.16 mil (4 μm) entrance window, a 0.1 mil (2.5 μm) exit window. The H_2 gas pressure used was 100 torr, and the gas cell was cooled with liquid nitrogen to 77 K. Due to small pinholes in the thin exit window, a leak rate of about 2 torr/hr was observed in the gas target. We compensated for this loss by adding about 20 torr of H_2 gas to the target every 8-12 hours. After tuning, the ^{7}Be beam had 14 MeV total energy and a production rate of $1.5*10^{5}$ p/s with about 90 nA of ^{7}Li beam on target, resulting in an estimated production rate of about 1667 eV/nC. Earlier beam development runs have shown that ^{7}Be secondary beam with energies as low as 8 MeV total energy can be produced if desired for future experiments.

A low energy solution was also requested by Dr. Rogachev's group for ^{9}Li secondary beam, which had been produced previously at intermediate energy with the ^{11}B+^{9}Be 2-proton removal reaction [2]. The 2n-transfer reaction ^{18}O(^{7}Li,^{9}Li)^{16}O was considered the best production reaction candidate because the Q-value is -6.1 MeV (versus -15.6 MeV for the ^{11}B+^{9}Be reaction). However, ^{7}Li+^{18}O reaction required ^{18}O gas as the target. Thus, if the MARS gas target was cooled with the traditional liquid N2 to ~77 K, the ^{18}O gas volume would partially liquify depending on the final temperature of the MARS gas target. In the equilibrium conditions, the partial liquification of ^{18}O occurred at about 180 torr pressure, but with heating from the beam, the pressure increased over time to 250 torr. Due to these unstable conditions, it was decided to run the ^{18}O gas at room temperature instead of cooling it to keep the gas pressure in the target more stable. The result of the lower energy ^{9}Li secondary beam is as follows. ^{7}Li beam at 10.3 MeV/u from the K150 cyclotron impinged on the MARS gas target to produce ^{9}Li secondary beam. The MARS gas target was filled with 775 torr of ^{18}O gas at room temperature. The

resulting ^{9}Li secondary beam had 59.6 MeV total energy (6.6 MeV/u) and a production rate of 9 eV/nC. Thus, with 200 nA of ^{7}Li in the MARS coffin FC, we had a typical rate of about 1.8*10^{3} p/s for ^{9}Li. Contaminant beams of 6He (2 eV/nC) and ^{3}H (unknown rate) were also present at the same focal plane position. While the production rate for ^{9}Li was about 5 times higher with the ^{11}B+^{9}Be reaction, the lower secondary beam energy obtained with ^{7}Li+^{18}O made it the preferred choice for the experiment. The experiment with the ^{9}Li from this production method had already been carried out in October 2020.

^{20}F beam was developed this year for an upcoming half-life measurement for Dr. Melconian's group using the tape drive setup. First, the d(^{21}Ne,^{20}F)^{3}He reaction was attempted with 28 MeV/u ^{21}Ne beam from the K500 cyclotron. The MARS gas target was filled with deuterium gas at a pressure of 2 atm and cooled with liquid nitrogen to 77K. A production rate of 1180 eV/nC was obtained with about 8% contamination from ^{20}Ne^{9+} and ^{18}O^{8+}. Next, the ^{21}Ne+^{9}Be reaction was tried. The total production rate for ^{20}F was still about 1130 eV/nC, but the total contamination was a bit higher, closer to 12%, mostly from ^{18}O^{8+}. However, contamination from ^{20}Ne^{9+} was not observed in the ^{21}Ne+^{9}Be reaction. With this production rate, ^{20}F^{9+} at rates greater than 105 p/s should be possible. The ^{20}F half-life measurement is planned for the coming year.

^{35}Ar beam was developed this year for an upcoming transfer reaction measurement with Dr. Christian's group. The p(^{35}Cl,^{35}Ar)n reaction was chosen with 14 MeV/u ^{35}Cl beam from the K150 cyclotron. The MARS gas target was filled with hydrogen gas at a pressure of 0.5 atm and cooled with liquid nitrogen to 77K. A production rate of 700 eV/nC was obtained, with a tail of ^{32}S contamination. To see if more production was possible, the target pressure was increased to 500 torr and 1000 torr and MARS was retuned for each case. The ^{35}Ar production was unchanged in each case; it was still about 700 eV/nC. However, higher target pressures, in particular the 500 torr case, reduced the contamination from the ^{32}S tail at the MARS focal plane. With this production rate, ^{35}Ar at rates greater than 10^{5} p/s should be possible for future experiments.

Finally, production of ^{95}Zr from the d(^{94}Zr,^{95}Zr)p reaction was attempted. In the measurement, a ^{94}Zr beam at 13 MeV/u from the K500 cyclotron impinged on the MARS gas target. The gas target was filled with deuterium gas at a pressure of 250 torr and cooled to 77K with liquid nitrogen. Due to the relatively low beam energy and the heavy mass of the beam and product, it was nearly impossible to separate ^{95}Zr from the charge states of the ^{94}Zr primary beam. Perhaps the best case was ^{95}Zr^{35+}, where the ^{95}Zr^{35+} was separated from ^{94}Zr^{35+} by a few millimeters. Even in this case, it was not possible to separate ^{95}Zr^{35+} from the tail of ^{94}Zr^{34+} in y-position. It may be possible to obtain more mass dispersion if higher voltage on the velocity filter is used. However, a cleaner ^{95}Zr secondary beam is only possible via direct acceleration of ^{95}Zr either from a ^{95}Zr radioactive source (t1/2 = 64 days) or a re-accelerated ^{95}Zr beam from the Light Ion Guide.

A summary of the rare isotope beams produced this year with MARS is given in Table I.

Table I. Summary of MARS RIBs for 2020-2021.

RIB beam	Reaction	Primary Beam	Purity	Intensity on Target
^{7}Be	p(^{7}Li,^{7}Be)n	^{7}Li at 3.5 MeV/u	100%	1.5*10^{5} p/s
^{9}Li	^{18}O(^{7}Li,^{9}Li)^{16}O	^{7}Li at 10.3 MeV/u	~10%	1.8*10^{3} p/s
^{20}F	d(^{21}Ne,^{20}F)^{3}He ^{9}Be(^{21}Ne,^{20}F)X	^{21}Ne at 28 MeV/u	~92% ~88%	~10^{5} p/s
^{35}Ar	p(^{35}Cl,^{35}Ar)n	^{35}Cl at 14 MeV/u	~99%	~10^{5} p/s
^{95}Zr	d(^{94}Zr,^{95}Zr)p	^{94}Zr at 13 MeV/u		inconclusive

[1] R.E. Tribble, R.H. Burch, and C.A. Gagliardi, Nucl. Instrum. Methods Phys. Res. **A285**, 441 (1989).

.

SECTION VI

PUBLICATIONS

PAPERS PUBLISHED

April 1, 2020 – March 31, 2021

***K*-shell internal conversion coefficient for M4 decay of the 30.8 keV isomer in ^{93}Nb**, V. Horvat, E.E. Tereshatov, J.C. Hardy, N. Nica, C.M. Folden, III, V.E. Iacob and M.B. Trzhaskovskaya, Phys. Rev. C **102**, 014310 (2020).

^{19}Ne level structure for explosive nucleosynthesis, M.R. Hall, D.W. Bardayan, T. Baugher, A. Lepailleur, S.D. Pain, A. Ratkiewicz, S. Ahn, J.M. Allen, J.T. Anderson, A.D. Ayangeakaa, J.C. Blackmon, S. Burcher, M.P. Carpenter, S.M. Cha, K.Y. Chae, K.A. Chipps, J.A. Cizewski, M. Febbraro, O. Hall, J. Hu, C.L. Jiang, K.L. Jones, E.J. Lee, P.D. O'Malley, S. Ota, B.C. Rasco, D. Santiago-Gonzalez, D. Seweryniak, H. Sims, K. Smith, W.P. Tan, P. Thompson, C. Thornsberry, R.L. Varner, D. Walter, G.L. Wilson, and S. Zhu, Phys. Rev. C **10**2, 045802 (2020).

Almost medium-free measurement of the Hoyle state direct-decay component with a TPC, J. Bishop, G.V. Rogachev, S. Ahn, E. Aboud, M. Barbui, A. Bosh, C. Hunt, H. Jayatissa, E. Koshchiy, R. Malecek, S. T. Marley, E.C. Pollacco, C.D. Pruitt, B.T. Roeder, A. Saastamoinen, L.G. Sobotka and S. Upadhyayula, Phys. Rev. C **102**, 041303(R) (2020).

An effective way of measuring the excitation function for (α,n) (α,n) reactions at low energies, E.M. Gazeeva, A.A. Bezbakh, V.Z. Goldberg, M.S. Golovkov, B. Zalewski, Zh.K. Kurmanaliyev, D.K. Nauruzbayev, A.K. Nurmukhanbetova, and A. Serikov, Bulletin of the Russian Academy of Sciences: Physics **84**, 420 (2020).

Astatine partitioning between nitric acid and conventional solvents: indication of covalency in ketone complexation of {AtO}$^{+}$, Jonathan D. Burns, Evgeny E. Tereshatov, Mallory A. McCarthy, Lauren A. McIntosh, Gabriel C. Tabacaru, Xin Yang, Michael B. Hall, and Sherry J. Yennello, Chem. Commun. **56**, 9004 (2020).

Astrophysical *S* - factor for the ^{3}He(α,γ)^{7}Be reaction via the asymptotic normalization coefficient (ANC) method, G.G. Kiss, M.La Cognata, C. Spitaleri, R. Yarmukhamedov, I. Wiedenhöver, L.. Baby, S. Cherubini, A. Cvetinović, G.D'Agata, P. Figuera, G.L. Guardo, M. Gulino, S. Hayakawa, I. Indelicato, L. Lamia, M. Lattuada, F. Mudò, S. Palmerini, R.G. Pizzone, G.G. Rapisarda, S. Romano, M.L. Sergi, R. Spartá, O. Trippella, A. Tumino, M. Anastasiou, S.A. Kuvin, N. Rijal, B. Schmidt, S.B. Igamov, S.B. Sakuta, K.I. Tursunmakhatov, Zs. Fülöp, Gy. Gyürky, T. Szücs, Z. Halász, E. Somorjai, Z. Hons, J. Mrazek, R.E. Tribble and A.M. Mukhamedzhanov, Phys. Lett. B **807**, 135606 (2020).

Beam energy dependence of net-Λ fluctuations measured by the STAR experiment at the BNL Relativistic Heavy Ion Collider, J. Adam, D.M. Anderson, C A. Gagliardi, A. Hamed, L. He, T. Lin, X. Liu, Y. Liu, S. Mioduszewski, N.R. Sahoo, P.K. Sahu and R.E. Tribble, Phys. Rev. C **102**, 024903 (2020).

Beam-energy dependence of the directed flow of deuterons in Au+Au Au+Au collisions, J. Adam, D. M. Anderson, C.A. Gagliardi, A. Hamed, T. Lin, X. Liu, Y. Liu, S. Mioduszewski, N.R. Sahoo and R.E. Tribble, Phys. Rev. C **102**, 044906 (2020).

Beam-energy dependence of the production of light nuclei in Au + Au collisions, Wenbin Zhao, Chun Shen, Che Ming Ko, Quansheng Liu, and Huichao Song, Phys. Rev. C **102**, 044912 (2020).

Beta-delayed charged-particle spectroscopy using TexAT, J. Bishop, G.V. Rogachev, S. Ahn, E. Aboud, M. Barbui, P. Baron, A. Bosh, E. Delagnes, J. Hooker, C. Hunt, H. Jayatissa, E. Koshchiy, R. Malecek, S. T. Marley, R. O'Dwyer, E.C. Pollacco, C. Pruitt, B.T. Roeder, A. Saastamoinen, L.G. Sobotka, and S. Upadhyayula, Nucl. Instrum. Methods Phys. Res. **A964**, 163773 (2020).

Chaos, percolation and the coronavirus spread, Aldo Bonasera and Suyalatu Zhang, Front. Phys. **8**, 00171 (2020).

Chaos, percolation and the coronavirus spread: a two-step model, Hua Zheng and Aldo Bonasera, Eur. Phys. J. Plus **135**, 799 (2020).

Charged particle track reconstruction with SπRIT Time Projection Chamber, J.W. Lee, G. Jhang, G. Cerizza, J. Barney, J. Estee, T. Isobe, M. Kaneko, M. Kurata-Nishimura, W.G. Lynch, T. Murakami, C.Y. Tsang, M.B. Tsang, R. Wang, B. Hong, A.B. McIntosh, H. Sakurai, C. Santamaria, R. Shane, S. Tangwancharoen, S.J. Yennello, and Y. Zhang, Nucl. Instrum. Methods Phys. Res. **A965**, 163840 (2020).

Charmed hadron chemistry in relativistic heavy-ion collisions, Shanshan Cao, Kai-Jia Sun, Shu-Qing Li, Shuai Y.F. Liu, Wen-Jing Xing, Guang-You Qin and Che Ming Ko, Phys. Lett. B **807**, 135561 (2020).

Constraining the in-medium nucleon-nucleon cross section from the width of nuclear giant dipole resonance, Rui Wang, Zhen Zhang, Lie-Wen Chen, Che Ming Ko and Yu-Gang Ma, Phys. Lett. B **807**, 135532 (2020).

Correlation between time and angular alignment in molecular dynamics simulations of heavy ion collisions, B. Harvey, M. Youngs, A.B. McIntosh, A. Jedele, A. Abbott, J. Gauthier, K. Hagel, A. Hannaman, A. Hood, K. Krieble, Y.-W. Lui, L.A. McIntosh, A. Rodriguez Manso, M. Sorensen, Z. Tobin, R. Wada, A. Zarrella, and S. J. Yennello, Phys. Rev. C **102**, 064625 (2020).

Corrigendum: Balmer emission induced by proton impact on atomic hydrogen (2019 *J. Phys. B: At. Mol. Opt. Phys.* 52 105701), I.B. Abdurakhmanov, O. Erkilic, A.S. Kadyrov, I. Bray, S.K. Avazbaev and A. M. Mukhamedzhanov, J. Phys. B **53**, 139501 (2020).

Diagnostic methodologies of laser-initiated ^{11}B(p,α)2α fusion reactions, Fabrizio Consoli, Riccardo De Angelis, Pierluigi Andreoli, Aldo Bonasera, Mattia Cipriani, Giuseppe Cristofari, Giorgio Di Giorgio, Danilo Giulietti and Martina Salvadori, Front. Phys. **8**, 561492 (2020).

Effects of cluster correlations on fragment emission in ^{12}C+^{12}C at 50 MeV/nucleon, R. Han, Z. Chen, R. Wada, A. Ono, G. Tian, F. Shi, X. Zhang, B. Liu, and H. Sun, Phys. Rev. C **102**, 064617 (2020).

Energy density functional and sensitivity of energies of giant resonances to bulk nuclear matter properties, S. Shlomo and A.I. Sanzhur, Nucl. Phys. At. Energy **21**, 113 (2020).

Enhanced production of strange baryons in high-energy nuclear collisions from a multiphase transport model, Tianhao Shao, Jinhui Chen, Che Ming Ko, and Zi-Wei Lin, Phys. Rev. C **102**, 014906 (2020).

First measurement in the Gamow window of a reaction for the γ - process in inverse kinematics: ^{76}Se(α,γ)^{80}Kr, J. Fallis, C. Akers, A.M. Laird, A. Simon, A. Spyrou, G. Christian, D. Connolly, U. Hager, D.A. Hutcheon, A. Lennarz, P. O'Malley, S.J. Quinn, J. Riley, A. Rojas, C. Ruiz, and M. Williams, Phys. Lett. B **807**, 135575 (2020).

First measurement of Λ_c baryon production in Au+Au collisions at $\sqrt{s_{NN}}$ = 200 GeV, J. Adam, D. M. Anderson, C.A. Gagliardi, A. Hamed, T. Lin, X. Liu, Y. Liu, S. Mioduszewski, N.R. Sahoo, and R.E. Tribble, Phys. Rev. Lett. **124**, 172301 (2020).

Fission-fragment excitation energy sharing beyond scission, Aurel Bulgac, Phys. Rev. C 102, 044609 (2020).

Hydrophobic amine-based binary mixtures of active pharmaceutical and food grade ingredients: characterization and application in indium extraction from aqueous hydrochloric acid media, Joseph M. Edgecomb, Evgeny E. Tereshatov, Guillaume Zante, Maria Boltoeva and Charles M. Folden, III, Green Chem. **22**, 7047 (2020).

Implementing chiral three-body forces in terms of medium-dependent two-body forces, Jeremy W. Holt, Mamiya Kawaguchi and Norbert Kaiser, Front. in Phys. **8**, 100 (2020).

Intensity of a weak 519-keV γ ray following β decay of the superallowed emitter ^{34}Ar determined via the ^{33}S(p,γ)^{34}Cl reaction, H.I. Park, J.C. Hardy, M. Bencomo, V.E. Iacob, I.S. Towner, K.T. Macon, W.P. Tan, M. Brodeur, A. Boeltzig, B. Frentz, S.L. Henderson, J. Long, S. McGuinness, O. Olivas-Gomez, P. O'Malley, G. Seymour, B Vande Kolk, and A. Kayani, Phys. Rev. C **102**, 045502 (2020).

International network of nuclear structure and decay data evaluators, Paraskevi Dimitriou, Shamsuzzoha Basunia, Lee Bernstein, Jun Chen, Zsoltan Elekes, Xiaolong Huang, Hideki Iimura, Ashok

Jain, John Kelley, Tibor Kibedi, Filip Kondev, Stefan Lalkovski, Elizabeth McCutchan, Ivan Mitropolsky, Gopal Mukherjee, Alexandru Negret, Caroline Nesaraja, Ninel Nica, Sorin Pascu, Alexander Rodionov, Balraj Singh, Sukhjeet Singh, Michael Smith, Alejandro Sonzogni, Janos Timar, Jagdish Tuli, Marco Verpelli, Dong Yang and Viktor Zerkin, International Conference on Nuclear Data for Science and Technology, Eur. Phys. J. Web of Conferences **239**, 15004 (2020).

Investigation of the linear and mode-coupled flow harmonics in Au+Au collisions at $\sqrt{s_{NN}}$ = 200 GeV, J. Adam, D.M. Anderson, C.A. Gagliardi, A. Hamed, T. Lin, X. Liu, Y. Liu, S. Mioduszewski, N.R. Sahoo, and R.E. Tribble, Phys. Lett. B **809**, 135728 (2020).

Isoscalar and isovector giant resonances in closed shells nuclei and bulk properties of nuclear matter, S. Shlomo, Phys. Atom. Nuclei **83**, 599 (2020).

Isotopic equilibrium constants for very low-density and low-temperature nuclear matter, J.B. Natowitz, H. Pais, G. Röpke, J. Gauthier, K. Hagel, M. Barbui, and R. Wada, Phys. Rev. C **102**, 064621 (2020).

Light nuclei production in Au+Au collisions at $\sqrt{s_{NN}}$ = 5−200 GeV from JAM model, Hui Liu, Dingwei Zhang, Shu He, Kai-Jia Sun, Ning Yu and Xiaofeng Luo, Phys. Lett. B **805**, 135452 (2020).

Mean Field Theory, Vladimir M. Kolomietz and Shalom Shlomo, World Scientific Publishing Company, Incorporated, 2020.

Measurement of D^0 -meson + hadron two-dimensional angular correlations in Au+Au collisions at $\sqrt{s_{NN}}$=200 GeV, J. Adam, D.M. Anderson, C.A. Gagliardi, A. Hamed, T. Lin, X. Liu, Y. Liu, S. Mioduszewski, N.R. Sahoo, and R.E. Tribble, Phys. Rev. C **102**, 014905 (2020).

Measurement of away-side broadening with self-subtraction of flow in Au+Au collisions at $\sqrt{s_{NN}}$ =200 GeV, J. Adam, D.M. Anderson, C.A. Gagliardi, A. Hamed, T. Lin, X. Liu, Y. Liu, S. Mioduszewski, N.R. Sahoo, and R.E. Tribble, Chinese Phys. C **44**, 104001 (2020).

Measurement of groomed jet substructure observables in p+p collisions at $\sqrt{s}$ = 200 with STAR, J. Adam, D.M. Anderson, C.A. Gagliardi, A. Hamed, T. Lin, X. Liu, Y. Liu, S. Mioduszewski, N.R. Sahoo, and R.E. Tribble, Phys. Lett. B **811**, 135846 (2020).

Measurement of inclusive J/ψ polarization in p+p collisions at $\sqrt{s}$ =200 GeV by the STAR experiment, J. Adam, D.M. Anderson, C.A. Gagliardi, A. Hamed, T. Lin, X. Liu, Y. Liu, S. Mioduszewski, N.R. Sahoo, and R.E. Tribble, Phys. Rev. D **102**, 092009 (2020).

Measurement of inclusive charged-particle jet production in Au+Au collisions at $\sqrt{s_{NN}}$ =200 GeV, J. Adam, D.M. Anderson, C.A. Gagliardi, A. Hamed, T. Lin, X. Liu, Y. Liu, S. Mioduszewski, N.R. Sahoo, and R.E. Tribble, Phys. Rev. C **102**, 054913 (2020).

Measurement of the central exclusive production of charged-particle pairs in proton-proton collisions at $\sqrt{s}$ =200 GeV with the STAR detector at RHIC, J. Adam, D.M. Anderson, C.A. Gagliardi, A. Hamed, T. Lin, X. Liu, Y. Liu, S. Mioduszewski, N.R. Sahoo, and R. E. Tribble, JHEP **2020**, 178 (2020).

Neutron elastic scattering on calcium isotopes from chiral nuclear optical potentials, T.R. Whitehead, Y. Lim and J.W. Holt, Phys. Rev. C **101**, 064613 (2020).

Nuclear data sheets for A=153, N. Nica, Nucl. Data Sheets **170**, 1 (2020).

Nuclear liquid-gas phase transition with machine learning, Rui Wang, Yu-Gang Ma, R. Wada, Lie-Wen Chen, Wan-Bing He, Huan-Ling Liu and Kai-Jia Sun, Phys. Rev. Research **2**, 043202 (2020).

Observation of *T=3/2* isobaric analog states in ^{9}Be using *p*+ ^{8}Li resonance scattering, C. Hunt, G.V. Rogachev, S. Almaraz-Calderon, A. Aprahamian, M. Avila, L.T. Baby, B. Bucher, V.Z. Goldberg, E.D. Johnson, K.W. Kemper, A.N. Kuchera, W.P. Tan, and I. Wiedenhöver, Phys. Rev. C **102**, 014615 (2020).

One-center close-coupling approach to two-center rearrangement collisions, I.B. Abdurakhmanov, C. Plowman, A.S. Kadyrov, I. Bray, and A.M. Mukhamedzhanov, J. Phys. B: At. Mol. Opt. Phys. **53**, 145201 (2020).

Pre-equilibrium neutron emission in fission or fragmentation, Aurel Bulgac, Phys. Rev. C **102**, 034612 (2020).

Precise β branching-ratio measurement for the $0^{+} \rightarrow 0^{+}$ superallowed decay of ^{34}Ar, V.E. Iacob, J.C. Hardy, H.I. Park, M. Bencomo, L. Chen, V. Horvat, N. Nica, B.T. Roeder, A. Saastamoinen, and I.S. Towner, Phys. Rev. C **101**, 045501 (2020).

Primary yields of protons measured using CR-39 in laser-induced deuteron-deuteron fusion reactions, Yue Zhang, Long-Xiang Liu, Hong-Wei Wang, Yu-Gang Ma, Bai-Fei Shen, Guo-Qiang Zhang, Mei-Rong Huang, Aldo Bonasera, Wen-Peng Wang, Jian-Cai Xu, Shun Li, Gong-Tao Fan, Xi-Guang Cao, Yong Yu, Jian-Jun He, Chang-Bo Fu, Suyalatu Zhang, Xin-Rong Hu, Xin-Xiang Li, Zi-Rui Hao, Jun-Wen Wang, Han Xue, and Hai-Juan Fu, Nucl. Sci. Tech. **31**, 8 (2020).

Probing the neutron-proton asymmetry dependence of the nuclear source temperature with light charged particles, Y. Huang, W. Lin, H. Zheng, R. Wada, X. Liu, G. Qu, M. Huang, P. Ren, J. Han, M.R. D. Rodrigues, S. Kowalski, T. Keutgen, K. Hagel, M. Barbui, A. Bonasera, and J.B. Natowitz, Phys. Rev. C **101**, 064603 (2020).

Probing the partonic degrees of freedom in high-multiplicity *p*-Pb collisions at $\sqrt{s_{NN}}$ =5.02 TeV, Wenbin Zhao, Che Ming Ko, Yu-Xin Liu, Guang-You Qin and Huichao Song, Phys. Rev. Lett. **125**, 072301 (2020).

Properties of strange quark stars with isovector interactions, He Liu, Jun Xu and Che Ming Ko, Phys. Lett. B **803**, 135343 (2020).

Spin polarizations in a covariant angular momentum conserved chiral transport model, S.Y.F. Liu, Y.F. Sun, and C.M. Ko, Phys. Rev. Lett. **125**, 062301 (2020).

Yield ratio of hypertriton to light nuclei in heavy-ion collisions from $\sqrt{(s_{NN})}$ = 4.9 GeV to 2.76 TeV, T.H. Shao, J.H. Chen, C.M. Ko, K.J. Sun, and Z.B. Zu, Chinese Phys. C **44**, 114001 (2020).

Number of constituent quark scaling of elliptic flows in high multiplicity p-Pb collisions at $\sqrt{(s_{NN})}$ = 5.02 TeV, W.B. Zhao, C.M. Ko, Y.X. Liu, G.Y. Chen, and H.C. Song, Nucl. Phys. **A1005**, 121876 (2021).

Local spin polarizations in relativistic heavy ion collisions, S. Y. F. Liu, Y. F. Sun, and C. M. Ko, Nucl. Phys. **A1005**, 121895 (2021).

Symmetry energy investigation with pion production from Sn+Sn systems, G. Jhang *et al.*, Phys. Lett. B **813**, 136106 (2021).

Effects of QCD critical point on light nuclei production, K.J. Sun, F. Li, and C.M. Ko, Phys. Lett. B **816,** 136258 (2021).

Reconstruction of neutral-triggered charged recoil jets in s $\sqrt{s}$ =200 GeV p+p collisions at the STAR experiment, Derek Anderson, XLIX International Symposium on Multiparticle Dynamics (ISMD 2019), Eur. Phys. J. Web of Conferences **235**, 05005, (2020).

Astrophysical S-factor for the ^{3}He(α, γ)^{7}Be reaction via the asymptotic normalization coefficient (ANC) method, G.G. Kissa, M. La Cognata, C. Spitaleri, R. Yarmukhamedov, I. Wiedenhöver, L.T. Baby, S. Cherubini, A. Cvetinovic, G. D'Agatab, P. Figuera, G.L. Guardo, M. Gulino, S. Hayakawa, I. Indelicato, L. Lamiab, M. Lattuada, F. Mudò, S. Palmerini, R.G. Pizzone, G.G. Rapisarda, S. Romano, M.L. Sergi, R. Spartà, O. Trippella, A. Tumino, M. Anastasiou, S.A. Kuvin, N. Rijal, B. Schmidt, S.B. Igamov, S.B. Sakuta, K.I. Tursunmakhatov, Zs. Fülöp, Gy. Gyürky, T. Szücs, Z. Halász, E. Somorjai, Z. Hons, J. Mrázek, R.E. Tribble, A.M. Mukhamedzhanov, Phys. Lett. B **807**, 135606 (2020).

Status on ^{12}C + ^{12}C fusion at deep sub-barrier energies: impact of resonances on astrophysical S* -factors, C. Beck, A.M. Mukhamedzhanov, X. Tang, Eur. Phys. J. A **56**, 87 (2020)

Trojan horse method as an indirect approach to study resonant reactions in nuclear astrophysics, A.M. Mukhamedzhanov, A.S. Kadyrov, and D.Y. Pang, Eur. Phys. J. A **56**, 233 (2020).

A new waveform analysis technique to extract good energy and position resolution from a dual-axis duo-lateral position-sensitive detector, M.W. Aslin, A. Hannaman, M.D. Youngs, A.B. McIntosh, A. Abbott, P. Adamson, J. Gauthier, K. Hagel, A. Jedele, Y.-W. Lui, L.A. McIntosh, M.Q. Sorensen, Z.N. Tobin, R. Wada, A. Wakhle, and S.J. Yennello, Nucl. Instrum. Methods Phys. Res. **A985**, 164674 (2021).

Effect of hydrophobic ionic liquids aqueous solubility on metal extraction from hydrochloric acid media: Mathematical modelling and trivalent thallium behavior, Evgeny E. Tereshatov, Valérie Mazan, Maria Boltoeva and Charles M. Folden, III, Sep. Purif. Technol. **255**, 117650 (2021).

Local spin polarizations in relativistic heavy-ion collisions, Shuai Y.F. Liu, Yifeng Sun and Che Ming Ko, in: Quark Matter 2019, Wuhan, China, Nucl. Phys. **A1005**, 121895, (2021).

Measurements of D-D fusion neutrons generated in nanowire array laser plasma using Timepix3 detector, Peter Rubovič, Aldo Bonasera, Petr Burian, Zhengxuan Cao, Chang-Bo Fu, Defeng Kong, Haoyang Lan, Yao Lou, Wen Luo, Chong Lv, Yu-Gang Ma, Wenjun Ma, Zhiguo Ma, Lukáš Meduna, Zhusong Mei, Yesid Mora, Zhuo Pan, Yinren Shou, Rudolf Sýkora, Martin Veselský, Pengjie Wang, Wenzhao Wang, Xueqing Yan, Guoqiang Zhang, Jiarui Zhao, Yanying Zhao and Jan Žemlička, Nucl. Instrum. Methods Phys. Res. **A985**, 164680 (2021).

Nonmonotonic energy dependence of net-proton number fluctuations, J. Adam, D.M. Anderson, C.A. Gagliardi, A. Hamed, T. Lin, X. Liu, Y. Liu, S. Mioduszewski, N.R. Sahoo, and R.E. Tribble, Phys. Rev. Lett. **126**, 092301 (2021).

Nuclear temperature and its dependence on the source neutron-proton asymmetry deduced using the Albergo thermometer, Y. Huang, H. Zheng, R. Wada, X. Liu, W. Lin, G. Qu, M. Huang, P. Ren, J. Han, A. Bonasera, K. Hagel, M.R.D. Rodrigues, S. Kowalski, T. Keutgen, M. Barbui, and J.B. Natowitz, Phys. Rev. C **103**, 014601 (2021).

Number of constituent quark scaling of elliptic flows in high multiplicity *p*-Pb collisions at $\sqrt{s_{NN}}$ = 5.02 TeV, Wenbin Zhao, Che Ming Ko, Yu-Xin Liu, Guang-You Qin and Huichao Song, in: Quark Matter 2109, Wuhan, China, Nucl. Phys. **A1005**, 121876 (2021).

Performance of position-sensitive resistive silicon detectors in the Forward Array Using Silicon Technology (FAUST), L.A. McIntosh, A.B. McIntosh, K. Hagel, M.D. Youngs, L.A. Bakhtiari, C.B. Lawrence, P. Cammarata, A. Jedele, L.W. May, A. Zarrella, and S.J. Yennello, Nucl. Instrum. Methods Phys. Res. **A985**, 164642 (2021).

Properties of isoscalar giant multipole resonances in medium-heavy closed-shell nuclei: A semi microscopic description, M.L. Gorelik, S. Shlomo, B.A. Tulupov, and M.H. Urin, Phys. Rev. C **103**, 034302 (2021).

Proton pairing in neutron stars from chiral effective field theory, Yeunhwan Lim and Jeremy W. Holt, Phys. Rev. C **103**, 025807 (2021).

QCD critical point from the Nambu-Jona-Lasino model with a scalar-vector interaction, Kai-Jia Sun, Che Ming Ko, Shanshan Cao, and Feng Li, Phys. Rev. D **103**, 014006 (2021).

Rapid recovery of At-211 by extraction chromatography, Jonathan D. Burns, Evgeny E. Tereshatov, Geoffrey Avila, Kevin J. Glennon, Andrew Hannaman, Kylie N. Lofton, Laura A. McCann, Mallory A. McCarthy, Lauren A. McIntosh, Steven J. Schultz, Gabriel C. Tabacaru, Amy L. Vonder Haar and Sherry J. Yennello, Sep. Purif. Technol. **256**, 117794 (2021).

Recent measurements of heavy quarkonium production in Au+Au, p+Au and p+p collisions at STAR, Yanfang Liu, in: Quark Matter, Wuhan, China, Nucl. Phys. **A1005**, 121993 (2021).

Semi-classical approximation description of static properties of nuclei, S. Shlomo and A.I. Sanzhur, Mod. Phys. Lett. A **36**, 2130008 (2021).

Symmetry energy investigation with pion production from Sn + Sn systems, G. Jhang, A.B. McIntosh, and S.J. Yennello, Phys. Lett. B **813**, 136016 (2021).

The ^{3}He+^{5}He→α+α reaction below the Coulomb barrier via the Trojan Horse Method, C. Spitaleri, S. Typel, C.A. Bertulani, A.M. Mukhamedzhanov, T. Kajino, M. Lattuada, A. Cvetinović, S. Messina, G.L. Guardo, N. Soić, M. Milin, S.S. Perrotta, Chengbo Li, P. Čolović, G. D'Agata, D. Dell'Aquila, C.G. Fatuzzo, M. Gulino, S.Q. Hou, M.La Cognata, D. Lattuada, D. Nurkić, R. Popočovski, N. Skukan, S. Szilner, O. Trippella, M. Uroić, and N. Vukman, Eur. Phys. J. A **57**, 20 (2021).

Valence states of cyclotron-produced thallium, Evgeny E. Tereshatov, Miroslava Semelová, Kateřina Čubová, Pavel Bartl, Mojmír Němec, Jan Štursa, Václav Zach, Charles M. Folden, III, Jon Petter Omtvedt and Jan John, New J. Chem. **45**, 3377 (2021).

SECTION VII

APPENDIX

TALKS PRESENTED

April 1, 2020 – March 31, 2021

Preparing DAPPER to measure photon strength functions, **A. Abbott**, CENTAUR Group Meeting, Virtual, Texas (March 2021).

Climate surveys and assessments to achieve your goals, **S.J. Yennello**, **Invited talk**, APS - IDEA, Virtual, United States (February 2021).

Almost medium-free measurement of the Hoyle state direct-decay component with a TPC, **J. Bishop**, Previews of the Future in Low-Energy Experimental Nuclear Physics: A Postdoctoral Seminar Series, Online, College Station, Texas (February, 2021).

Design and testing of YAP:Ce array for DAPPER, **A. Abbott**, 2021 National Nuclear Security Administration (NNSA) Stewardship Science Academic Programs (SSAP) Symposium, Virtual, United States (Feburary 2021).

CENTAUR:Expanded opportunities in a virtual world, **S.J. Yennello**, **Invited talk**, 2021 National Nuclear Security Administration (NNSA) Stewardship Science Academic Programs (SSAP) Symposium, Virtual, United States (February 2021).

Beam rate dependent effects on single crystalline diamond detector, **M. Sorensen**, 2021 National Nuclear Security Administration (NNSA) Stewardship Science Academic Programs (SSAP) Symposium, Virtual, United States (February 2021).

The search for alpha - clustered toroidal nuclei in ^{28}Si, **A. Hannaman**, Fall Meeting of the Division of Nuclear Physics, Virtual, New Orleans, Louisiana (October 2020).

Chiral effective field theory for nuclear matter and neutron stars, **J. Holt**, **Invited talk**, Hadron in Nucleus 2020, Yukawa Institute for Theoretical Physics, Kyoto, Japan (March 2021).

Hot and dense neutron-rich matter in supernovae and neutron star mergers, **J. Holt**, **Invited talk**, Stony Brook University, Stony Brook, New York (November 2020).

Spin and density response functions for hot and dense nuclear matter from chiral nuclear forces, **E. Shin**, DNP Fall Meeting 2020, APS Division of Nuclear Physics, Virtual Meeting, United States (October 2020).

Constraining the nonanalytic terms of the nuclear symmetry energy with chiral nuclear forces, **P. Wen**, 2020 Fall Meeting of the APS Division of Nuclear Physics, United States (November 2020).

Nucleon-nucleus global optical potential from chiral effective field theory, **T. Whitehead**, 2020 Fall Meeting of the APS Division of Nuclear Physics, Virtual Meeting, United States (November 2020).

Modifications to the ^{6}He-CRES experiment for ion bunching and trapping, **D. McClain**, 2021 National Nuclear Security Administration (NNSA) Stewardship Science Academic Programs (SSAP) Symposium, Virtual, United States (February 2021).

Commissioning the Texas A&M University penning trap via offline mass measurements, **M. Nasser**, 2021 National Nuclear Security Administration (NNSA) Stewardship Science Academic Programs (SSAP) Symposium, Virtual, United States (February 2021).

Nuclear frontiers with active targets, RAON colloquium (virtual), **G. Rogachev**, **Invited talk**, RAON, Daejon, South Korea (December 2020).

Nuclear frontiers with active targets, **G. Rogachev**, **Invited talk**, FLNR seminar, Flerov Laboratory for Nuclear Reactions, Dubna, Russia (March 2021).

Origin of the elements, **G. Rogachev**, **Invited talk**, Lecture to Woodlands Science Academy students, Woodlands Science Academy, Woodlands, Texas (September 2020).

Texas A&M Cyclotron Institute and CENTAUR as generators of nuclear talent, **S.J. Yennello**, **Invited talk**, WANDA21, Virtual, United States (February 2021).

Toward inclusive excellence in nuclear science, **S.J. Yennello**, **Invited talk**, ChETEC Action Split Period 4 Main Event, Virtual, Croatia (September 2020).

The photon strength function of ^{60}Fe with DAPPER, **M. Sorensen**, Virtual Joint Nuclear and Astrophysics Seminar, Texas A&M, College Station, Texas (January 2021).

Getting involved in undergraduate research, Conference for Undergraduate Women in Physics, **S.J. Yennello**, **Invited talk**, Virtual, United States (January 2021).

Background free measurement of β-delayed protons from ^{27}P for the astrophysical ^{26}mAl(p,γ)^{27}Si reaction, **A. Saastamoinen**, Joint Nuclear and Astrophysics Seminar, Physics and Astronomy / Cyclotron Institute, Texas A&M University, College Station, Texas (December 2020).

Texas A&M evaluation center precision internal conversion coefficients measurements follow-up, **N. Nica**, Nuclear Data Week 2020, USDNP Meeting, Dec 1-4, Brookhaven National Laboratory, Upton, New York (December 2020).

Texas A&M evaluation center strategic priorities, **N. Nica**, Nuclear Data Week 2020, USNDP Meeting, Dec 1-4, Brookhaven National Laboratory, Upton, New York (December 2020).

Texas A&M University US nuclear data program Texas A&M evaluation center report 2020, **N. Nica**, Nuclear Data Week 2020, USNDP Meeting, Dec 1-4, Brookhaven National Laboratory, Upton, New York (December 2020).

State of the art experiments with active target detectors developed at Cyclotron Institute, **Y. Koshchiy**, Cyclotron Institute seminar, Cyclotron Institute, Texas A&M University, College Station, Texas (December 2020).

Nuclear chemistry: Fundamental chemistry impacting society, **S.J. Yennello**, **Invited presentation**, College Station High School Science Club, College Station High School, College Station, Texas (November 2020).

Curing cancer from the inside: The promise of targeted alpha therapy, **S.J. Yennello**, **Invited talk**, Distinguished Lecture in Chemistry, UT Dallas, Dallas, Texas (November 2020).

Developing isotope production capabilities with heavy-ion beams at Texas A&M University, **L. McIntosh**, Division of Nuclear Physics of American Physical Society, Virtual, United States (November 2020).

Isolation of ^{211}At from bismuth target in nitric acid media using hydrophobic organic solvents, **A. Vonder Haar**, 2020 Fall Meeting of the APS Division of Nuclear Physics, New Orleans, Louisiana, virtual (October 2020).

Silicon characterization for DAPPER, **A. Abbott**, 2020 Fall Meeting of the APS Division of Nuclear Physics, New Orleans, Louisiana, virtual (October 2020).

Benchmarking an active catcher array for the Study of multinucleon transfer reactions, **A. Hood**, 2020 Fall Meeting of the APS Division of Nuclear Physics, New Orleans, Louisiana, virtual (October 2020).

High-precision half-life measurement of ^{29}P, **P. Shidling**, 2020 Fall Meeting of the APS Division of Nuclear Physics, New Orleans, Louisiana, virtual (October 2020).

Kr+C reactions to explore the asymmetry dependence of the nuclear caloric curve, **A. McIntosh**, 2020 Fall Meeting of the APS Division of Nuclear Physics, New Orleans, Louisiana, virtual (October 2020).

Searching for BSM physics via the precision frontier: β decay experiments using atom and ion traps, **D. Melconian**, **Invited talk**, NSCL/FRIB Virtual Nuclear Science Seminar, MSU/NSCL, East Lansing, Michigan (October 2020).

Gamma ray detection in DAPPER array for (d,pγ) reactions, **M. Sorensen**, 2020 Fall Meeting of the APS Division of Nuclear Physics, New Orleans, Louisiana, virtual (October 2020).

Measurement of neutron-induced enhancement of the triple-alpha process with a TPC, **J. Bishop**, Virtual Joint Nuclear and Astrophysics Seminar, Texas A&M University, College Station, Texas (September 2020).

Future neutron detection capabilities at TRIUMF for nuclear astrophysics and structure, **G. Christian**, **Invited talk**,TRIUMF Science Week, TRIUMF (virtual), Vancouver, Canada (August 2020).

Nuclear forensics research at Texas A&M University, **C.M. Folden III**, ACS Fall 2020 Virtual Meeting & Expo, San Francisco, California (August 2020).

Extraction and separation of iridium(IV) and rhodium(III) from hydrochloric acid media by a quaternary ammonium-based hydrophobic eutectic solvent, **V. Zakusilova**, ACS Fall 2020 Virtual Meeting & Expo, San Francisco, California (August 2020).

Studying stellar nucleosynthesis through heavy-ion gated transfer reactions, **G. Christian**, **Invited talk**, Argonne National Laboratory Heavy Ion Discussion, Argonne National Lab (virtual), Lemont, Illinois (August 2020).

DAPPER: Preparations to measure iron 60's photon strength function, **M. Sorensen**, CENTAUR SAC Virtual Meeting, College Station, Texas (August 2020).

Development of DAPPER for measuring ^{60}Fe gamma ray strength function, **A. Abbott**, 2020 CENTAUR SAC Virtual Meeting, Cyclotron Institute, College Station, Texas (August 2020).

Advancing research in Texas through experiments in medical isotope science, **S.J. Yennello**, **Invited talk**, NIDC At-211 meeting, ORAU, virtual, United States (July 2020).

Contemporary nuclear physics, **C.M. Ko**, **Invited talk**, Sichuan University, Chengdu, China (July 2020).

Chiral kinetic modeling of vorticity and polarization, **C.M. Ko**, **Invited talk**, Institute of Nuclear Theory Program on Criticality and Chirality in Heavy ion Collisions, Seattle, Washington (virtual) (May 2020).

Probing the nuclear symmetry energy with rare isotope beams, **C.M. Ko**, **Invited talk**, C2R2 Seminars, Korea (February 2021).

Probing QCD critical point with light nuclei production, **K.J. Sun**, **Invited talk**, The 10^{th} RHIC BES Theory and Experimental Online Seminar (virtual), United States (October 2020).

Particle gated transfer reactions: A tool for studying stellar nucleosynthesis, **G. Christian**, **Invited talk**, UK Locodown Seminar Series, U. Liverpool (virtual), Liverpool, United Kingdom (May 2020).

Measurements of the $^{16}C + ^{12}C$ and $^{16}C + ^{13}C$ fusion cross sections with implications for astrophysics, **A. Hood**, APS April Meeting (virtual), Washington D.C., United States (April 2020).

RESEARCH PERSONNEL AND ENGINEERING STAFF

April 1, 2020 - March 31, 2021

Faculty and Research Group Leaders

Bonasera, Aldo - Senior Scientist
Christian, Gregory - Assist. Prof. of Physics- To 6/19
Fries,Rainer - Assoc. Professor of Physics
Folden, III, Charles M. - Assoc.. Prof. of Nuclear Chemistry
Gagliardi, Carl A. - Professor of Physics
Hardy, John C. - Professor Emeritus
Holt, Jeremy - Assist. Professor of Physics
Ko, Che Ming – Professor of Physics
Melconian, Dan - Assoc. Professor of Physics
Mioduszewski, Saskia - Professor of Physics
Natowitz, J. B. - Professor Emeritus
Rapp, Ralf - Professor of Physics
Rogachev, Grigory - Professor of Physics and Head of Department of Physics and Astronomy
Shlomo, Shalom - Senior Scientist
Tribble, Robert E. – Professor of physics (20%)
Yennello, Sherry J. - Professor of Chemistry, Bright Chair, Director
Youngblood, Dave H. - Professor Emeritus
Zhanov, Akram M. - Senior Scientist

Research Staff

Ahn, Sunghoon – Assist. Research Scientist – To 9/20
Ärje, Juha – Research Scientist
Barbui, Marina - Assist. Research Scientist
Chubaryan, Grigor - Research Scientist
Clark, Henry - Accelerator Physicist (50%)
Gauthier, Jerome - From 6/2/19
Goldberg, Vladilen - Research Scientist, Retired
Hagel, John C. - Research Scientist (50%)
McIntosh, Lauren –Assist. Research Scientist
Horvat, Vladimir - Research Scientist (50%)
Iacob, Victor - Research Scientist
Koshchiy, Yevgen - Assoc. Research Scientist – From 3/1/2021
Lui, Yiu-Wing - Research Scientist
McIntosh, Alan - Assist. Res. Scientist
McIntosh, Lauren –Assist. Research Scientist
Nica, Ninel - Associate Research Scientist
Rodrigues, Marcia Dias - Assist. Res. Scientist
Saastamoinen, Antti (50%)
Shidling, Praveen - Assist. Research Scientist
Tereshatov, Evgeny - Assist. Research Scientist
Wada, Roichi (40%)

Accelerator Physics and Radiation Line Staff

Avila, Geoffrey – Research Assistant – From 11/1/2019
Brinkley, Joseph - Research Associate (28%)
Clark, Henry - Accelerator Physicist (50%)
Horvat, Vladimir - Research Scientist (50%)
Hyman, Bruce - Research Associate
Kim, George - Accelerator Physicist
May, Don – Senior Accelerator Physicist
Roeder, Brian - Accelerator Physicist
Park, Hyo-In - Accelerator
Saastamoinen, Antti (50%)
Tabacaru, Gabriel - Accelerator Physicist

Computer Systems Staff

Burch, Jr. Robert Lead Microcomputer/LAN Administrator
Hagel, John C. Research Scientist (50%)

Engineering Staff

Molitor, Stephen Senior Mechanical Engineer – From 7/2020
Olsen, Robert Senior Mechanical Engineer

Postdoctoral Research Associates

Bishop, Jack
Childers, Katherine – From 1/27/2021
Hood, Ashley
Kolhinen, Veli Sakari
Kordell, Michael – From 8/6/18
Lin, Ting
Liu, Shuai – To 9/24/19
Pan, Jinjin – From 9/1/2020
Parker, Cody
Sun KaiJia

STUDENTS

April 1, 2020 - March 31, 2021

Graduate Students and Research Assistants

Abbott, Austin
Aboona, Bassam
Aboud, Eric
Anderson, Derek
Atchison, Joseph
Bennett, Eames – To 8/31/2020
Bosh, Alexandra – To 2/28/2021
Dede, Stefania
Edgecomb, Joseph – To 8/28/2019
Garza, Fabian – To 1/31/2021
Glennon, Kevin
Hannaman, Andy
Harris, Emily
Haynes, Isaac – From 12/8/2020
Henderson, Lawrence
Hunt, Curtis
Hunt, Ethan – To 3/31/2020
Jedele, Andrea - To 12/31/2020
Kim, Byunggyu
Liu, Yanfang
Loftin, Sarah – From 12/8/2020
McCain, David
Mildon, Jordan – From 12/8/2020
Nasser, Morgan
Onyango, Thomas
Ozmetin, Asim
Ramiriez, Mariah – To 1/15/2021
Robicheaux, Stephen
Roosa, Michael
Sarver, Issac
Schroeder, Benjamin – To 4/30/2020
Schultz, Steven – From 9/1/2020
Scriven, Dustin
Sengupta, Arjun
Settlemyre, Thomas – From 8/6/19
Shin, Eunkyoung
Sorensen, Maxwell
Tang, Zhanduo
Tobin, Zachary
Wen, Pengshen – From 8/8/2019
Whitehead, Taylor
Zakusilova, Vera – From 9/26/19
Zamora, Cirilo – From 3/1/2021- To 6/12/2021

Undergraduates and Student Technicians

Ascione, Alexander
Griffin, Morgan – To 5/31/2021
Iles, Haley – To 5/2020
Jeffery, Logan
Jeske, Colby
Lofton, Kylie – From 9/21/2020
Roa, Karthik
Vonder Haar, Amy –From 6/15/2020 - To 3/31/2021

ORGANIZATIONAL CHART - CYCLOTRON INSTITUTE

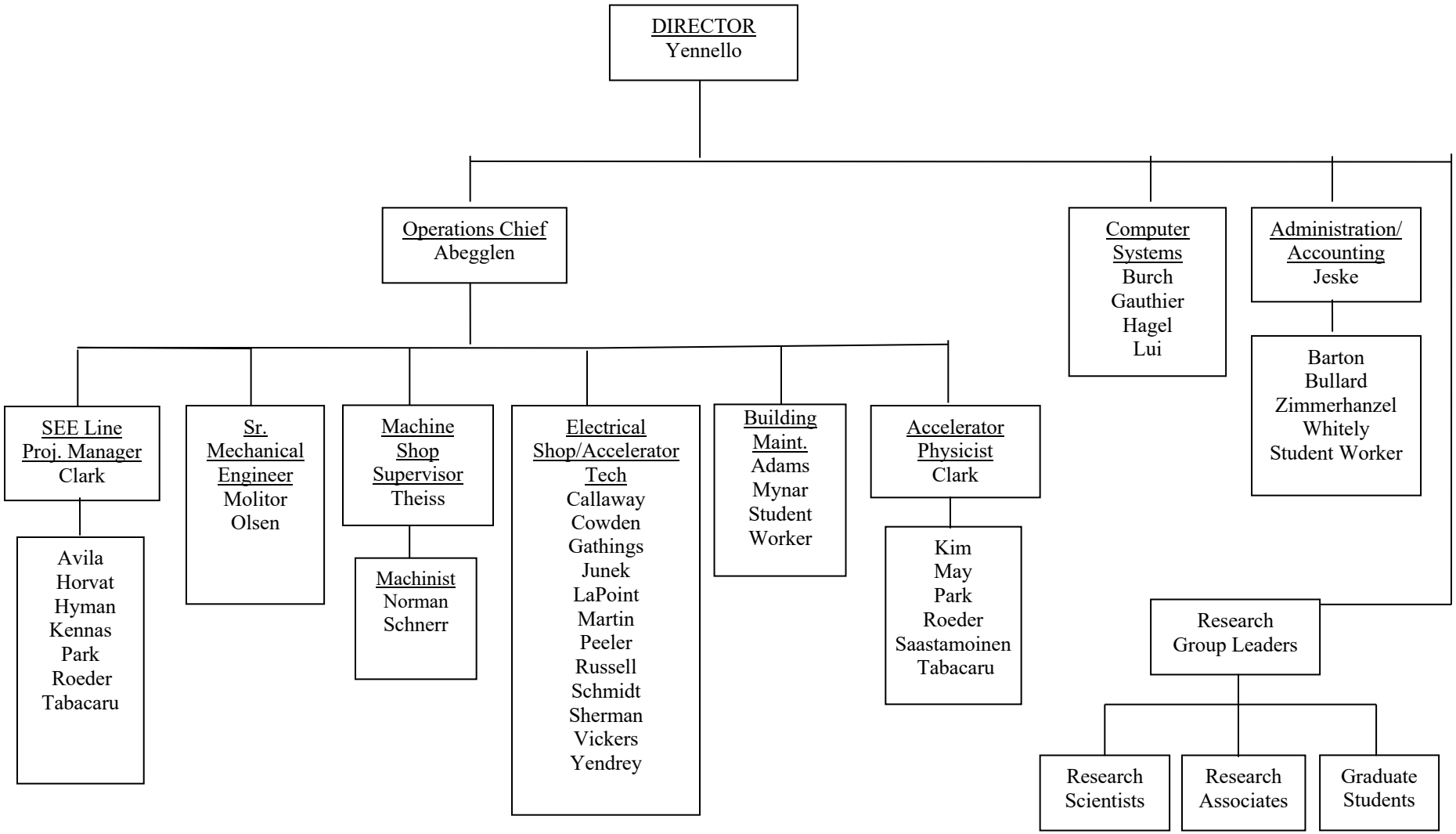

STUDENTS WHO RECEIVED GRADUATE DEGREES
FROM THESIS WORK CONDUCTED
AT
THE CYCLOTRON INSTITUTE

April 1, 2020 – March 31, 2021

Name	Year	Thesis Title	Advisor	Present Position
Eames Bennett	2020	*Mean-field investigation of strength functions of giant resonances compared with the unexpected experimental characteristics*	G. Christian	Los Alamos national laboratory, Los Alamos, New Mexico
Andrea Jedele	2020	*Searching for neutron-proton equilibration at Fermi energies*	S.J. Yennello	Post Doc., GSI, Germany
Taylor Whitehead	2021	*α-capture reaction rate for $^{22}Ne(\alpha,n)^{25}Mg$ reaction via sub-Coulomb α-transfer and its effect on final abundances of s-process isotopes*	C.M. Folden III	N/A

INSTITUTE COLLOQUIA AND SEMINARS

April 1, 2020 - March 31, 2021

2020

September 8	Dr. Alessandro Lovato, Physicist, Argonne National Laboratory, Lemont, Illinois	*An overview of nuclear quantum Monte Carlo*
September 29	Dr. Corina Andreoiu, Associate Professor, Department of Chemistry, Simon Fraser University, Burnaby, British Columbia, Canada	*Decay spectroscopy experiments with GRIFFIN at TRIUMF*
October 13	Dr. G. Wendell Misch, Los Alamos National Laboratory, Los Alamos, New Mexico	*Neutrinos from pre-supernova stars*
November 24	Dr. Kevin John, Chemistry Deputy Division Leader and Ac-225 Tri-Lab Project Manager, Los Alamos National Laboratory, Los Alamos, New Mexico	*High-energy accelerator production and radiochemical processing of ^{225}Ac for cancer therapy*
December 1	Dr. Yevgen Koshchiy, Assistant Research Scientist, Cyclotron Institute, Texas A&M University, College Station, Texas	*State of the art experiments with active target detectors, developed at Cyclotron Institute*

2021

March 9	Dr. Julia Even, Assistant Professor and Rosalind Franklin fellow, Van Swinderen Institute for Particle Physics and Gravity, University of Groningen, Groningen, Netherland	*The next steps towards the outskirts of the nuclear landscape*